Molecular Hydrogen Line Emission From Photodissociation Regions

Antonio Chrysostomou

Presented for the Degree of Doctor of Philosophy
at the University of Edinburgh
1992

Dedicated To My
Mother and Father

This thesis is my own composition except where specifically indicated in the text.

November 1992

Dedicated To My
Mother and Father

Contents

1 Introduction 1

1.1 The Modelling of Photodissociation Regions 3
1.1.1 The H_2 Molecule 3
1.1.2 Photodissociation of the H_2 Molecule 4
1.1.3 Fluorescence of the H_2 Molecule 5
1.1.4 Pure Fluorescent H_2 Emission in PDRs 7
1.1.5 H2 Emission From High Density PDRs 12
1.2 Gas Heating and Cooling Mechanisms in PDRs 23
1.2.1 Gas Heating 24
1.2.1.1 Photoelectric Emission From Dust Grains 24
1.2.1.2 H_2 Vibrational Heating 26
1.2.1.3 H_2 Formation Heating 26
1.2.1.4 H_2 Photodissociation Heating 28
1.2.1.5 Absorption of Grain Infrared Emission 29
1.2.1.6 Cosmic Ray Heating 29
1.2.1.7 Heating by Carbon Ionisation 29
1.2.2 Gas Cooling 30
1.2.2.1 Cooling By Atomic Fine-Structure Transitions 30
1.2.2.2 Cooling By Molecular Line Emission 31
1.2.2.3 Cooling By Gas - Grain Interactions 33
1.3 Observations Of Photodissociation Regions 35
1.3.1 Far Infrared Observations 35
1.3.2 Near Infrared Observations 36
1.3.3 Submillimetre And Radio Observations 40
1.4 Organisation and Aims Of The Thesis 42

2 The Structure Of Photodissociation Regions 43

2.1 Introduction 43
2.2 The Structure Of Photodissociation Regions 44
2.2.1 The Analytical Model 44
2.2.2 Energy Balance In The Model 47
2.2.2.1 Photoelectric Heating 48
2.2.2.2 H_2 Vibrational Heating 49

2.2.2.3 Atomic Cooling 50
2.2.2.4 Gas-Grain Collisional Cooling 51

2.2.3 Density And Temperature Profiles 52
2.2.3.1 Hydrogen Density Profiles 52
2.2.3.2 Heating and Cooling Profiles 55
2.2.3.3 Temperature Profiles 59

2.3 Near Infrared Observations of Photodissociation Regions 59

2.3.1 Observations and Data Reduction 60
2.3.1.1 Data Reduction Procedure 61
2.3.1.2 Calibration of Data 66

2.3.2 Results 67
2.3.2.1 The H_2 v=1-0 S(1) Image 68
2.3.2.2 The Brackett γ Image 68
2.3.2.3 The 3.28 mm Image 73
2.3.2.4 Comparison of 3.28 mm Image With H_2 and Br γ 74

2.3.3 Discussion 77
2.3.3.1 Clumping and Morphological Structure 77
2.3.3.2 Attenuation of Ultraviolet Photons in PDRs 79
2.3.4 Conclusions 84

3 Near Infrared Spectroscopy Of H_2 In M17 Northern Bar 86

3.1 Introduction 86
3.2 Observations And Data Reduction 87
3.2.1 Data Reduction Procedure 89
3.2.2 Wavelength and Flux Calibration 90
3.2.3 Line Fitting 92
3.3 Results 93
3.3.1 The Appearance of the Data 93
3.3.2 Extinction and Intensity Measurements 93
3.4 Discussion 100
3.4.1 Physical Conditions and Line Ratios 100
3.4.2 Geometry and Clumping 103
3.4.3 Excitation Temperatures And The Ortho To Para Ratio 108
3.5 Conclusions 114

4 The Ortho to Para Abundance Ratio In PDRs 115
4.1 Introduction 115
4.2 The Ortho to Para Abundance Ratio 116
4.2.1 Calculation Of The Ortho to Para Ratio In A PDR 118
4.2.1.1 Gas-Gas Interactions 120
4.2.1.2 Gas-Grain Interactions 123
4.2.1.3 H2 Formation on Grains 123
4.2.1.4 Model Results 124
4.2.2 Observations Of The Ortho To Para Ratio 133
4.2.3 Alternative Models 134
4.2.3.1 Residence Time After Formation 134
4.2.3.2 The Dynamic PDR Model 136
4.2.3.3 Spin Exchange During The Fluorescent Cascade 137
4.2.4 Line Ratios And The Ortho To Para Ratio 141
4.2.5 H2 Reformation Spectrum 145

5 Conclusions and Future Prospects 149
5.1 Conclusions 149
5.2 Future Prospects 154

6 References 157

Abstract

The work presented in this thesis is dedicated to the study of the physical properties of photodissociation regions (PDRs), the surface layers of molecular clouds which are irradiated by ultraviolet radiation. The structure of PDRs is investigated with the development of an anlytical model which incorporates the essential heating and cooling mechanisms in a PDR. The main parameters in the model are the density and the incident ultraviolet radiation field, above the ambient value in the solar neighbourhood, impinging on the surface (G_0) which dissociates the molecules in the PDR. It is demonstrated that when the ratio (n/G_0) is high ($> 100\ cm^{-3}$) the attenuation of ultraviolet photons is dominated by H_2 self shielding which brings the HI/H_2 transition zone close to the surface of the cloud ($A_v < 1$). When the ratio is of order unity then the attenuation of ultraviolet photons is dominated by dust grains in the PDR. In this case, the HI/H_2 transition zone occurs at a depth of $A_v \sim 2 - 3$.

Images of the PDR in the northern bar of M17 show that there is a spatial coincidence, accurate to ~ 1 arcsec, of the H_2 and 3.28 μm emission regions (the 3.28 μm emission being a tracer of the hot edge of the PDR delineated by the HII/HI transition) placing a lower limit to the density in the clumps of $10^5\ cm^{-3}$. This coincidence is also observed in other PDR sources (eg. NGC 2023) and can be readily explained if the sources are clumpy. It is not clear in the northern bar of M17, where $G_0 \sim 10^4$, whether shielding by dust or H_2 molecules is dominating the attenuation of ultraviolet photons. A uniform, high density PDR model is sufficient to reproduce the observed H_2 line intensity, however the images clearly reveal structures at the 2 arcsec level suggesting that a clumpy model is a realistic solution.

Long slit K band spectroscopy measurements were taken in the northern bar of M17, where up to 16 H_2 lines were identified. Analysis of the data suggests that the emission can only be explained if the H_2 molecules are being excited radiatively, rather than by shocks. The diagnostic line ratio of the H_2 v=1-0 S(1) and 2-1 S(1) transitions is approximately 3 over the region observed implying that the lower levels of the molecule are slightly thermalised by the warm gas. The constancy of the ratio further implies that that the collisional deexcitation rate must be constant along this region. This may be taken to mean that the physical conditons do not change along the region and that we are observing the surface of the PDR. The profile of the molecular emission along the slit can be successfully modelled if it is assumed that the large scale surface geometry in the region can be described by a parabola.

The ortho to para ratio of H_2, measured in three PDR sources (M17 northern bar, NGC 2023 and Hubble 12), is less than the expected value for a hot (~ 300 K) gas in thermodynamic equilibrium (ie. 3). The measured values fall in the range 1.3 - 2.3. Modelling the ortho to para ratio using the rates of spin conversion of the H_2 molecule do not satisfy the observations. Some other form of processing the ortho to para ratio must be occuring and three different models are considered. First, a different reformation mechanism is considered which allows the newly formed molecule to reside on the surface of the grain for a certain amount of time before it evaporates into the gas. The second model describes a dynamic PDR. Hot gas at the surface of the

PDR is allowed to escape setting up an advancing photodissociation front. If the front advances in to the cooler gas before there is enough time for spin changing interactions to take place, then the measured ortho to para ratios will have values characteristic of the cooler (T ~ 50 - 150 K) gas. Both of these models can successfully reproduce the observed ortho to para ratios. The third model assumes that there is some processing of the ortho to para ratio during the fluorescent cascade, after it has been excited by ultraviolet photons. This model is not successful at reproducing the observed ortho to para ratios as the cross sections in the excited states are so large compared to the radiative decay rate that the ortho to para ratio is determined at the gas temperature, giving ratios ~ 3.

Column densities calculated from the emission from NGC 2023 has shown an excess of emission above the pure fluorescent cascade in levels which are highly rotationally ($J \geq 6$) and vibrationally ($v = 3 - 6$) excited. In according with theoretical predictions, this may be the first direct evidence of the formation of H_2 occuring in excited levels.

Acknowledgements

I have greatly enjoyed my last three years in Edinburgh and (as always) there are a few people that I wish to thank. First on the list is Peter Brand. He has been a great supervisor and friend since I arrived and all his help, discussions (grillings?), questions and especially his boundless enthusiasm for the subject have been a great help to me. I eagerly look forward to our future collaborative work and hope that it carries on in the same vein (but the next time I buy the drinks in Uncle Billy's bar!)

I should also like to take this opportunity to thank some my friends from the years B.E (Before Edinburgh). I would like to thank Christophe (wherever he is) for first getting me interested in Astronomy. Thanks to Andy for letting me be a big brother to a little brother that I never had. To Rula & Dietmar, Peter, Neil & Alison, David, James and finally (but never the least) Nevin. Thank you for the making three years in the East End of London bareable and even enjoyable - from Queen Mary's, to Clement's Road, to Upton Park.

When I first came to Edinburgh I had nowhere to stay, but thanks to the hospitality of one of the nicests redheads I have ever met (I don't think there have been many more than one) I was saved from the streets. Thanks also to Gordon who owns the flat (and also for Gold Bars and Alfred Hitchcock!). To Suzie (or Suzanne, or Sooz, or "Yo, Red!") I give special thanks for being a close friend. Thanks also to the others who arrived at the same time as me : Amadeu for being a compatriot, for being somebody else to talk starformation to, for an office mate and for being tricky with a football; Pippa for knowing the answers to all those questions you always wanted to know the answers to, but were too afraid or embarassed to ask; David for having a VAXstation named after you. There are a few oldtimers which also deserve a mention on this page, especially: Steeeve Torchinsky ("whassamadder Steve, you got a problem or summin'?"), Keef ("ooh, sorry!") Keith Ballard and Chris Davis. Thanks are also due to people like the two Phil's for many useful discussions. Phil Puxley ("shield it Mare!") and Mary Heaton ("Oh God, it's got kreetures") are especially thanked for their friendship.

I would like to thank my collaborators (Mike Burton and Alan Moorhouse) for their help which cannot go by unnoticed. Alan introduced me to data reduction, observing at UKIRT and Uncle Billy's. What a love-hate relationship they all turned out to be! Mike introduced me to the finer points of PDRs (If you wanna know what that means - read the bloody thesis!) and helped me immeasurably with the development of parts of this thesis. I would also like to thank him for being part Australian otherwise I would not have seen my first Kangaroo this summer or heard so many stories about them ["Bloody 'Roo Bahstahds - they get everywhere" - Charlie the Coonabarabran taxi driver (1992)].

This section cannot, absolutely CANNOT, go by without the mention of a few of my flatmates. First we have Bobby Nichol - what a guy! Then there is Mike Read - jeez what a marvellous guy! And of course there's Bob Mann - what can I say, what a wonderful guy! Oh and please don't forget Andy Connolly - the man is dynamite! All of these people have been friends (almost) beyond comparison. From the pubs to the golf courses, from the footy fields to the squash courts, from the clubs to those long enjoyable evenings we've spent in front of the telly, absolutely bored out of our heads! Their memories will linger with me wherever I go!

There are also a couple of institutions which need to be thanked. The Science and Engineering Reasearch Council for a studentship and money for travel and subsistence. To the staff of UKIRT for running and operating such a wonderful telescope. To Renault for building the R5 GT Turbo.

I would like to thank my best friend and πρoτω κoυμπαρo, Nav, for being exactly that. He has been an excellent friend and has always been there when I needed a friend to be there, from the first years in Tulse Hill to the present and into the future. I love the man. Another person I love dearly (but in a different sort of way) is Mila. There is not much I can say to express what I feel for her. She will know what I mean when I thank her for the 3rd of April 1992, 1:30am. The happiest moment in my life.

I have reserved the last paragraph for my family. I want to express my special thanks to my sisters, Sophia and Teresa. They have always looked after their little brother from the beginning and they continue to do so. I'm not complaining! I love you both. My parents have been a tower of strength, support and love. They have always encouraged, helped, and loved me and I hope they are happy with what they have done.

It is with great pride, affection and love that I dedicate this thesis to my mother and father.

1 Introduction

The infrared emission from molecular hydrogen has been detected from a wide variety of astronomical sources over the past 15 years (Shull & Beckwith 1982; Gatley & Kaifu 1987). The first detections of the emission were attributed to the shock excitation of the molecule and quickly the detection of molecular hydrogen was considered a signature of interstellar shocks. This was despite the early prediction by Gould & Harwitt (1963) who suggested that infrared emission from molecular hydrogen might be observed in places where the molecule is exposed to ultraviolet radiation. The theory states that the molecule is excited to its first electronic level after absorbing an ultraviolet photon and then decays down to the ground state, where it fluorescently decays down its vibrational and rotational levels emitting infrared photons. The theory predicts that fluorescent emission from molecular hydrogen should occur widely in the interstellar medium. It is only the lack of instrumental sensitivity which prevented the early searches from finding any fluorescent emission from interstellar molecular hydrogen. However, the first detection of a fluorescent spectrum from molecular hydrogen was finally made in 1987 (Gatley *et al.* 1987; Gatley & Kaifu 1987) in a reflection nebula called NGC 2023. This nebula, and others like it, is a typical example of a photodissociation region (PDR).

Photodissociation regions are found wherever molecular gas is exposed to ultraviolet radiation. PDRs are rather complex structures, chemically and thermally, with the ultraviolet radiation playing a major role in regulating the heating mechanisms and the chemical networks. The ultraviolet radiation field can affect the chemistry down to a depth of $A_V \sim 10$, and hence PDRs represent a large portion of galactic gas, excepting the deepest and densest cloud cores.

Figure 1.1 shows a schematic diagram (reproduced from Tielens & Hollenbach 1985a) displaying the structure of a PDR. Photons with energies greater than 13.6 eV are absorbed in the HII region. There is a sharp HII/HI interface where the PDR begins. Initially the gas is mainly atomic as the relatively high UV flux quickly dissociates the hydrogen molecules. Photodissociation of other molecules such as CO also occurs and atoms with ionisation potentials less than 13.6 eV are ionised (eg. C, S, Fe, Si). It is only when the UV flux is sufficiently attenuated by dust extinction that the atomic hydrogen turns into molecular hydrogen. This occurs at a depth of typically $A_V \sim 1 - 2$.

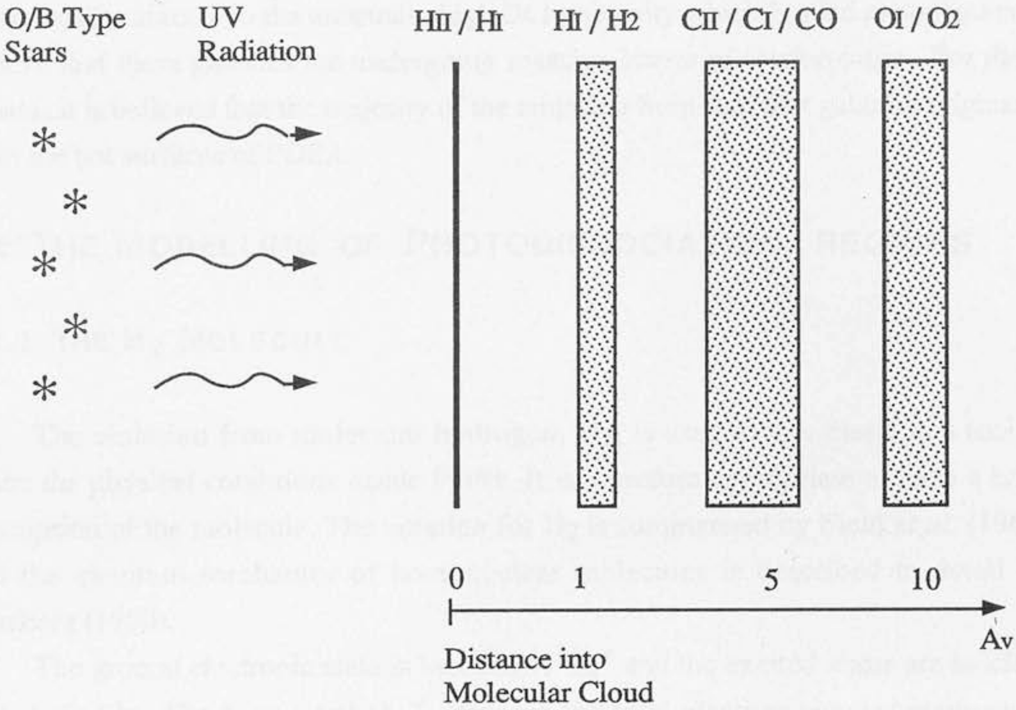

FIGURE 1.1 : A schematic representation of the structure of a photodissociation region adapted from Tielens & Hollenbach (1985a). The diagram shows the chemical transition regions described in the text.

Deeper in, C^+ recombines to form C and CO at a depth of $A_v \sim 2$- 4. Between $A_v \sim 5$ - 10, any O that is not locked in CO is converted to O_2 and H_2O. The PDR is heated primarily by the ejection of energetic electrons from dust grains (photoelectric heating) and cools by the emission of radiation from fine-structure transitions (eg, from C^+ and O) and molecular emission (eg, from H_2 and CO). The heating and cooling mechanisms are discussed in more detail later in this chapter.

Photodissociation regions are found in various astronomical sites. They are present in reflection nebulae and the predominantly neutral clouds about HII regions where recent star formation has taken place. They are also found in planetary nebulae and diffuse clouds exposed to the ambient interstellar radiation. Another interesting and important class of objects where PDRs are thought to exist are starburst galaxies. Observations of [CII] 158 μm and CO J=1-0 emission (Crawford *et al.* 1985) in various starburst galaxies has shown a tight correlation of these emission features together with an anti correlation with HI emission. [CII] 158 μm emission is also a reliable tracer of ultraviolet radiation. Therefore, the [CII] emission cannot be associated with the atomic gas but instead with the molecular gas which consequently must be irradiated by ultraviolet light. These galaxies also have large infrared luminosities suggesting the presence of copious amounts of hot dust heated by ultraviolet radiation from massive stars. It is the unusually high IR luminosity which has led astronomers to believe that these galaxies are undergoing massive *bursts* of starformation. For these reasons it is believed that the majority of the emission from starburst galaxies originates from the hot surfaces of PDRs.

1.1 THE MODELLING OF PHOTODISSOCIATION REGIONS

1.1.1 THE H_2 MOLECULE

The emission from molecular hydrogen, H_2, is used in this thesis as a tool to probe the physical conditions inside PDRs. It is therefore appropriate to have a brief description of the molecule. The notation for H_2 is summarised by Field *et al.* (1966) and the quantum mechanics of homonuclear molecules is described in detail by Herzberg (1950).

The ground electronic state is labelled $X^1\Sigma_g{}^+$ and the excited states are labelled alphabetically. The term symbol, Σ, denotes the total electron angular momentum projected onto the internuclear axis, k (eg. Σ=0, Π=1, Δ=2, etc. in units of Planck's constant h). The total spin angular momentum quantum number for the two electrons takes the values of S=0,1; the value of (2S+1) is the left superscript of the term symbol. The subscripts g or u, and the superscripts + or - (for Σ states) are concerned with the overall symmetry properties of the electronic wavefunction. In a diatomic molecule any plane through the internuclear axis is a plane of symmetry. For a Σ state, the electronic eigenfunction remains unchanged (+) or changes sign (-) when reflected in any plane passing through both nuclei. Similarly, if the two nuclei in the molecule have the same charge the field in which the electrons move has a centre of symmetry. As a consequence of this symmetry, the electronic eigenfunctions remain unchanged (g) or change sign (u) when reflected about this centre of symmetry.

Each electronic state is split into a series of energy levels by the vibrational and rotational motion of the nuclei (Figure 1.2). The nuclear rotation, together with the electronic angular momentum and the total electron spin combine to form the total angular momentum vector, J. The total degeneracy, or statistical weight, of each level is given by g_j=(2J+1)(2I+1), where I=0,1 is the total nuclear spin. For H_2, whose nuclei are identical fermions, the total wavefunction must be antisymmetric with respect to an interchange of the nuclei. Therefore, to preserve the overall antisymmetry of the total wavefunction whenever J is even, I must be odd, ie. I=1. These states are nuclear triplet states and are known as the ortho states of H_2. Conversely, whenever J is odd, I must be even, ie. I=0. These are nuclear singlet states and are known as the para states of H_2.

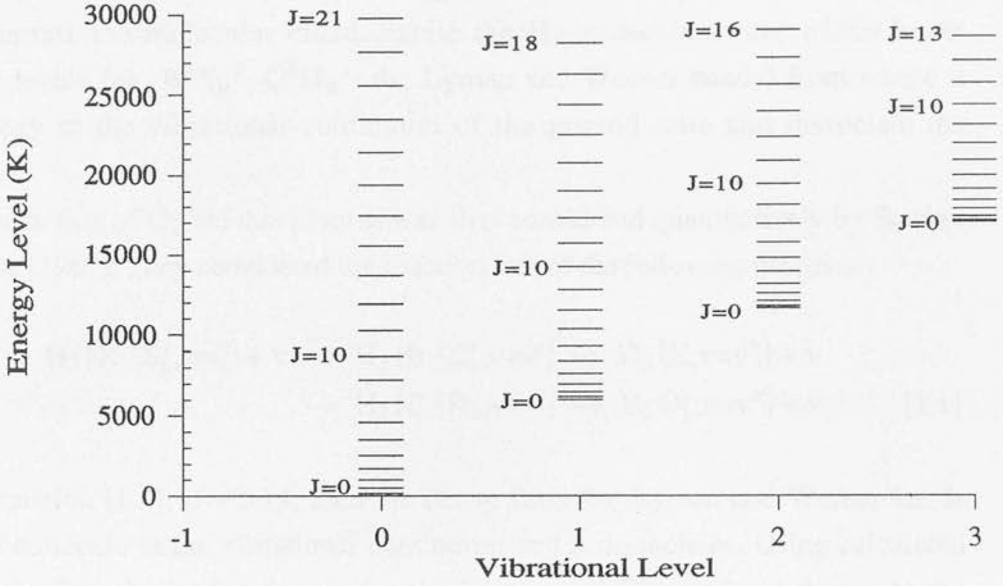

FIGURE 1.2 : A plot representing the energy level structure of the first three vibrational levels of the hydrogen molecule.

The selection rules for the electronic dipole transitions are summarised by Field *et al.* (1966). Briefly, the electronic angular momentum changes by $\Delta\Lambda=0, \pm1$ while the electron spin does not change. States with subscript g combine only with states with subscript u, and vice versa. States with + or - symmetries combine only with like states. In the ground electronic state, dipole transitions between different vibrational and rotational levels are forbidden, however, much slower quadrupole transitions are allowed. The selection rules for the rotational quantum number are, $\Delta J= (J''-J') = +2, 0, -2$ and these transitions are labelled O(J''), Q(J''), S(J'') respectively. There are no rules for the change in the vibrational quantum number due to anharmonicities in the electronic potential function.

1.1.2 Photodissociation of the H_2 Molecule

Before the 1960's it was believed that H_2 could only be dissociated by being electronically excited to the photodissociation continuum which begins at 14.7 eV (Field *et al.* 1966). Since molecular clouds would be shielded from radiation more energetic than 13.6 eV by HII regions, it was thought that an H_2 molecule would only be dissociated if it found itself in an HII region. It was Solomon (see Field *et al.* 1966) who first suggested the possibility of the molecule dissociating via decays into the vibrational continuum of the ground state. Ultraviolet photons with energies less than 13.6 eV could penetrate the molecular cloud, excite the H_2 molecule to one of the lower electronic levels (eg. $B^1\Sigma_u^+$, $C^1\Pi_u$ - the Lyman and Werner bands) from where it would decay to the vibrational continuum of the ground state and dissociate the molecule.

Dissociation of H_2 via this process was first considered quantitatively by Stecher & Williams (1967). They considered the reaction rate of the following process,

$$\begin{aligned} H_2\left(X\ {}^1\Sigma_g^+, v{=}0\right) + \nu &\rightarrow H_2\left(B\ {}^1\Sigma_u^+, v{=}v'\right) \rightarrow H_2\left(X, v{=}v''\right) + \nu \\ &\rightarrow H_2\left(C\ {}^1\Pi_u, v{=}v'\right) \rightarrow H_2\left(X, v{=}v''\right) + \nu \end{aligned} \qquad [1.1]$$

In equation [1.1], if v">14, then the decay from the Lyman and Werner bands leaves the molecule in the vibrational continuum and it dissociates. Using calculated values of the Franck-Condon factors for the Lyman and Werner band decays to the ground state, Stecher & Williams (1967) found that 11% of absorptions through the Lyman bands and 6% through the Werner bands lead to dissociation.

Dalgarno & Stephens (1970) developed a proper quantum mechanical description of this bound-free emission process. In their calculations dissociation through the Lyman bands occurs 23% of the time, while dissociation through the Werner band emission is negligible.

The actual fraction of ultraviolet absorptions which lead to dissociation depends on a few factors including the radiation field, the attenuation of shorter wavelength photons by grains (ie. there is a depth dependence) and the oscillator strengths of absorption and emission to and from the Lyman and Werner band systems. Accurate calculations of the latter are available (Allison & Dalgarno 1970; Dalgarno & Stephens 1970) but the difficulty lies in how the radiative transfer is treated.

1.1.3 FLUORESCENCE OF THE H_2 MOLECULE

As already mentioned in section 1.1.2, approximately 10 - 20% of ultraviolet absorptions dissociate the H_2 molecule. The remaining 80 - 90% decay to bound states of the ground state and then cascade through the vibrational and rotational levels emitting infrared photons. It was Gould & Harwitt (1963) who suggested that near infrared radiation at 2 μm would be produced from H_2, which has been exposed to ultraviolet light, via this method. Furthermore, they recognised the Orion Nebula as a very likely source for this radiation.

In Figure 1.2 we see the energy level structure of the rotational and vibrational levels of the ground state. By considering the cascade through these levels, the infrared emission spectrum from H_2 was first calculated by Black & Dalgarno (1976). Entry into the cascade is provided in two ways. The ultraviolet absorption and fluorescence discussed above and the formation of *hot molecules*, ie. the formation of H_2 on grain surfaces in some excited rotational - vibrational state. The formation of H_2 is still largely an unsolved mystery. It is now strongly believed that in molecular clouds H_2 forms primarily on the surfaces of grains but one can only guess as to how the 4.5 eV of binding energy is distributed amongst the different degrees of freedom. In their calculation, Black & Dalgarno (1976) used very simple assumptions. They assumed equipartition of the binding energy between the kinetic energy of the newly formed molecule, the internal energy of the grain lattice and the internal energy of the molecule. The 1.5 eV of molecular internal energy is then distributed statistically among the rotation - vibration levels. Cascade entry rates from molecular formation is calculated from this distribution.

The population, $n^*(v'J')$, of one of the excited electronic states is governed by,

$$\sum_{v''J''} n\left(v''J''\right) R\left(v''J'',v'J'\right) = n^*\left(v'J'\right) A^*\left(v'J'\right) \qquad [1.2]$$

where, $n\,(v''J'')$ = population of a level in the ground state; $R\,(v''J'', v'J')$ = the rate of absorption from the ground state in a particular line to the electronic state; $A^*\,(v'J')$ = the total probability of a radiative transition out of level $v'J'$.

Once the populations, $n^*(v'J')$, are evaluated the cascade entry rates can be calculated,

$$Q(v_0J_0) = \sum_{v'J'} n^*\left(v'J'\right) A^*\left(v'J',v_0J_0\right) \qquad [1.3]$$

where $A^*(v'J',v_0J_0)$ = the probability of a specific electronic transition to a level v_0J_0.

The equilibrium population of any level vJ can now be calculated by assuming that it is populated by a cascade which began at v_0J_0,

$$n(vJ)\,A(vJ) = \sum_{v'=v}^{v_0} \sum_{J=0}^{J_{max}} n\left(v'J'\right) A\left(v'J',vJ\right) \qquad [1.4]$$

where n(v′J′) = the population of a level higher than vJ which has been populated by the cascade starting at v_0J_0; A(v′J′, vJ) = the probability of radiatively populating level vJ from level v′J′.

Every transition in the rotation - vibration cascade gives rise to an infrared photon. Once having done the cascade calculation, the intensity in any line can be computed by,

$$I\left(v'J',v''J''\right) = \frac{1}{4\pi}\int n\left(v'J'\right) A\left(v'J',v''J''\right) dx \qquad [1.5]$$

Note that the integral over the path length requires a depth dependent model. As the path length is increased, two competing processes occur. As one goes deeper into a cloud the exciting ultraviolet radiation becomes attenuated and so the rate of excitation decreases. However, deeper into the cloud the abundance of H_2 increases as the rate of destruction by photodissociation decreases. At a depth of typically $A_v \sim 1 - 3$, the exciting ultraviolet radiation is nearly all extinguished and the emission from the fluorescent cascade ceases.

The ultraviolet flux density in the model of Black & Dalgarno (1976) is fixed at the cloud boundary to be $G_0 = 10$ times the value of the ambient interstellar radiation field (ISRF) as measured by Habing (1968). Shull (1978) points out that for these low fluxes the cascade through the rotational - vibrational levels is entirely determined by the radiative decay rates, but that for ultraviolet fluxes of $G_0 > 10^4$ a cascading molecule is likely to absorb another Lyman or Werner photon and be *repumped* to the electronic level - multiple pumping. Shull's calculations show that in the low flux case 63% of all cascades pass through the v=1 level, whereas for very high fluxes, $G_0 > 10^6$, that number is drastically reduced by ~3000 to only 0.02%.

1.1.4 PURE FLUORESCENT H_2 EMISSION IN PDRS

A complete cascade calculation which solves the populations for nearly every energy level of H_2 was conducted by Black & van Dishoeck (1987). They used models with low ultraviolet fluxes ($G_0 < 10^3$), avoiding complications due to multiple pumping. To avoid the problem of collisional redistribution (see section 1.1.5) the models were cold (T ~ 100 K) and of low density ($n \leq 10^4$ cm^{-3}). The motive behind applying such conditions was to build a model which would produce the best estimate of a pure fluorescent spectrum from a PDR, and to see how it compares with observations. In all of their models, the PDR considered is a plane parallel, uniform density, isothermal slab of static gas.

The model is depth dependent and at every depth step the model is in steady state equilibrium, ie. all destruction and formation processes for each level vJ are in statistical equilibrium (cf. equation [1.2]). In this way, the level populations at each depth step can be solved and using equation [1.5] the integrated intensities of the emission lines can be calculated. It turns out that, for these low densities and when the gas is isothermal, the relative intensities (ie. line ratios) are insensitive to the input parameters, ie. density, ultraviolet radiation field, molecule reformation rate, grain cross section. However, the absolute intensities depend critically on these factors and how the intensities scale is discussed later in this section.

In steady state equilibrium models, formation and destruction processes are always in balance. That is, for every hydrogen molecule destroyed by dissociation another is formed. In the Black & van Dishoeck model, they find that the dissociation rate of molecular hydrogen is to the order of 10% in good agreement with Stecher & Williams (1967). This means that the contribution to the excitation from reformation will be to the same order. It is therefore important to consider the effects of reformation on the spectrum. Black & van Dishoeck use three different reformation models for comparison. Their standard reformation model statistically distributes one third of the binding energy amongst the internal energy levels of the molecule (cf. Black & Dalgarno 1976),

$$k_{vJ} \propto g_N(2J+1)\exp\left[-\frac{E(v,J)}{17{,}416}\right] \qquad [1.6a]$$

where $g_N = 1$ for even J, $g_N = 3$ for odd J; E(v, J) = energy of level vJ in units of temperature (17416 K = 1.5 eV).

The second formation model, taken from Leonas & Pjarnpuu (1981), has the initial population distribution upon formation given by,

$$k_{vJ} \propto \begin{cases} g_N/4 & , \quad v=14 \ \ J=0,1 \\ 0 & \quad\quad v\neq 14 \end{cases} \qquad [1.6b]$$

The third formation model is taken from a suggestion by Duley & Williams (1986) which says that the molecules are formed with an amount of vibrational excitation comparable to the difference between the binding energy of the molecule and the depth of a potential well on an amorphous silicate surface. It turns out that this means that molecules would then be formed with $v<7$. The initial rotational excitation is described by a thermal distribution at the effective formation temperature, T_f.

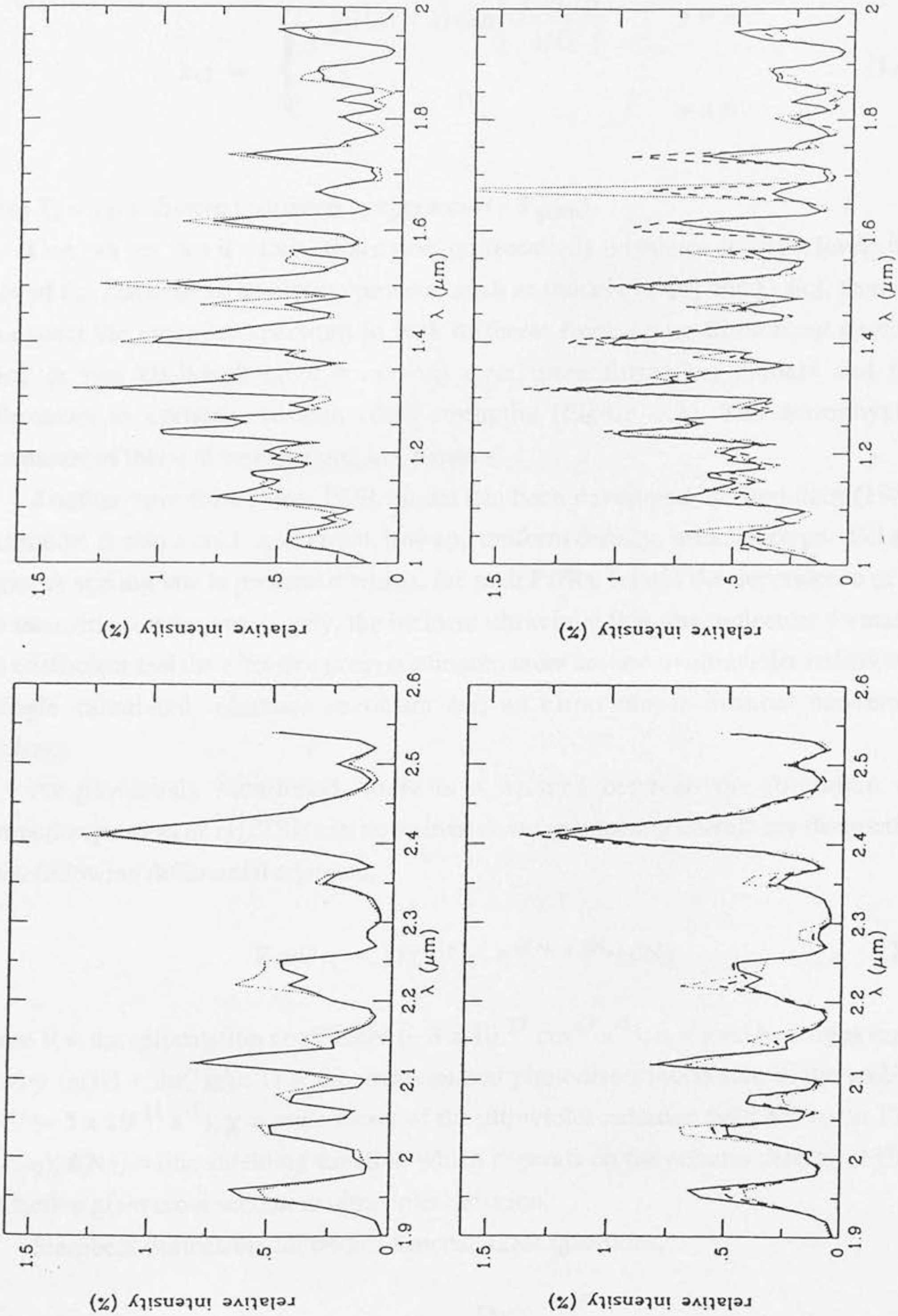

FIGURE 1.3 : Fluorescent spectra showing the difference in emission spectra from models using different reformation models. Model [1.6a] is shown by the solid line and model [1.6b] by the dotted line in the left hand panels. In the right hand panels, model [1.6a] is shown by the solid line, model [1.6c] for $T_f = 15$ K by the dotted line and $T_f = 65$ K by the dashed line. These spectra are from Black & van Dishoeck (1987).

$$k_{vJ} \propto \begin{cases} g_N (2J+1) \exp\left[-\dfrac{E(6,J)}{kT_f}\right] & , \quad v = 6 \\ 0 & \quad\;\; v \neq 6 \end{cases} \qquad [1.6c]$$

where T_f = the effective formation temperature ($\sim T_{grain}$).

One can see that if a formation model preferentially populates different levels than those of the fluorescent excitation process, such as models [1.6b] and [1.6c], then one can expect the emission spectrum to look different from a pure fluorescent cascade. Black & van Dishoeck have compared their three formation models and find differences in certain emission lines strengths (Figure 1.3). The astrophysical importance of this will be discussed in Chapter 4.

Another pure fluorescent PDR model has been developed by Sternberg (1988). This model is also a cold, isothermal, low and uniform density, static plane parallel slab of gas. A scaling law is presented which, for such PDRs, relates the dependence of the line intensities on the gas density, the incident ultraviolet flux, the molecular formation rate coefficient and the effective grain continuum cross section to ultraviolet radiation, to a single calculated reference spectrum and an ultraviolet-to-infrared conversion efficiency.

As previously mentioned, there is a balance between the formation and destruction process of H_2. This can be written down (neglecting cosmic ray destruction) as the following differential equation,

$$R n dN_1 = D\chi\, f(N_2)\, e^{-\sigma(N_1 + 2N_2)}\, dN_2 \qquad [1.7]$$

where R = the reformation coefficient ($\sim 3 \times 10^{-17}$ cm^{+3} s^{-1}); n = total hydrogen nuclei density ($n(H) + 2n(H_2)$); D = the unattenuated photodissociation rate in the ambient ISRF ($\sim 5 \times 10^{-11}$ s^{-1}); χ = scale factor of the ultraviolet radiation field above the ISRF (cf. G_0); $f(N_2)$ = line shielding function which depends on the column density of H_2; σ = effective grain cross section to ultraviolet radiation.

Sternberg defines the following dimensionless quantities,

$$\alpha = \frac{D\chi}{Rn} \qquad [1.8a]$$

$$G(N_2) = \int_0^{N_2} \sigma\, f(N_2')\, e^{-2\sigma N_2'}\, dN_2' \qquad [1.8b]$$

The integral in equation [1.8b] converges to a constant as $N_2 \rightarrow \infty$. Integrating equation [1.7] one is left with an expression for the total H column density in the PDR (Sternberg 1988),

$$N_1^{TOT} = \frac{1}{\sigma}\ln(\alpha G + 1) \qquad \mathrm{cm}^{-2} \qquad [1.9]$$

For simplicity, we can imagine a two level molecule which has a ground state as one of the levels and a bound excited state as the other level, the latter level used to represent the population of radiatively excited hydrogen molecules. These molecules are also subject to a formation-destruction equilibrium which can be expressed as,

$$\mathrm{Destruction} = \mathrm{Formation}$$

$$N^* A = \int_0^{\infty} P\chi\, f(N_2)\, e^{-\sigma(N_1 + 2N_2)}\, dN_2 \qquad [1.10]$$

where N^* = the column density of radiatively excited molecules; A = radiative decay probability to the ground state; P = unattenuated pumping rate (s^{-1}) from the ground state to an excited state, via the electronic level, in the ambient ISRF.

Using equation [1.7] to change the variable of integration (Sternberg 1988),

$$N^* = \frac{Rn}{A}\left(\frac{P}{D}\right) N_1^{TOT} \qquad \mathrm{cm}^{-2} \qquad [1.11]$$

Sternberg measures the efficiency by which incident ultraviolet radiation is converted into infrared fluorescent emission by defining the parameter,

$$Y(\alpha) = \frac{N^*}{\chi} \qquad [1.12a]$$

which, using equations [1.11] and [1.9], can be written as,

$$Y(\alpha) = \frac{1}{\alpha}\left(\frac{P}{A}\right)\frac{1}{\sigma}\ln[\alpha G + 1] \qquad \mathrm{cm}^{-2} \qquad [1.12b]$$

The rate of molecular formation, R, is much slower than the unattenuated rate of photodissociation, D, such that $\alpha \gg 1$. However, since the onset of line shielding occurs for very small column densities ($N_2 \sim 10^{14}$ cm^{-2}; Sternberg 1988) compared to $1/\sigma$, the constant $G \ll 1$. Therefore the product αG can be either smaller or larger than unity and

$\alpha G \sim 1$ for $(\chi / n) \sim 0.01$ cm^3 (Sternberg 1988). When $\alpha G \ll 1$, the conversion efficiency is independent of α, and when $\alpha G > 1$ the efficiency decreases as $\ln(\alpha G) / \alpha$. We can understand a bit more about the physical conditions in these two regimes if we consider the continuum opacity σN_1^{TOT} defined in equation [1.9]. When $\alpha G \ll 1$ then $\sigma N_1^{TOT} \ll 1$ and the total ultraviolet continuum opacity is given by $2\sigma N_2$. In other words, the attenuation of ultraviolet photons is dominated by the self shielding of H_2 molecules alone. When $\alpha G > 1$ then σN_1^{TOT} becomes important and the total ultraviolet continuum opacity is given by $\sigma(N_1 + 2N_2)$, ie. shielding is dominated by dust. Whether line shielding dominates the ultraviolet continuum opacity or not has important consequences on the structure of a PDR, and this shall be discussed in more detail later in this chapter and in Chapter 2.

It is now possible to define the scaling law of line intensities derived by Sternberg (1988). Using equation [1.12] we find that the intensities scale as,

$$\frac{I(n,\chi,R,\sigma)}{I(n_0,\chi_0,R_0,\sigma_0)} = \frac{\chi}{\chi_0}\frac{Y(\alpha)}{Y(\alpha_0)} \qquad [1.13]$$

where the suffix of 0 denotes the values given from the reference spectrum.

When $\alpha G \ll 1$, then the line intensity is proportional to χ, inversely proportional to σ and independent of the molecular formation rate. When $\alpha G > 1$, then the line intensity increases logarithmically with respect to χ. If we ignore small logarithmic factors then the intensity also scales inversely to σ and directly with the molecular formation rate, Rn.

1.1.5 H_2 EMISSION FROM HIGH DENSITY PDRS

The theory of PDRs was advanced when Tielens & Hollenbach (1985a; hereafter TH) developed a model which dealt with the energy and chemical balance of a cloud, exposed to an external ultraviolet flux, as a function of depth into the cloud from the neutral surface. The chemical balance deals with the chemical networks of atomic species such as C, O, Si, S, Fe, Mg and H, and various molecular species such as H_2, H_3^+, CO, SiO, SiH, CH, CH_3, etc. All in all, the chemical network includes reactions between 41 different species. Here, examples of all types of reactions involved in the modelling are given :

Photoionisation reactions :

$$C + \nu \rightarrow C^+ + e^- \qquad [1.14a]$$

Photodissociation reactions :

$$\mathrm{H_2O} + \nu \rightarrow \mathrm{OH} + \mathrm{H} \qquad [1.14b]$$

Ion-Molecule reactions :

$$\mathrm{H^+} + \mathrm{CH} \rightarrow \mathrm{CH^+} + \mathrm{H} \qquad [1.14c]$$

Electron Recombination reactions :

$$\mathrm{Si^+} + \mathrm{e^-} \rightarrow \mathrm{Si} \qquad [1.14d]$$

Neutral-Neutral reactions :

$$\mathrm{C} + \mathrm{OH} \rightarrow \mathrm{CO} + \mathrm{H} \qquad [1.14e]$$

Vibrationally Excited Hydrogen reactions :

$$\mathrm{H_2^*} + \mathrm{OH} \rightarrow \mathrm{H_2O} + \mathrm{H} \qquad [1.14f]$$

Cosmic Ray Ionisation reactions :

$$\mathrm{H_2} + \mathrm{CR} \rightarrow \mathrm{H^+} + \mathrm{H} + \mathrm{e^-} \qquad [1.14g]$$

Charge Exchange reactions :

$$\mathrm{He^+} + \mathrm{Si} \rightarrow \mathrm{Si^+} + \mathrm{He} \qquad [1.14h]$$

Radiative Association reactions :

$$\mathrm{C^+} + \mathrm{H_2} \rightarrow \mathrm{CH_2^+} \qquad [1.14i]$$

Reactions of Negative Ions :

$$\mathrm{H^-} + \mathrm{C^+} \rightarrow \mathrm{H} + \mathrm{C} \qquad [1.14j]$$

Reactions with an Activation Barrier :

$$\mathrm{H_2} + \mathrm{C} \rightarrow \mathrm{CH} + \mathrm{H} \qquad [1.14k]$$

Calculation of the level populations takes into account not only the ultraviolet flux but also the 2.7 K microwave background and the infrared radiation field from the heated dust in the PDR. The radiative transfer used to calculate the line intensities is handled by the escape probability formalism (de Jong *et al.* 1980; TH). Briefly, the probability that a photon escapes through the nearest boundary is approximated by,

$$\begin{aligned} \beta_{\rm esc}(\tau) &= \frac{1 - \exp(-2.34\tau)}{4.68\tau} && \tau < 7 \\ &= \left\{4\tau\left[\ln\left(\frac{\tau}{\sqrt{\pi}}\right)\right]^{0.5}\right\}^{-1} && \tau \geq 7 \qquad [1.15] \end{aligned}$$

where τ = the optical depth in the line.

The heating and cooling mechanisms in the PDR model are dealt with in greater detail in section 1.2. Briefly, the total heating and cooling mechanisms are in equilibrium throughout the PDR, which allows for the temperature of the gas to be calculated, ie.

$$\sum_{i} \Gamma_i(T,x) = \sum_{j} \Lambda_j(T,x) \qquad [1.16]$$

where Γ_i (T, x) = the heating rate of mechanism i at depth x; Λ_j (T, x) = the cooling rate of mechanism j at depth x; T = temperature.

The PDR is predominantly heated by the photoelectric effect on grains ejecting energetic electrons into the gas and is principally cooled by the fine-structure emission lines of [OI] 63 μm and [CII] 158 μm.

The main free parameters in the model are the gas density, n, and the scale factor of the ultraviolet flux, G_0, as measured relative to the ISRF. Other parameters include the turbulent Doppler width, the abundances of the atomic species relative to H, the yield and threshold energy of the photoelectric effect on grains, the emission optical depth at 100 μm and the dust colour temperature. Table 2 of TH lists the values of all these "standard model" parameters. As for all other models already discussed, this PDR is also a static, one dimensional, uniform density slab of gas. However, the density of the standard model of TH is higher than previously considered ($n = 2.3 \times 10^5$ cm^{-3}) and the PDR is not isothermal, since the heating and cooling rates vary with depth. The equations of chemical equilibrium and thermal balance are solved simultaneously to calculate the atomic and molecular abundances and the gas temperature as functions of depth into the PDR.

This model was used to fit to the observed emission from fine-structure lines and some of the low lying CO rotational lines in the PDR in Orion's Bar (Tielens & Hollenbach 1985b). They also found that they could explain the extended H_2 v=1-0 S(1) emission, the carbon recombination lines and a CI line at 9858 Å with a model which suggests that a fairly uniform density ($\sim 10^5$ cm^{-3}) PDR lies behind the Trapezium stars in the Orion Nebula. The intensity of the ultraviolet flux is best fitted if it is $G_0 \sim 10^5$ times above the ISRF.

Most recently the emphasis has been to take the models of TH and Black & van Dishoeck and to extend their parameter space to higher and lower densities and ultraviolet fluxes. In the lower regime, Hollenbach, Takahashi & Tielens (1991) have extended the TH model to include densities of $100 \leq n\ (cm^{-3}) \leq 10^5$ and ultraviolet fluxes of the range $1 \leq G_0 \leq 10^4$. Burton, Hollenbach & Tielens (1990; hereafter BHT) have taken the TH model to the higher regime to include densities of $10^3 \leq n\ (cm^{-3}) \leq 10^7$ and ultraviolet fluxes of $10^3 \leq G_0 \leq 10^5$. Sternberg & Dalgarno (1989; hereafter SD) on the other hand have taken the Black & van Dishoeck (1987) model and extended its parameter space to higher densities and ultraviolet fluxes. In their models, the range of densities is $10^3 \leq n\ (cm^{-3}) \leq 10^7$ while the range in ultraviolet fluxes is 10

$\leq G_0 \leq 10^5$. In the following, I will discuss the high density models of BHT and SD, their similarities as well as their differences.

The BHT model is a slightly evolved version of the TH model, in that there is a more detailed treatment of H_2 and CO. In the TH model, H_2 is treated as a simple two level system (cf. Sternberg 1988) with a ground state and an excited psuedolevel at v=6, representing the population of fluorescently excited molecules. This approximation is retained in the BHT model in calculating the chemical and thermal balance. However, BHT calculate individual level populations of the H_2 molecule, and then line intensities once the temperature and abundances have been calculated at each depth step. The line emission includes a contribution from a thermal component, calculated from the statistical distribution at the local gas temperature and density, and a fluorescent contribution which is given by the excitation rate multiplied by the fraction cascading through that line in the limit of low density and ultraviolet radiation field (this fraction is given by Black & van Dishoeck 1987). The fluorescent component is then modified to account for any collisional deexcitation of the excited levels and for multiple pumping. The intensity of the fluorescent component is given as (BHT),

$$I_{\mathrm{fluo}} = \frac{1}{4\pi} \int \frac{n_2 \, P \, f_j E_j}{\left(\frac{1}{f_{\mathrm{mult}}} + \frac{n}{n_{\mathrm{crit}}}\right)} \, dx \qquad [1.17]$$

where n_2 = density of H_2; P = excitation rate to electronic level; $f_j E_j$ = the fraction of energy going through the emission line (Black & van Dishoeck 1987); f_{mult} = the fraction of molecules in an excited level which radiatively decay before being reexcited (Shull 1978); n_{crit} = the critical density when collisional deexcitations become important.

Other changes from the TH model include the photodissociation rates and self shielding of CO which have been updated in the BHT model following the detailed radiative transfer calculations of van Dishoeck & Black (1988). Most of the findings of the BHT model will be dealt with in greater detail, and in comparison to observations, in later chapters. It will suffice at this stage to summarise the salient points which have developed from the BHT model.

When the gas density in the PDR is sufficiently high relative to the ultraviolet radiation field,

$$\frac{n}{G_0} > 40 \ \mathrm{cm}^{-3} \qquad [1.18]$$

self shielding of the molecules can bring the HI / H_2 and CII / CI / CO atomic-molecular transition zones closer to the surface of the molecular clouds, where the molecules can feel the full effect of heating by the ultraviolet radiation and at this stage, the collisional deexcitation of excited H_2 also becomes an important source of heating. The number given in equation [1.18] is only to be used as a "rule-of-thumb" guide. It is calculated analytically (BHT) by balancing the formation and destruction of H_2 and assuming that the grain attenuation of the ultraviolet radiation is negligible, since we are stipulating that self shielding is dominant. For self shielding to be important for $A_v \leq 1$, this requires the column density to be $N \leq 10^{21}$ cm^{-2}. Imposing this condition to the formation-destruction balance yields the inequality in [1.18].

Line ratios have commonly been used as diagnostics to determine excitation conditions in various objects (eg. Hayashi *et al.* 1985; Brand *et al.* 1988). A common diagnostic has been the H_2 v=1-0 S(1) to v=2-1 S(1) intensity ratio to differentiate between ultraviolet and shock excitation. In a shock, the energy levels are populated from the ground state up and hence the lower levels are always more populated than the higher ones. For H_2, the v=1, J=3 level is at T ~ 6950 K above the ground state while v=2, J=3 is at T ~ 12,550 K, and the transitions of the v=1-0 S(1) to v=2-1 S(1) lines, at $\lambda = 2.1218$ μm and $\lambda = 2.247$ μm respectively, make them an ideal target since not only are they weakly affected by differential extinction but their intensity ratio is a good probe of the excitation conditions. For a shock this intensity ratio is ~ 10 (Shull & Hollenbach 1978). If ultraviolet radiation is exciting the molecule then the energy levels are populated from a radiative cascade and in general the population will tend to be more evenly distributed. The intensity ratio in the case of a fluorescent cascade is ~2 (Black & van Dishoeck 1987). The advantage of using this ratio as a diagnostic between these two excitation mechanisms is clear. However, what the models of BHT and SD have shown is that at high densities ($n > n_{crit}$) and ultraviolet radiation fields, where gas temperatures in the PDR can rise to T ~ 500 - 3000 K, the lower levels appear as if they are *thermalised*, as for a shock. This is due to the combined effect of an increase in importance of the thermal component of the emission, and of the collisional deexcitation of excited levels. Consequently, the diagnostic line ratio of the v=1-0 S(1) to 2-1 S(1) transitions is greater than 2 and in certain conditions can be as large as (or larger than) 10. Hence, the gas appears as though it is being shock excited even though ultraviolet photons are responsible for the excitation. This phenomenon is clearly seen in Figures 1.4a and 1.4b. Figure 1.4a illustrates the difference between column density against energy level plots for a fluorescing source (PDR) and a shock excited or thermal source. In a shock, the level populations all lie along a single curve and the vibrational and

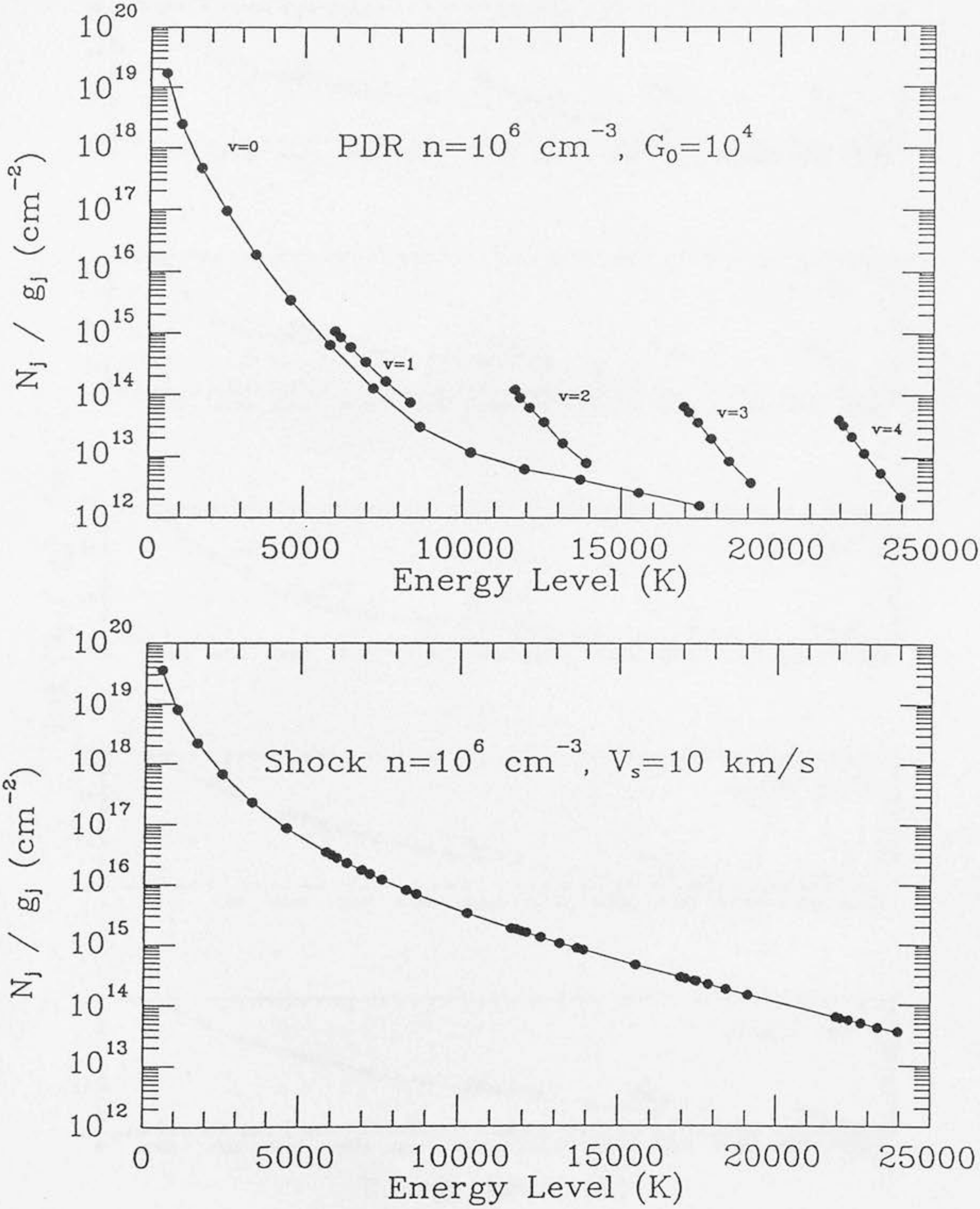

FIGURE 1.4a : Plots of column density against energy level showing the difference in the appearance between fluorescent excitation and shock excitation. The level populations have been normalised to their statistical weights (g_j) assuming an ortho to para ratio of 3. The diagram is taken from Burton (1992).

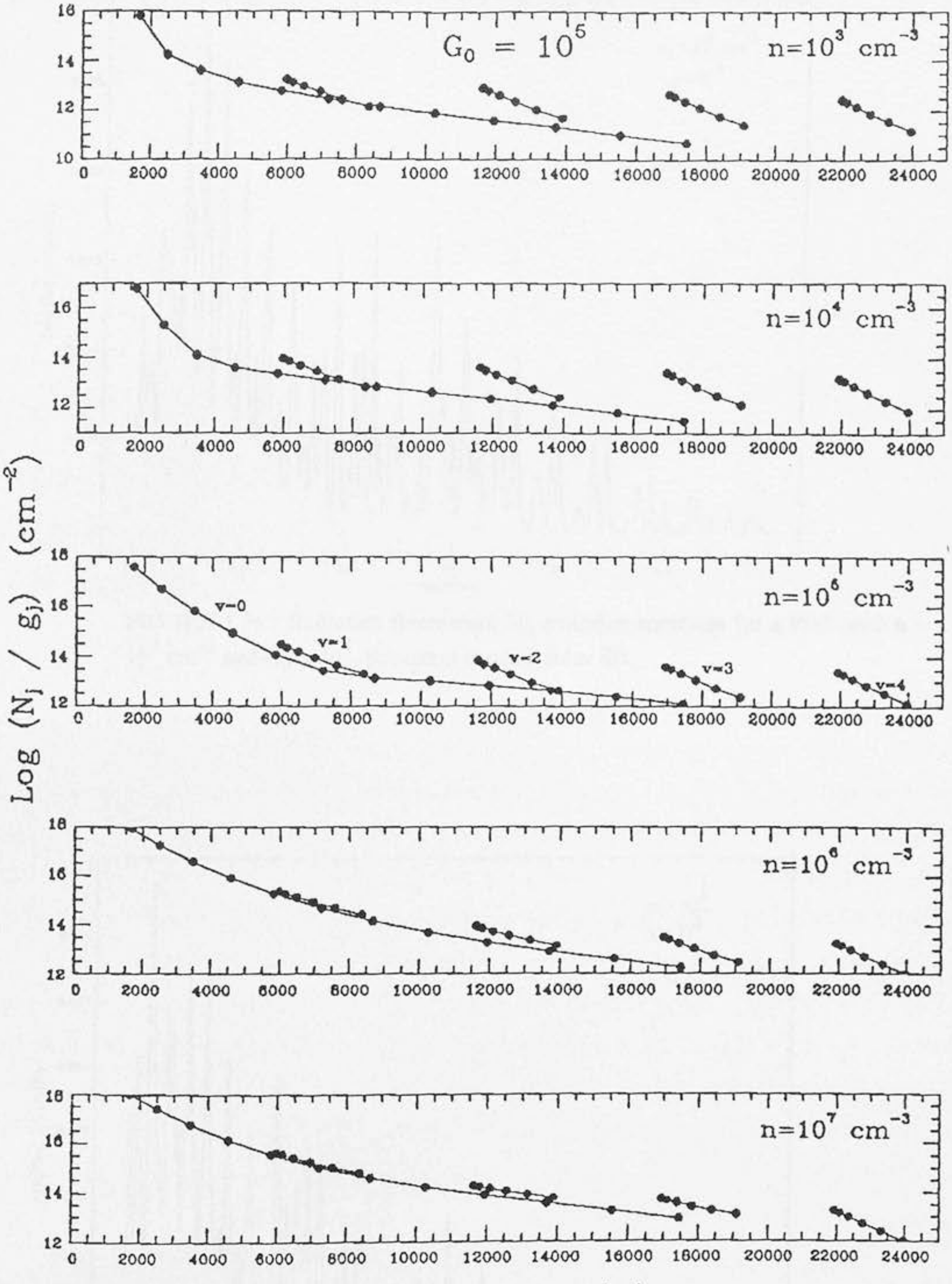

FIGURE 1.4b : Plots of column density against energy levels for various PDR models. The level populations have been normalised to their statistical weights (g_j) assuming an ortho to para ratio of 3. The ultraviolet flux is fixed at $G_0 = 10^5$ and the densities range from $n = 10^3$ - 10^7 cm^{-3}. The plots show up to the 4th vibrational level and the first few rotational levels. The diagram is taken from BHT.

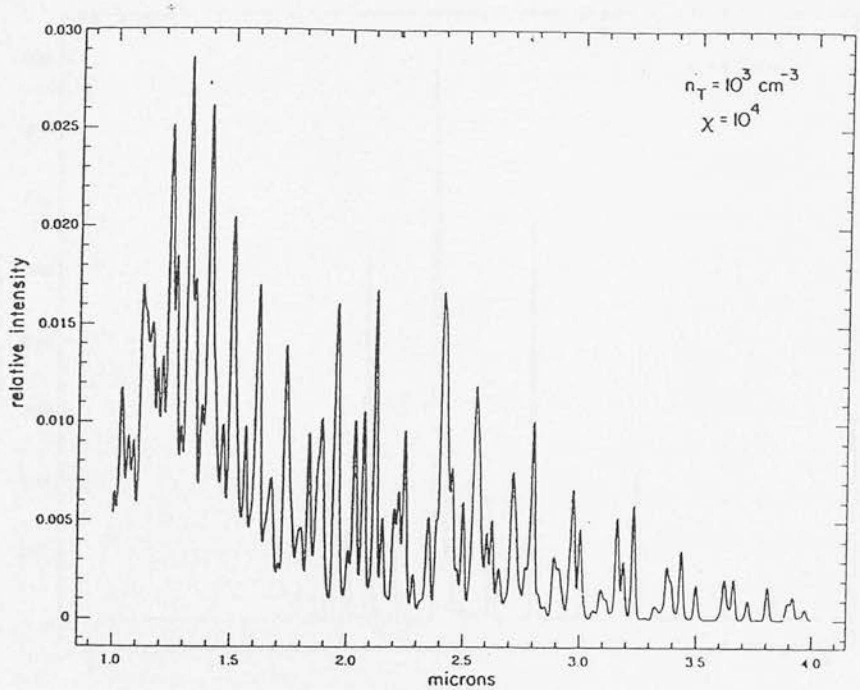

FIGURE 1.5a : Radiative fluorescent H_2 emission spectrum for a PDR with n = 10^3 cm^{-3} and $G_0 = 10^4$. Spectrum is taken from SD.

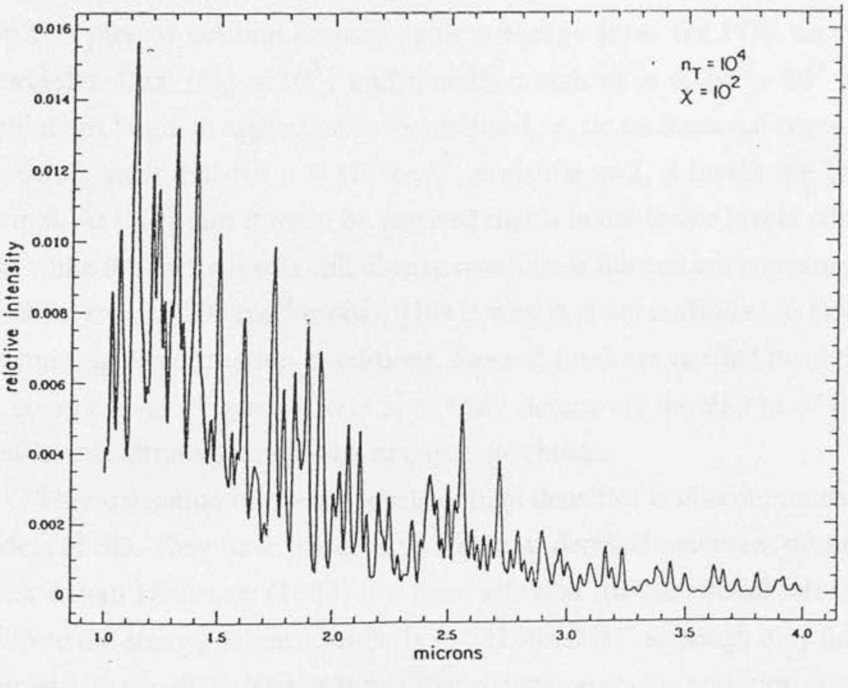

FIGURE 1.5b : Collisional fluorescent H_2 emission spectrum for a PDR with n = 10^4 cm^{-3} and $G_0 = 100$. Spectrum is taken from SD.

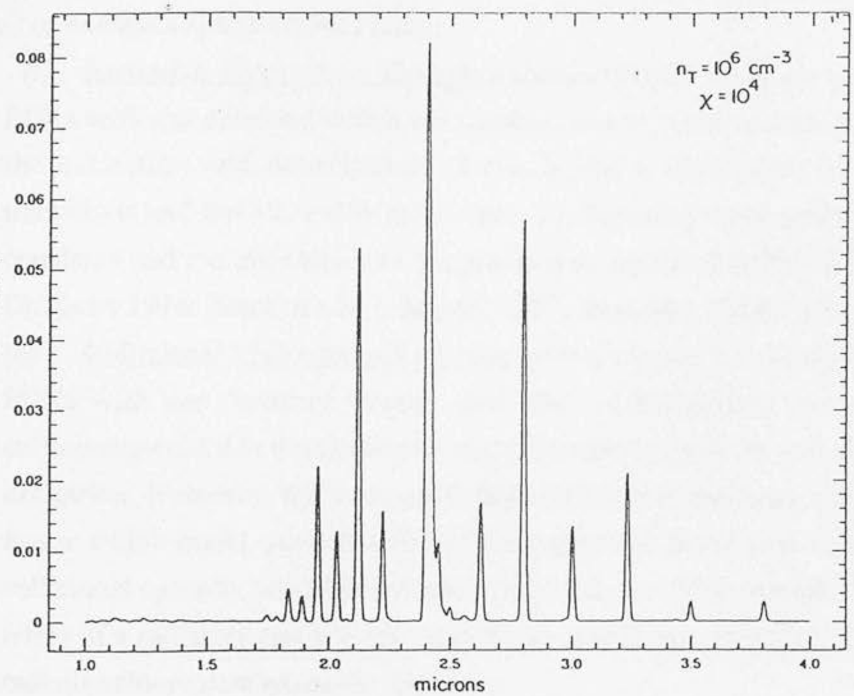

FIGURE 1.5c : Thermal H_2 emission spectrum for a PDR with $n = 10^6$ cm^{-3} and $G_0 = 10^4$. Spectrum is taken from SD.

rotational excitation temperatures are the same. In a fluorescent source, each vibrational level stands up from the others such that it is not possible to put a single curve through all the points, and the vibrational and rotational excitation temperatures differ. Figure 1.4b is a plot of column density against energy level for PDR models with a fixed ultraviolet flux ($G_0 = 10^5$) and density range of $n = 10^3$ - 10^7 cm^{-3}. The level populations begin to appear more thermalised, ie. lie on the same curve, as the density is increased, such that for $n = 10^7$ cm^{-3}, even the v=2, 3 levels are beginning to look thermal. At this point it must be stressed that it is the lower levels which thermalise at first, while the upper levels still clearly retain their fluorescent appearance, eg. the v=3,4 levels for the $n = 10^5$ cm^{-3} model. This is why it is not sufficient to just use two lines in determining the excitation conditions. Several lines are needed from disparate parts of the energy level diagram if one is to truly determine the nature of the excitation, ie. whether it is ultraviolet radiation or energetic shocks.

Thermalisation of energy levels at high densities is also demonstrated by the PDR models of SD. They have undertaken a similar detailed treatment of the H_2 molecule as Black & van Dishoeck (1987) but have allowed for collisional interactions and have followed the energy balance similarly to TH and BHT, although they do not cater for the chemistry in the PDR. The effect of thermalisation on the emission spectra is seen most markedly in Figure 1.5, which are outputs from the SD models. The authors define 3 types of emission spectra from PDRs :

(i) Radiative Fluorescent Emission spectra (figure 1.5a) are produced in PDRs with gas densities which are smaller than the critical density such that the excitation and deexcitation of the levels is dominated by radiative transitions and therefore line ratios are only dependent on known molecular constants and are insensitive to the gas density and ultraviolet flux (Black & Dalgarno 1976; Black & van Dishoeck 1987; Sternberg 1988; SD),

(ii) Collisional Fluorescent Emission spectra (figure 1.5b) are produced in PDRs with gas densities greater than the critical density but which are sufficiently cold that the ultraviolet excitation rate dominates over the thermal excitation. However, the collisional deexcitation rate becomes an important factor which could quench some of the emission. Branching ratios from a collisional cascade, although unknown, are likely to differ from the branching ratios of a radiative cascade and so one can expect line ratios to differ from a radiative fluorescent emission spectrum.

(iii) Thermal Emission Spectra (figure 1.5c) are produced in PDRs with gas densities larger than the critical density and with an ultraviolet flux sufficient to warm the gas so that the thermal excitation of the low lying levels of the molecule becomes important and may even dominate over radiative excitation. Also, the levels which are populated by radiative transitions are collisionally quenched. In this case, both absolute and relative intensities of the emission will depend on the size and temperature of the warm part of the PDR.

Although the thermalisation of energy levels at high densities is clearly an important phenomenon, it is still hard to make accurate predictions using these models simply because the absolute scale of the thermalisation effect is still ill defined as the relevant collision cross sections of the hydrogen molecule are largely unknown - collision cross sections for the first vibrational level are uncertain by an order of magnitude. This is borne out in the differences between the two models. The collisional deexcitation rate of H_2 in warm gas is dominated by collisions with H and for this rate, the two models use two different formulations (for v= 1 - 0 deexcitations):

$$\text{BHT}: \quad 10^{-12}\,T^{0.5}\exp\left(-\frac{1000}{T}\right) \qquad \text{cm}^{+3}\,\text{s}^{-1} \qquad [1.19a]$$

$$\begin{aligned}\text{SD}: \quad & 10^{-12}\,T^{0.5}\exp\left(-\frac{1000}{T}\right) \quad T > 1635\,\text{K} \quad \text{cm}^{+3}\,\text{s}^{-1} \\ & 1.4\times 10^{-13}\,T^{0.5}\exp\left[\left(\frac{T}{125}\right)-\left(\frac{T}{577}\right)^{2}\right] \quad T < 1635\,\text{K} \quad \text{cm}^{+3}\,\text{s}^{-1} \qquad [1.19b]\end{aligned}$$

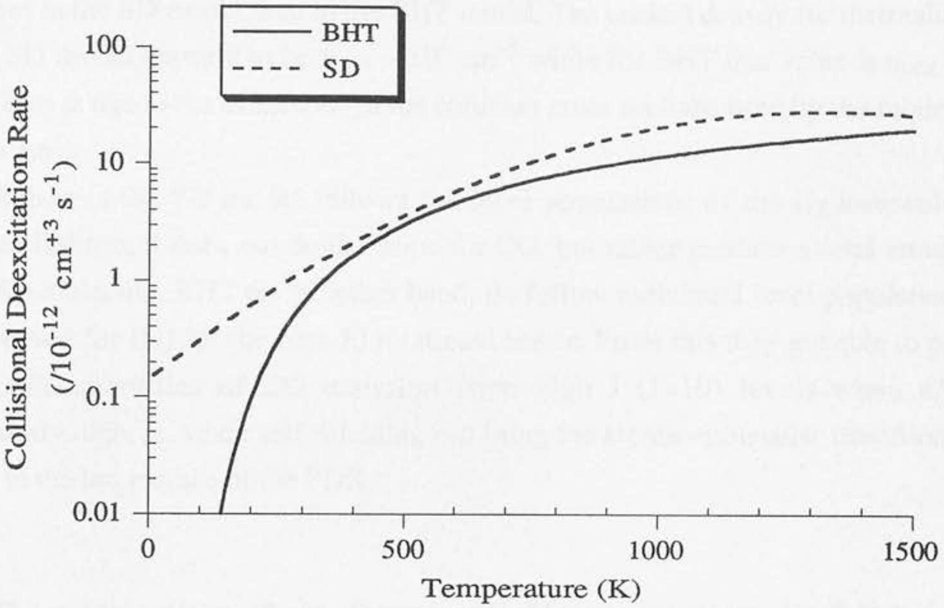

FIGURE 1.6 : Comparison of the collision deexcitation rates used by the BHT and SD models, given by equations [1.19a] and [1.19b], as a function of temperature. The collision rates for SD are higher for cooler temperatures which is why the SD models begin to thermalise for cooler, ie. for lower densities and ultraviolet fields, than the BHT models.

Most regions of the PDR ($A_v > 0.1 - 0.5$) will be cooler than 1500 K so there is obviously a difference in the way that the collisional deexcitation process is treated between the two models. This difference is highlighted in Figure 1.6 which compares the two rates, [1.19a] and [1.19b], as a function of temperature.

Further differences between the two models exist in the way that the important heating process of the photoelectric effect is treated. The heating rate due to this process is handled using formulations developed by de Jong (1980), in the TH and BHT models, and by Draine (1978), used in the SD model. The photoelectric heating in the BHT model is ~ 3 times higher than in the SD model due to the higher efficiencies in the de Jong treatment. Furthermore, the C and O abundances used by SD are a factor of ~ 10 times lower than in the TH and BHT models. This reduces the number of free electrons, made available by the ionisation of C, and therefore increases the positive charge of the grains, thereby reducing their photoelectric efficiency. Fine-structure emission lines, temperature profiles, H, H_2 and CO abundances through the PDR agree well between the two models. However, abundances of OH, H_2O and CH are up to ~ 100 times larger in the SD model, at $A_v \sim 1$. H_2 emission lines agree well for the lower levels (v = 0, 1) but at high densities emission from the higher levels ($v \geq 2$) is greater in the BHT model. The emission spectrum from H_2 seems to thermalise for lower densities in the SD model than in the BHT model. The critical density for thermalisation in the SD model appears to be $n_{crit} \sim 10^4$ cm^{-3} while for BHT this value is $n_{crit} \sim 10^5$ cm^{-3}. This is due to the difference in the collision cross sections used by the models (cf. Figure 1.6).

Whereas the SD model follows the level populations of the H_2 molecule in a detailed fashion, it does not do the same for CO, but rather predicts a total emissivity from the molecule. BHT on the other hand, do follow individual level populations for CO (but not for H_2) for the first 50 rotational levels. From this they are able to predict detectable quantities of CO emission from high J (J>10) levels when n/G_0 is sufficiently high, ie. when self shielding can bring the atomic-molecular transition zone closer to the hot surface of the PDR.

1.2 GAS HEATING AND COOLING MECHANISMS IN PDRS

The heating of molecular or atomic gas in the interstellar medium can occur in various ways. For instance, the passage of a shock wave through the gas will heat it via the collisional interactions which are incurred. The cooling of molecular clouds occurs predominantly via the radiative decay of collisionally excited atoms or molecules. If the emitted photon manages to escape the molecular cloud without being reabsorbed by the gas or dust then this results in the cooling of the gas. Therefore, radiative transfer plays an important role.

In the following sections, I will discuss the interaction between the gas and incident ultraviolet radiation as a source of gas heating. The role of dust grains in mediating photon energy into kinetic energy (ie. gas heating) shall be discussed as well as other gas heating processes which are either directly or indirectly a consequence of the ultraviolet radiation. The physical processes which lead to gas cooling and the approximations which are used in PDR models to deal with this complex problem will be briefly discussed.

1.2.1 GAS HEATING

1.2.1.1 Photoelectric Emission From Dust Grains

Heating of gas by photoelectric emission occurs when a high energy ultraviolet photon interacts with a dust grain resulting in the ejection of a high energy electron into the gas. If these electrons carry more energy than electrons recombining back onto the grain, then this results in the net heating of the gas. Gas heating by the photoelectric effect depends on a number of parameters concerning the grain material and model, the gas and of course the ultraviolet flux. The important parameters are:

(i) the threshold energy or work function of the grain ($E_{gr} \sim 6 - 8$ eV),

(ii) the photoelectric yield ($Y \sim 0.1$) - ie, the number of electrons ejected per photon absorption,

(iii) the sticking probability of recombining electrons (~ 0.5 - 1.0),

(iv) the geometrical grain cross section per hydrogen nucleus,

$$\frac{n_{gr}\,\sigma_{gr}}{n_H} \sim 10^{-21}\ \mathrm{cm}^{+2}$$

(v) the grain efficiency for absorbing ultraviolet photons (~ 0.75),

(vi) the gas temperature,

(vii) the ultraviolet flux.

One can define a heating efficiency for the photoelectric effect, ε, simply as the ratio of heat input into the gas to the total of ultraviolet energy absorbed by the grains. Typically, for every 10 eV photon absorbed, one out of ten times (ie. $Y \sim 0.1$) a 1 eV electron will be ejected. The surplus 9 eV has gone into the electron overcoming the work function of the grain, the coulomb barrier of the grain if it is charged, and in dissipation in the grain lattice as the electron scatters to the surface (Hollenbach 1989). Therefore the heating efficiency is approximately evaluated to be,

$$\varepsilon = \frac{\text{Energy Into Gas}}{\text{Energy Into Grain}} \sim \left(\frac{1\ \mathrm{eV}}{10\ \mathrm{eV}}\right) Y \approx 0.01 \qquad [1.20]$$

Therefore, typically only 1% of the energy absorbed by the grains goes into gas heating via the photoelectric effect. Therefore, the number of photoelectrons introduced into the gas will be very small due to the combination of the small efficiency and the small number density of grains ($n_{gr} \sim 10^{-15}\ n_H$). The electron density in PDRs is therefore traced by the density of ionised material in the gas, which is important for modelling purposes when we consider the number of chemical reactions and networks which depend on electron recombination.

In his analysis, de Jong (1977) calculates the photoelectric heating rate by first considering the charge on a dust grain. This is found by equating the rate of photoejection of electrons from the grains to their rate of recombination,

$$\int_{\nu_0}^{\nu_H} (\sigma_{gr})_\nu \, Y \, \frac{c u_\nu}{h\nu} \, d\nu \; = \; n_e v_e \sigma_{gr} \left(1 + \frac{h\nu_0 - h\nu_{gr}}{kT} \right) \qquad [1.21]$$

where σ_{gr} = geometric cross section of grain; ν_0 = energy barrier electrons need to overcome before ejection ($h\nu_0 = h\nu_{gr} + V_0$); ν_H = Lyman limit where the radiation field is cut off; u_ν = energy density (assumed flat, $u_\lambda = 4 \times 10^{-24}\ G_0\ \mathrm{W\ cm^{-3}}$); n_e = electron density; v_e = root mean square velocity of electrons.

The factor in parenthesis on the right hand side of equation [1.21] takes into account the enhanced recombination rate when the grains are positively charged. Equation [1.21] can be reduced to a cubic equation (de Jong 1977; TH) from which the electrostatic potential, V_0, can be obtained. The cubic equation is written in terms of $x = (\nu_0/\nu_H)$, for which Hollenbach, Takahashi & Tielens (1991) provide an approximate analytic solution,

$$x \sim 1 - \frac{0.28}{\gamma + 0.5} \qquad [1.22a]$$

where,

$$\gamma \approx 0.1 \, \frac{G_0}{n} \, e^{-\tau} \, T^{0.5} \qquad [1.22b]$$

Equation [1.22a] is accurate to within 10% in the limits of $\gamma \rightarrow 0$ and $\gamma \rightarrow \infty$ (Hollenbach, Takahashi & Tielens 1991). When $\gamma \rightarrow 0$, x reduces to its minimum value (x = 0.44, for a work function of 6 eV) which implies neutral charge grains. When $\gamma \rightarrow \infty$, $x \rightarrow 1$ which implies that the grains are highly positively charged. Therefore the parameter γ is a measure of the ratio of the rate at which ultraviolet photons hit the grains to the rate at which electrons recombine on them.

The heating rate by the photoelectric effect is defined to be (de Jong 1980),

$$\begin{aligned} \Gamma_{PE} &= \int (n_{gr}\sigma_{gr})_\nu \, Y \, c u_\nu \, d\nu \\ &= 4.86 \times 10^{-33} \, n \, G_0 \, e^{-\tau} \, \frac{(1 - x)^2}{x} \quad \mathrm{W\ cm^{-3}} \end{aligned} \qquad [1.23]$$

1.2.1.2 H_2 Vibrational Heating

At high densities the radiative cascade of an excited H_2 molecule is interrupted by collisions with other gas particles. This collisional deexcitation process will transform the energy stored in the fluorescent cascade into heating of the gas. The critical density at which this process becomes important is defined by,

$$n_{cr} = \frac{A}{\gamma} \qquad \text{cm}^{-3} \qquad [1.24]$$

where A = spontaneous radiative decay rate (s^{-1}); γ = collisional deexcitation rate coefficient ($cm^{+3}\ s^{-1}$).

The heating rate by H_2 vibrational heating is given to be (BHT),

$$\begin{aligned}\Gamma_{H_2} &= [\gamma_H n(H) + \gamma_{H_2} n(H_2)]\, n^*(H_2)\, E_f \\ &= 3.2 \times 10^{-19} [\gamma_H n(H) + \gamma_{H_2} n(H_2)]\, n^*(H_2) \qquad \text{W cm}^{-3} \qquad [1.25]\end{aligned}$$

With the two level approximation used in the models of TH and BHT, E_f represent the amount of energy offered to the gas after a collisional deexcitation from the pseudolevel at v=6. This energy is, E_f = 2 eV (BHT). The collision cross section with H atoms is given by equation [1.19a] while the cross section for collisions with H_2 is (BHT),

$$\gamma_{H_2} = 1.4 \times 10^{-12}\, T^{0.5} \exp\left[-\frac{18100}{(T + 1200)}\right] \qquad \text{cm}^{+3}\ \text{s}^{-1} \qquad [1.26]$$

H_2 vibrational heating is most effective at high densities and temperatures. It becomes the dominant heating mechanism in extremely dense conditions ($n \sim 10^7$ cm^{-3}, $G_0 \sim 10^4$) where it dominates over the photoelectric effect in the hot atomic region of the PDR.

1.2.1.3 H_2 Formation Heating

Hydrogen molecules are formed most effectively on the surfaces of grains.

Hydrogen atoms are trapped onto the grain surface, they then migrate about it until they meet another hydrogen atom where they interact to form an H_2 molecule. The binding energy released upon formation (~ 4.5 eV) then flows into the various degrees of freedom : translational energy as the molecule is ejected from the grain surface, internal energy of the grain lattice and of the H_2 molecule. The translational motion directly heats the gas, while it will take collisional interactions to transform the internal energies into gas heating (see section 1.2.1.2). The heating rate from the formation of H_2 is (Hollenbach 1989),

$$\Gamma_{\mathrm{form}} = 0.5\left(\frac{n_{gr}\sigma_{gr}}{n}\right) n\, n_H\, v_{th}\, \beta \left[E_{ej} + E_{vr}\left(\frac{1}{1+\frac{n_{cr}}{n}}\right)\right] \qquad [1.27]$$

where n_H = the atomic hydrogen density; β = the probability of H_2 formation on the grain; E_{ej} = translational energy of the H_2 molecule after formation and ejection; E_{vr} = rotational-vibrational internal energy of the H_2 molecule.

The factor of 0.5 reflects the fact that it takes two hydrogen atoms to make a H_2 molecule. The terms to the left of β describe the rate at which hydrogen atoms collide with grains. The factor in parenthesis gives the fraction of excited H_2 molecules which are collisionally, as opposed to radiatively, deexcited. An accurate quantitative calculation of H_2 formation as a heating mechanism is difficult due to the uncertain knowledge of how β varies with gas and grain temperatures as hydrogen atoms can evaporate before combining to form molecules if the grain is too hot. The estimates of E_{ej} and E_{vr}, and the collisional deexcitation rates are also uncertain. However, it is still possible to make assumptions and in their model, SD assume that one third of the available binding energy is converted into kinetic energy, and one third is statistically distributed among the internal energy levels of the molecule (cf. Black & Dalgarno 1976 and equation [1.6a]). Their heating rate due to H_2 formation is given as,

$$\begin{aligned}\Gamma^{SD}_{\mathrm{form}} &= R(T)\, n\, n_H\, E_f \\ &= 2.15\times 10^{-35}\, f_a\, S(T)\, n\, n_H\, T^{0.5} \quad \mathrm{W\ cm^{-3}} \qquad [1.28]\end{aligned}$$

where,

$$\begin{aligned}R(T) &= 3\times 10^{-17}\, f_a\, S(T)\, T^{0.5} \qquad \mathrm{cm^{+3}\ s^{-1}} \\ &= \text{molecular formation rate coefficient}\end{aligned}$$

$$\begin{aligned}S(T) &= \left[1.0 + 0.04(T+T_{gr})^{0.5} + (2.0\times 10^{-3}T) + (8.0\times 10^{-6}T^2)\right]^{-1} \\ &= \text{gas - grain sticking coefficient}\end{aligned}$$

$$f_a = \left[1.0 + 10^4 \exp\left(-\frac{600}{T_{gr}}\right)\right]^{-1}$$

= fraction of atoms which enter impurity sites and go on to form molecules before evaporating

The models of TH and BHT purposely fail to consider ejection of excited molecules into the gas after formation as a source of heating. They reason that since, in equilibrium, nine molecules are excited by ultraviolet photons for every molecule formed or destroyed formation heating must be small when compared to the sum of heating from photodissociation, collisional and photoelectric heating.

1.2.1.4 H_2 Photodissociation Heating

The radiative decay from the excited electronic state to the vibrational continuum of the ground state results in the dissociation of the molecule, and the heating rate associated with this dissociation is given by,

$$\Gamma_{PD} = 0.1\, E_{diss}\, n_{H_2}\, P(v_0 \rightarrow v^*) \qquad [1.29]$$

where $P(v_0 \rightarrow v^*)$ = excitation rate out of the ground state into the excited electronic state; E_{diss} = energy made available to the gas due to dissociation (~ 0.4 eV).

The factor of 0.1 caters for the fact that approximately one in ten excitations lead to dissociation. In their model, TH give the heating rate due to dissociation as,

$$\Gamma_{PD} = 1.36 \times 10^{-30}\, n_{H_2}\, \beta(\tau)\, G_0\, e^{-2.5A_v} \qquad \mathrm{W\ cm^{-3}} \qquad [1.30]$$

where $\beta(\tau)$ = self shielding factor, which accounts for the depletion of line photons deeper into the cloud due to line absorptions.

The self shielding factor also takes into consideration the effect of line overlap, ie. that you cannot extend further out into the line wings to achieve absorption in the same line. In comparison, the model by SD has ignored the effect of line overlap. They argue that even when lines do overlap in the wings, the line opacity will generally be much smaller than the continuum opacity, and therefore line overlap can be ignored. With no continuum opacity then the space between absorption lines is dominated by the damping wings. With continuum opacity then line overlap becomes important only if the effective grain cross section is very small ($\sigma_{gr} \ll 1.5 \times 10^{-21}$ cm^2) or the line separation is very small ($\Delta\lambda \ll 0.1$ nm).

1.2.1.5 Absorption of Grain Infrared Emission

When a grain absorbs an ultraviolet photon it momentarily heats up to a high temperature, sometimes as high as ~ 1000 K, and then it cools by reradiating the energy in the infrared. These infrared photons are then absorbed by the gas. The excited atoms or molecules are then collisionally deexcited, which transfers the energy into the gas and thus heats it. This process only dominates when $T_{gr} > T$, ie. deep in opaque molecular clouds where the photoelectric heating mechanism is negligible.

1.2.1.6 Cosmic Ray Heating

Heating by cosmic rays becomes the dominant heating process deep into molecular clouds ($A_v \sim 10$) where the photoelectric effect and gas - grain interactions are negligible. Furthermore, the rate of cosmic ray ionisation also dominates several chemical channels at these depths since the electron abundance is governed by this rate. Cosmic ray ionisation produces energetic electrons and about 8 eV of energy is deposited into the gas per primary ionisation (TH). The heating rate is,

$$\begin{aligned}\Gamma_{CR} &= 1.5 \times 10^{-18}\, \zeta\, n_{H_2} \\ &= 4.5 \times 10^{-35}\, n_{H_2} \qquad \text{W cm}^{-3} \qquad [1.31]\end{aligned}$$

where ζ = rate of cosmic ray ionisation ($= 3 \times 10^{-17}\ \text{s}^{-1}$).

1.2.1.7 Heating by Carbon Ionisation

The ionisation potential of carbon is 11.26 eV and so carbon exists mostly in ionic form at the edges of PDRs where high energy ultraviolet photons are plentiful. The heating rate due to the ejection of electrons into the gas after carbon ionisation is (TH),

$$\Gamma_C = 2.2 \times 10^{-29}\, n_C\, G_0 \exp\left(-2.4 A_v - \tau_C - \frac{\tau b}{\pi v_1^2}\right)\left(1 + \frac{\tau b}{\pi v_1^2}\right)^{-1} \qquad \text{W cm}^{-3} \quad [1.32]$$

where n_C = number density of neutral carbon; τ_C = optical depth due to self absorption by carbon; b = Voigt parameter (= $9.2 \times 10^{-3} / \Delta v_d$); v_1 = corresponds to frequencies halfway between neighbouring lines (= $500 / \Delta v_d$); Δv_d = turbulent Doppler line width.

The first factor in the exponential term describes ultraviolet attenuation by dust, the second by self absorption and the third by H_2 absorption. This process is important to the chemistry of PDRs since at the cloud edges the electron abundance is governed by the photoionisation and recombination of metals such as C and S.

1.2.2 GAS COOLING

1.2.2.1 Cooling By Atomic Fine-Structure Transitions

The main source of coolant in PDRs are the fine-structure transitions of various neutral and ionised species (eg. C^+, Si^+, C, O, S). In an optically thin medium, the cooling rate due to a transition between levels i and j (i > j) is given by (Hollenbach & McKee 1979),

$$\Lambda_{ij} = n_i A_{ij} E_{ij} \qquad [1.33]$$

When the optical depth in the line is not negligible then escaping photons may be reabsorbed by the gas or dust. The cooling of the gas now depends on the probability that a photon will escape from the gas without being reabsorbed. This probability is given by the escape probability formalism (de Jong *et al.* 1980), β_{esc}, and is defined in equation [1.15]. The cooling rate is now given as (TH),

$$\Lambda_x(\nu_{ij}) = n_i A_{ij} h\nu_{ij} \beta_{esc}(\tau_{ij}) \left\{ \frac{[S_x(\nu_{ij}) - P(\nu_{ij})]}{S_x(\nu_{ij})} \right\} \qquad [1.34]$$

where x = refers to a certain atomic species; n_i = number density of that species in level i; $S_x(\nu_{ij})$ = source function; $P(\nu_{ij})$ = background radiation.

The term in braces is a compensating factor normalised such that any contribution to the radiation at ν_{ij} which is due to background radiation is removed and ensures that the cooling function goes to zero when the radiation in that line is due to the background continuum only. The optical depth averaged over the line is given by,

$$\tau_{ij}(z) = \frac{A_{ij}\, c^3}{8\pi\, \nu_{ij}^3} \int_0^z n_i(z) \left[\frac{n_j(z)\, g_i}{n_i(z)\, g_j} - 1 \right] \frac{dz}{\Delta\nu_D} \qquad [1.35a]$$

where z = depth into the cloud.

The source function is given by,

$$S_x(\nu_{ij}) = \frac{2h\nu_{ij}^3}{c^2} \left(\frac{n_j\, g_i}{n_i\, g_j} - 1 \right)^{-1} \qquad [1.35b]$$

and the background radiation consists of two terms: the 2.7 K cosmic background radiation and the infrared emission due to dust at temperature T_{gr},

$$P(\nu_{ij}) = B(\nu_{ij}, T{=}2.7\ \mathrm{K}) + \tau_{gr}(\nu_{ij}) B(\nu_{ij}, T_{gr}) \qquad [1.35c]$$

To calculate the cooling function it is necessary to solve the equations of statistical equilibrium to obtain the population density of level i, n_i. In a complete model, the resulting equation is very complex, however, one can obtain a simplified solution by only considering the equilibrium for a two level system. The solution to the cooling function is now given by,

$$\Lambda_x(ij) = \frac{n_{tot}\, A_{ij}\, E_{ij}\, \beta_{esc}(\tau_{ij})}{1 + \frac{g_j}{g_i} \exp\left(\frac{E_{ij}}{kT} \right) \left(1 + \frac{n_{cr}\, \beta_{esc}}{n} \right)} \qquad [1.36]$$

Values for A_{ij}, E_{ij}, n_{cr}, g_i and g_j are given in Table 4 of TH for the major atomic coolants in PDRs. Using these values it is possible to derive a cooling function for a PDR due to fine-structure atomic transitions.

1.2.2.2 Cooling By Molecular Line Emission

In photodissociation regions, molecular cooling is dominated by the transitions of H_2 and CO with H_2O and SiO becoming more important in the deepest regions. On the surfaces of PDRs, cooling by the rotation - vibration transitions of H_2 is the dominant molecular coolant. The subject of H_2 emission as a cooling mechanism and its use as a tool in PDR physics is dealt with in other places, and constitutes the major part of this thesis.

Cooling by CO is a complicated process in PDRs, because the abundance of CO is very much dependent on the photochemical evolution of the molecule as a function of optical depth into the PDR. Because of the photodissociation of CO it does not become a major component of the PDR until after self shielding of the destructive photons has occurred. Also, chemical reactions have to channel the C, C^+ and O atoms to produce CO. All this does not happen until $A_V \sim 3 - 5$, although at high densities it is possible to observe transitions from the high J levels of CO at optical depths of $A_V \leq 1$ (BHT). There are various chemical channels which can form CO but the major ones (ie. faster ones) all involve OH, which plays a crucial role in determining the CO structure in PDRs. At the edges of PDRs most of the carbon is in ionic form and the C^+ recombines to form neutral carbon. Both of these forms of carbon react with OH to form CO:

(a)
$$\begin{aligned} C^+ + OH &\rightarrow CO^+ + H \\ CO^+ + H_2 &\rightarrow HCO^+ + H \\ HCO^+ + e^- &\rightarrow CO + H \end{aligned} \qquad [1.37a]$$

(b)
$$C + OH \rightarrow CO + H \qquad [1.37b]$$

Therefore the formation of CO is dependent on the presence of OH, whose formation is triggered by the following charge exchange reaction,

$$O + H^+ \rightarrow O^+ + H \qquad [1.37c]$$

The ionised oxygen atom then goes on to react with H_2 molecules before ultimately recombining to form OH. Because of this initial charge exchange reaction, the formation of OH is quite temperature sensitive as reaction [1.37c] has an activation barrier of 230 K (Hollenbach, Takahashi & Tielens 1991). Therefore, for low densities ($n < 10^4$ cm^{-3}) where the temperature is kept low, OH formation is suppressed and CO can only form deeper into the cloud via other chemical channels involving, for instance, CH (eg. $CH + O \rightarrow CO + H$). The effectiveness of CO as a coolant is therefore diminished in low density PDRs. For denser PDRs, and consequently warmer, a combination of increased OH formation and increased CO self shielding allows CO to form at shorter optical depths through all chemical routes available to it. Similarly to H_2, this also makes the structure of the PDR with respect to the CO molecule, very model dependent.

Because of the complex chemical and photochemical networks which form and destroy CO, together with the model dependence of these processes, it is difficult to analytically formulate the density structure of the molecule through a PDR and derive a cooling function. The only way is to run a complete chemical model in the same way as the TH and BHT models. However, for completeness and in recognition of its importance as a coolant, an analytical solution for CO rotational cooling would proceed with the solution for the population of levels J, followed by a sum over all J for the escaping radiation,

$$\Lambda_{CO} = n\, n_{CO}\, L_{rot} = \sum_{J=1}^{\infty} n_J\, A_J\, \Delta E_J\, \beta_{esc}(\tau) \qquad [1.38]$$

where n_{CO} = total CO density; n_J = density in level J.

1.2.2.3 Cooling By Gas - Grain Interactions

The collisional process between gas and grain particles results in gas cooling when the colliding gas particle has a higher temperature than the grain. For instance, a gas molecule strikes the cooler grain with average kinetic energy 2kT and rebounds or is *re-evaporated* with a lower kinetic energy. The cooling rate of the gas by this process is given by (Hollenbach 1989),

$$\Lambda_{G\text{-}G} = \left(\frac{n_{gr}\,\sigma_{gr}}{n}\right) n^2\, v_{th}\, \alpha_T \left(2kT - 2kT_{gr}\right) \qquad [1.39]$$

where v_{th} = average thermal velocity of the colliding gas particle ($=\sqrt{(2kT/m)}$); α_T = thermal accommodation coefficient.

The thermal accommodation coefficient is defined as when the incident gas particle becomes thermalised with the grain surface (ie. the grain accommodates the molecule) and leaves with an average kinetic energy $2kT_{gr}$, ie. $\alpha_T = 1$ (Burke & Hollenbach 1983). In general though, $\alpha_T < 1$ because bouncing particles do not completely accommodate. Most models use $\alpha_T \sim 0.3$, which is typical for gases and grains at $T \sim 100$ K. Inserting all constant parameters into [1.39],

$$\Lambda_{G\text{-}G} = 3.26 \times 10^{-41}\, n^2\, T^{0.5} \left(T - T_{gr}\right) \qquad \mathrm{W\ cm^{-3}} \qquad [1.40]$$

Note that if the grain temperature lies above the gas temperature, then the gas -

grain interaction results in gas heating. This mechanism is only dominant deep in molecular clouds ($A_V > 3 - 5$). The grain temperature is therefore an important parameter which needs to be monitored through a PDR. The grain temperature follows from the balance between photon absorption and photon emission,

$$4\pi a^2 \int_0^\infty Q_a(\nu)\, \pi B(\nu, T_{gr})\, d\nu = \pi a^2 \int_0^\infty Q_a(\nu)\, F(\nu)\, e^{-\tau_\nu}\, d\nu + 4\pi a^2 \int_0^\infty Q_a(\nu)\, \pi J_{gr}(\nu)\, d\nu \tag{1.42}$$

where $Q_a(\nu)$ = absorption efficiency of grains; a = dust grain radius; $B(\nu, T_{gr})$ = black-body emission at temperature T_{gr}; $J_{gr}(\nu)$ = mean radiation field due to dust emission.

The left hand side describes the photon emission of the dust. The first term on the right hand side describes the ultraviolet photon absorption while the last term describes absorption from the infrared emission of the dust. The dust emission is characterised by a constant temperature T_0 and a total emission optical depth $\tau_{gr} = \tau_{100\mu m}\,(100\ \mu m / \lambda)$, where $\tau_{100\mu m}$ is the 100 μm emission optical depth (eg. TH). Following Hollenbach, Takahashi & Tielens (1991),

$$T_{gr} = \left\{2.66 \times 10^5 G_0 e^{-1.8A_v} + 143.5 + 112.1\, G_0^{1.2}\left[0.42 - \ln\left(4.21 \times 10^{-4} G_0^{0.2}\right)\right]\right\}^{0.2} \tag{1.43}$$

Using this formula the temperature of dust grains in PDRs can be monitored as a function of optical depth.

The model of Burke & Hollenbach (1983) treats the gas - grain surface interaction as if the gas particle were striking a single surface particle which is attached by a "spring" to a fixed lattice (the *soft cube* model). This model ignores lattice and quantum mechanical effects which allows for a simple description of the gas - grain collision process. During a collision a particle's momentum parallel to the grain surface is conserved, but not the momentum in the normal direction. Depending on the amount of momentum transferred in the interaction, the gas particle may rebound with greater or lesser energy than initially, resulting in heating or cooling of the gas. Alternatively, the gas particle may lose so much energy in the interaction that it hops on the surface and becomes trapped, also resulting in cooling of the gas.

1.3 OBSERVATIONS OF PHOTODISSOCIATION REGIONS

1.3.1 FAR INFRARED OBSERVATIONS

The first observational evidence for neutral atomic and partially ionised gas at the interfaces between HII regions and surrounding neutral clouds came from observations of optical lines of neutral carbon (Hippelein & Münch 1978) and from radio recombination lines of carbon (Pankonin *et al.* 1977). An important discovery was the detection of the [CII] 158 μm fine-structure ($^2P_{3/2}$ - $^2P_{1/2}$) transition of singly ionised carbon toward the Orion A HII region (Russell *et al.* 1980) and that in the starforming region of M17 the emission extends over 20′ (12 pc) away from the central OB cluster of stars (Russell *et al.* 1981). From their data, Russell *et al.* (1981) concluded that the HI cloud associated with the [CII] emission had a density $n_H \sim 2 \times 10^3$ cm^{-3}, whereas the theoretically expected density for a HI cloud which is associated with [CII] emission was only $n_H \sim 30$ cm^{-3}. One interpretation of the [CII] data in M17 is that the far infrared line originates not only from the atomic but also from the molecular gas. More recent observations of the [CII] 158 μm fine-structure line in M17 has been carried out by Stutzki *et al.* (1988). They find that there is strong [CII] emission associated with CO J=7-6 emission suggesting that both components arise in the warm HII region - molecular cloud interface. Furthermore, they confirm that there is weaker [CII] emission which extends over 15 pc throughout the molecular cloud (Figure 1.7). Emission this extensive cannot be explained by a model of a single cloud exposed to ultraviolet radiation, as in the model of TH. These observations require that the molecular cloud is clumpy or filamentary so that the ultraviolet radiation from the central stars can penetrate into the dense molecular cloud to a depth of several parsecs, thus creating bright and extended [CII] emission from the photodissociated surfaces of dense clumps, or sheets, of gas deep in the molecular cloud.

The emission from the [CII] 158 μm fine-structure line has also been observed outside of our galaxy. Crawford *et al.* (1985) have observed this line in various external galaxies and found that there is a distinct correlation of this emission with that from the CO J=1-0 transition and with far infrared continuum emission from warm dust (Figure 1.8). At the same time they found that there is an anti correlation with HI emission. Since the [CII] 158 μm and far infrared continuum emissions are good tracers of ultraviolet radiation they came to the inevitable conclusion that the associated [CII] 158 μm and CO lines must arise from the dense photodissociated surfaces of molecular

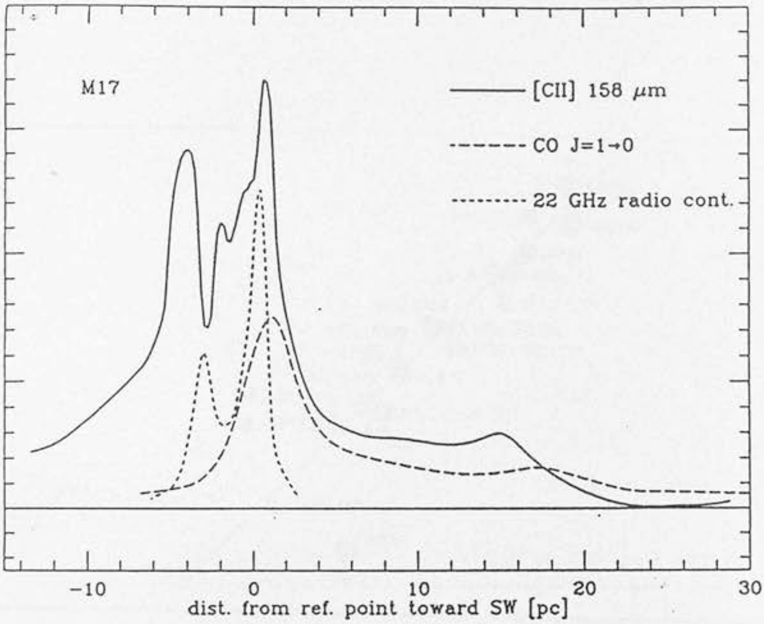

FIGURE 1.7 : [CII] 158 μm emission taken along a strip through the ionisation front and into the molecular cloud in the southwestern bar of M17. Radio continuum emission and CO emission are also shown for comparison. The diagram clearly shows the extent of the [CII] emission into the molecular cloud. Diagram taken from Stutzki *et al.* (1988).

clouds around newly formed stars. Furthermore, they pointed out the dangers of using the integrated emission from CO in starburst galaxies to calculate the molecular hydrogen content of the galaxy, since where the CO is being detected it is also being exposed to radiation which will destroy it, therefore making the often used CO/H_2 abundance ratio unreliable. For a more concise account of observations of far infrared lines (eg. [OI] 63 μm, [SiII] 34 μm) see the review by Genzel *et al.* (1989).

1.3.2 NEAR INFRARED OBSERVATIONS

Observations of PDRs in the near infrared have been absent from the literature until recently when, with the advent of sensitive instrumentation, it is now possible to map sources and follow up with spectral observations. The first maps were made of the H_2 v=1-0 S(1) transition at $\lambda = 2.12$ μm. Various objects such as reflection nebulae (NGC 2023; Figure 1.9a), HII regions (M17, Orion's Bar) and planetary nebulae (Ring Nebula, Dumbell Nebula) were all mapped and copious amounts of H_2 emission was detected and attributed to excitation by ultraviolet photons (see review by Gatley & Kaifu 1987).

The first infrared spectrum from fluorescently excited H_2 was first measured in the reflection nebula NGC 2023 (Gatley *et al.* 1987; Figure 1.9b). H and K band spectra

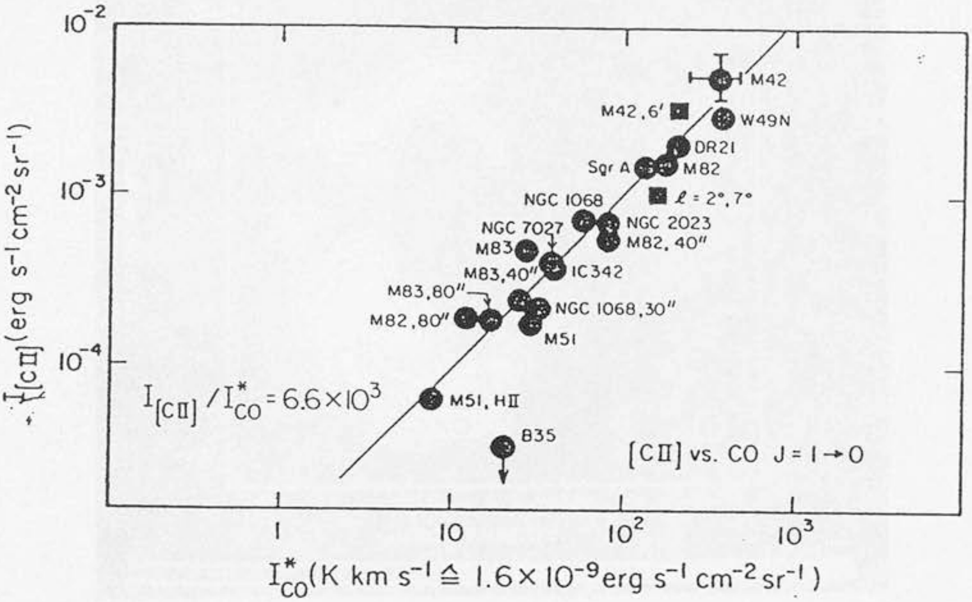

FIG. 5a

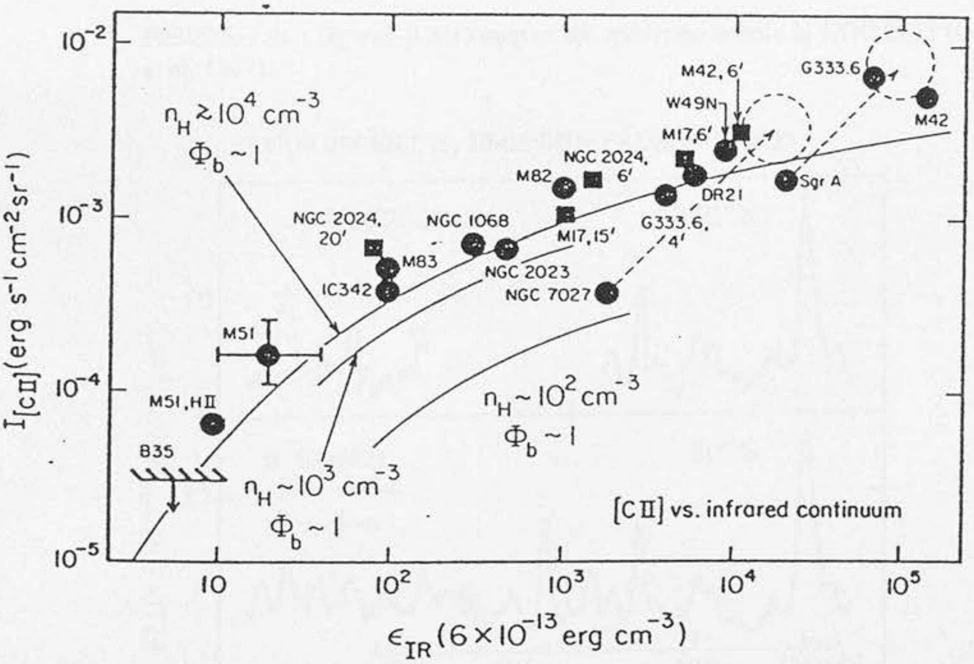

FIGURE 1.8 : The correlation between [CII] 158 μm intensity and CO emission (*top*) and with the intensity of the far infrared continuum (*bottom*). The thin line in the top diagram represents the best fit line. In the bottom diagram, the thin lines represent the predicted [CII] intensities as a function of the infrared energy density for the given hydrogen densities and unit beam filling factor. Diagram taken from Crawford *et al.* (1985).

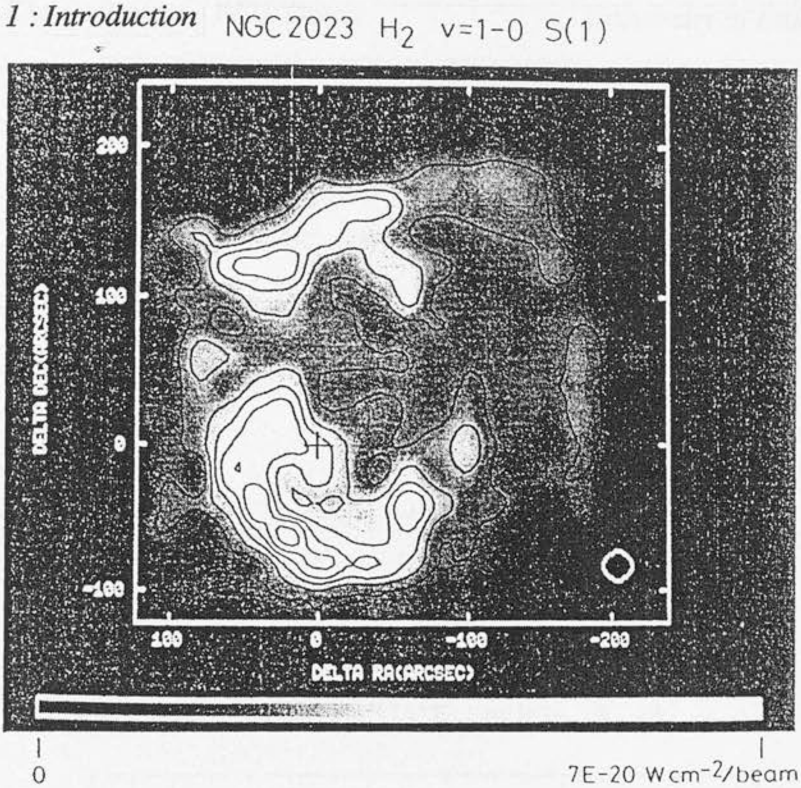

FIGURE 1.9a : H_2 v=1-0 S(1) map of the reflection nebula in NGC 2023 (Gatley *et al.* 1987).

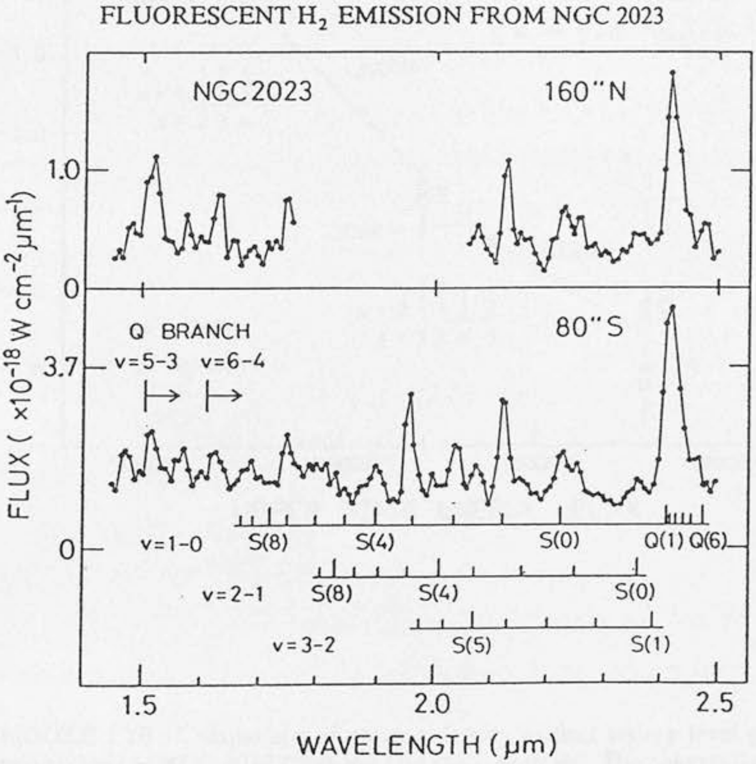

FIGURE 1.9b : H_2 spectrum from the reflection nebula in NGC 2023 (Gatley *et al.* 1987).

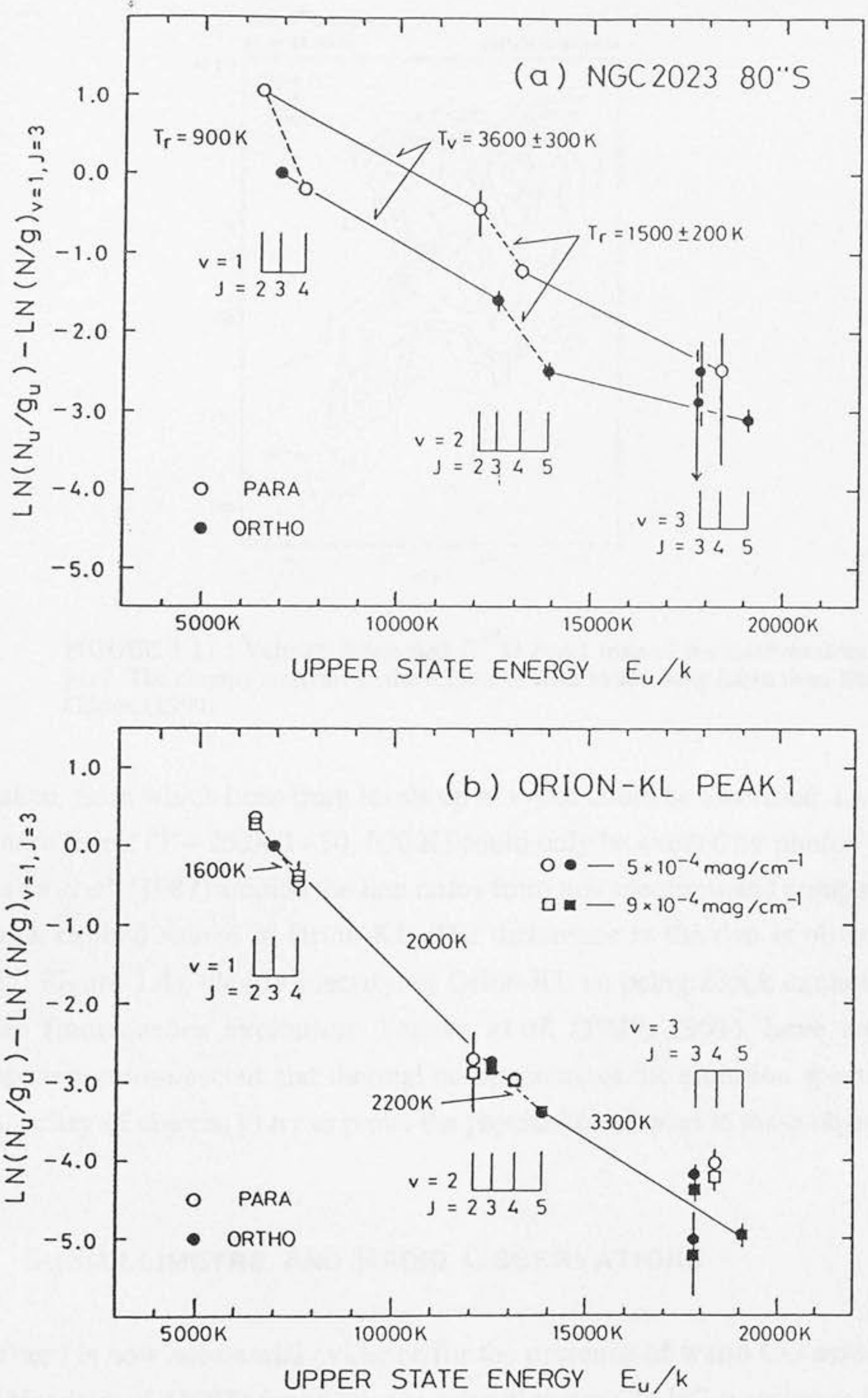

FIGURE 1.10 : Comparison of column density against energy level plots for the two regions of NGC 2023 (*top*) and Orion-KL (*bottom*). The column densities have been normalised to their statistical weights. The plots clearly show the difference in appearance between fluorescent excitation (NGC 2023) and thermal excitation (Orion-KL). The plots are taken from Hasegawa *et al.* (1987).

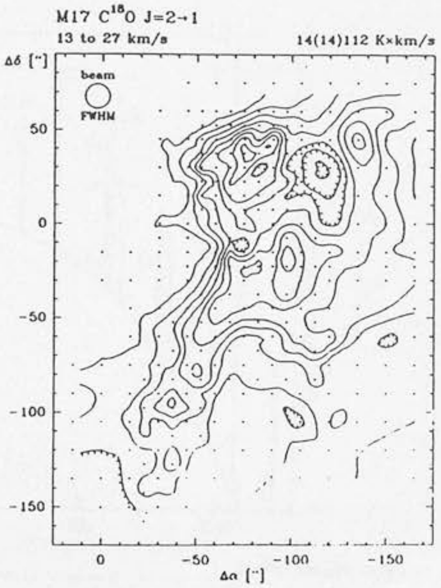

FIGURE 1.11 : Velocity integrated $C^{18}O$ J=2-1 map of the southwestern bar of M17. The clumpy structure in the region is clear to see. Map taken from Stutzki & Güsten (1990).

were taken, from which lines from levels up to v=5,6 could be identified. Line emission from these levels (T ~ 25,000 - 30, 000 K) could only be excited by photon absorption. Hasegawa *et al.* (1987) studied the line ratios from this spectrum and compared them to the shock excited source in Orion-KL. The difference in the two is obvious (Figure 1.10; cf. Figure 1.4), clearly identifying Orion-KL as being shock excited and NGC 2023 as fluorescence excitation. Tanaka *et al.* (1989, 1991), have attempted to decompose the fluorescent and thermal components of the emission spectrum of H_2, from a variety of objects, to try to probe the physical conditions in these objects.

1.3.3 SUBMILLIMETRE AND RADIO OBSERVATIONS

There is now substantial evidence for the presence of warm CO associated with PDRs. Harris *et al.* (1987) found intense submillimetre CO J=7-6 emission in M17 and S106. Far infrared emission from the same regions suggests that the warm CO gas has temperatures of T ~ 150 - 400 K (Harris *et al.* 1987). The distribution of CO flux with rotational quantum number in the PDR in Orion suggests the presence of gas densities ~ 10^6 cm^{-3} and temperatures ~ 200 K.

Felli *et al.* (1984) have mapped the whole of the M17 complex in the radio continuum and find that the ionised material is highly clumped. They interpret their findings as emission coming from the ionised surfaces of neutral, high density clumps

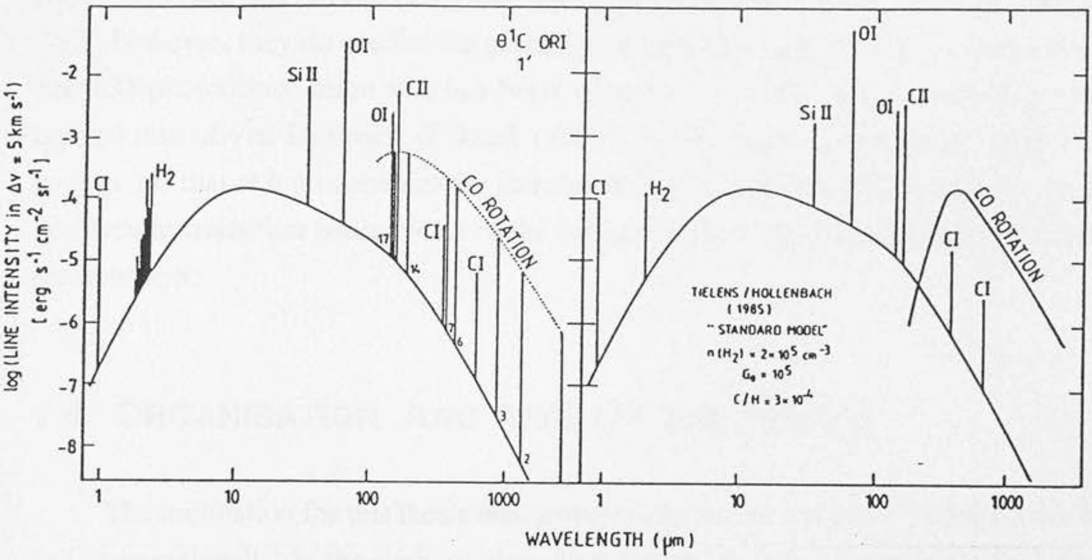

FIGURE 1.12 : Comparison of the observed line emission from the Orion PDR (*left*) and the line emission predicted by the standard model of TH (*right*). Diagram taken from Genzel *et al.* (1989).

left over from the molecular cloud after the ionisation front had passed into the molecular gas. The clumpy nature of the M17 molecular cloud was further investigated by Stutzki & Güsten (1990) who mapped some of the region covered by Stutzki *et al.* (1988) in the transitions of $C^{18}O$ J=2-1 and $C^{34}S$ J=2-1 (Figure 1.11). Their map reveals a clumped structure and a decomposition of the data shows up ~ 180 clumps in the region. The mass spectrum of the clumps closely follows a power law,

$$\frac{dN}{dM} = M^{-\alpha} \qquad \alpha = 1.7 \pm 0.15 \qquad [1.43]$$

and the clump - interclump density contrast is ~ 23. These findings agree well with the model proposed by Stutzki *et al.* (1988) although the density contrast needs to be slightly higher to explain the extensive penetration depth of the ultraviolet photons (Stutzki & Güsten 1990). Once again, for a more concise account of observations of PDRs, both galactic and extragalactic, in the submillimetre and radio, see the review by Genzel *et al.* (1989).

The success of the PDR model in predicting structure and line emissivities from these objects has been very good. Figure 1.12 shows a comparison of the line intensities from the standard model of TH compared to the observed intensities from the PDR in Orion's Bar (Genzel *et al.* 1989). The agreement between the two is very good. However, the model does fail to predict the presence of high J CO emission, which must be arising from the warmest and densest regions. The reason is that in the standard model, most of the CO is dissociated in zones with T > 100 K. In the model of BHT, however, they do predict the presence of high J CO emission from dense PDRs. The CO photodissociation rate has been altered in the BHT model according to the revised rate of van Dishoeck & Black (1988), but the main reason for the high J CO emission is that at high densities the increase in H_2/CO self shielding brings the atomic - molecular transition zones closer to the surface thereby exposing the CO to a warmer environment.

1.4 ORGANISATION AND AIMS OF THE THESIS

The motivation for this thesis was prompted by recent advances, both theoretically and observationally, in the study of photodissociation regions. Theoretically the subject has evolved greatly. From the first considerations of the possibility of dissociating the H_2 molecule and possibly observing its fluorescent cascade, to the highly complicated models which follow the level populations of some 200 - 250 energy levels and of the energy and chemical balance of some 50 different species and their chemical networks. The development of these models has been reviewed in the preceding sections. Observationally, the subject has been dominated by the work done in the submillimetre. However, with the recent advances in detector technology it is now possible to make accurate measurements of these regions in the near infrared and far infrared wavelengths, both in mapping and spectral modes.

It has become clear that the emission spectrum from the H_2 molecule is sensitive to the physical conditions in PDRs, making it an excellent probe of PDRs and PDR physics. However, these models have up till now gone largely unchallenged by observational tests. The aim of this thesis is to show a way of how the theoretical models should be tested. This will be done using our own observational evidence and analysis.

In chapter 2, the structure of photodissociation regions is investigated using a simple analytical model and our own observations of the molecular and ionised gas in our sources. In chapter 3, we follow up with spectral observations of the emission from the H_2 molecule and discuss what the physical conditions in our source may be. In chapter 4 further analysis of our spectral observations is carried out and we discuss the importance of the ortho to para ratio of molecular hydrogen and the formation of the molecule in photodissociation regions. In chapter 5, I summarise the conclusions and look ahead to future work and prospects, and briefly discuss how the subject will evolve in the near future in the light of this work.

2 The Structure Of Photodissociation Regions

2.1 INTRODUCTION

The standard photodissociation region (PDR) models of Tielens & Hollenbach (1985a; hereafter TH) and Black & van Dishoeck (1987) are parameterised by the density and by G_0, the incident ultraviolet flux in units of the local interstellar radiation field (ISRF) - 1.6×10^{-3} erg s^{-1} cm^{-2} in the 6 - 13.6 eV band (Habing 1968). In these models, the photodissociation of H_2 is balanced by reformation on dust grains. At the surface of the molecular cloud the ultraviolet flux is so great that the H_2 molecules are quickly destroyed. Deeper into the cloud ($A_v \sim 1$ - 3) the flux is sufficiently attenuated by dust that the molecular abundance increases.

Burton, Hollenbach & Tielens (1990; hereafter BHT) and Sternberg & Dalgarno (1989) have modelled PDRs at high densities ($n \geq 10^5$ cm^{-3}). At these densities, collisional redistribution of the low lying rotation - vibration levels of H_2 is effective and the spectrum from these levels appears thermalised. Increasing the density in the models with respect to G_0 also affects the structure of a PDR since self shielding is more effective as the ratio of n/G_0 rises. The attenuation of ultraviolet photons then occurs over a shorter optical depth into the cloud than would result from dust extinction alone. The effect is to move the HI/H_2 transition zone towards the cloud surface where $A_v \leq 1$, changing the structure of the PDR and increasing the conversion of ultraviolet flux to heat via collisional deexcitation of the fluorescently excited H_2, in addition to the photoelectric effect.

In this chapter, I will investigate the properties of the structure of PDRs with the help of an analytical model and observations of PDRs. Firstly, I will describe the development of the analytic model and then the structure of the PDR in detail with respect to the abundances of atomic and molecular hydrogen, and also discuss the energy balance between heating and cooling and how the temperature profile of the gas is related to the structure. In the latter part of the chapter I will describe our observations of the PDRs in M17, Orion's Bar and NGC 2023.

2.2 THE STRUCTURE OF PHOTODISSOCIATION REGIONS

2.2.1 THE ANALYTICAL MODEL

The formation and destruction of molecular hydrogen is held in equilibrium in PDR models. The formation of H_2 occurs on the surfaces of grains whereas there are many pathways for H_2 to be destroyed, including cosmic ray ionisation, direct photodissociation (TH), and various chemical channels. The ionisation of H_2 can happen via charge exchange reactions in PDRs, since the ionisation limit is 15.4 eV above the ground state (Field *et al.* 1966) and only photons with energies less than 13.6 eV may be found in PDRs. However, such photons are able to photoionise H_2 if it is in some vibrationally excited state ($v \geq 4$). Out of all these destructive processes, the photodissociation of H_2 is the most rapid, at the surface of the PDR. Therefore, balancing reformation with the destruction of H_2 by photodissociation we have,

$$R n n_H = 0.1 \int F_0 e^{-\tau_{gr}} n_2 e^{-\tau_2} \sigma_\nu \, d\nu \qquad [2.1]$$

where R = reformation rate (= $3 \times 10^{-17} S(T) T^{0.5}$ $cm^{+3} s^{-1}$; TH); S(T) = gas-grain sticking coefficient (see equation [1.28]); n = total hydrogen nucleus density (= $n_H + 2n_2$); n_H = atomic hydrogen density; n_2 = molecular hydrogen density; F_0 = incident ultraviolet flux (= $3 \times 10^{-8} G_0$ photons $cm^{-2} s^{-1} Hz^{-1}$; Shull 1978); τ_{gr} = dust optical depth (= $N_{gr} \sigma_{gr}$); τ_2 = optical depth due to line extinction (= $N_2 \sigma_\nu$); σ_ν = effective absorption cross section of H_2.

The factor of 0.1 accounts for the fact that approximately 10% of all absorptions will lead to dissociation of the molecule (Stecher & Williams 1967). The model which is described here is a constant density (ie. not clumped), static, one dimensional PDR. The incident radiation field covers the band between 6 eV and 13.6 eV. This range in ultraviolet radiation is the same as used by TH. In this model, the radiation field, F_0, and the dust optical depth, τ_{gr}, are both assumed to be flat. The justification for this follows from TH who made a comparison between their flat radiation field and the wavelength dependent distribution of Draine (1978). They found that differences in the model results due to the two estimates were small. The extinction of this radiation by dust is, $\tau_{gr} = k_\lambda A_v$, where A_v is the visual extinction. Changing the value of k_λ does make a difference to the model since for smaller effective grain cross sections, the H_2 becomes more competitive for ultraviolet photons, and hence we get a larger column density of fluorescently excited molecular hydrogen. Also, for the different processes which occur in the TH model, eg. the photoelectric effect and photoionisation reactions, a different value of k_λ is needed. In this model the same values for k_λ are adopted, wherever necessary, as used by TH in their standard model.

The effective absorption cross section is treated in the following way,

$$\sigma_\nu = \sum_j b_j \varphi(\nu - \nu_j) \qquad [2.2a]$$

where
$$\varphi(\nu - \nu_j) = \frac{a}{\pi} \frac{1}{a^2 + \delta\nu^2} \qquad [2.2b]$$

and a = the doppler line width of the absorption lines; $\varphi(\nu)$ = Lorentzian line profile; $b_j = 2.65 \times 10^{-2} f_j \ \mathrm{cm}^2 \ \mathrm{Hz}^{-1}$; f_j = oscillator strength of line j; $\delta\nu = (\nu - \nu_j)$.

The summation in [2.2a] is over all absorption lines from the ground v=0 state to the electronically excited levels of the Lyman and Werner bands. The oscillator strengths, f_j, are taken from Allison & Dalgarno (1970). The doppler line width is taken to be the same as for the standard model of TH, $a = 2.7 \ \mathrm{km\ s}^{-1}$. Since the absorption cross sections for the line centres (or *Doppler cores*) are very large, the optical depth for these photons will be very large. Therefore, over the extent of the PDR we can assume that any absorption of ultraviolet photons by H_2 will occur out in the line wings, where the line profile is described by the Lorentzian function in [2.2b]. In the Lorentzian wings we have $\delta\nu^2 \gg a^2$, so we can write,

$$\varphi(\nu - \nu_j) = \frac{a}{\pi \, \delta\nu^2} \qquad [2.2c]$$

The form of the integrand in equation [2.1] now becomes easier,

$$R n n_H = 0.1 \, F_0 \, e^{-\tau_{gr}} n_2 \sum_j b_j \int \varphi(\nu - \nu_j) \, e^{-N_2 \sigma_\nu} \, d\nu \qquad [2.3]$$

The form of the exponential term in the integrand also simplifies if we assume that only one absorption line is considered during the integration, so that there are no other adjacent lines contributing to the absorption, ie. there is no line overlap.

Using all of these assumptions in the model and carrying out the integration over ν, we arrive at,

$$Rn\,dN_H = 0.1\,F_0\,e^{-\tau_{gr}} \sum_j \sqrt{\frac{b_j\,a}{N_2}}\,dN_2 \qquad [2.4]$$

where we have made the substitutions,

$$n_H = \frac{dN_H}{dl} \qquad n_2 = \frac{dN_2}{dl}$$

Substituting in the known parameters and rearranging equation [2.4] we arrive at the final form of our analytic description of a PDR,

$$dN_2 = 8.0 \times 10^{-14}\,S(T)\,T^{0.5}\,\frac{n}{G_0 e^{-\tau_{gr}}}\sqrt{N_2}\,dN_H \qquad [2.5]$$

The free parameters are the density, n, and the incident ultraviolet radiation field, G_0, which are the only inputs to the model. The initial conditions assume that at the very edge of the cloud, ie. $A_v = 0$, all of the hydrogen is in atomic form ($n_H = n$). The model is then stepped along in units of distance from which the optical depth is calculated using $A_v = 2 \times 10^{-21}$ N. Since we are assuming a constant density model, at each depth step the abundance of H_2 and H can be calculated. The model calculation is stopped when the density of atomic hydrogen reaches zero.

The density of the fluorescently excited H_2 molecules is also calculated. In the same way as TH and BHT, fluorescently excited H_2 is treated as a separate species, which is characterised by the population of a pseudolevel of H_2 at v=6. This means that the fluorescently excited H_2 population is also subject to a formation - destruction chemical equilibrium which we can express as,

$$9Rnn_H = n_2^*\,(A + n\gamma + P + 10P_D) \qquad [2.6]$$

where n_2^* = density of fluorescently excited H_2; A = radiative decay rate from the pseudo-level (= $2 \times 10^{-7}\ s^{-1}$; BHT); nγ = collisional deexcitation rate; P = ultraviolet excitation rate from this level; P_D = direct photodissociation rate from this level (= 10^{-11}

$G_0\, e^{-2.5A_v}\, s^{-1}$; TH).

The left hand side of equation [2.6] gives the formation rate of fluorescently excited H_2, since in equilibrium, Rnn_H is equal to the destruction rate of H_2 by photodissociation (equation [2.1]), which is nine times the rate at which H_2 is fluorescently excited. The collisional deexcitation rate from v=6 is unknown, so it has been approximated to by the v=1-0 deexcitation rate on the basis (BHT) that on average it takes six $\Delta v=1$ collisional deexcitations to get to the ground state, and the collision rates from v>1 are faster than for v=1. Similarly, the radiative decay rate from this level has been taken to be $2 \times 10^{-7}\ s^{-1}$, since typically six $\Delta v=1$ radiative decays are required with individual rates of $\sim 1.2 \times 10^{-6}\ s^{-1}$ (BHT). Absorption of a soft ultraviolet photon can lead to direct photodissociation of the excited molecule, and this rate is give by P_D (TH). Finally, the excited molecule can be reexcited to the Lyman and Werner bands from this level (multiple pumping) at a rate given by,

$$P = F_0\, e^{-\tau_{gr}} \sum_j \sqrt{\frac{b_j\, a}{N_2^*}} \qquad [2.7]$$

where N_2^* = column density of fluorescently excited hydrogen.

The summation is taken over the absorptions to the Lyman and Werner bands from the v=6 level (Allison & Dalgarno 1970). Finally, the density of excited molecular hydrogen can be calculated at each depth step by rearranging equation [2.6],

$$n_2^* = \frac{9Rnn_H}{(A + n\gamma + P + 10P_D)} \qquad [2.8]$$

2.2.2 ENERGY BALANCE IN THE MODEL

In chapter 1, the heating and cooling of gas irradiated by an ultraviolet flux was discussed. Here, the balance between these rates and how they are incorporated into the analytical model shall be discussed. Chapter 1 showed that there are at least 8 possible mechanisms for heating the gas and one need only count the number of atomic and molecular species present in a molecular cloud to get the number of cooling channels. In the analytical model, only the most dominant processes are considered.

The temperature of the gas is calculated at each depth step once the abundances of H, H_2 and fluorescently excited H_2 have been calculated. The temperature is derived by balancing the heating and cooling rates, ie. (cf. equation [1.16]),

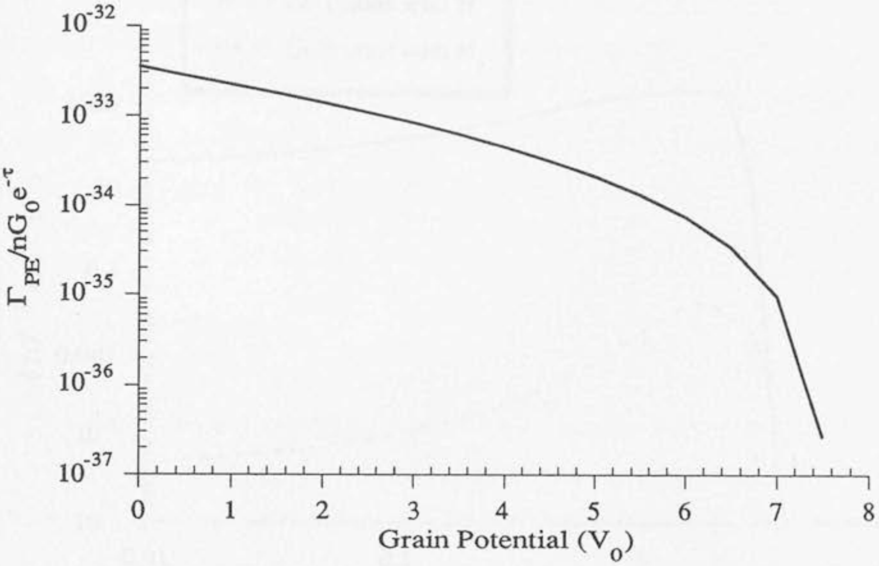

FIGURE 2.1: A measure of the photoelectric heating rate (work function = 6 eV) as a function of grain charge. The rate is from the model of de Jong (1980), equation [1.22], and is normalised to the density and ultraviolet radiation field.

$$f(T) = \sum_i \Gamma_i(T,x) - \sum_j \Lambda_j(T,x) = 0 \qquad [2.9]$$

Equation [2.9] is then solved iteratively, using Brent's Method (Press *et al.* 1986), until the root is found. This root represents the temperature of the gas in energy balance, for the densities and ultraviolet flux at a depth x. Repeating for every depth step, the temperature profile of the PDR is obtained.

2.2.2.1 Photoelectric Heating

The heating rate by the photoelectric effect used in the model is given by equation [1.23] (de Jong 1980). This is the same form as used for the TH model. From equations [1.22] it can be seen that the heating efficiency is dependent on the grain charge, V_0, which in turn is dependent on the strength of the ultraviolet radiation field and the electron density. Figure 2.1 shows how the heating rate, normalised to the density and ultraviolet field, varies as a function of the grain charge. At high potentials the heating rate is very low. This is because a grain with a strong positive charge

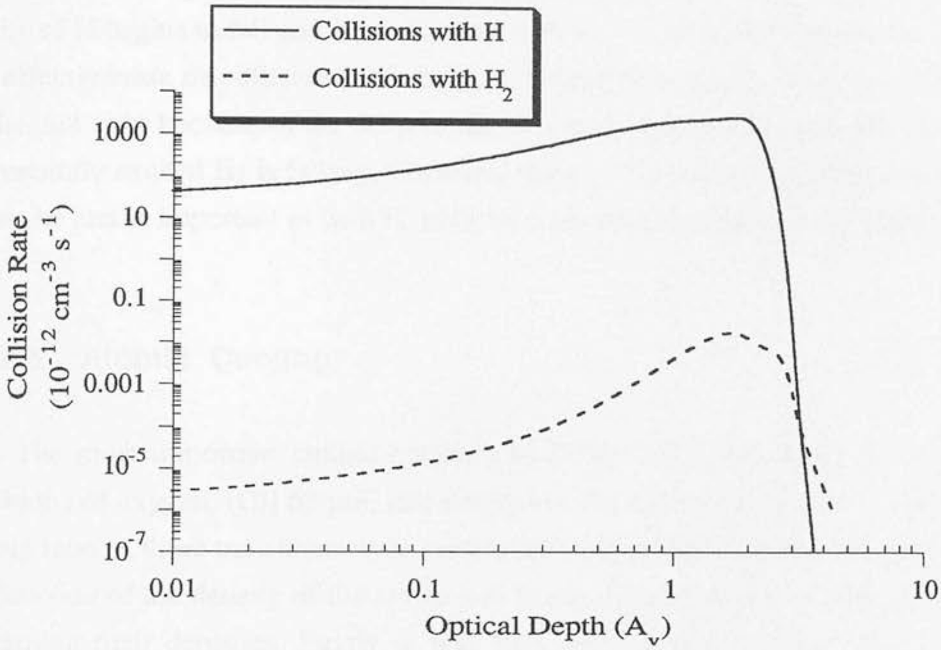

FIGURE 2.2 : The collisional deexcitation rate of fluorescently excited molecular hydrogen with H and H_2 as a function of optical depth into a one dimensional, uniform and static PDR model, characterised by the input parameters, $n = 10^4$ cm^{-3} and $G_0 = 10^4$.

requires the photoelectron to lose a lot of energy to overcome the strong coulomb attraction of the grain. Therefore, any photoelectrons which are ejected will not have a lot of kinetic energy to offer towards gas heating. Conversely, at low potentials the attractive coulomb force is decreased allowing photoelectrons to be ejected into the gas with more energy, and thus increasing the heating efficiency.

2.2.2.2 H_2 Vibrational Heating

The heating of the gas due to collisional deexcitation of fluorescently excited molecular hydrogen is expressed by equation [1.25]. The collisional deexcitation rates are not very well determined and the approximation used by BHT is incorporated into the analytical model (see equations [1.19a], [1.26]). The collision rate with H dominates that with H_2 for all temperatures. However, the heating rate is also a function of the densities of H, H_2 and H_2^*, all of which evolve as functions of depth into the PDR. Figure 2.2 shows a plot of the collision rates ($n(H_2^*)\, n_x\, \gamma_x$) as functions of depth into a PDR modelled for density $n = 10^4$ cm^{-3} and $G_0 = 10^4$. For most of the extent of the

PDR ($A_v \leq 3$) the heating rate is dominated by collisions with H. However, deeper in, when self shielding has stopped the dissociation of H_2 and its abundance rises, the density of H begins to fall and it is collisions with H_2 which then dominate the heating. The effectiveness of collisional heating as a whole has greatly diminished at these depths, not only because of the drop in the H density but also because the density of fluorescently excited H_2 is falling. However, since collisional deexcitation of H_2^* with H_2 can be just as important as with H, both rates are incorporated into the model.

2.2.2.3 Atomic Cooling

The most important atomic coolants in PDRs are those of the fine-structure transitions of oxygen, [OI] 63 μm, and singly ionised carbon, [CII] 158 μm (TH). The cooling rates of these transitions were calculated from equation [1.36]. The cooling rate is a function of the density of the atoms and hence some assumptions had to be made concerning their densities. Firstly, it was assumed that the densities of the cooling species remain constant throughout the region of interest, ie. up to $A_v \sim 4 - 5$. For oxygen, this is a good assumption. The complete chemical model of BHT shows that, for a model with $n = 10^6$ cm^{-3} and $G_0 = 10^4$, the oxygen abundance does indeed stay constant until it drops slightly at $A_v \sim 2.5$, when some of the oxygen goes into making CO. For C^+, the situation is slightly different. At the surface of the cloud, $A_v < 2 - 4$, all of the atomic carbon is in the form of C^+ (if it is not locked into CO or in hydrocarbons) and its density remains constant over this region until C^+ recombines to form C and CO, and is depleted away. This transition zone is variable with depth for different models due to self shielding. In high density models ($n \gg G_0$) the transition is close to the surface and the approximation does not hold. However, for these models the cooling is dominated by [OI] 63 μm emission and gas-grain collisions. For lower density models ($n \leq G_0$) the transition zone occurs deep in the PDR ($A_v \sim 4 - 5$) and the assumption holds, which is fortunate since [CII] 158 μm cooling is important for these models.

The second assumption is that all the oxygen and carbon are in atomic and singly ionised forms, respectively, and their densities are given by the following abundances (TH),

$$\begin{aligned} n(C^+) &= 3 \times 10^{-4}\, n \\ n(O) &= 5 \times 10^{-4}\, n \end{aligned} \qquad [2.10]$$

The cooling rates which are used in the analytical model for [OI] and [CII] cooling are,

$$\text{[OI] 63 }\mu\text{m}: \qquad \Lambda_{OI} = \frac{1.4 \times 10^{-28}\ n\ \beta_{esc}(\tau_{OI})}{1 + \frac{5}{3}\exp\left(\frac{228}{T}\right)\left(1 + \frac{4.7 \times 10^{5}\ \beta_{esc}}{n}\right)} \quad \text{W cm}^{-3} \qquad [2.11a]$$

* See below

$$\tau_{OI} = 1.66 \times 10^{-21}\left[\frac{\exp\left(\frac{228}{T}\right) - 1}{1 + \frac{5}{3}\exp\left(\frac{228}{T}\right)}\right]\int n\, dz \qquad [2.11b]$$

$$\text{[CII] 158 }\mu\text{m}: \qquad \Lambda_{CII} = \frac{9.14 \times 10^{-31}\ n\ \beta_{esc}(\tau_{CII})}{1 + 0.5\exp\left(\frac{92}{T}\right)\left(1 + \frac{2.8 \times 10^{3}\ \beta_{esc}}{n}\right)} \quad \text{W cm}^{-3} \qquad [2.12a]$$

$$\tau_{CII} = 4.16 \times 10^{-22}\left[\frac{\exp\left(\frac{92}{T}\right) - 1}{1 + 0.5\exp\left(\frac{92}{T}\right)}\right]\int n\, dz \qquad [2.12b]$$

where, the escape probability formalism is evaluated in equation [1.15] and the optical depths, τ, are derived from equation [1.35a] assuming that the levels are collisionally excited in LTE. All constants are taken from Table 4 in TH.

2.2.2.4 Gas-Grain Collisional Cooling

The cooling of gas by collisions with grain particles occurs only when the gas temperature is higher than the grain temperature. Because of the n^2 dependence (equation [1.40]), gas-grain collisions are important coolants, especially for high density PDRs. Gas-grain collisional cooling is also proportional to $T^{1.5}$ (for $T \gg T_{gr}$) hence the temperature profile of the PDR will tend to approximate to the profile of the gas-grain collisional cooling function.

* Since writing, it was noted that the factor of 5 in equations [2.11a] and [2.11b] should be 5/3. After re-running the model, it was found that this change does not significantly change any of the results in this thesis.

2.2.3 DENSITY AND TEMPERATURE PROFILES

2.2.3.1 Hydrogen Density Profiles

In Figure 2.3(a-d), the densities of atomic, molecular and fluorescently excited hydrogen are plotted as functions of optical depth into one dimensional, uniform and static PDRs. In all cases, one can see how the density is dominated by atomic hydrogen at the cloud edge and deeper in the hydrogen turns molecular. One thing to notice from figures2.3(a-c) is how self shielding has affected the structure of the PDR at high densities. Figure 2.3a shows that the HI/H_2 transition occurs at a depth of $A_v \sim 3$, consistent with the models of TH. However as (n/G_0) is increased above unity, self shielding of H_2 becomes increasingly more important (BHT; see section 1.1.5 and equation [1.18]). An increase in self shielding means that the destructive ultraviolet photons are attenuated sooner so that the atomic hydrogen is able to change into its molecular form for shallower depths. This is demonstrated by Figures 2.3(b-c). In Figure 2.3c, $(n/G_0) = 1000$ cm^{-3} and the transition zone occurs at $A_v \sim 0.15$.

A possibly better estimate of where the transition zone occurs may be given by following the density profile of fluorescently excited molecular hydrogen, since it is emission from this species which can be observed. The density profile is given by equation [2.8]. In Figures 2.3(a-c), the density at the edge of the cloud is very low because the ultraviolet flux is high and is able to destroy the excited H_2, along with rapid collisional deexcitations in the hot gas. As we go deeper in, the ultraviolet photons suffer extinction and the density rises to a sharp peak as the rates of ultraviolet absorption and collisional deexcitations decreases. The fall off after the peak occurs because there are no more photons available to excite the molecular hydrogen and at these depths excited H_2 may only form from the formation process of H_2 on the surface of grains. This is dependent on the H density and so the density of excited H_2 falls very quickly with the H density. In Figure 2.3a there is a small dip in the density profile of excited H_2 just before it reaches its peak. This is caused by a rise in temperature at this point (see later), momentarily increasing the collisional deexcitation rate.

By examining Figures 2.3(a-c) one can see that the depth at which the peak in excited H_2 density occurs is also dependent on the physical conditions, namely n and G_0. Not surprisingly, as the density is increased (and n/G_0 rises) the peak moves closer to the surface and generally occurs very near the HI/H_2 transition zone. When our

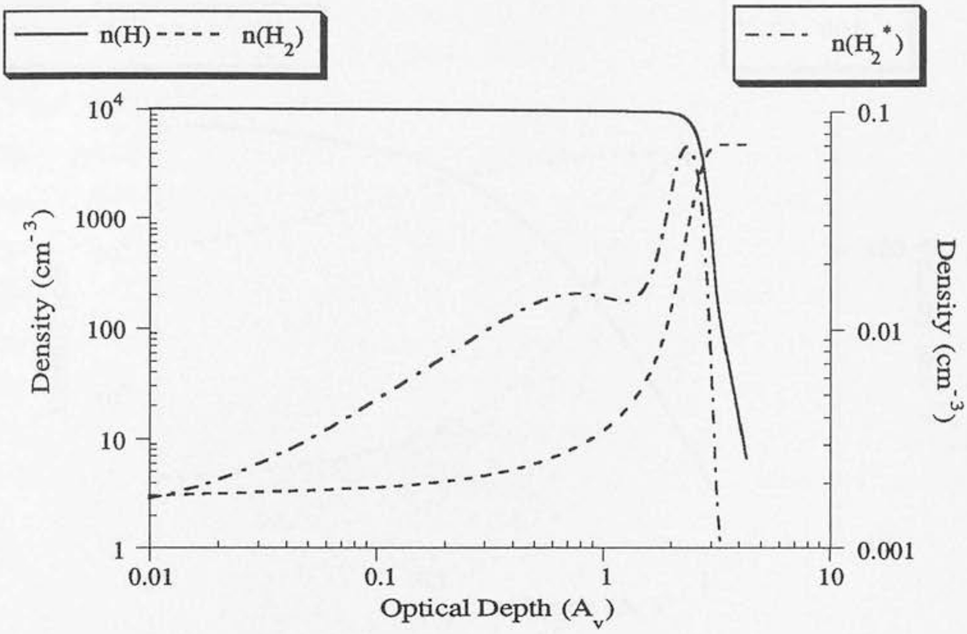

FIGURE 2.3a : PDR model run showing the density structure as a function of optical depth for a model with $G_0 = 10^4$ and $n = 10^4$ cm^{-3}. The left hand axis gives the density for H and H_2 while the right hand axis gives the density for fluorescently excited H_2.

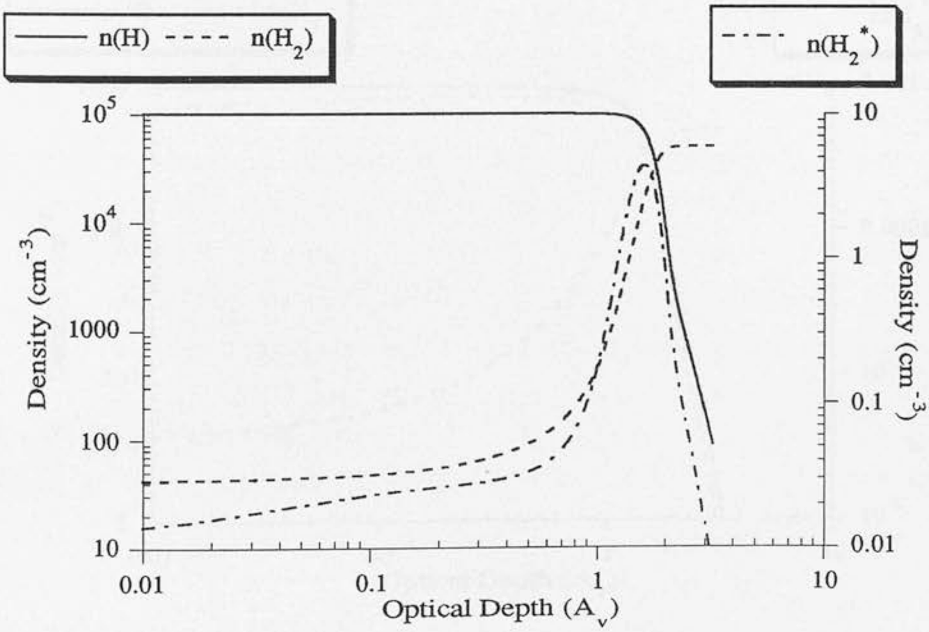

FIGURE 2.3b : The same as for Figure 2.3a but for a model with $G_0 = 10^4$ and with $n = 10^5$ cm^{-3}.

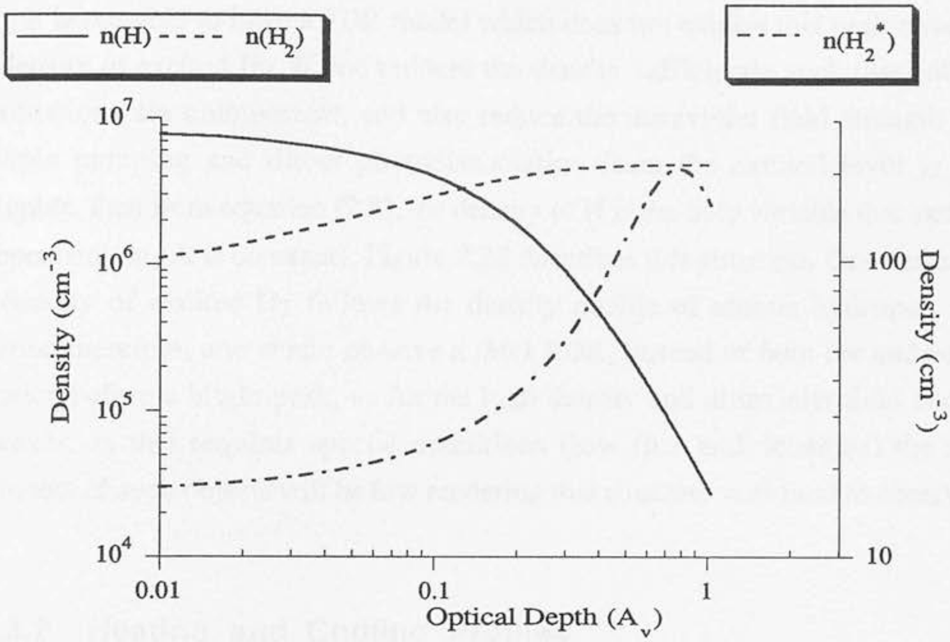

FIGURE 2.3c : The same as for Figure 2.3a but for a model with $G_0 = 10^4$ and with $n = 10^7$ cm^{-3}.

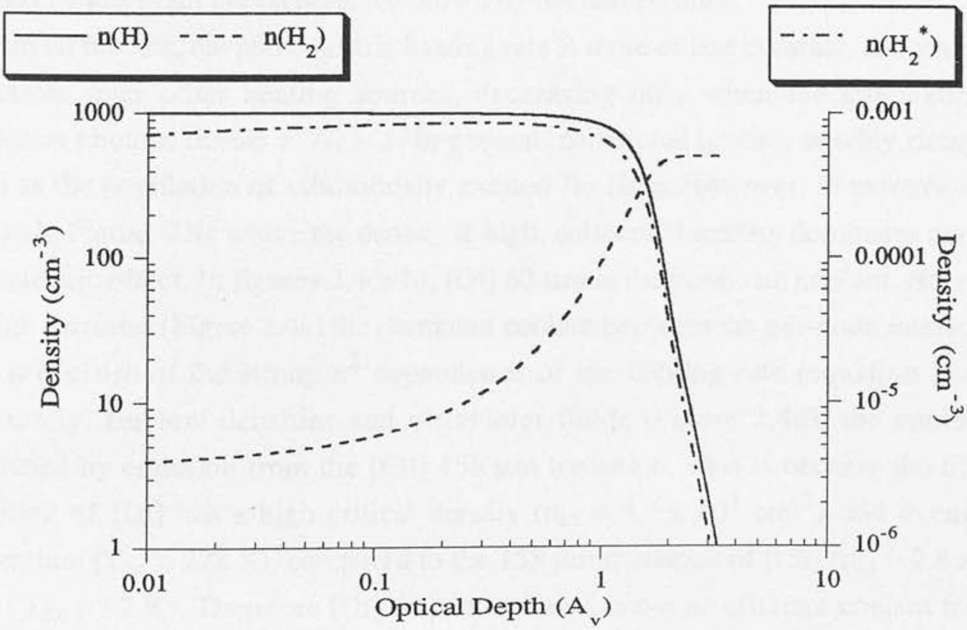

FIGURE 2.3d : The same as for Figure 2.3a but for a model with $G_0 = 100$ and with $n = 10^3$ cm^{-3}.

observations are discussed later in this chapter, this fact will be taken advantage of.

It is possible to have a PDR model which does not exhibit this peak structure in the density of excited H_2. If one reduces the density sufficiently such that collisional deexcitations are unimportant, and also reduce the ultraviolet field strength so that multiple pumping and direct photodissociation from the excited level is almost negligible, then from equation [2.8], the density of H is the only variable that excited H_2 is dependent on (A is constant). Figure 2.3d describes this situation. One can see how the density of excited H_2 follows the density profile of atomic hydrogen. In this situation therefore, one would observe a *thick* PDR, instead of faint (or undetectable) emission before a bright peak, as for the high density and ultraviolet field situations. However, as this requires special conditions (low flux and densities) the surface brightness of such objects will be low rendering this structure very hard to observe.

2.2.3.2 Heating and Cooling Profiles

In Figures 2.4(a-d) plots of the rates of heating and cooling are shown as functions of optical depth into one dimensional, uniform and static PDRs. The heating rates by the photoelectric effect and the collisional deexcitation of fluorescently excited H_2 are shown by the solid curves. The cooling rates by [OI] 63 μm and [CII] 158 μm and also by gas-grain interactions are shown by the dashed lines.

In all models, the photoelectric heating rate is more or less constant, and generally dominates over other heating sources, decreasing only when the attenuation of ultraviolet photons occurs at $A_v \sim 1$. In general, collisional heating steadily rises with depth as the population of vibrationally excited H_2 rises. However, in extreme cases such as in Figure 2.4c where the density is high, collisional heating dominates over the photoelectric effect. In figures 2.4(a-b), [OI] 63 μm is the dominant coolant. However, for high densities (Figure 2.4c) the dominant coolant becomes the gas-grain interaction. This is because of the strong n^2 dependence of the cooling rate (equation [1.40]). Conversely, for low densities and ultraviolet fields (Figure 2.4d), the cooling is dominated by emission from the [CII] 158 μm transition. This is because the 63 μm transition of [OI] has a high critical density ($n_{cr} = 4.7 \times 10^5$ cm^{-3}) and excitation temperature ($T_{ex} = 228$ K), compared to the 158 μm transition of [CII] ($n_{cr} = 2.8 \times 10^3$ cm^{-3} ; $T_{ex} = 92$ K). Therefore [OI] 63 μm emission is not an efficient coolant for the colder, lower density PDRs.

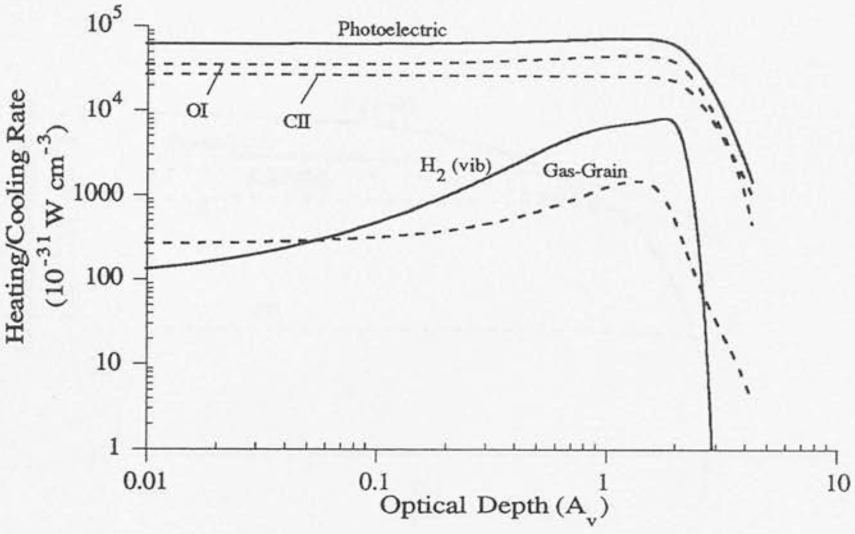

FIGURE 2.4a : Heating and Cooling rates as a function of optical depth for a PDR model with $G_0 = 10^4$ and with $n = 10^4$ cm^{-3}. The heating rates are shown by solid curves while the cooling rates are represented by dashed curves.

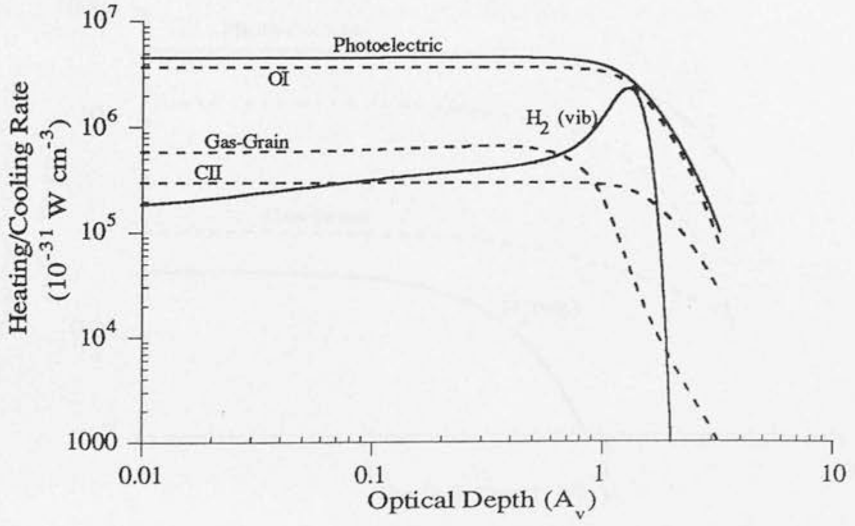

FIGURE 2.4b : The same as for Figure 2.4a but for a model with $G_0 = 10^4$ and with $n = 10^5$ cm^{-3}.

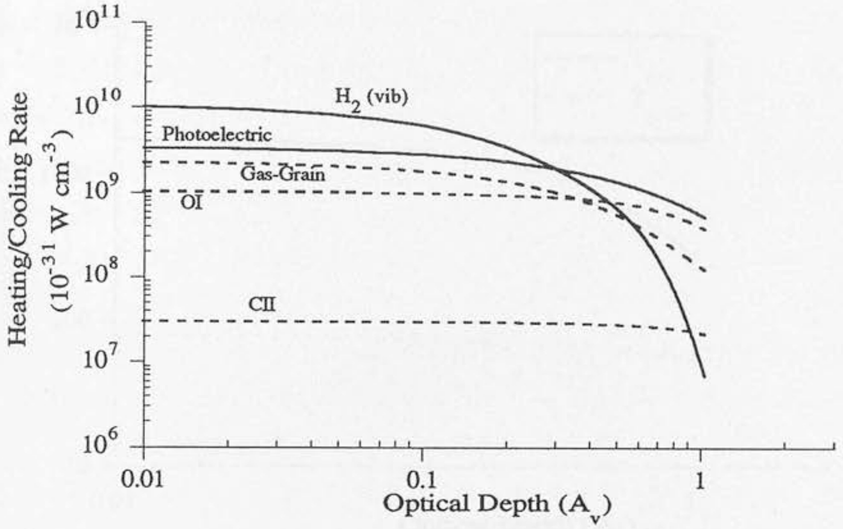

FIGURE 2.4c : The same as for Figure 2.4a but for a model with $G_0 = 10^4$ and with $n = 10^7$ cm^{-3}.

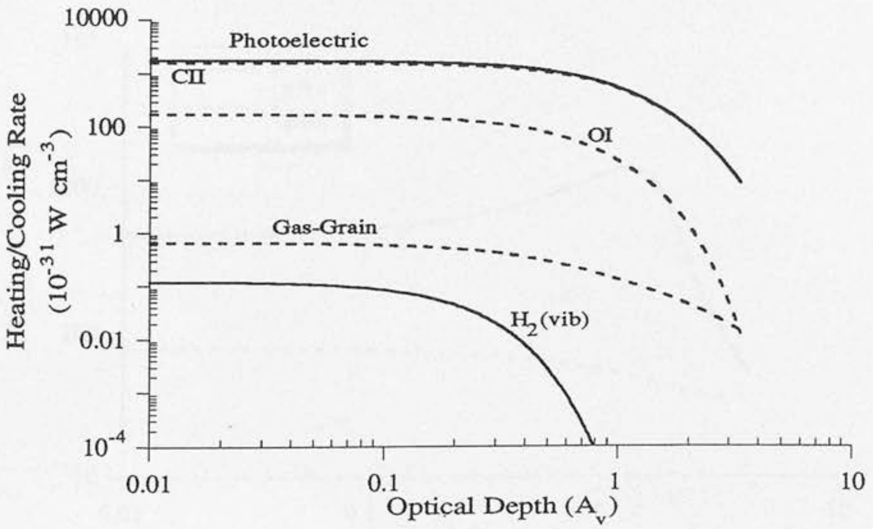

FIGURE 2.4d : The same as for Figure 2.4a but for a model with $G_0 = 10^2$ and with $n = 10^3$ cm^{-3}.

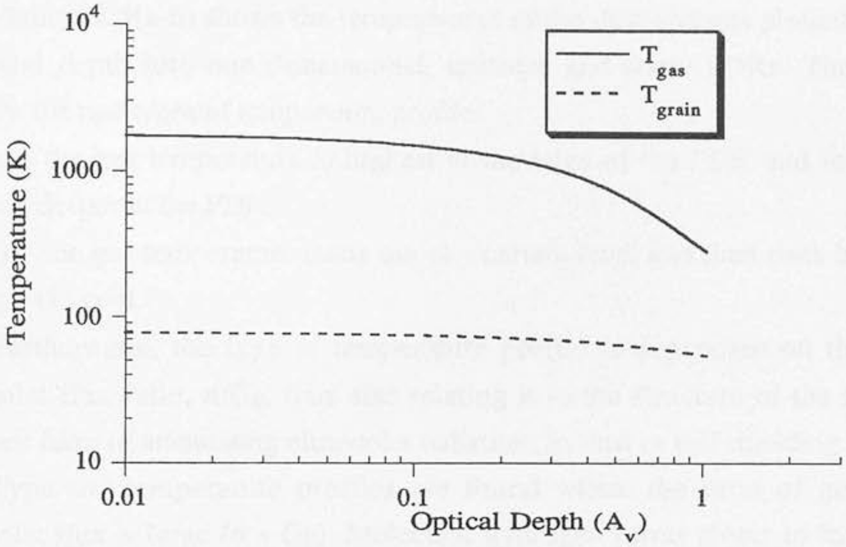

FIGURE 2.5a : Temperatures of the gas and dust in a PDR as a function of optical depth into a PDR model with $G_0 = 10^4$ and with $n = 10^7$ cm^{-3}.

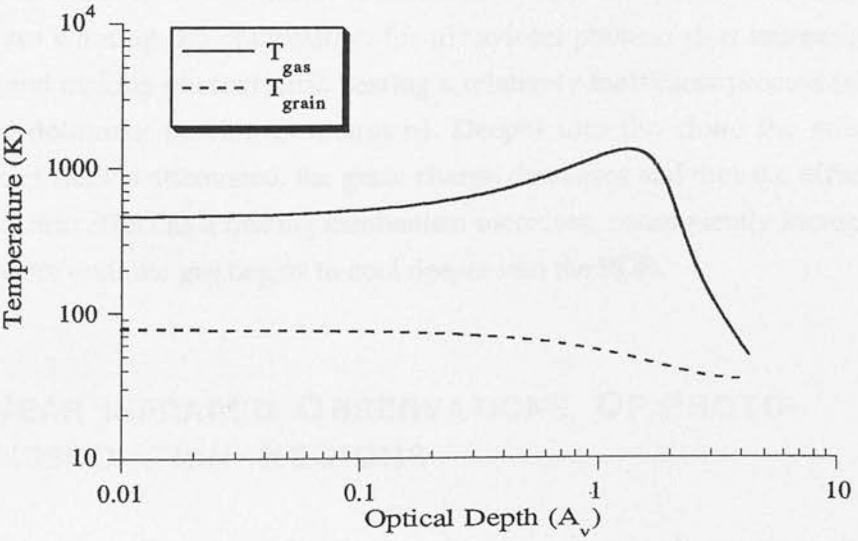

FIGURE 2.5b : The same as for Figure 2.5a but for a model with $G_0 = 10^4$ and with $n = 10^4$ cm^{-3}.

2.2.3.3 Temperature Profiles

Figures 2.5(a-b) shows the temperatures of the dust and gas plotted as functions of optical depth into one dimensional, uniform and static PDRs. The plots show evidence for two types of temperature profile:

(a) the gas temperature is highest at the edge of the PDR and then falls away deeper in the PDR,

(b) the gas temperature starts out at a certain level and then rises before it begins to cool.

Furthermore, the type of temperature profile is dependent on the density to ultraviolet flux ratio, n/G_0, thus also relating it to the structure of the PDR and the dominant form of attenuating ultraviolet radiation, ie. dust or self shielding.

Type *(a)* temperature profiles are found where the ratio of gas density to ultraviolet flux is large ($n \gg G_0$). Molecular hydrogen forms closer to the edge of the PDR and the attenuation of ultraviolet radiation is dominated by line shielding. As H_2 molecules are winning the competition for ultraviolet photons, the grain charge is low and the photoelectric heating efficiency is high. In very dense models, a large source of heating at the PDRs edge comes from the collisional deexcitation of fluorescently excited H_2.

Type *(b)* temperature profiles are found where the ratio of the gas density to ultraviolet flux is low ($n \le G_0$). Molecular hydrogen forms at an optical depth of $A_v \sim 1$ and the attenuation of ultraviolet radiation is dominated by dust shielding. Now, dust grains are winning the competition for ultraviolet photons thus increasing the grain charge and making photoelectric heating a relatively inefficient process (although it is still the dominant heating mechanism). Deeper into the cloud the strength of the ultraviolet field is attenuated, the grain charge decreases and thus the efficiency of the photoelectric effect as a heating mechanism increases, consequently increasing the gas temperature until the gas begins to cool deeper into the PDR.

2.3 NEAR INFRARED OBSERVATIONS OF PHOTO-DISSOCIATION REGIONS

The observations I will discuss here consist in part of observations of Orion's Bar and NGC 2023, but concentrate mainly on observations of M17, in particular the northern bar.

M17 (also known as the Omega Nebula, NGC 6618) is an HII region at a distance of 2.2 kpc (Harper *et al.* 1976; Stutzki *et al.* 1988). At this distance 1 arcsec is equivalent to 0.01 pc. M17 has been extensively mapped in the radio continuum (Felli, Churchwell & Massi 1984), in Brγ and H_2 (Meadows 1986; Gatley & Kaifu 1987) and in the infrared continuum (Harper *et al.* 1976; Gatley *et al.* 1979). These maps reveal two obvious regions of emission; a bar which stretches across the north and another which runs south to west. Felli *et al.* (1984) also note that their 21cm continuum map of the northern bar closely corresponds to the optically visible bar, indicating that the visual extinction in this region is not very large. This suggests that the associated molecular cloud lies behind the northern bar. The southwestern bar, on the other hand, is strongly obscured at visible wavelengths indicating that the southwestern molecular cloud forms part of the foreground gas. This view is further supported by JHK maps of the M17 region (Lada *et al.* 1991) in which the northern bar is dominated by emission in the J band while the southwestern bar is dominated by emission in the K band, indicating an increasing gradient in extinction towards the southwestern bar. Submillimetre and far infrared observations of hot carbon species in the southwestern bar (Harris *et al.* 1987; Stutzki *et al.* 1988; Stutzki & Güsten 1990) reveal the presence of warm, dense gas extending deep into the molecular cloud, implying that the southwestern bar is a clumped region, the density in the clumps ranging from 10^5 to 10^6 cm^{-3} (Stutzki & Güsten 1990). Infrared spectroscopy of H_2 has only been carried out in the northern bar by Tanaka *et al.* (1989), who determined that the H_2 emission in a 19.6 arcsec beam comes from fluorescent excitation, little affected by thermal reprocessing. The inference from this is that the gas is of low density. M17, therefore, appears to contain two regions of different densities, both being illuminated and equidistant from the same source of photons ($L \sim 6 \times 10^6 L_o$ - Harper *et al.* 1976) and forms an excellent laboratory for the study of PDR physics.

2.3.1 OBSERVATIONS AND DATA REDUCTION

Infrared images were obtained of emission from fluorescent molecular hydrogen, ionised hydrogen and the 3.28 μm emission feature, at the interface between the HII region and the molecular cloud in M17. All observations were carried out on the 3.8m United Kingdom Infrared Telescope (UKIRT), on the summit of Mauna Kea, Hawaii. The instrument used for these observations was the infrared array camera (IRCAM) which has a 62 x 58 pixel InSb array. The observations of the southwestern bar were taken using a pixel scale of 1.24 arcsec per pixel, while the observations of the northern bar used the camera in the mode which provided 0.62 arcsec per pixel. However, in general, seeing conditions degrade this resolution to approximately 1 arcsec per pixel.

All observations were taken through narrow band, circular variable filters (CVF) with a 1% bandwidth. Some of the observations in the northern bar of M17 used the CVF merely as a blocking filter to isolate the target lines and a tuneable Fabry-Perot etalon (FP) was placed ahead of the camera to increase the line to continuum ratio for the 2 μm lines. The spectral resolution of the FP was typically 110 km s^{-1} (FWHM), much broader than the expected width of emission lines from PDRs, which are only broadened by turbulent motions in the PDR (ie. $\Delta v_d \sim 3$ km s^{-1}).

On chip exposure times in the K window varied from 300 seconds for the fainter H_2 v=1-0 S(1) line ($\lambda = 2.122$ μm), to only 60 seconds for the bright H^+ Brackett γ recombination line ($\lambda = 2.167$ μm). For observations at 3 μm, the thermal sky emission limits the on chip exposure times to only 1 second, so 150 coadds were used to increase the signal-to-noise ratio. Nearby continuum measurements were also made. In the L window, the CVF was set at 3.1 μm (a filter designed for an ice feature) and in the K window, continuum observations were made at 2.1 μm. For the observations using the FP, the continuum was measured by detuning the FP by 740 km s^{-1}. Frequent sky observations through each filter were obtained by nodding the telescope approximately 600 arcsec west from the source.

2.3.1.1 Data Reduction Procedure

Every frame read from the array has a background signal due to the electronics of the instrument and the chip. This signal is known as the dark current and it increases with time. It is therefore required to remove this signal from every frame. This is done by closing the shutter, so that no photons fall onto the chip, and reading the array for the same length of time as the object exposures. The dark current is monitored regularly during the night as a check on the behaviour of the array. In general, it was found that variations in the dark current became apparent on a time scale of approximately two hours. For this reason, the dark current was observed regularly and removed from each frame by making sure that the dark frame used was the one which was closest in time to the object frame.

Next, the frames have to be flatfielded, which involves removing the pixel-to-pixel variations which are intrinsic to the array and the filter. A flatfield is produced by exposing the chip to a uniform (flat) source of radiation. This can be done by either exposing the chip to the telescope dome or to the sky. For these observations, flatfields were obtained by observing clear regions of the sky. Firstly, the dark current is removed. Then, each sky frame is normalised to its mean value. This effectively removes the sky emission which will differ over the course of a single night, as one observes through different air masses. However, before normalisation occurs, any bad pixels that are present in the sky frames, due to "hot" pixels on the array or cosmic ray events, are removed. These pixels are removed by interpolating between neighbouring pixels. The removal of bad pixels now allows for accurate calculations of means over a large area of the array. After normalisation, the sky frames are median filtered. This procedure stacks all the normalised sky frames on top of each other and then goes to the same pixel position on each frame and uses the median of these pixel values to create a new frame - the flatfield. The median is used to ensure that only a "sky" value is passed onto the flatfield frame, since sometimes the sky frame can contain images of stars. To ensure that these stars do not fall in the same position and hence contaminate the flatfield frame, the sky observations are made following a *jitter* pattern, ie. each sky observation is offset by ± 10 - 20 arcsec north and/or east from the previous sky position. It is preferable when producing a flatfield that many sky frames used, to remove any chance coincidences of stars on different frames contaminating the flatfield, and to add to the signal to noise ratio of the flatfield. The resultant image, now only contains the intrinsic pixel-to-pixel variations of the array and filter itself. Dividing this frame into the object frames leaves only the emission structure of the source and the sky on the frame. At this stage, any bad pixels present on the object frames may be removed.

The object frames are then mosaiced together. This is not straightforward because the sky emission changes during the night. This variable sky emission is accounted for by matching all frames to a single reference frame of the mosaic. The matching is done by adding or subtracting a constant value to neighbouring frames until there is no mismatch in the mean counts of overlapping regions. The sky emission from all frames is then equal to the sky emission from the reference frame, ie. as if all frames were observed at the same airmass. The sky emission can then be calculated from a sky frame nearest in time to the reference frame. It is then possible to remove the sky emission from the whole mosaic. This, of course, does not remove the continuum emission.

Figures 2.6(a-c) shows how this technique has worked for our early observations of the southwestern bar of M17. The images are centred on the bright star SAO 161357 with coordinates $18^h\ 17^m\ 34.497^s$, $-16^\circ\ 13'\ 24.24''$ (1950). Figure 2.7 shows a cut across the region of emission between the coordinates $(-41'',-30'')$ to $(-41'',-55'')$. The solid line gives the level of the continuum emission and the crosses is the reading

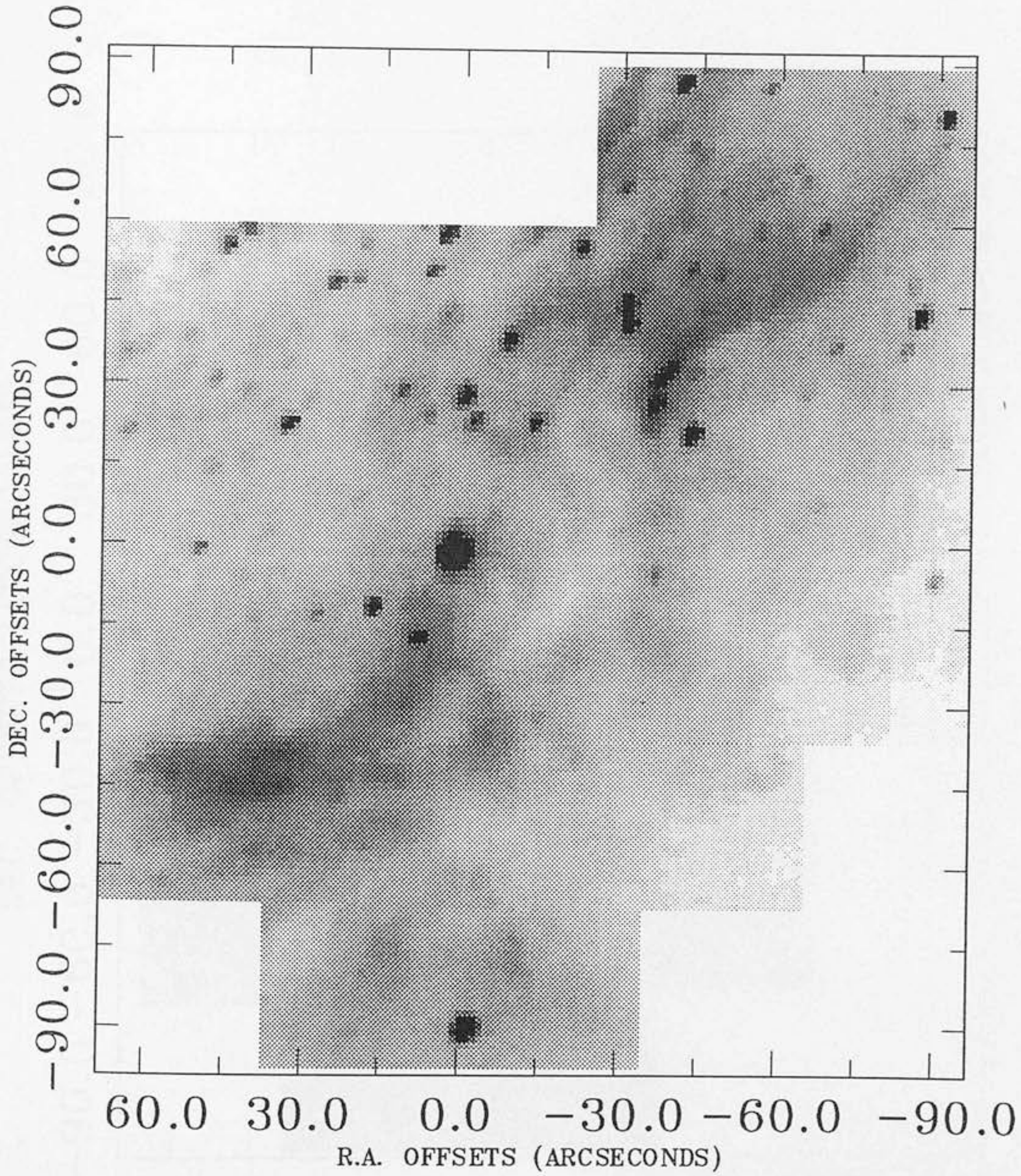

FIGURE 2.6a : Image of the southwestern bar of M17 in the light of Brackett γ recombination radiation of H^+.

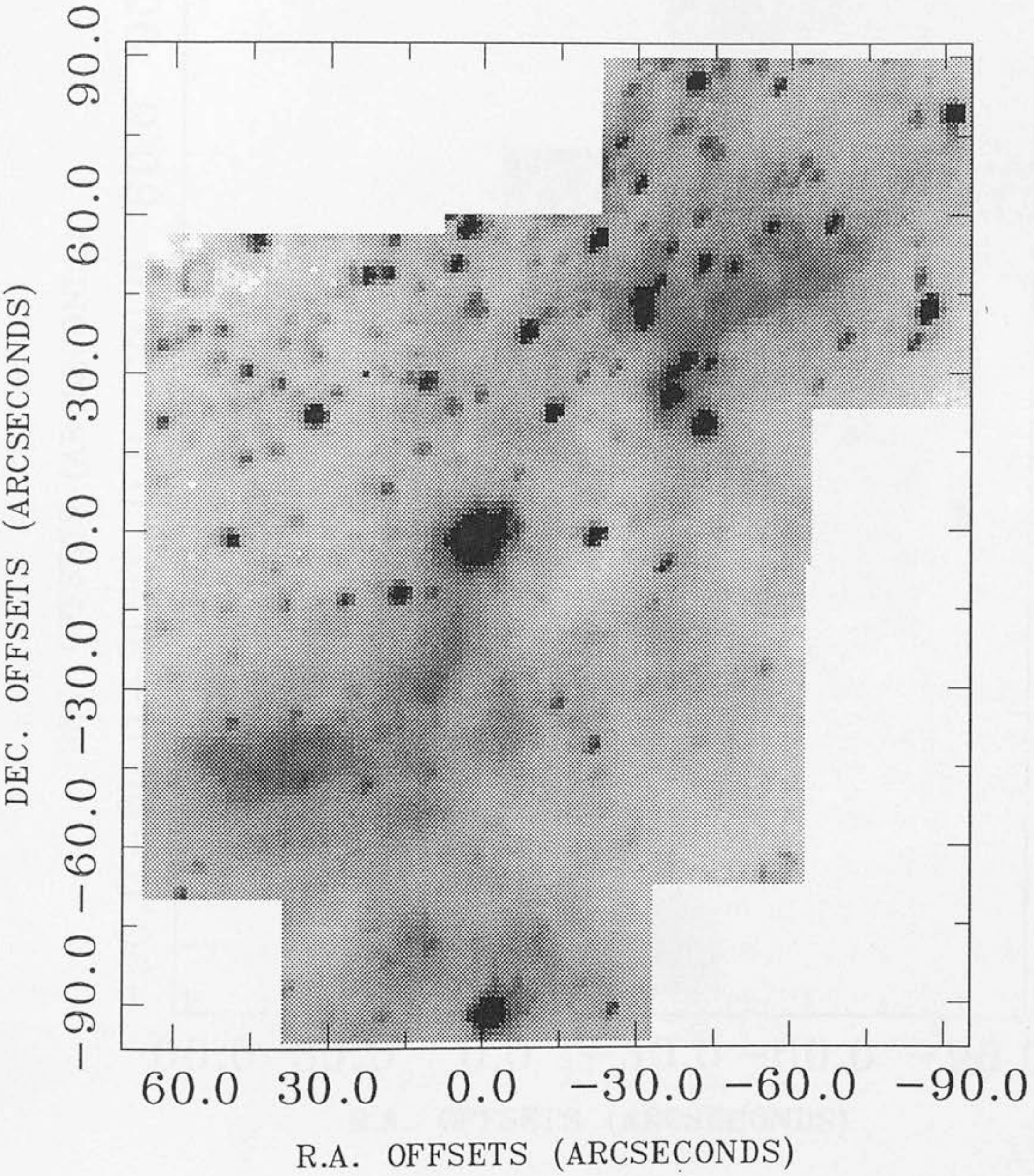

FIGURE 2.6b : Image of the southwestern bar of M17 in the light of the H_2 v=1-0 S(1) transition.

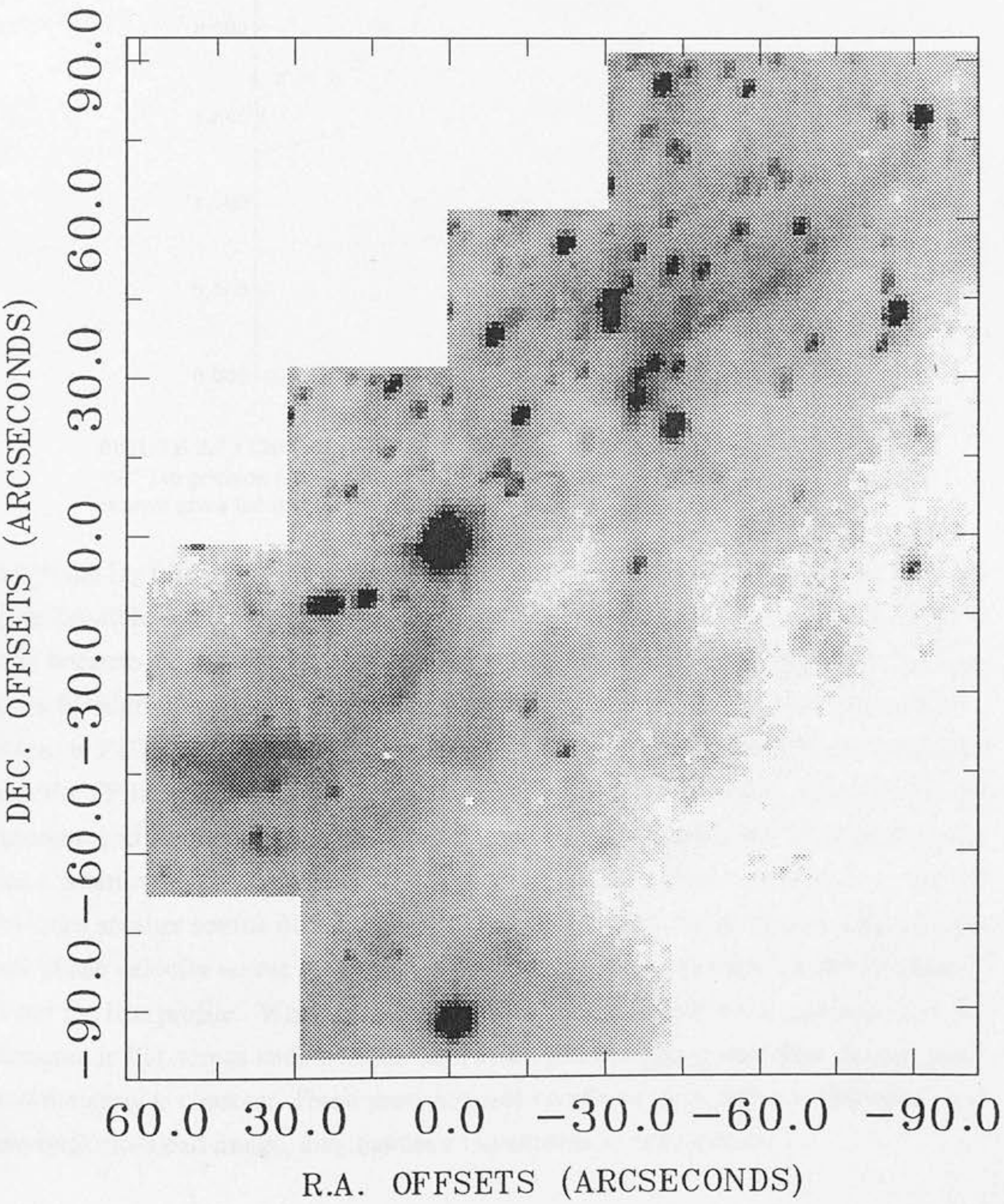

FIGURE 2.6c : Image of the southwestern bar of M17 in the continuum radiation at a wavelength of 2.1 µm.

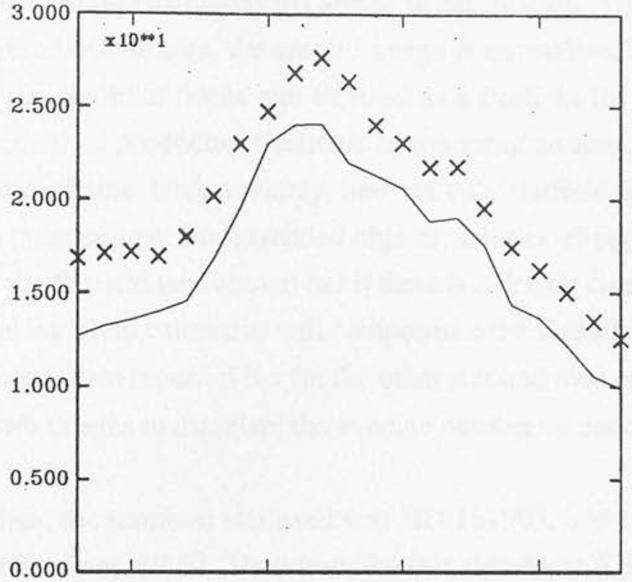

FIGURE 2.7 : Cut in the H_2 and 2.1 μm continuum images from position (-41´´, -30´´) to position (-41´´, -55´´). The solid line shows the continuum level while the crosses gives the level in the H_2 image for every pixel along the cut.

through the H_2 filter. One can see that if 10% error bars are added to the data, it would not be possible to distinguish the line emission from continuum emission. This is purely because the 1% filter is too broad, allowing more continuum than line emission to pass through the filter, and hence the continuum dominates. This will always be a problem in PDRs where there is hot dust present. It is for this reason that it was decided to use the FP in front of the CVF, which also provides a unique way of removing the continuum and sky emissions simultaneously by simply detuning the FP from the peak of the transmission profile of the target line and onto the continuum. However, the FP introduces another source of pixel-to-pixel variation across the array as a consequence of the phase velocity across the chip (65 km s^{-1} from centre to edge for the 100 km s^{-1} FP) and the line profile. When measuring the continuum this is not a problem since the continuum is flat across such a small bandwidth and the power received at each pixel across the array is constant. These pixel-to-pixel variations were left uncorrected for and in the final mosaiced image, they manifest themselves as edge effects.

2.3.1.2 Calibration of Data

Flux calibration of the data is done by observing a standard star of known magnitude. Firstly, the star needs to be observed through each filter twice, one image offset from the other by approximately 10 arcsec in declination. Then, after removing the dark current from both images, the second image is normalised to the mean of the sky emission and the resultant frame can be used as a flatfield for the first. This is a more desirable method of producing flatfields as the array structure may be prone to change over a period of time. Unfortunately, one can only flatfield using this method if one is observing a point source. For extended objects, a series of sky frames need to be observed to create the flatfield (see above) but if there is a drastic change in the structure of the pixel-to-pixel variations, then this will compromise the flatfield.

This procedure is then repeated but for the other star and then aperture photometry is carried out on both images to calculate the average number of counts on the array due to the star.

For all our data, the standard star used was HD 161903, spectral type A2, which has a magnitude at K of $m_K = 7.02$. Therefore, the flux density at K is,

$$m_K = -2.5 \log\left(\frac{S_K}{S_0}\right) \qquad [2.13]$$

where $S_0 = 620$ Jansky at K and therefore $S_K = 9.6 \times 10^{-27}$ W m^{-2} Hz^{-1}.

Next we assume that the star is a blackbody with an effective temperature of T ~ 9300 K. At 2 μm, therefore, this allows us to use the Rayleigh-Jeans approximation which says that if $hc < \lambda kT$ we can write,

$$\frac{S_\lambda}{S_K} = \left(\frac{2.2}{\lambda}\right)^4 \qquad [2.14]$$

which allows us to calculate the flux density from the star at the wavelengths of the filter transmissions. Equating the number of counts from the star to the flux density of the star, allows one to calibrate the number of counts to flux density.

2.3.2 RESULTS

Images of the PDR in the northern bar of M17 are shown in Figures 2.8 (a-c). The (0,0) coordinate in these images is $18^h\ 17^m\ 50.7^s$, -16° 9′ 47″ (1950). In all these images the source of UV photons, an obscured cluster of maybe 100 OB stars which power the HII region (Beetz *et al.* 1976; Lada *et al.* 1991), is from the southwest (bottom right). Figure 2.8a shows a mosaic of seven frames in the H_2 v=1-0 S(1) line, a region of some 80 x 90 $arcsec^2$ in extent. Figure 2.8b shows the same region but imaged in the Brackett γ hydrogen recombination line. Figure 2.8c shows the emission from the 3.28 μm feature and is once again of the same region but the image area is smaller than for Figure 2.8a, representing a combination of only 4 frames. This is because adverse weather conditions at the time these observations were made prevented further observations in the L band. Figure 2.8d shows the continuum emission at 3.1 μm. Comparing Figures 2.8c and 2.8d, which are plotted to the same levels, it is clear that the emission structure we observe at 3.28 μm is due only to the carrier of the feature and is above any continuum emission that may be present.

2.3.2.1 The H_2 v=1-0 S(1) Image

The most obvious features in the H_2 image (Figure 2.8a) are the two prominent ridges of emission which run across the image. A possible explanation for this structure obviously lies in the morphology of the cloud surface, such as a wrinkle in which emission is enhanced by limb brightening, or the clumping of dense material within a less dense medium. The peak intensity measured at the brightest pixel is $I \sim 1.5 \times 10^{-7}$ $W\ m^{-2}\ sr^{-1}$.

Edge effects in this mosaic are caused by the angular dependence of the transmission profile of the FP. Unfortunately, difficulties at the telescope meant that it was not possible to align the FP so that the peak transmission fell onto the centre of the array, but instead it was towards the southeast corner (bottom left) of the array. The phase shift towards the northwest was therefore larger.

2.3.2.2 The Brackett γ Image

The emission of Brackett γ traces the presence of ionised gas. The Br γ emission peaks in an extensive area approximately 40 arcsec south of (0,0) where the ionised HII region is located (Figure 2.8b). There is a ridge of emission which runs northwest. A comparison of this image with the high resolution radio continuum measurements made by Felli *et al.* (1984) shows that it coincides with the edge of the ionisation front. The ridge of emission to the northwest reveals itself as a small (~ 20 arcsec long) ridge in their map also (see later and Figure 2.10).

The emission measure at the brightest pixel is ~ 1.9 Mpc cm^{-6}. Felli *et al.* (1984)

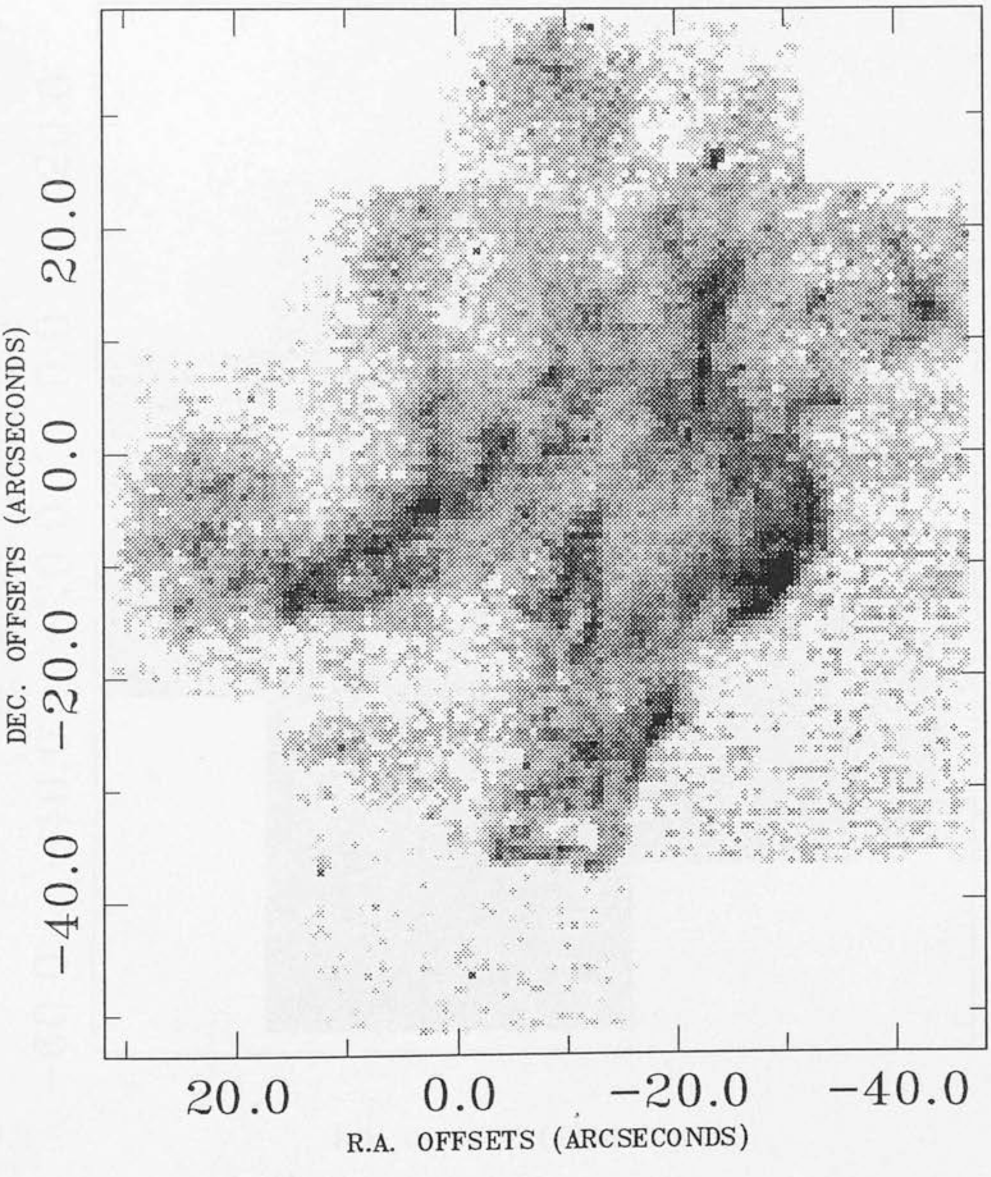

FIGURE 2.8a : Image of the northern bar of M17 in the light of the H_2 v=1-0 S(1) transition. The continuum has been subtracted. The image is plotted from a lower level at 0 data counts to an upper level at 65 data counts. The calibration is 2.3 x 10^{-20} W m^{-2} per data count.

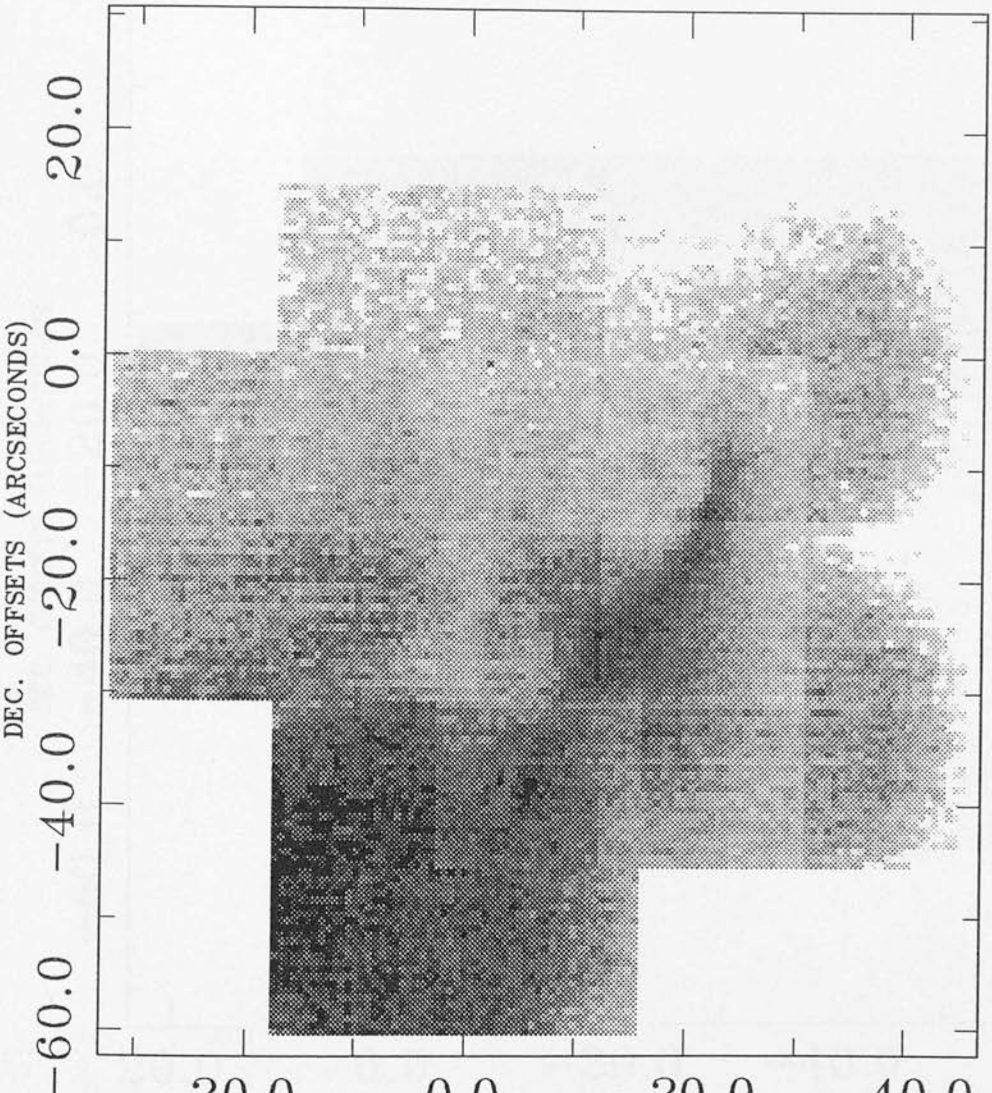

FIGURE 2.8b : Image of the northern bar of M17 in the light of Brackett γ recombination radiation from H^+. The continuum has been subtracted. The image has been plotted from a lower level at 0 data counts to an upper level at 4 counts. The calibration is 2.5×10^{-18} W m^{-2} per data count.

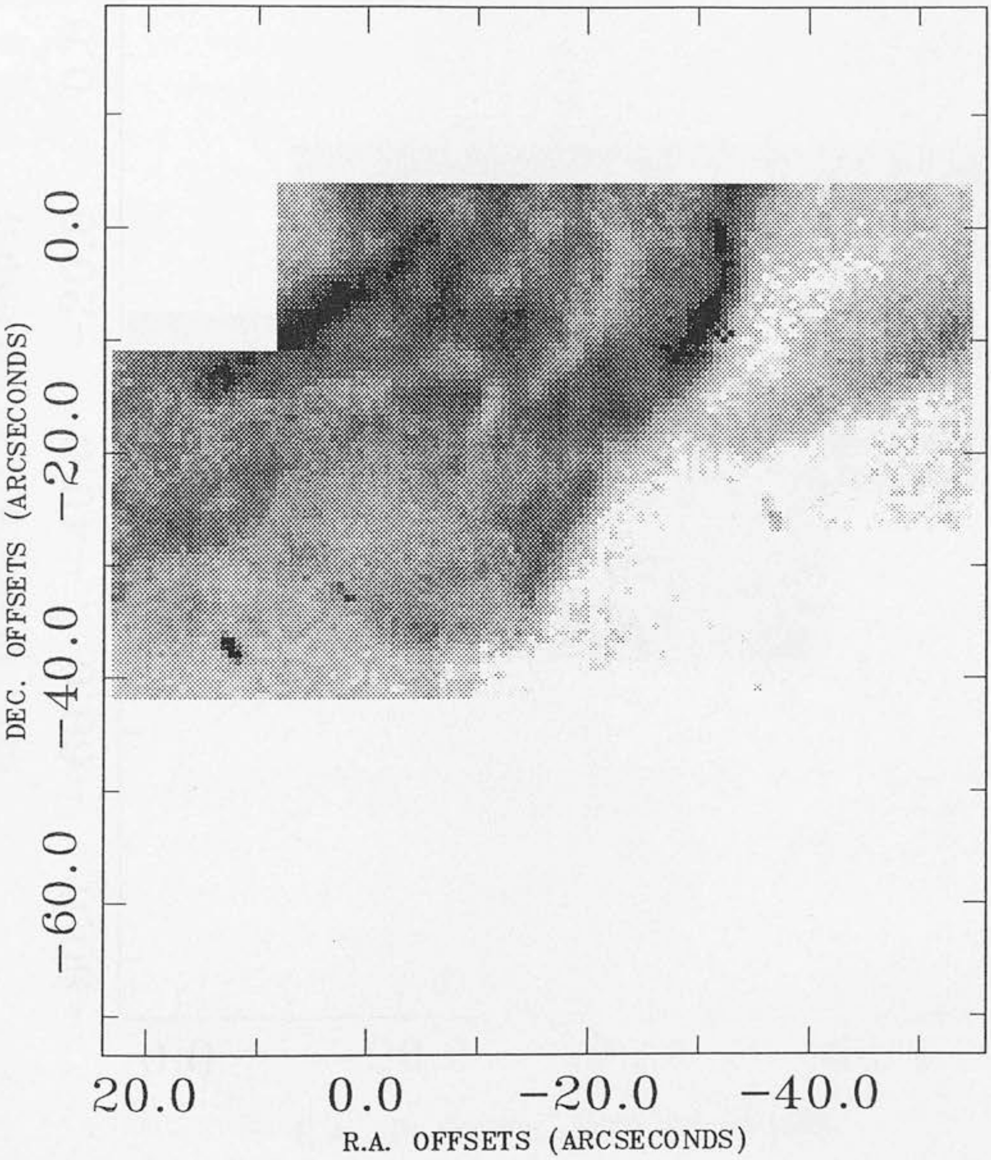

FIGURE 2.8c : Image of the northern bar of M17 in the light of the 3.28 μm emission feature. The continuum has not been subtracted. The image is plotted from a lower level at 0 data counts to an upper level at 65 data counts. The calibration is 3.1×10^{-31} W m^{-2} Hz^{-1} per data count.

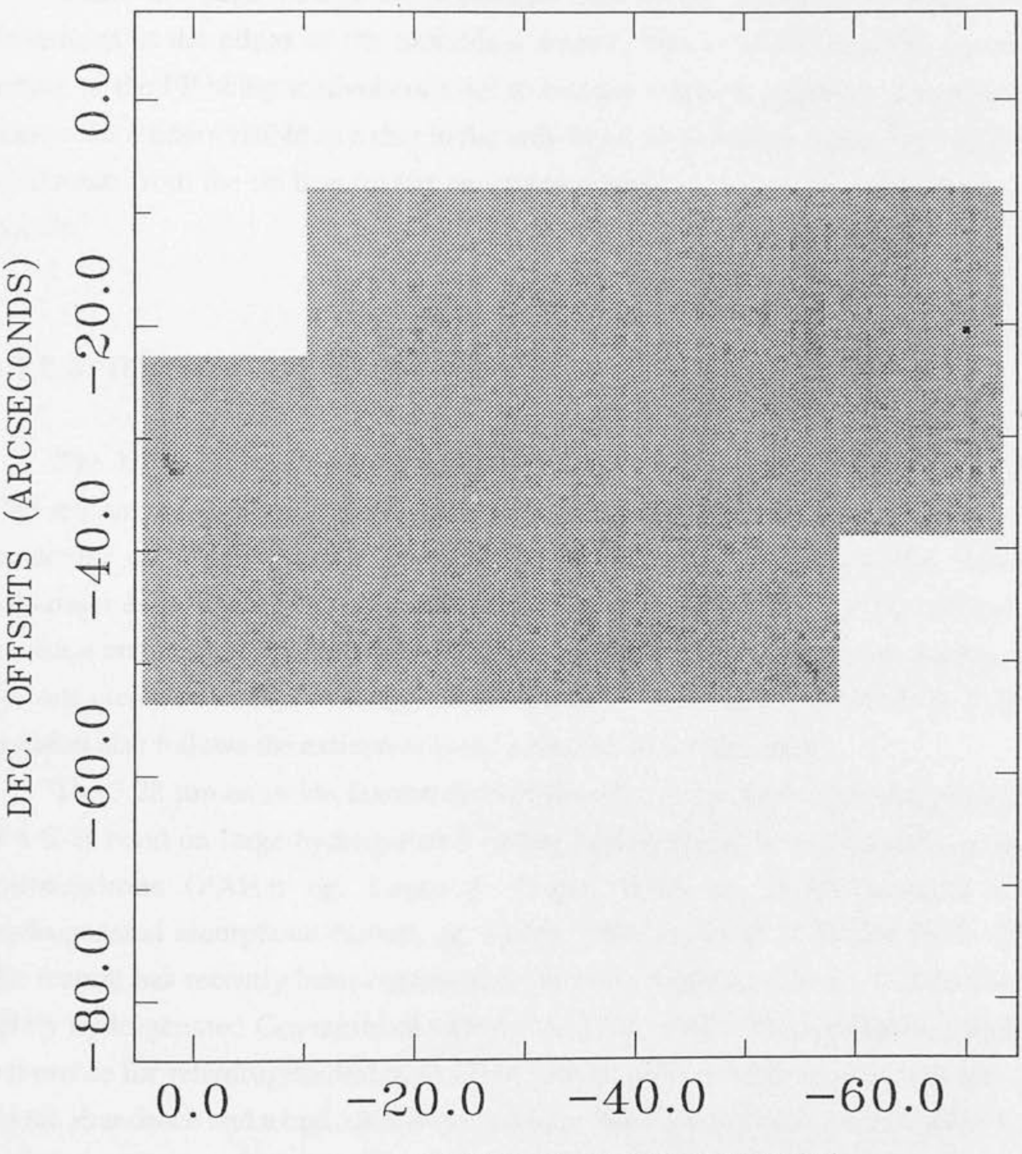

FIGURE 2.8d : Image of the northern bar of M17 in the continuum radiation at a wavelength of 3.1 μm. The image is plotted to the same levels as for the 3.28 μm image (Figure 2.8c). The continuum image is flat implying that the structure that is observed in Figure 2.8c is due to the 3.28 μm emission feature.

have calculated an average emission measure across the whole of the northern bar to be 1.9 Mpc cm^{-6}. Using as a size scale the width of the ionisation front (~ 0.95 pc) we infer an ionised gas density of $n_i \sim 10^3$ cm^{-3} and therefore a density for the neutral cloud of $n \sim 10^5$ cm^{-3}.

There are edge effects contaminating this image, apparent as semi circular distortions at the edges of the individual frames. These result from the continuum setting of the FP being inadvertently set to include a telluric emission line, which the phase shift renders visible as a ring in the individual continuum images. Subtracting this continuum from the on line frames caused the subsequent contamination in the final mosaic.

2.3.2.3 The 3.28 μm Image

The 3.28 μm emission feature has been assumed to delineate the molecular cloud - HII region interface (eg. Burton *et al.* 1988) and thus to be a tracer of the edge of the molecular cloud. In observations of Orion's Bar (Burton *et al.* 1988; Sellgren, Tokunaga & Nakada 1990) the 3.28 μm emission peaks ahead of the ionised gas emission and behind the molecular hydrogen emission peak, relative to the source of photons (see also Duley, Williams & Moorhouse 1991). The fall off of the 3.28 μm emission also follows the extinction of the radiation which excites it.

The 3.28 μm emission feature derives from the fundamental stretching vibration of a C-H bond on large hydrogenated carbon molecules such as polycyclic aromatic hydrocarbons (PAHs; eg. Leger & Puget 1984) or rehydrogenated HACs (hydrogenated amorphous carbon, eg. Duley 1985; Duley & Williams 1988, 1990). The feature has recently been suggested as possibly originating from the excitation of lightly hydrogenated C_{60} molecules (Webster 1991, 1992). The conditions which are favourable for rehydrogenation in the HAC model such as high temperature gas, high atomic abundance and a high ultraviolet radiation field are conditions which are found at the edges of PDRs. Within an HII region, the flux of ionising photons strips hydrogen from, and can destroy, the large molecules. At the interface with a molecular cloud the flux of ionising photons diminishes, and energetic hydrogen atoms can penetrate the HAC lattice and cause bulk rehydrogenation. A high ultraviolet field raises the grain temperature and creates localised hot-spots on the grain (10-100 hot-spots, T ~ 1000 K) which is sufficient for the energetic hydrogen atoms to overcome the activation energy for bulk rehydrogenation, leading to 3.28 μm emission (Duley & Williams 1990). Further into the cloud, the temperature drops, the hydrogen abundance decreases, the ultraviolet radiation field is attenuated and consequently 3.28 μm emission falls away (Duley, Williams & Moorhouse 1991). In the PAH model, to produce 3.28 μm emission the PAHs must be free molecules close to the cloud surface. In the HII region, the ionising flux and presence of hot electrons will rapidly dehydrogenate and destroy the PAHs. Inside the molecular cloud, away from the surface, the 3.28 μm emission reduces as the ultraviolet photons which excite the feature are extinguished.

The 3.28 μm image (Figure 2.8c) shows the two ridges of emission seen in the H_2 image. Comparing this to the continuum image at 3.1 μm (Figure 2.8d), which is plotted to the same levels as for Figure 2.8c, one can see that the 3.28 μm emission feature is very bright above the continuum and traces the structure of the molecular cloud. There is also an extended knot of emission centred at (15´´,-25´´), not seen in H_2, and a faint ridge of emission to the west, outside the field of view of the H_2 image. A mean flux density of the 3.28 μm feature (not continuum subtracted) through the filter is calculated because the band emission is quite broad (Bregman *et al.* 1989; Geballe *et al.* 1989). At the brightest point the flux density is, $F \sim 5.2 \times 10^{-5}$ W m^{-2} μm^{-1} sr^{-1}.

2.3.2.4 Comparison of 3.28 μm Image With H_2 and Br γ

The relationship between the 3.28 μm, H^+ and H_2 emission regions is very important in understanding the structure of PDRs. In plane parallel, uniform density PDR models, the H^+ emission from the HII region (if one is present) peaks before the molecular emission region (TH). If the geometry of the PDR surface is more complicated then one would expect to observe a correlated emission structure as the separate emission regions follow the shape of the cloud surface. On the other hand, if the PDR gas is highly clumped, with lower density interclump gas, then ionising photons may penetrate deeper inside the molecular cloud. In such a situation one might expect to observe a coincidence of all three emission regions.

Figure 2.9a shows the 3.28 μm image overlaid by a contour map of the H_2 emission. The coincidence of the two emission regions is evident. Figure 2.9b shows the 3.28 μm image overlaid by a contour map of the Br γ emission. The Br γ emission peaks inside the 3.28 μm and H_2 emission regions. The ridge of Br γ emission to the northwest follows the western ridge in the 3.28 μm and H_2 emission regions, ie. the molecular cloud. There is no corresponding Br γ emission (and very little 21 cm continuum emission - Felli *et al.* 1984) associated with the 3.28 μm and H_2 emission regions to the northeast of the image. For comparison, in the Orion Bar, the Br γ emission region peaks inside the 3.28 μm and H_2 emission regions, and the

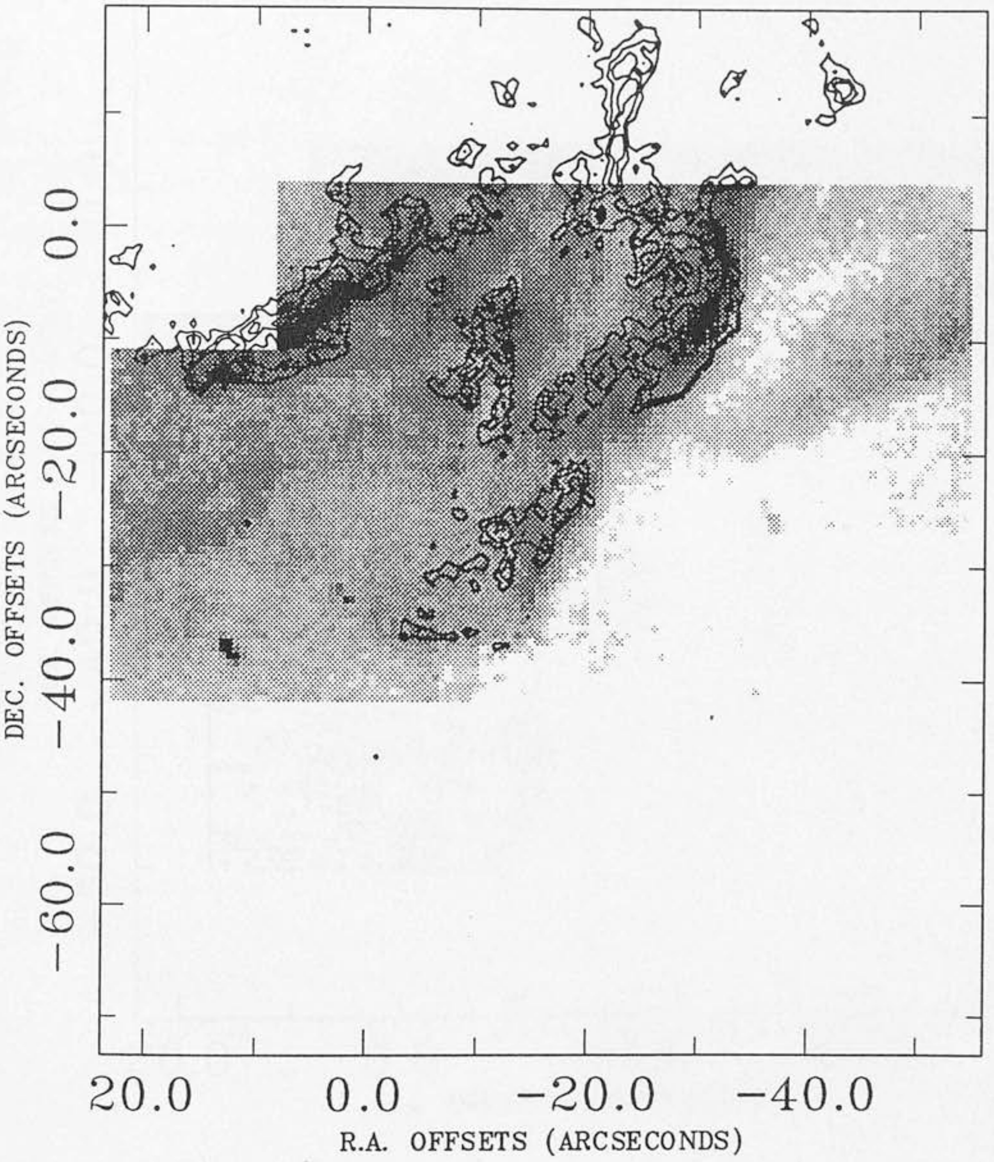

FIGURE 2.9a : Image of the northern bar of M17 in the light of the 3.28 μm emission feature overlaid by a contour map of the H_2 v=1-0 S(1) image. The contour levels are plotted from a base level at 30 data counts and at intervals of 10 data counts. The spatial coincidence of the two emission features is clear to see.

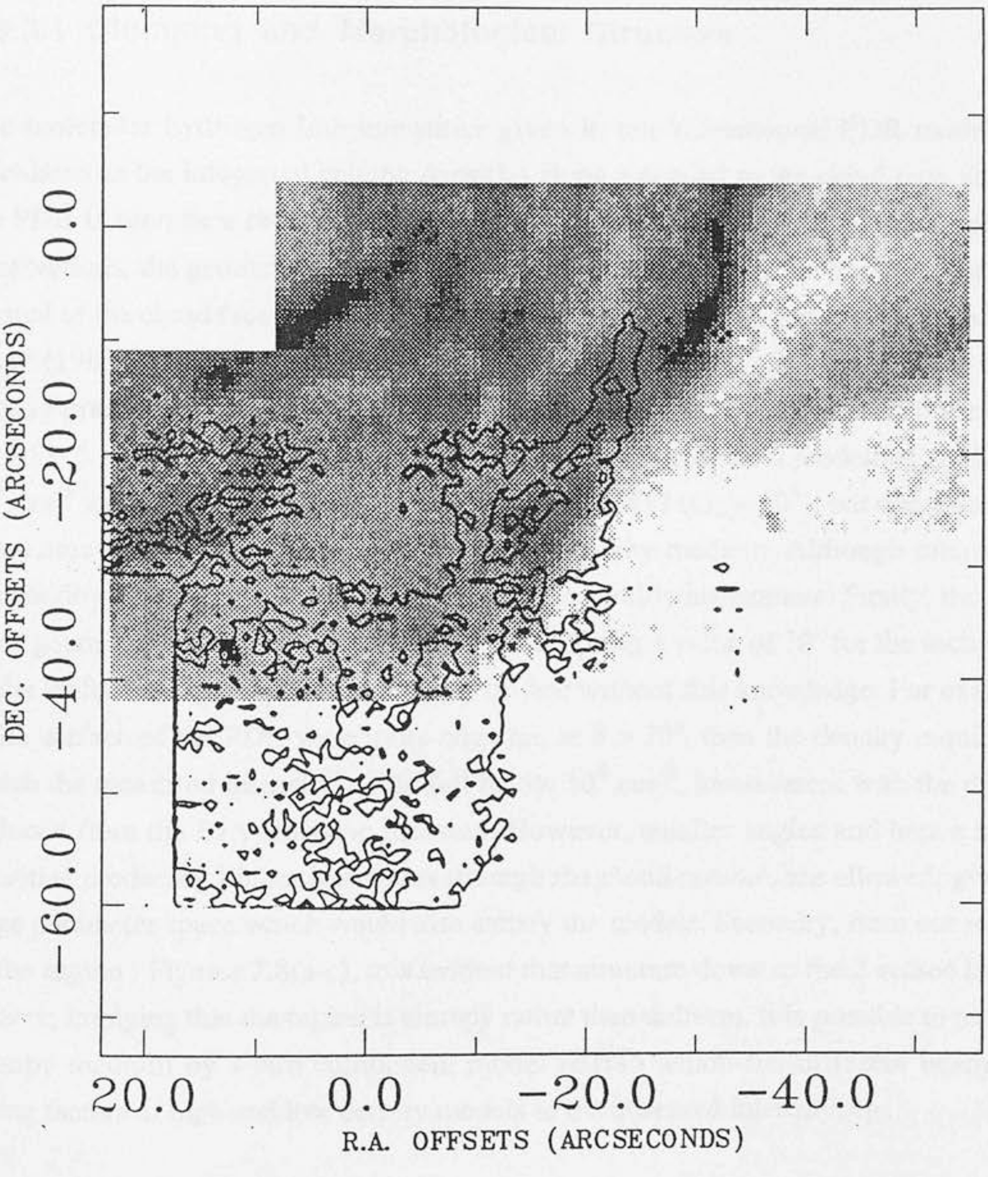

FIGURE 2.9b : Image of the northern bar of M17 in the light of the 3.28 μm emission feature, overlaid by a contour map of the Brackett γ recombination radiation image. The contour levels are plotted from a base level at 2 data counts and at intervals of 1 data count.

recombination radiation quickly dies away in the neutral cloud, by 85 % at the molecular hydrogen peak (Sellgren *et al.* 1990).

2.3.3 DISCUSSION

2.3.3.1 Clumping and Morphological Structure

The molecular hydrogen line intensities given in one dimensional PDR models are calculated as the integrated column densities along a normal to the cloud face, ie. as if the PDR is seen face on. Therefore, to make a detailed comparison with models and observations, the geometry of the region must be considered, ie. the angle between the normal of the cloud face and the line of sight to the observer. Following Icke, Gatley & Israel (1980) and Felli *et al.* (1984), then if we adopt a value of 70° inclination of the density gradient to our line of sight, then the intensity at the brightest pixel if seen face on is $I \sim 5 \times 10^{-8}$ W m^{-2} sr^{-1}. This agrees well with the theoretical modelling (BHT) for 10^5 cm^{-3} gas with an ultraviolet flux appropriate to M17 ($G_0 \sim 10^4$), but does assume a beam area filling factor of unity, ie. a uniform density medium. Although interesting, the validity of this result has to be doubted for the following reasons. Firstly, the small scale geometry in the region is unknown and choosing a value of 70° for the inclination of the surface at a pixel position is rather *ad hoc* without this knowledge. For example, if the surface of the PDR were more edge on, ie $\theta > 70°$, then the density required to match the measured intensity would fall below 10^4 cm^{-3}, inconsistent with the density deduced from the Br γ emission measure. However, smaller angles and hence higher densities producing higher intensities through the cloud normal, are allowed, giving a large parameter space which would also satisfy the models. Secondly, from our images of the region , Figures 2.8(a-c), it is evident that structure down to the 2 arcsec level is present, implying that the region is clumpy rather than uniform. It is possible to model a clumpy medium by a two component model (BHT) which fits different beam area filling factors of high and low density models to the observed intensity, eg.

$$I_{obs} = \alpha I(n_1) + \beta I(n_2) \qquad [2.15]$$

where α,β = beam area filling factors for clumps with densities n_1 and n_2.

A possible fit to the line flux occurs if 20% of the flux in the beam comes from gas at $n \sim 10^7$ cm^{-3} and 45 % from gas at $n \sim 10^5$ cm^{-3}. To make accurate fits in a two component model, further data points from fine-structure and CO rotational lines are necessary in addition to the H_2 data. BHT have conducted such a study on the southwestern bar of M17, and find that it is best fitted by a clumpy model which has 80 % of the beam area filled by gas at $n = 10^4$ cm^{-3} and 20 % by denser gas embedded within it at a density of $n = 10^7$ cm^{-3}.

In the two component PDR model, the emission is dominated by the high density component in the beam (BHT). If a two component PDR model is necessary to describe the PDR in the northern bar of M17, one would expect the H_2 emission spectrum to have thermalised line ratios. This is in contradiction to the results obtained by Tanaka *et al.* (1989), who measured the diagnostic lines of the 1-0 S(1) and 2-1 S(1) transitions of H_2 in the northern bar of M17, and found that their ratio was consistent with pure fluorescent emission in low density gas (ie. 1-0/2-1 ~ 2). However, they were using a large aperture beam (19.6 arcsec) and from our images it is clear that structures on scales much smaller than this exist in the region.

Figure 2.9b shows the Br γ emission in relation to the 3.28 μm emission. A close comparison of the Br γ image to the 21 cm continuum map by Felli *et al.* (1984) shows a good correspondence between the northwestern ridge of Br γ emission and a small (~ 20 arcsec long) feature in the radio continuum map, whose emission measure has been increased relative to its immediate surroundings by virtue of its higher density (Figure 2.10). The radio continuum map also confirms a decrease of emission to the northeast, where H_2 and 3.28 μm emission is prominent.

Two models are considered to explain these observations.

First, the absence of recombination radiation in the northeast is due to a depletion of ionising photons sustaining the ionisation of the HII region, and so we are looking at a cross section of the region (see Figure 2.11a). The PDR in Orion's Bar is believed to have a similar morphology, being seen edge on (eg. Tielens & Hollenbach 1985b). In Orion, the 3.28 μm emission feature is observed to peak ahead of the ionisation front (Sellgren *et al.* 1990), but then quickly dies away to an optical depth of $A_v \sim 2$, as the exciting radiation is attenuated. In the northern bar of M17 the 3.28 μm emission is also seen ahead of the Br γ emission, but is still strong in emission up to 20 arcsec away from the ionisation front delineated by the Br γ emission, corresponding to an optical depth of $A_v \sim 38$, assuming a uniform model in this edge on geometry with a density of at least 10^5 cm^{-3}. This large optical depth may be reconciled by the presence of clumping, which will allow high energy far-ultraviolet photons to penetrate further into the molecular cloud, producing warm surfaces on clumps and thereby exciting the 3.28 μm feature into emission. Of course, H_2 will also be excited at these surfaces thereby giving a natural explanation for the spatial coincidence of the two emission features. The idea of clumping of PDRs has already been invoked by Stutzki *et al.* (1988) to explain the detection of [CII] - first ionisation potential = 11.3 eV - on a scale of 15 pc, in the southwestern bar of M17.

Alternatively, if one is looking at the surface of the molecular cloud, then since the 3.28 μm emission traces the edge of the neutral cloud and the Br γ emission the ionisation front, one would expect some correlation between the two emission features. However, no correlation is evident; to the northeast of the image the 3.28 μm emission is bright but the Br γ emission , if present, is below the detection threshold. In terms of the emission measure, this corresponds to a drop in the ionised density by a factor of 3 assuming a small, if not negligible, change in the length scale. If we are looking at the top edge of the ionisation front (see Figure 2.11b), then it is possible to imagine the ionised material streaming away, under pressure, over the surface of the molecular cloud into a lower density medium, consequently decreasing in density as it does so. Meanwhile, this surface is still irradiated by soft ultraviolet photons exciting the 3.28 μm and H_2 features into emission. Such a model would be consistent with a blister HII region model (eg. Icke *et al.* 1980).

In the southwestern bar of M17, comparing the molecular maps of the region from Stutzki *et al.* (1988) and Stutzki & Güsten (1990) to the radio continuum (Felli *et al.* 1984) also reveals an anti correlation between the molecular and ionised regions. However, as there is [CII] emission associated with the radio continuum and molecular emission (Stutzki *et al.* 1988), another plausible scenario may be that there exists a large predominantly atomic transition zone between the ionised and photodissociation regions. The ionisation fraction in this zone would have to be low enough such that the emission measure would be below our detection threshold.

2.3.3.2 Attenuation of Ultraviolet Photons in PDRs

In a PDR model, there are two characteristic regimes depending on the density n, and the ultraviolet field G_0. In one, the ultraviolet attenuation is dominated by dust shielding and in the other by line shielding. The condition that line shielding dominates over dust shielding is approximately given by (BHT),

$$\frac{n}{G_0} > 40 \text{ cm}^{-3} \qquad [2.16]$$

Dust extinction dominates when (n/G_0) falls below this value. For high values of this ratio, the dominant line shielding of ultraviolet photons brings the HI/H_2 transition zone to an optical depth $A_v < 1$, closer to the edge of the cloud where the gas is still hot

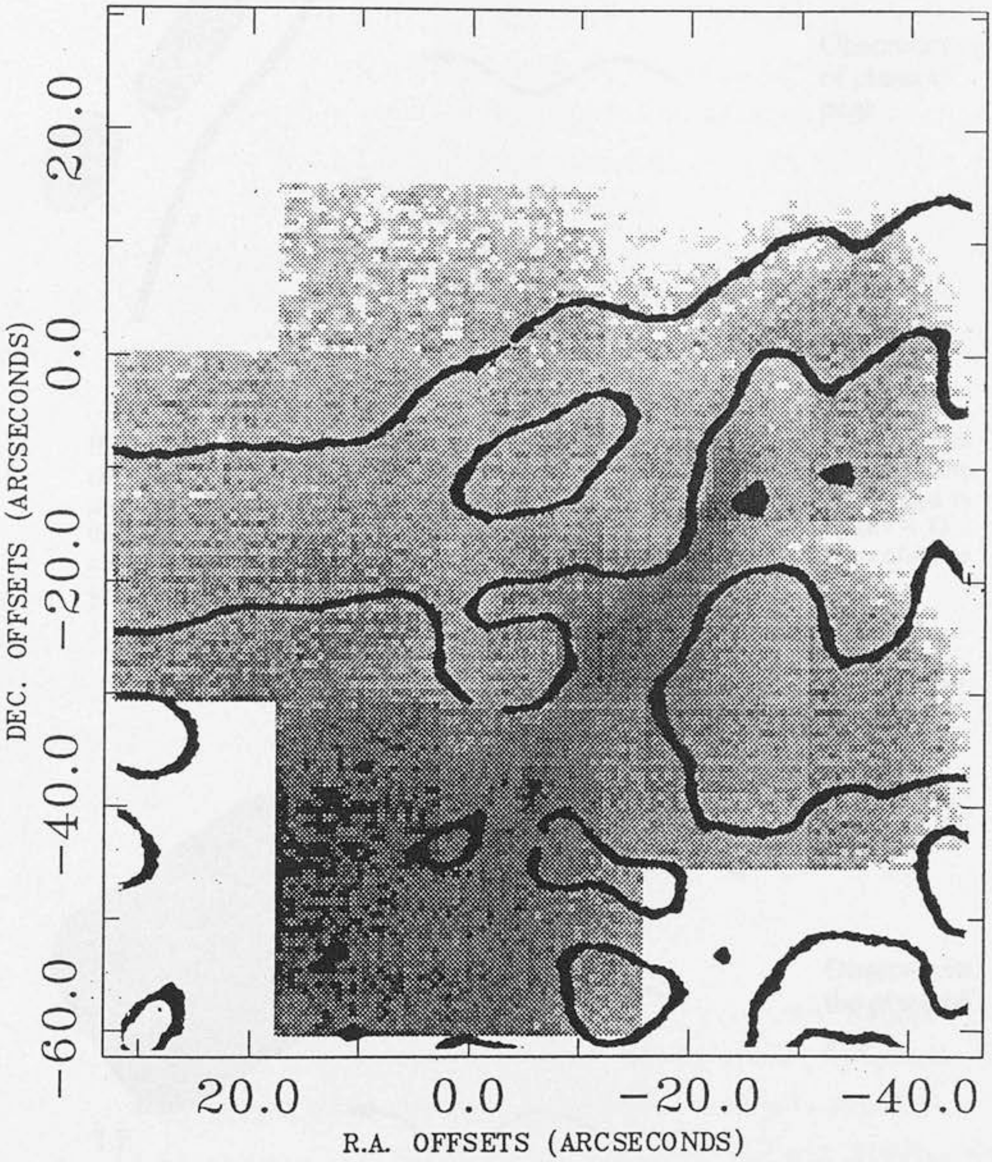

FIGURE 2.10 : Image of the northern bar of M17 in the light of Brackett γ recombination radiation, overlaid by a contour map of the 21 cm continuum emission from Felli *et al.* (1984).

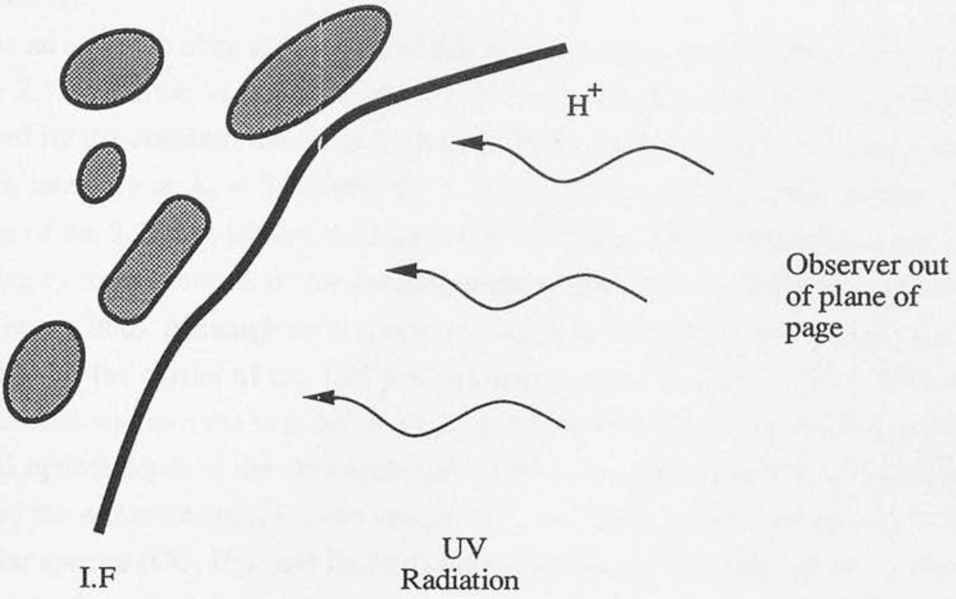

FIGURE 2.11a : Schematic diagram showing the HII region and the ionisation front (IF) as a cross section, with the observer out of the plane of the page. The molecular cloud is to the left of the ionisation front with high density clumps in dark shading. The clumpy molecular cloud allows ultraviolet photons (hv < 13.6 eV) to penetrate deep into the molecular cloud and illuminate the surfaces of dense clumps.

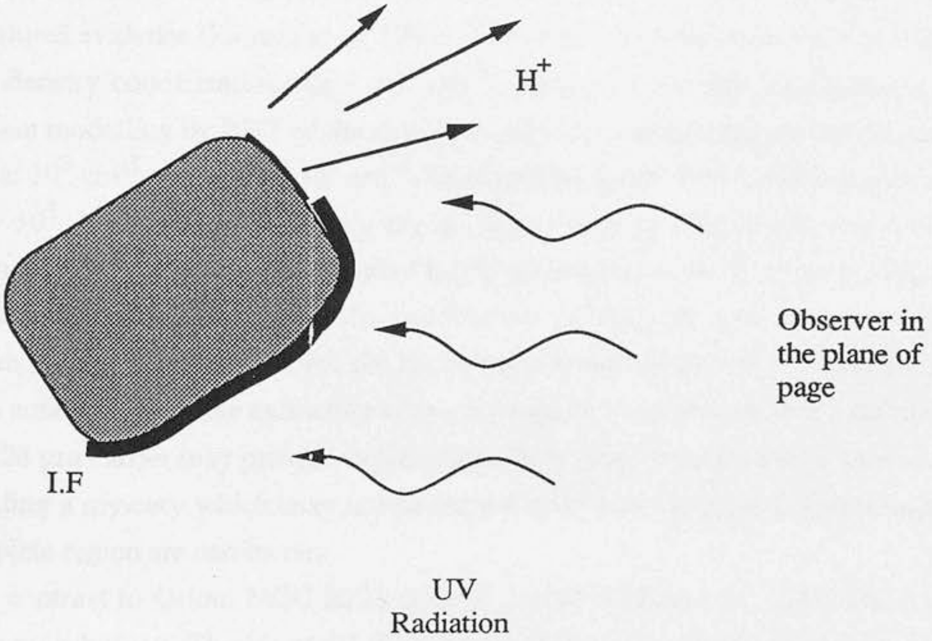

FIGURE 2.11b : Schematic diagram showing the HII region and ionisation front as a cross section. In this case, the observer is in the plane of the page. The ionised material at the top is streaming away into vacuum, decreasing in density and hence emission measure (until it is below our detection threshold), and therefore only emission from the H_2 and 3.28 μm features (dark shading) is seen at this position.

(T ~ 1000 K).

As an example of an application of this theory, images of the PDR in Orion's Bar (Figure 2.12a; Burton *et al.* 1988) show a structure which seems to be successfully described by the standard model of Tielens & Hollenbach (1985a,b) in which the H_2 peaks in intensity at $A_v \sim 3$, behind the 3.28 μm feature, ie. the cloud surface. The intensity of the 3.28 μm feature in Orion's Bar decreases with distance into the cloud, according to the extinction of the exciting ultraviolet radiation (Sellgren *et al.* 1990; Burton *et al.* 1988). Although no chemical or complete thermal balance model has been developed for the carrier of the 3.28 μm emission feature, Sellgren *et al.* (1990) infer their conclusions from the fact that the spatial extent of the 3.28 μm emission occurs over one optical depth of the ultraviolet radiation. Tielens & Hollenbach (1985b) have modelled the emission from ionised species (C^+, Si^+, Fe^+), neutral species (C, O) and molecular species (CO, H_2), and find that the emissions are best modelled by a density to ultraviolet flux ratio of,

$$\frac{n}{G_0} \sim 1 \ \mathrm{cm}^{-3} \qquad [2.17]$$

satisfying the inequality (equation [2.16]) for dust shielding, and for producing the stratified structure of the H_2 and 3.28 μm emission in the models. However, recent observational evidence (Parmar *et al.* 1991; Graf *et al.* 1990) has revealed the presence of high density condensations ($n \sim 10^7$ cm^{-3}) present in the Bar. Furthermore, two component modelling by BHT of the emission give beam area filling factors for the gas of 10% at 10^7 cm^{-3} and 90% at 10^5 cm^{-3}, irradiated by an ultraviolet field characterised by $G_0 = 10^5$. If the region is clumpy the question arises of why the H_2 and 3.28 μm emission features are separated instead of being spatially correlated? Other peculiarities about the image in Figure 2.12a is the fact that the 3.28 μm emission peaks ahead of a minimum in the H_2 emission while the H_2 emission peaks behind of a minimum in the 3.28 μm emission. Variable extinction across the region or the uncertain photochemistry of the 3.28 μm carrier may provide explanations. It is clear that the PDR in Orion's Bar is providing a mystery which may not be solved until more extensive observations of the complete region are carries out.

In contrast to Orion, NGC 2023 (Figure 2.12b; Burton *et al.* 1988) has a quite different morphology. The H_2 and 3.28 μm emission regions are spatially coincident, implying that line shielding may be dominating the extinction and bringing the HI/H_2 transition zone close to the surface, and hence causing the spatial coincidence between the H_2 and 3.28 μm emission regions. Recent measurements of reflection and planetary nebulae have shown that the spatial coincidence of the 3.28 μm and H_2 emission

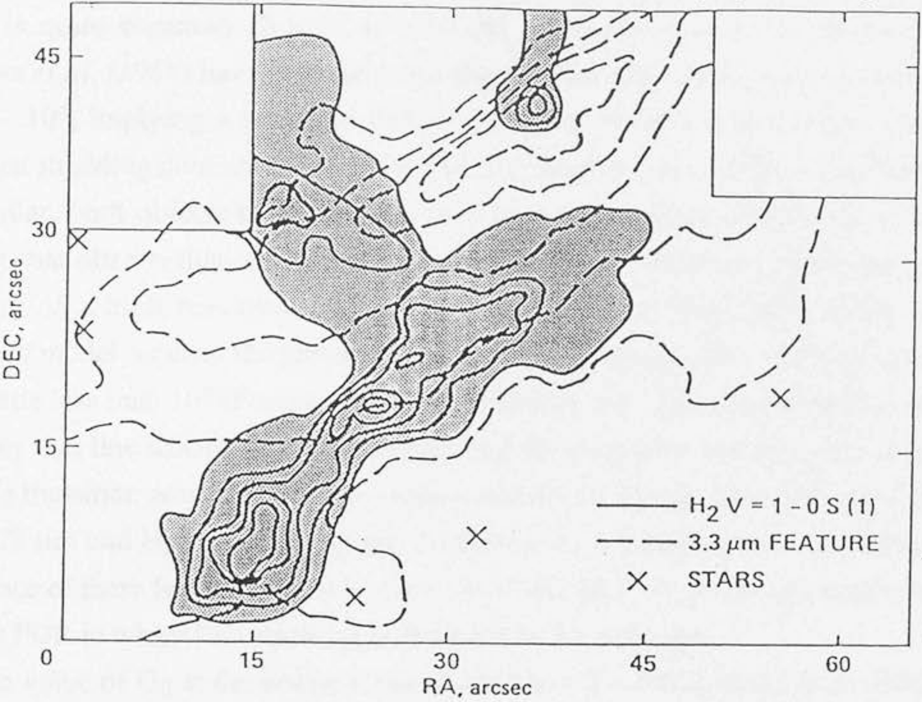

FIGURE 2.12a : The PDR in Orion's Bar showing the H_2 emission (shaded contour) and the 3.28 μm emission. This figure is taken from Burton *et al.* (1988). The spatial separation between the H_2 and 3.28 μm emission regions is ~ 15 arcsec corresponding to $A_v \sim 1$ (assuming $n = 10^5$ cm^{-3}), in agreement with the theoretical predictions. Note that this image has been flipped east to west during the data reduction such that northeast is at the top right hand corner.

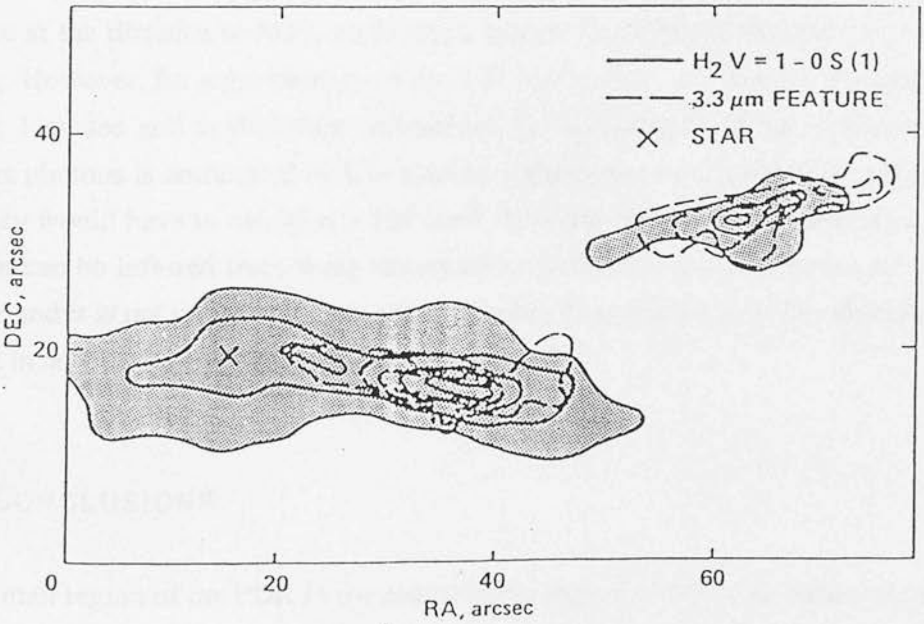

FIGURE 2.12b : The PDR in NGC 2023 showing the H_2 emission (shaded contour) and the 3.28 μm emission. This figure is taken from Burton *et al.* (1988). In this object the two emission features are both spatially coincident, seemingly in contradiction to the theory. This image has also been flipped east to west during the data reduction such that northeast is at the top right hand corner.

regions is quite common (Burton *et al.* 1988; Moorhouse *et al.* in preparation). Hasegawa *et al.* (1987) have inferred a low density for NGC 2023, with $n \sim 10^4$ cm^{-3} and $G_0 \sim 10^4$, implying a value for (n/G_0) similar to the Orion Bar and the regime where dust shielding dominates the extinction. The angular scales of the two objects are very similar, both objects being at a distance of approximately 450 pc away, hence implying that observation and theory do not agree in this instance. However, recent modelling of a high resolution H_2 emission spectrum of NGC 2023 using a two component model requires the presence of high density gas, $n \sim 10^5 - 10^6$ cm^{-3}, and G_0 to be a little less than 10^4 (Burton *private communication*). The value of (n/G_0) would thus imply that line shielding may be dominating the extinction and therefore bringing the HI/H_2 transition zone closer to the surface and producing the observed coincidence of the 3.28 μm and H_2 emission regions. Furthermore, in a clumpy medium the spatial coincidence of these features would be tight. So, NGC 2023 can be simply explained by a clumpy PDR in which line shielding is dominating the extinction.

The value of G_0 at the northern bar of M17 is $\sim 3 \times 10^4$ (Stutzki *et al.* 1988). If dust shielding is dominating the far ultraviolet attenuation, the separation of the 3.28 μm and H_2 emission regions is of order $A_v \sim 1$. Our observations show that the emission regions are spatially coincident, and therefore ruling out gas densities of $n < 10^5$ cm^{-3} since any separation of order $A_v \sim 1$ would then be resolvable. For example, for a gas density of $n = 10^4$ cm^{-3}, a separation of $A_v = 1$ is equivalent to a spatial separation of 6.5 arcsec at the distance to M17, assuming a gas-to-dust ratio of the form $A_v = 2 \times 10^{-21} N_H$. However, for a gas density of $n = 10^5$ cm^{-3}, an $A_v = 1$ spatial separation is less than 1 arcsec and is therefore unresolved by our images. If the extinction of ultraviolet photons is dominated by line shielding then equation [2.16] tells us that the gas density would have to satisfy $n > 10^6$ cm^{-3}. Without further information, the only result that can be inferred from these observations is that the gas density must be $n \geq 10^5$ cm^{-3}, and it is not possible to determine whether dust shielding or line shielding is dominant in attenuating the ultraviolet photons in M17.

2.3.4 CONCLUSIONS

A small region of the PDR in the northern bar region of M17 has been imaged in the light of the H_2 v=1-0 S(1) transition, the Br γ recombination line of H^+ and the 3.28 μm emission feature.

A single component high density ($n \sim 10^5$ cm^{-3}, $G_0 \sim 10^4$) PDR model is sufficient to reproduce the H_2 line intensity observed if further assumptions are made concerning the morphology and small scale geometry of the region. However, the fact that our images reveal structure on a scale of 2 arcsec suggests that a two component (ie. clumped) PDR model is probably the preferred solution.

Structurally, the Br γ emission correlates well with 21 cm radio continuum observations (Felli *et al.* 1984), however, it is not clear whether we are observing the surface of the molecular cloud illuminated by ultraviolet photons, or whether we are looking at a cross section of the region, ie. near edge on as in Orion's Bar.

The bright parts of the H_2 and 3.28 μm emission regions are spatially coincident, to an accuracy of ~ 1 arcsec. This agrees with similar observations of reflection nebulae by Burton *et al.* (1988) and Moorhouse *et al.* (in preparation). A high density region (n $\geq 10^5$ cm^{-3}) is required to explain the spatial coincidence of the H_2 and 3.28 μm emission regions, however, it is not clear whether the extinction of the ultraviolet photons in the region is dominated by dust shielding or by line shielding.

3 Near Infrared Spectroscopy Of H_2 In M17 Northern Bar

3.1 INTRODUCTION

The infrared emission from rotation - vibration transitions of the H_2 molecule can arise as a consequence of the absorption of an ultraviolet photon by the molecule exciting it to either the Lyman or Werner bands of the first electronic state. This is quickly followed by a radiative decay back into the ground state. Ten percent of these decays will fall into the vibrational continuum and dissociate the molecule (Stecher & Williams 1967) while the remaining 90 percent will fall into discrete, bound levels of the ground state from whence they cascade down the rotational - vibrational levels, emitting infrared photons as they do so (Black & Dalgarno 1976).

This infrared spectrum has been computed by several authors (eg. Black & Dalgarno 1976; Black & van Dishoeck 1987; Sternberg & Dalgarno 1989). Recent models of photodissociation regions (PDRs) have shown that for densities above a critical density ($n_{cr} \sim 10^4$ - 10^5 cm^{-3}) collisional redistribution of the population of the rotation - vibration levels of H_2, alters the spectrum such that it appears thermalised, as if shock excited (Burton, Hollenbach & Tielens 1990, hereafter BHT; Sternberg & Dalgarno 1989). For instance, the diagnostic ratio of the H_2 v=1-0 S(1) and 2-1 S(1) transitions has been commonly used to discriminate between shocked and fluorescent excitation of H_2, this ratio being approximately 2 for fluorescent excitation (Black & van Dishoeck 1987) and of order 10 for shock excitation (Shull & Hollenbach 1978). However, collisional interactions in high density PDRs can raise the value of this diagnostic ratio, eg. for a density of 10^6 cm^{-3} and an incident ultraviolet flux which is

10^4 times the ambient value in the solar neighbourhood, the ratio can take values of ~ 8 - 10. Clearly, this ratio by itself cannot be relied upon to determine the nature of the excitation since high density gas in a photon dominated region can imitate the effect of shocks.

The infrared emission spectrum from fluorescently excited H_2 was first detected and identified in spectra taken of the reflection nebula, NGC 2023 (Gatley *et al.* 1987; Hasegawa *et al.* 1987). Recently, complete JHK spectra from NGC 2023 have been obtained by Burton *et al.* (1992, in preparation) which show that the emission is slightly thermalised requiring the presence of high density material, most probably in the form of small condensations of gas (ie. clumps). Infrared spectroscopy of H_2 has also been carried out in a number of sources, including the northern bar of M17, by Tanaka *et al.* (1989). They inferred that the H_2 emission in the northern bar of M17 within a 19.6 arcsec beam comes from radiatively excited H_2, little affected by thermal reprocessing, and therefore implying that the gas density is low. In this chapter I will discuss our own spectral observations of the northern bar of M17 and their implications for the physical conditions and morphology in the region and on the PDR models.

3.2 OBSERVATIONS AND DATA REDUCTION

K band spectra of the PDR in the northern bar of M17 were observed on the nights of 5 - 7 July 1991 with the United Kingdom Infrared Telescope (UKIRT) on Mauna Kea, Hawaii. The instrument used was the cooled grating spectrometer, CGS4, which has a long slit (90 arcsec) projected onto a 62 x 58 pixel InSb array chip. In the configuration employed only the middle 30 rows of the chip are illuminated giving the instrument a spatial resolution of 3 arcsec per pixel. The width of the slit was also 3 arcsec. The spectral resolution was $\Delta\lambda = 6.35 \times 10^{-3}$ μm (FWHM) at 2.2 μm, using the 75 lines per millimetre grating.

The northern bar in M17 is an extended source (~ 6 arcmin east to west - Felli *et al.* 1984) and nodding off source was required to obtain sky positions. The sky position is 624 arcsec west and 54 arcsec south of our reference position which is $18^h\ 17^m\ 48.62^s$, $-16° 9' 55''$ (1950). The angle of the slit projected on to the sky was fixed at -15° (north through east) so that the slit was placed over the bright ridge of H_2 emission present in the region (Figure 3.1).

The observations were sampled spectrally by moving the detector by half a pixel over 2 pixels giving integrations at 4 detector positions. This mode of sampling (ie. over 2 pixels) was used so as to minimise the number of "bad" positions on the spectrum

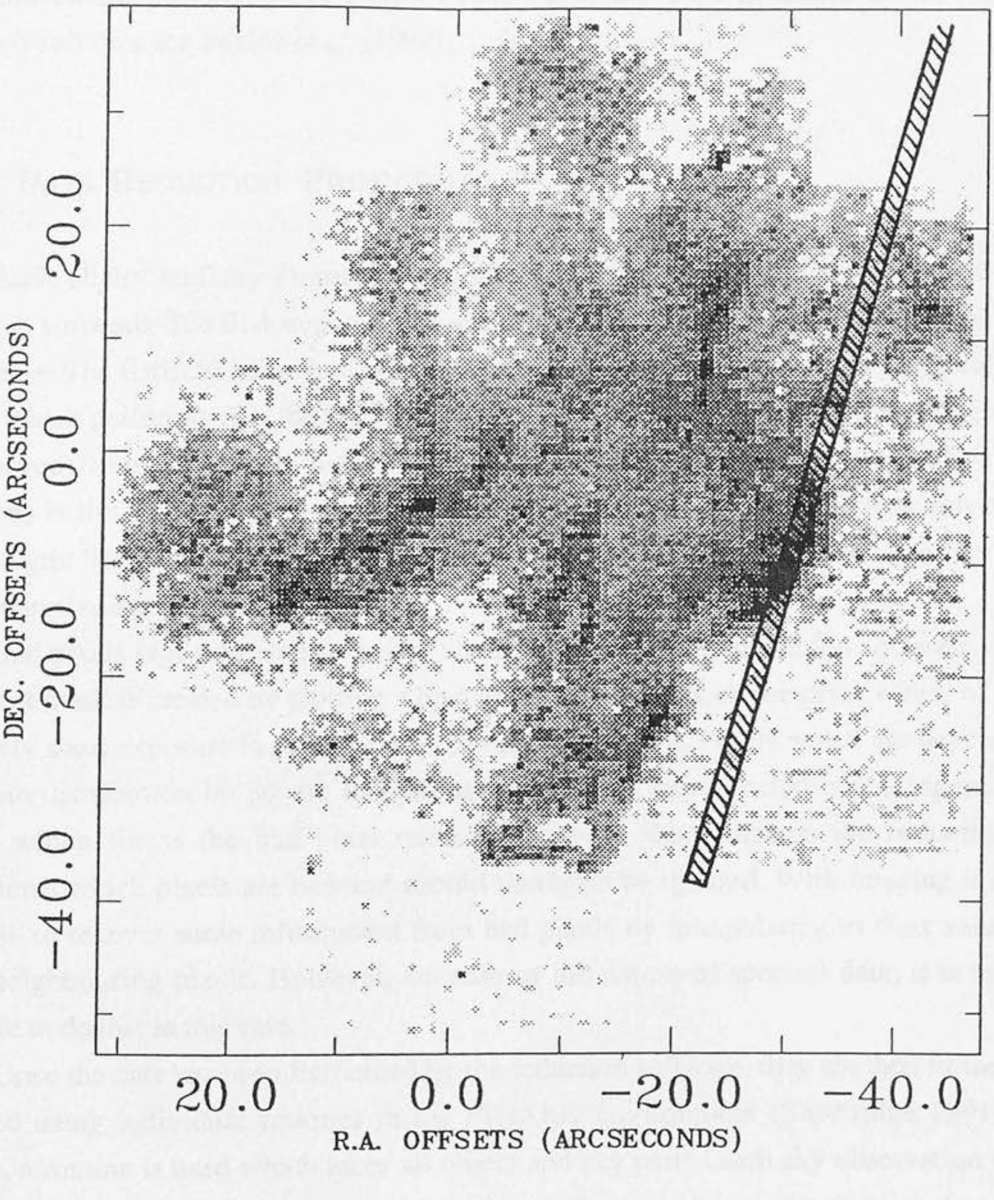

FIGURE 3.1 : Image of the northern bar of M17 in the light of the v=1-0 S(1) transition of molecular hydrogen (Chapter 2). The CGS4 slit is superposed on the image at the position where these observations were made.

due to bad pixels on the array. With this mode the spectral positions sampled by bad pixels will also be sampled by adjacent good pixels, and hence recovering the data. Only pairs of bad pixels on the array which happen to be adjacent will contribute to a "bad" spectral position. The reduction software interleaves the 4 integrations to give the final observation. In the following sections I will describe how the data was acquired and fully reduced and calibrated. For a more detailed account of the dedicated CGS4 data reduction software see Puxley *et al.* (1992).

3.2.1 DATA REDUCTION PROCEDURE

Each object and sky frame were flatfielded using the dedicated CGS4 data reduction software. The first step in the procedure is to acquire a "reduced" version of a bias frame. The flatfield frame in CGS4 is obtained by observing an internal blackbody source which uniformly fills the slit via an integrating sphere. The bias and dark current is removed from this frame and the resultant image (normalised by a blackbody function) is the intrinsic pixel-to-pixel gain variations of the array as a function of wavelength. The reduction software then reduces all the object, sky and arc lamp observations using this flatfield.

Bad pixels (eg. saturated or noisy) are also treated by the reduction software. A bad pixel mask is created by plotting a histogram of the errors on the pixel values of a relatively short exposure (a few seconds) of the dark current. Points which are beyond the main distribution by 3σ are flagged as bad and are incorporated into a separate image which forms the bad pixel mask. This mask then informs the reduction procedures which pixels are bad and should therefore be ignored. With imaging it is possible to recover some information from bad pixels by interpolating to their value from neighbouring pixels. However, because of the nature of spectral data, it is not possible to do that in this case.

Once the data has been flatfielded by the reduction software, they are then further reduced using individual routines in the FIGARO environment (Shortridge 1991). Firstly, a routine is used which takes all object and sky pairs (each sky observation is taken immediately before or after the object observation to make consecutive pairs), and subtracts the sky emission from the object observation. This practise also serves as an effective method of removing the dark current from the object frame, since over such a short time the dark current on the object and sky observations will be the same. The intensity of sky lines are known to vary with a period of ~ 10 minutes (Ramsay *et al.* 1992a) and since the time difference between our object and sky position was small (~

80 seconds), we found that the subtraction of sky line emission in this manner was very good. Because of the spatial extent of the object there was no sky in the slit, which meant that a second order correction of removing any residual sky line emission could not be performed. Next, the same pixel row from each sky subtracted object frame is extracted and placed into a separate frame. Each of these frames now contain spectra at the same pixel position (ie. spatial position) from all sky subtracted object frames.

Next, the spectra in these frames have any rippling removed. Ripples on the spectra are caused by the object moving in and out of the slit between integrations (ie. detector positions) so that the absolute fluxes on each integration in the observation differ. Therefore, when the reduction software comes to interleave these integrations, the differences manifest themselves as a ripple pattern on the spectrum. The image motion occurs as a consequence of wind bouncing the telescope, or seeing effects. The rippling is removed by first selecting a region of the spectrum where the ripple pattern is most evident, eg. the continuum. The mean of this region is calculated and the ripple spectrum is defined by the deviation of each point from this mean at the ripple period, from which a maximum and minimum amplitude are defined. From this information, one can extend the ripple spectrum so that it has the same coverage as the object spectrum. Then, the ripple spectrum is divided into the object spectrum to remove the ripples.

Finally, the spectra are coadded to give the resultant spectrum at that spatial position. The coadding is carried out by first calculating the mean number of counts of each spectrum in the frame, and then normalising each of these spectra to the average value from all spectra. The error on each spectral point is then calculated from the scatter of the value of that spectral point from the average. The normalisation is important here, for if the signal happened to be reduced due to the passage of a cloud across the beam, for instance, then the errors that would be calculated if the spectra were not normalised would be unrealistically large.

3.2.2 WAVELENGTH AND FLUX CALIBRATION

The wavelength scales of the spectra were calibrated by making observations of the known transitions from either an argon or krypton lamp. The wavelengths of the transitions were identified using the list published by Outred (1978). The calibrated wavelength scales from the lamp observations are then used to replace the estimated wavelength scale in the observations. The wavelength calibration was accurate to better than $\pm 5 \times 10^{-4}$ μm (~ 0.1 pixels).

Flux calibration was carried out by making observations of the standard star HD161903 ($m_K = 7.02$, spectral type = A2). Because the star is a point source, there is ample sky emission in the slit to enable sky observations to be taken by simply *sliding* the star perhaps 30 arcsec along the slit and calling this the sky frame. Then, each sky subtracted object frame has both a positive and a negative image of the standard star spectrum. If required, the negative image may be inverted and added to the signal of the positive image to increase the signal-to-noise ratio. This was not required for our data set.

Similarly to the sky subtracted source frames, the same row is extracted from every frame and placed in another frame. However, before this is done, any residual sky emission is removed. This is possible as there is ample sky present in the slit either side of the standard star. The residual sky lines are removed by simply fitting polynomials along the spatial direction either side of the stellar spectrum. These polynomials are then interpolated underneath the stellar spectrum removing the residual sky emission. Then, the spectrum is extracted, derippled, coadded and wavelength calibrated, as described in section 3.2.1.

Before this spectrum can be used as a flux calibrator, stellar absorption features are removed. The only stellar feature present in this part of the spectrum is a Brackett γ absorption feature which was removed by fitting to it with a Lorentzian profile (appropriate for collisionally broadened lines in the stellar atmosphere). Atmospheric absorption features are not removed because they are intrinsic to the atmosphere and so will also be present in the object spectrum. Division of the object spectrum by the stellar spectrum will remove these features. The stellar spectrum is then divided by a blackbody function at the effective temperature of the star ($T_{eff} = 9300$ K), which is normalised so that only the slope of the stellar spectrum is removed. The flux density from the star as a function of wavelength is then calculated from the magnitude at K, and divided into the stellar spectrum. The resultant spectrum is then divided into the object spectrum converting the number of data counts into a flux density. Algebraically, the flux calibration technique can be described by,

$$\frac{F_{obj}}{F_*} \times \mathrm{B.B(norm)} \times S_\lambda \qquad [3.1]$$

where F_{obj} = object spectrum (in data counts); F_* = stellar spectrum (in data counts); B.B (norm) = normalised blackbody function; S_λ = stellar flux density.

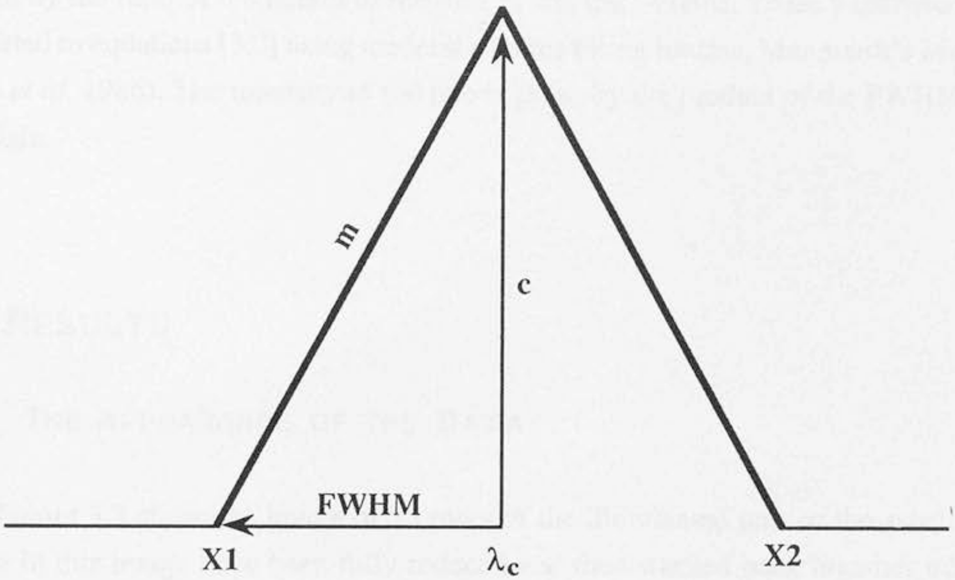

FIGURE 3.2 : Schematic diagram of the triangular instrumental profile of CGS4 used to calculate the line intensities. The symbols are defined in the text and equation [3.2].

3.2.3 LINE FITTING

The CGS4 instrumental profile is triangular in shape. This is because the slit has a top hat profile which is being projected onto the array whose pixels also have top hat profiles. Sampling slides the detector across the top hat profile of the slit and therefore produces a convolution of the two profiles, which is triangular. To calculate the intensities of the individual transitions a short routine was written to fit to triangular profiles, which I will briefly describe here.

In Figure 3.2, the variables X1 and X2 define where the edge of the line profile start and end. The line centre is given by λ_c. The height of the line is given by c and m is the gradient of the profile. The function of the triangle which is used to fit to the line is,

$$y = +m(\lambda - \lambda_c) + c + \text{continuum} \qquad X1 \le \lambda \le \lambda_c \qquad [3.2a]$$

$$y = -m(\lambda - \lambda_c) + c + \text{continuum} \qquad \lambda_c < \lambda \le X2 \qquad [3.2b]$$

$$y = \text{continuum} \qquad \text{otherwise} \qquad [3.2c]$$

There are therefore 5 parameters in the fit : the continuum under the line, the slope of the continuum, the line centre, the height of the line and the full width at half maximum (FWHM). The gradient of the triangular profile is not a parameter since it is defined by the ratio of the height of the line, c, and the FWHM. These parameters are then fitted to equations [3.2] using the least squares fitting routine, Marquardt's Method (Press *et al.* 1986). The intensity of the line is given by the product of the FWHM and the height.

3.3 RESULTS

3.3.1 THE APPEARANCE OF THE DATA

Figure 3.3 shows an image of 25 rows of the illuminated part of the array. The spectra in this image have been fully reduced and then stacked back together into an image. One can clearly see the bright Brackett γ (Br γ) hydrogen recombination line, which dominates the emission, at $\lambda = 2.166$ μm. The emission is especially bright at the top (ie. southeast) of the image where the slit falls on the HII region. The molecular cloud occurs below the 20th row, as evidenced by the H_2 emission, especially the v=1-0 Q-branch at around 2.4 μm and the 1-0 S(1) transition at 2.122 μm. In this figure it is clear to see how the continuum level rises and falls in the spatial direction.

Figure 3.4 gives another perspective of the spectra obtained in the K window. There are 27 spectra in all. In this figure, the HII region is at the bottom of the array and the cloud boundary is indicated by the dashed line. These results, showing the spatial variation of the ionised and molecular gas emissions are consistent with the results of Chrysostomou *et al.* (1992a) (see also Chapter 2), who imaged the same region in the lines of the Br γ and H_2 v=1-0 S(1) transitions. They showed that the Br γ emission peaks south of the molecular emission. Finally, 19 rows in which H_2 emission is present were added together to maximise the signal to noise ratio and the resultant spectrum, with emission features labelled, is shown in Figure 3.5.

3.3.2 EXTINCTION AND INTENSITY MEASUREMENTS

A frequently used method for measuring extinction is to ratio the v=1-0 S(1) and 1-0 Q(3) line intensities ($\lambda = 2.1218$ μm and $\lambda = 2.4237$ μm respectively). Both lines originate from the same upper energy level, v=1 and J=3, so that their ratio only

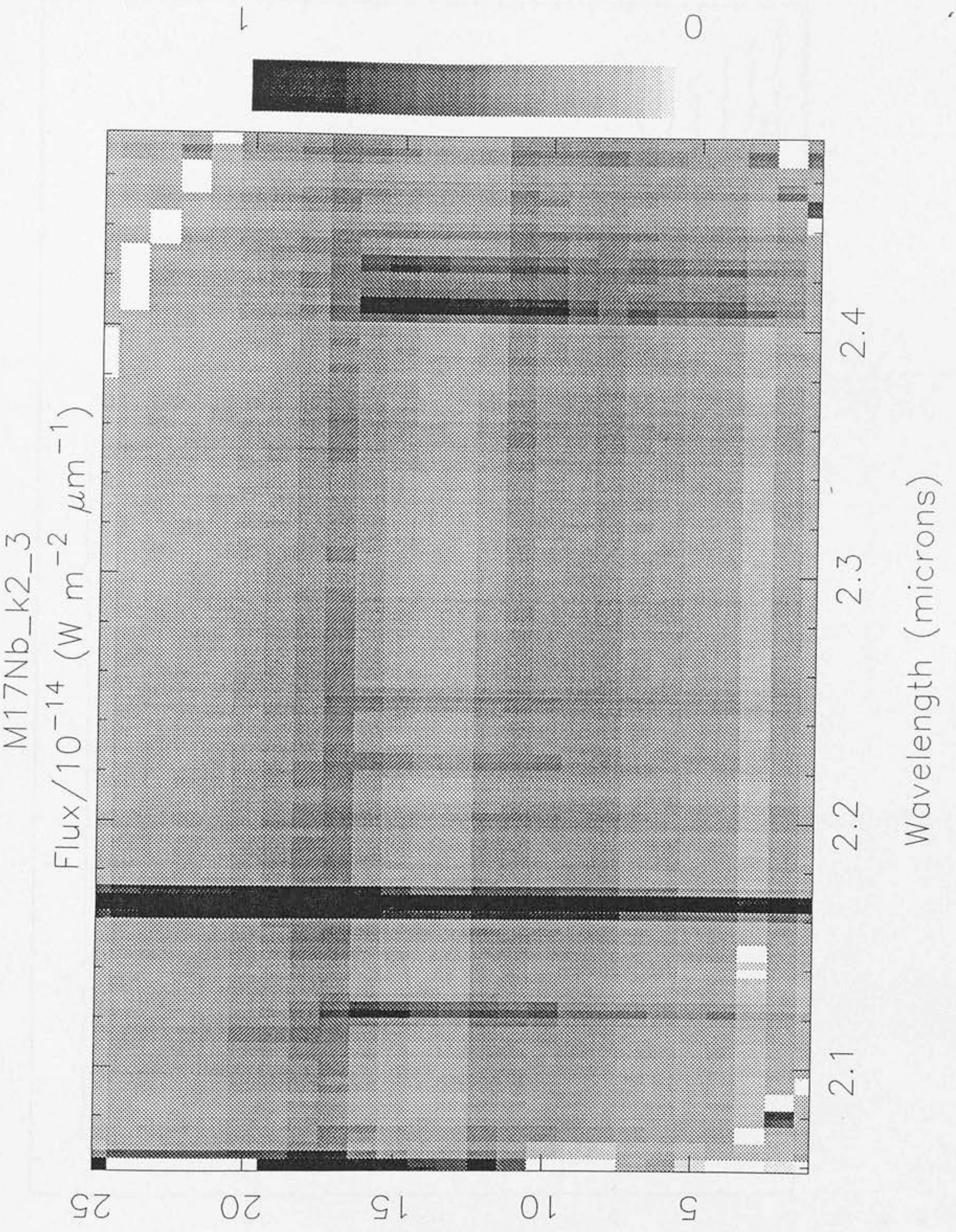

FIGURE 3.3 : Image of the CGS4 array showing the illuminated part of the array. The individual spectra in the image (rows) have been flatfielded, flux and wavelength calibrated and then stacked back together again to give this image.

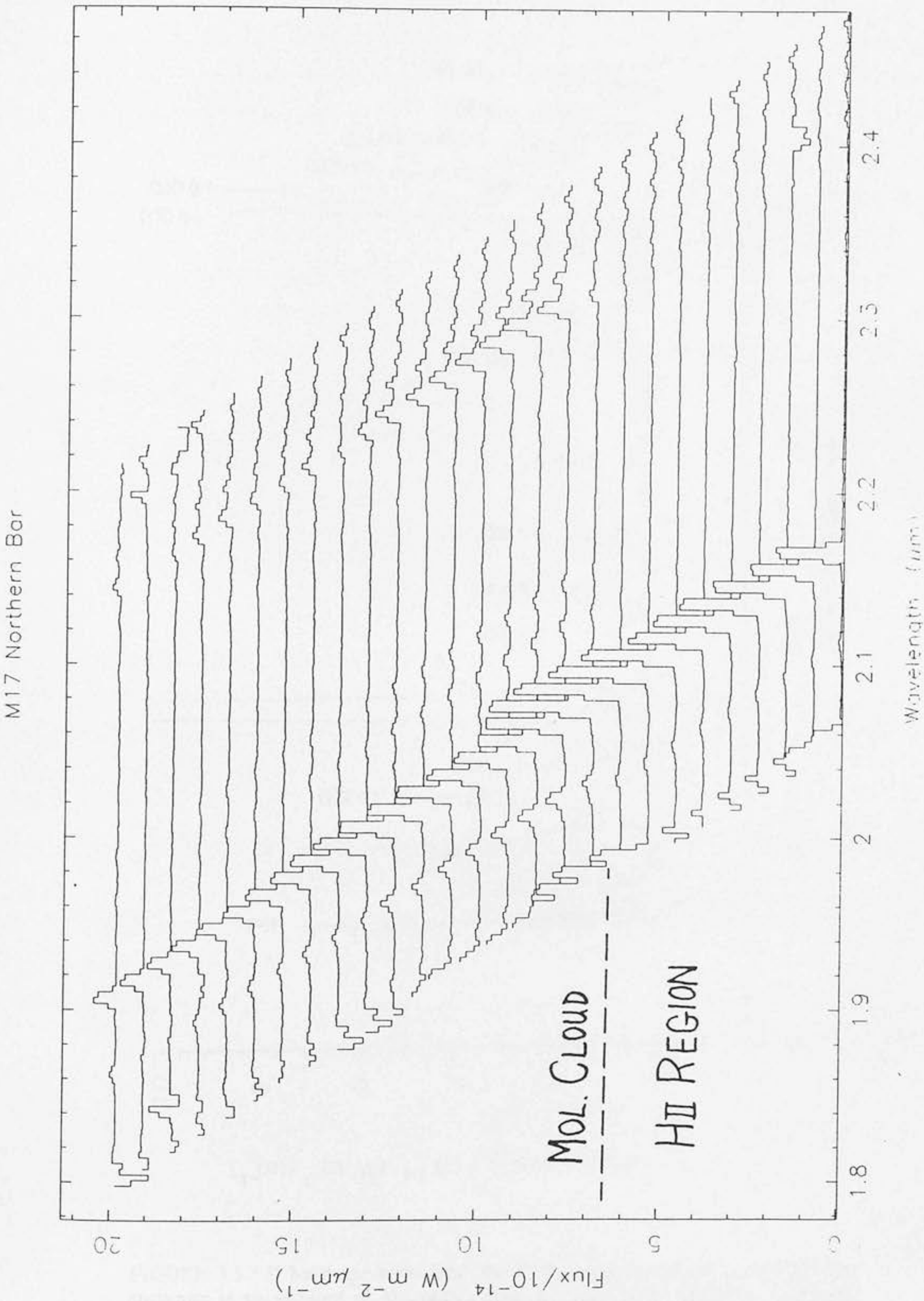

FIGURE 3.4 : Image of the array showing the 27 spectra obtained. North is at the top of the image and south at the bottom. The ionised region is to the south and the molecular cloud is to the north.

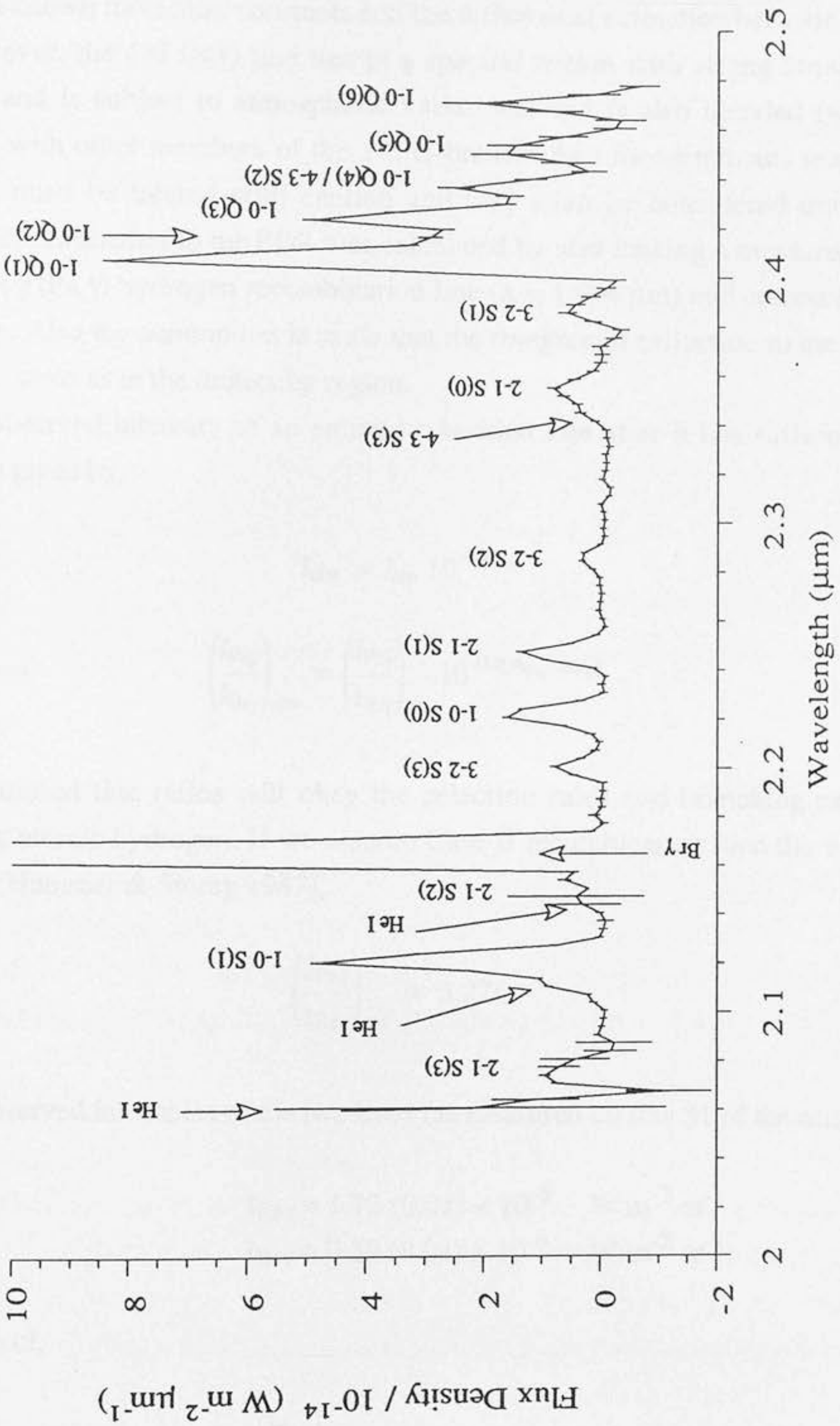

FIGURE 3.5 : K band spectrum from the PDR in the northern bar of M17. The spectrum is an addition of 19 spectra from the array over which the molecular emission extends. All the H_2 transitions have been labelled along with a few ionic recombination transitions from H and He. The flux density is measured in a 182.60 arcsec^2 beam, a consequence of adding the 19 rows.

depends on known molecular constants and the differential extinction between the two lines. However, the 1-0 Q(3) line lies in a spectral region with strong atmospheric extinction and is subject to atmospheric variations, and is also blended (with our resolution) with other members of the 1-0 Q-branch. Any measurements made with these lines must be treated with caution and may even be considered unreliable. Therefore, the extinction to the PDR was calculated by also making a measurement of the Paschen γ (Pa γ) hydrogen recombination line ($\lambda = 1.094\ \mu$m) and comparing it to the Br γ line. Also the assumption is made that the foreground extinction to the ionised region is the same as to the molecular region.

The observed intensity of an emitted transition line after it has suffered some extinction is given by,

$$I_{obs} = I_{em}\ 10^{-0.4A_{\lambda}} \qquad [3.3a]$$

$$\Rightarrow \qquad \left(\frac{I_{Pa\gamma}}{I_{Br\gamma}}\right)_{obs} = \left(\frac{I_{Pa\gamma}}{I_{Br\gamma}}\right)_{em} 10^{-0.4(A_{Pa\gamma}-A_{Br\gamma})} \qquad [3.3b]$$

The emitted line ratios will obey the selection rules and branching ratios of recombining atomic hydrogen. If we assume Case B recombination then the value of this ratio is (Hummer & Storey 1987),

$$\left(\frac{I_{Pa\gamma}}{I_{Br\gamma}}\right)_{em} = 3.276 \qquad [3.4a]$$

The observed intensities of the two lines (as measured on row 31 of the array) is,

$$I_{Pa\gamma} = 1.72\ (0.01) \times 10^{-6} \quad \mathrm{W\ m^{-2}\ sr^{-1}}$$
$$I_{Br\gamma} = 0.59\ (0.02) \times 10^{-6} \quad \mathrm{W\ m^{-2}\ sr^{-1}} \qquad [3.4b]$$

giving a ratio of,

$$\left(\frac{I_{Pa\gamma}}{I_{Br\gamma}}\right)_{obs} = 2.9 \pm 0.1 \qquad [3.4c]$$

Equation [3.3c] therefore gives,

$$A_{Pa\gamma} - A_{Br\gamma} = 0.12 \pm 0.02 \qquad [3.5]$$

TABLE 3.1 : EXTINCTION TOWARDS M17 NORTHERN BAR

β	E	A_K
1.0	0.26 (0.04)[a]	0.12 (0.02)
1.5	0.21 (0.03)	0.07 (0.01)
1.7	0.20 (0.03)	0.05 (0.01)
2.0	0.19 (0.03)	0.04 (0.01)

a) 0.26 (0.04) = 0.26 μm ± 0.04. The error is 1σ and is derived from uncertainties in the observations and the line fitting.

Next we assume that the extinction follows a power law of the form,

$$A_\lambda = E\lambda^{-\beta} \qquad [3.6]$$

where E = constant.

The power index, β, in equation [3.6] is not very well defined and is seen to vary in the literature between values of 1.0 - 2.0. The extinction constant, E, has therefore been calculated for some of the more common values of the power index found in the literature. The results are shown in Table 3.1, including the inferred extinction at K (2.2 μm).

These results indicate that, for power indices $\beta > 1$, the visual extinction to the northern bar is small, $A_V < 1$ (assuming that $A_V \sim 10A_K$). This is consistent with the fact that the northern bar of M17 is optically very bright and coincides with its infrared and radio counterparts (eg. see Felli *et al.* 1984), while on the other hand, the southwestern bar is heavily obscured in the optical, signifying that the associated molecular clouds lie behind the northern bar (producing low foreground extinction) and in front of the southwestern bar (giving high foreground visual extinction).

Whittet (1988) has analysed data in the literature and derived that the power index of the extinction curve is best fitted by $\beta \sim 1.7$. Draine (1989), from a different data set, adopted the value $\beta \sim 1.75$, for a region covering 0.7 - 5.0 μm. Cardelli, Clayton & Mathis (1989) adopt the Rieke & Lebofsky (1985) curve with $\beta \sim 1.6$. With this information in mind a power index of $\beta = 1.7$ is adopted for this work.

Finally, the line strengths were measured by fitting the triangular instrumental

TABLE 3.2 : LINE INTENSITIES AND COLUMN DENSITIES

Level / Line	Intensity [a] (10^{-8} W m^{-2} sr^{-1})	g_j[b]	λ[c] (μm)	A[d] (10^{-7} s^{-1})	E_j (K)	N_j / g_j (10^{18} m^{-2})
v = 1						
1 - 0 Q(1)	13.4 (0.05)	9	2.4066	4.29	6150	5.29 (0.20)
1 - 0 Q(2)	5.32 (0.64)	5	2.4134	3.03	6472	5.36 (0.65)
1 - 0 S(0)	3.15 (0.12)	5	2.2233	2.53	6472	3.50 (0.14)
1 - 0 Q(3)	9.01 (0.51)	21	2.4237	2.78	6952	2.37 (0.13)
1 - 0 S(1)	8.32 (0.28)	21	2.1218	3.47	6952	1.53 (0.05)
1 - 0 Q(4)[e]	4.47 (0.54)	9	2.4375	2.65	7585	2.89 (0.35)
1 - 0 Q(5)	2.50 (0.83)	33	2.4548	2.55	8366	0.46 (0.15)
1 - 0 Q(6)	2.57 (0.85)	13	2.4755	2.45	9288	1.26 (0.42)
v = 2						
2 - 1 S(0)	1.42 (0.24)	5	2.3556	3.68	12097	1.15 (0.19)
2 - 1 S(1)	2.54 (0.16)	21	2.2477	4.98	12552	0.34 (0.02)
2 - 1 S(2)	1.13 (0.15)	9	2.1542	5.60	13152	0.31 (0.04)
2 - 1 S(3)	1.27 (0.39)	33	2.0735	5.77	13892	0.09 (0.03)
v = 3						
3 - 2 S(1)	1.45 (0.32)	21	2.3865	5.14	17821	0.20 (0.04)
3 - 2 S(2)	0.70 (0.13)	9	2.2871	5.63	18389	0.20 (0.04)
3 - 2 S(3)	1.28 (0.13)	33	2.2014	5.63	19089	0.10 (0.01)
v = 4						
4 - 3 S(3)	0.89 (0.17)	33	2.3445	4.58	23959	0.09 (0.02)

a) 1.34 (0.05) 10^{-7} = 1.34 x 10^{-7} with a 1σ error of 0.05 x 10^{-7}. The intensities have been corrected for extinction. All errors are derived from uncertainties in the observations, the line fitting and the extinction estimate.

b) Statistical weight calculated assuming an ortho to para ratio of 3.

c) Wavelengths are in vacuum and taken from Black & van Dishoeck (1987).

d) The spontaneous radiative decay probabilities are taken from Turner, Kirby-Docken & Dalgarno (1977).

e) Blended with the 4-3 S(2) line at λ = 2.4355 μm.

profile to the lines in Figure 3.5. The intensity of a transition, j, is given by,

$$I_j = \frac{1}{4\pi}\frac{hc}{\lambda_j}\left(\frac{N_j}{g_j}\right)g_j A_j \qquad [3.7]$$

where λ_j = wavelength of the transition; A_j = spontaneous radiative decay rate of the transition; N_j = column density of the upper energy level of the transition; g_j = statistical weight of the upper energy level of the transition; h = Planck's constant; c = speed of light.

We can correct for the extinction suffered by the intensity of the emitted photons using equation [3.3a] and calculate the column density of the upper energy level, per state, using,

$$\left(\frac{N_j}{g_j}\right) = \frac{4\pi I_j \lambda_j}{hc\, A_j\, g_j}\, 10^{0.4A_\lambda} \qquad [3.8]$$

Table 3.2 shows the results. The errors quoted are due to 1σ uncertainties in the observations, the line fitting and the extinction correction.

3.4 DISCUSSION

3.4.1 PHYSICAL CONDITIONS AND LINE RATIOS

Figure 3.6 shows the column densities in the rotation - vibration levels of molecular hydrogen, plotted against the energy of the level above the ground state. These column densities have been divided by the statistical weights of the levels, $g_j = g_s g_J$, where $g_J = (2J + 1)$ is the rotational degeneracy and g_s is the spin degeneracy (g_s = 1 for even J; g_s = 3 for odd J).

The nature of the emission can be characterised by the appearance of these level populations. In shocks, the population of the vibrational and rotational levels all lie along one curve (eg. see the data for the shock in the Orion outflow in Brand *et al.* (1988) and Hasegawa *et al.* (1987) and also Figure 1.4a in Chapter 1). For the ultraviolet excitation of H_2 molecules, the series of rotational levels of each vibrational level are described by separate curves (see Hasegawa *et al.* 1987; Burton 1992). Hasegawa *et al.* (1987)

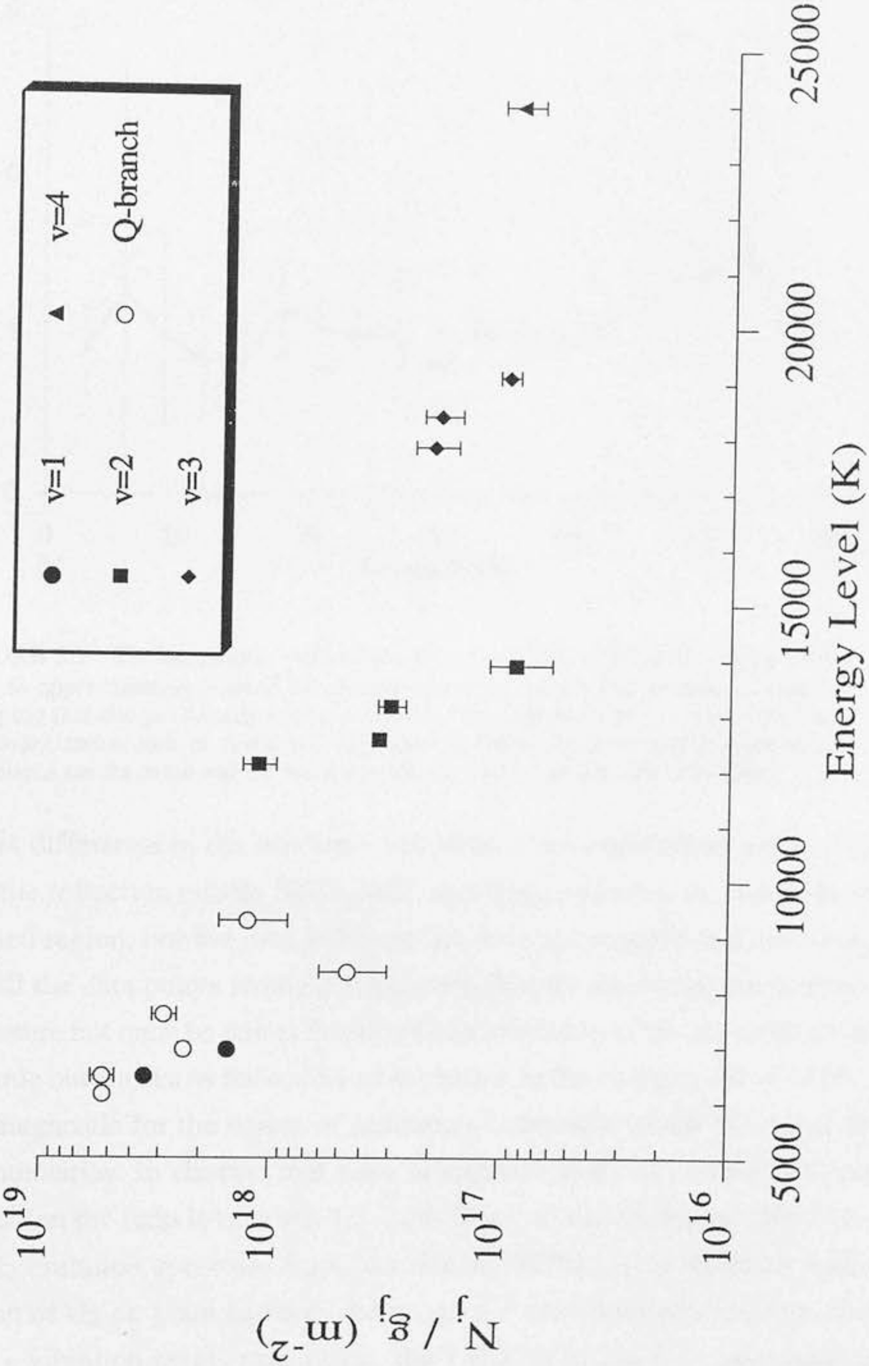

FIGURE 3.6 : A plot of column density against energy level showing the population distribution of the excited levels of the H_2 molecule. The column densities have been normalised to the level degeneracies assuming an ortho to para ratio of 3. The open circle points have been measured from transitions in the 1-0 Q-branch and therefore may not be reliable due to the variability of the atmospheric transmission at these wavelengths (see text).

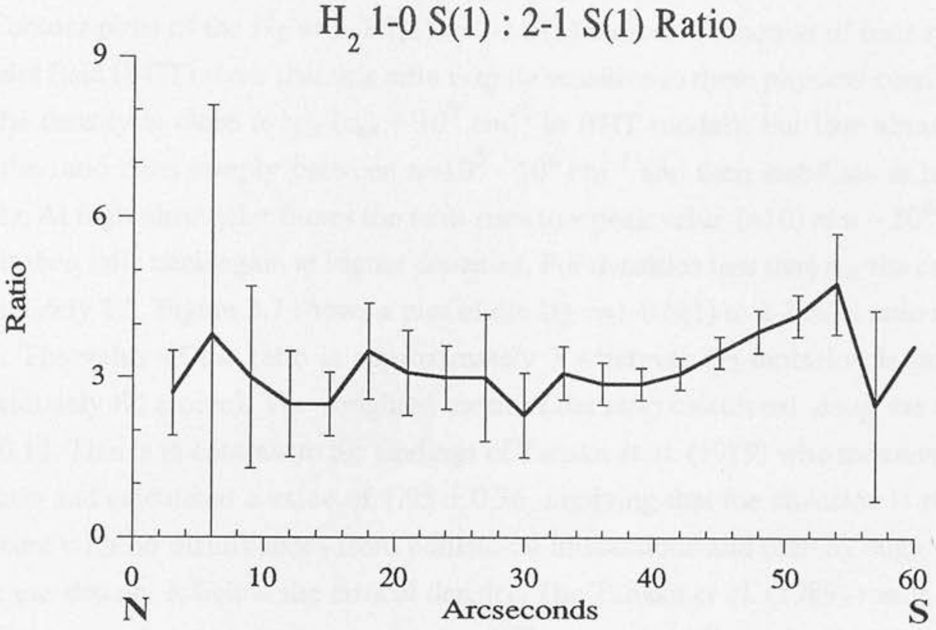

FIGURE 3.7 : The diagnostic ratio of the H_2 v=1-0 S(1) and 2-1 S(1) lines. The ratio is approximately 3 over the region where the molecular emission extends implying that the gas density is above critical. The constancy of the ratio says that the deexcitation rate is constant. This may be interpreted as that the physical conditions are the same and we are observing the surface of the molecular cloud.

showed that this difference in the rotation - vibration level populations exists in the emission from the reflection nebula NGC 2023, and they credit this to excitation in a photon dominated region. For the data in Figure 3.6, it is not possible to draw a single curve through all the data points strongly suggesting that the excitation mechanism is not thermal in nature but must be due to the ultraviolet excitation of the H_2 molecule and must therefore rule out shocks as the source of excitation in the northern bar of M17.

Another diagnostic for the nature of excitation is the ratio of the H_2 v=1-0 S(1) and 2-1 S(1) intensities. In shocks, this ratio is approximately 10, whereas in pure ultraviolet excitation the ratio is between 1.7 - 1.9. Black & van Dishoeck (1987) have modelled the H_2 emission spectrum from low density PDRs, using different models for the formation of H_2 on grain surfaces. Although the intensities of transitions from higher rotation - vibration levels may differ, the 1-0 S(1) to 2-1 S(1) ratio does not exceed the above limits, confirming this ratio as a good diagnostic for pure fluorescence. However, recent modelling of high density PDRs (BHT; Sternberg & Dalgarno 1989) has shown that collisions do alter the line ratios. The 1-0 S(1) to 2-1 S(1) ratio becomes larger with density and appears shock excited even though ultraviolet absorption is responsible for the excitation. This effect occurs in gas which is denser than a critical density, n_{cr}, defined as the density when the rate of deexcitation by collisions equals the spontaneous radiative decay rate.

Contour plots of the H_2 v=1-0 S(1) to 2-1 S(1) ratio as a function of density and ultraviolet field (BHT) show that this ratio is quite sensitive to these physical conditions when the density is close to n_{cr} ($n_{cr} \sim 10^5$ cm^{-3} in BHT model). For low ultraviolet fluxes the ratio rises steeply between n=10^5 - 10^6 cm^{-3} and then stabilises at higher densities. At high ultraviolet fluxes the ratio rises to a peak value (>10) at n ~ 10^6 cm^{-3} before it then falls back again at higher densities. For densities less than n_{cr} the ratio is approximately 1.7. Figure 3.7 shows a plot of the H_2 v=1-0 S(1) to 2-1 S(1) ratio along the slit. The value of the ratio is approximately 3 wherever H_2 emission is present (approximately 60 arcsec). The weighted mean of the ratio calculated along the slit is 3.25 ± 0.12. This is in contrast to the findings of Tanaka *et al.* (1989) who measured the same ratio and calculated a value of 1.95 ± 0.36, implying that the emission is purely fluorescent with no disturbances from collisional interactions and thereby suggesting that the gas density is below the critical density. The Tanaka *et al.* (1989) result is 3σ away from our value and the reason for the difference could lie in the fact that their observations were taken with a large aperture beam (19.6 arcsec) which will dilute the emission from smaller structures, eg. high density clumps. Our measurement of this ratio implies that the density must be above the critical density. Furthermore, the constancy of the ratio along the slit says that the deexcitation rate of these levels is constant and this may mean that the physical conditions are the same, suggesting that we are observing the surface of the molecular cloud.

3.4.2 GEOMETRY AND CLUMPING

Figure 3.8 shows the profile along the slit of the molecular and ionised emission. The shape of the emission profiles can be explained by a simple geometrical model. Figure 3.9 shows a schematic diagram of the *cusp* geometry we consider and represents a slight modification of the model described in Chapter 2 (Figure 2.11b) and in Chrysostomou *et al.* (1992a) (Figure 1b). The curvature of the surface of the PDR is described by a parabola of the form,

$$y^2 = 4ax \qquad [3.9]$$

where a = distance between the apex and focus of the parabola.

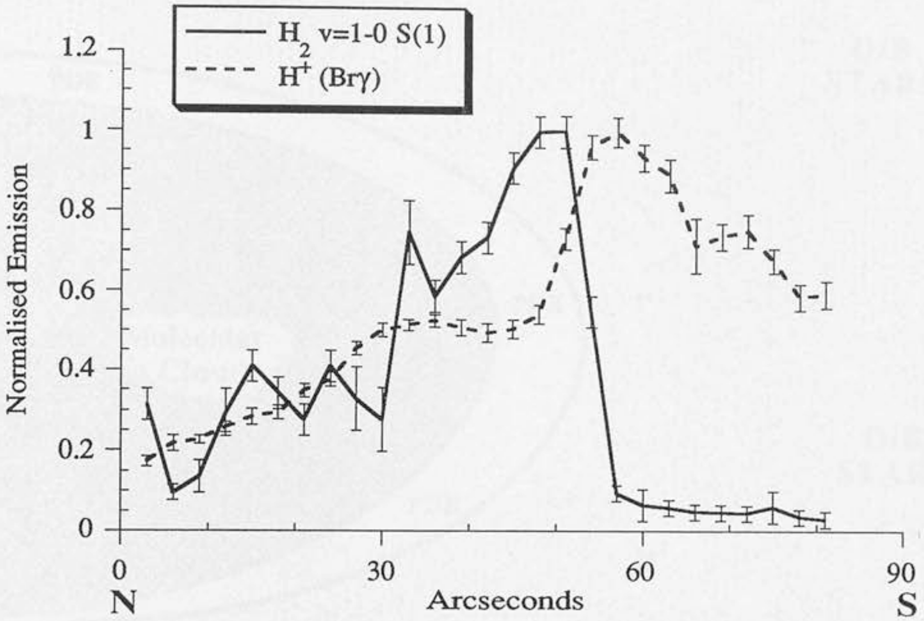

FIGURE 3.8 : Cuts along the spatial direction showing the emission from ionised (Brγ) and molecular (H_2 v=1-0 S(1)) material. Both cuts have been normalised to their peak emission. The peak intensity in the H_2 line is 1.5 x 10^{-7} W m^{-2} sr^{-1} and in the H^+ line it is 8.8 x 10^{-7} W m^{-2} sr^{-1}.

It is assumed that the PDR has constant column density (ie. thickness) in the direction of the source of photons. Enforcing this constant thickness on the PDR is equivalent to saying that the PDR is uniform and of constant density. The emission from the rear half of the PDR undergoes extinction as it passes through the ambient molecular gas. The thickness of the PDR is simulated by subtracting a constant number from the value of x, ie. effectively shifting the parabola of equation [3.9] by this amount. Once the intensity in our direction has been calculated along each point on the parabola, the intensities are then binned to match the number of CGS4 pixels sampling the H_2 emission region. In Figure 3.10, the result of modelling the molecular emission with this geometry is shown. The parameters used for this model are, a = 0.105 with a thickness of 0.23. The sharp rise of the emission is because the thickness of the PDR is unresolved by the CGS4 pixel (3 arcsec). Changes in the surface geometry (eg. corrugation) or density contrasts (ie. clumping) have not been considered here and may easily explain the differences in emissivity where the model deviates from the data. Such a simplistic cusp model, while not accurate in describing certain physical characteristics (clumping, surface geometry) can describe the gross geometrical structure of the region.

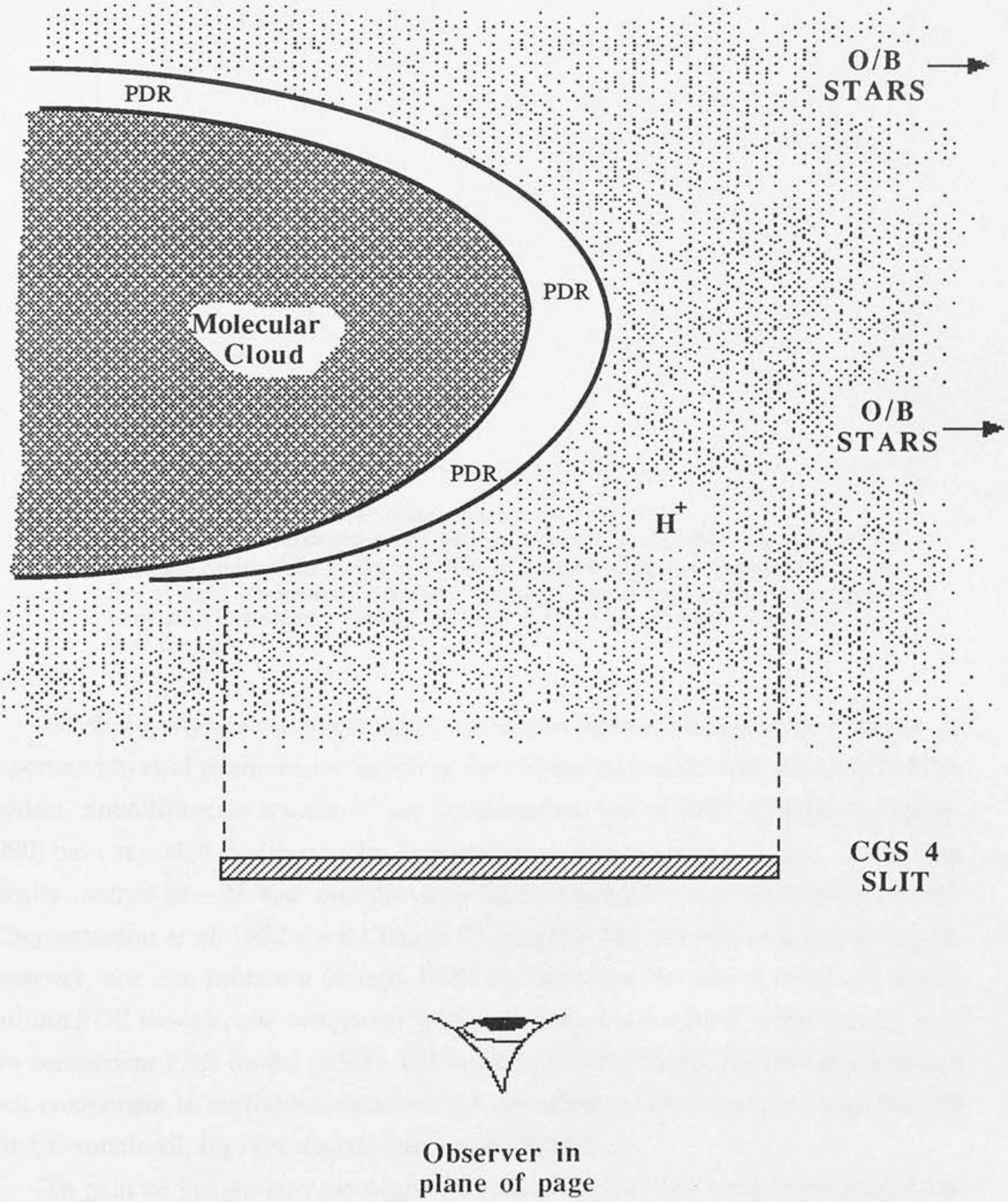

FIGURE 3.9 : Schematic diagram showing the HII region and molecular cloud in cross section. The observer is in the plane of the page. The CGS 4 slit in this position, and with the cloud geometry, will produce the emission profiles for the ionised and molecular emission in Figure 3.8.

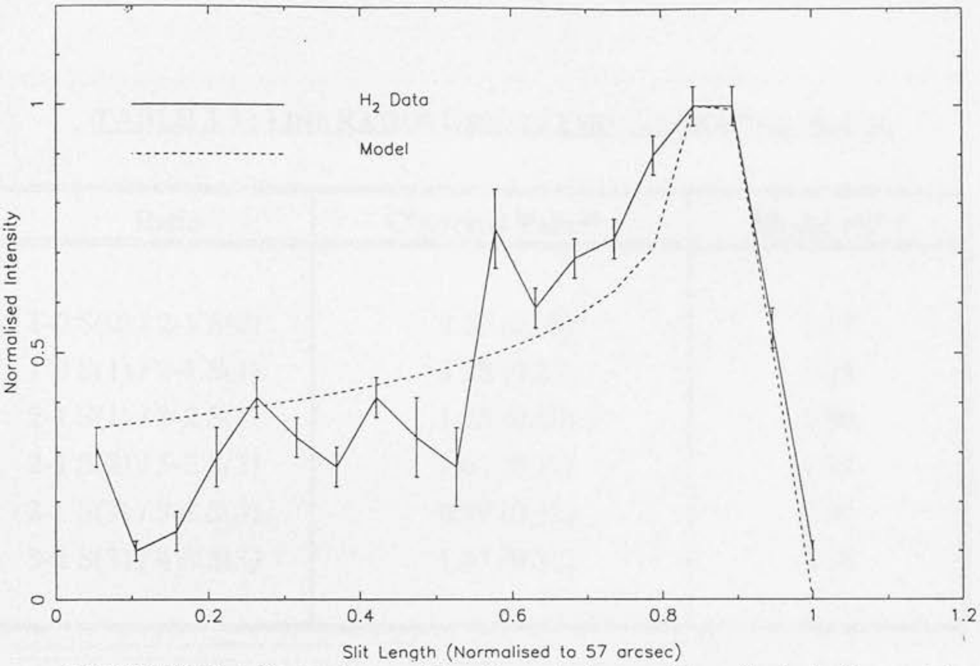

FIGURE 3.10 : Comparison of the H_2 emission profile with that of a model emission profile. The model is a PDR of constant thickness perpendicular to the line of sight. No account of density clumping or small scale surface geometry has been taken in the model and this may explain the instances where the model deviates from the data.

Of these physical characteristics mentioned above, clumping in PDRs is an important physical phenomenon which as yet has not been dealt with properly in PDR models. Submillimetre studies of the southwestern bar of M17 (Stutzki & Güsten 1990) have revealed that the molecular material is clumped with a clump - interclump density contrast of ~ 23. Our own previous infrared images in the northern bar of M17 (Chrysostomou *et al.* 1992a; see Chapter 2) suggests that this region is also clumped. However, one can imitate a clumpy PDR by summing the fluxes from two static, uniform PDR models, one component at high density and the other at low density ie. a two component PDR model (BHT). Different beam area filling factors are applied to each component to reproduce the observed intensities of emission lines (eg. [OI] 63 μm, CO rotational, H_2 - see also discussion in Chapter 2).

To gain an insight into the degree of clumping, this two component model has been used. A problem arises in the unknown small scale geometry of the object observed as higher intensities caused by limb brightening mimic the effect of higher densities or ultraviolet fields. For this reason, the same two component model has been used to fit to the observed line *ratios*, since a ratio minimises any complications due to the geometry of the object. Using this approach, six line ratios were measured (intensities from Table 3.2) and fitted to by a two component PDR model,

TABLE 3.3 : LINE RATIOS USED IN TWO COMPONENT MODEL

Ratio	Observed Value[a]	Model Fit[b,c]
1-0 S(0) / 2-1 S(0)	2.22 (0.38)[d]	2.87
1-0 S(1) / 2-1 S(1)	3.28 (0.23)	3.03
2-1 S(1) / 3-2 S(1)	1.75 (0.40)	1.80
2-1 S(2) / 3-2 S(2)	1.61 (0.37)	1.92
2-1 S(3) / 3-2 S(3)	0.99 (0.32)	2.09
3-2 S(3) / 4-3 S(3)	1.45 (0.32)	2.28

a) Ratios have been calculated from intensities given in Table 2.

b) Model ratios calculated from intensities given by the model of BHT.

c) The best fit corresponds to beam area filling factors of 76% at 10^5 cm^{-3} and 16% at 10^6 cm^{-3}.

d) 2.22 (0.38) = 2.22 ± 0.38. The error is 1σ and is derived from uncertainties in the observations, the line fitting and extinction estimate.

$$R = \frac{\alpha I_1(n_1) + \beta I_1(n_2)}{\alpha I_2(n_1) + \beta I_2(n_2)} \qquad [3.10]$$

where R = ratio between lines 1 and 2; $I_1(n_1)$, $I_2(n_2)$ = intensities of lines 1 and 2 as functions of densities n_1 and n_2 in a uniform PDR model; α, β = beam area filling factors.

The ultraviolet flux is held fixed at the appropriate value for the northern bar of M17, which is a factor of 10^4 above the ambient interstellar radiation field in the solar neighbourhood. The intensities are taken from the model by BHT. The values of the 4 parameters α, β, n_1, n_2 are determined by minimising the χ^2 value where,

$$\chi^2 = \sum_i \frac{(R_i - R_i^{obs})^2}{\sigma_i^2} \qquad [3.11]$$

where the sum is over the number of ratios in the data set; R_i = the value of the ith ratio from the two component model; R_i^{obs} = the value of the ith ratio from the data set; σ_i = the error on R_i^{obs}.

Table 3.3 shows the line ratios used in the model fit and their values, with the model results. The best fit to the ratios is described by a model which has 76 % of the beam area filled by gas at 10^5 cm^{-3} and 16% of the beam area filled by gas at 10^6 cm^{-3}. This is in good agreement with Chrysostomou *et al.* (1992a) who set a lower limit on the density in the region of 10^5 cm^{-3}. However, the results of the model fit does depend on the value of n_{cr} in the BHT model being correct. Sternberg & Dalgarno (1989) have used a lower value ($n_{cr} \sim 10^4$ cm^{-3}) due to their different formulation describing the collision process (see section 1.1.5 and Figure 1.6) and similar analysis with their model would give a lower density gas, or more of the gas being in the 10^5 cm^{-3} component.

3.4.3 EXCITATION TEMPERATURES AND THE ORTHO TO PARA RATIO

As well as the appearance of the column density plots, one can also characterise the nature of the emission by deriving excitation temperatures between rotational and vibrational levels, T_{rot} and T_{vib}. These temperatures would describe the relative populations of the rotation - vibration levels if the gas had kinetic temperatures of T_{rot} and T_{vib}, and was in local thermodynamic equilibrium (LTE). The column density in the levels is described by,

$$N_j = N_{H_2}\, g_j \frac{\exp(-E_j/kT_{ex})}{Z} \qquad [3.12]$$

where N_{H2} = total column density in all the levels; Z = partition function which is written as,

$$Z = \sum_j g_j \exp(-E_j/kT_{ex})$$

From the intensity of any transition (equation [3.7]) we have,

$$I_j = \frac{1}{4\pi} N_{H_2}\, g_j\, A_j \frac{hc}{\lambda_j} \frac{\exp(-E_j/kT_{ex})}{Z} \qquad [3.13]$$

Therefore to derive the excitation temperature, T_{ex}, the ratio of two lines must be taken to cancel out unknown variables such as N_{H2} and Z. To calculate rotational or vibrational excitation temperatures the following conditions must be met:

(i) for a rotational excitation temperature, the two transitions must have the same upper and lower vibrational levels and different upper and lower rotational levels, ie. between the two transitions,

$$\Delta v = 0 \quad ; \quad \Delta J \neq 0$$

(ii) for a vibrational excitation temperature, the two transitions must have different upper and lower vibrational levels and the same upper and lower rotational levels, ie. between the two transitions,

$$\Delta v \neq 0 \quad ; \quad \Delta J = 0$$

For the emission from the northern bar of M17, the vibrational excitation temperature was calculated with intensities from the 1-0 S(1) and 2-1 S(1) transitions, the rotational excitation temperature for the v=2 level was calculated with intensities from the 2-1 S(0) and 2-1 S(2) transitions. The results were

$$\begin{aligned} T_{vib}\,(2 \rightarrow 1) &= 3757\ \mathrm{K} \pm 127 \\ T_{rot}\,(v = 2) &= 796\ \mathrm{K} \pm 125 \end{aligned} \qquad [3.14]$$

The disparate values of the vibrational and rotational excitation temperatures is added proof to the fact that the excitation of molecular hydrogen in the northern bar of M17 must be by the absorption of ultraviolet photons, since in a shock these two values are the same because the population of the energy levels is dependent on the gas temperature (cf. equation [3.12]).

The ortho to para ratio in molecular hydrogen reflects the overpopulation of ortho H_2 (odd J) with respect to para H_2 (even J). The ortho to para ratio is first set in the H_2 formation process and in LTE this ratio is 3, due to the spin degeneracy of the ortho states. This assumption has been used in calculating the column densities in Table 3.2 and displayed in Figure 3.6. When divided by the degeneracy, the level populations of the rotational levels lie along a single curve (BHT), which is characterised by the rotational excitation temperature.

From the intensities given in Table 3.2, it is possible to calculate the ortho to para ratios for the data set. The rotational excitation temperatures for each vibrational level are calculated using two levels with the same spin to accommodate our ignorance of the ortho to para ratio. Ratioing two transitions from separate ortho and para states, allows the ortho to para ratio to be calculated. However, care must be taken here because the rotational excitation temperature changes with J; it gets higher with increasing J. To cater for this fact it is best to calculate the ortho to para ratio with the level which is straddled by the levels used to calculate the rotational excitation temperature. For

TABLE 3.4 : ROTATIONAL TEMPERATURE AND ORTHO TO PARA RATIO AS FUNCTIONS OF VIBRATIONAL LEVEL

Vibrational Level (v)	Rotational Temperature (K)	(Ortho : Para) ratio
2[a]	796 (125)[b]	1.60 (0.68)[c]
2[d]	976 (223)	1.83 (0.69)
3	1694 (547)	2.18 (1.37)
	weighted mean	1.77 (0.46)

a) Rotational temperature calculated using the 2-1 S(0) and 2-1 S(2) transitions and the ortho to para ratio calculated using the 2-1 S(0) and 2-1 S(1) transitions.
b) 796 (125) = 796 K ± 125. The error is 1σ and is derived from uncertainties in the observations, the line fitting and extinction estimate.
c) The errors are derived from maximum and minimum 1σ variations of the intensities and rotational temperature used to calculate the ortho to para ratio.
d) Rotational temperature calculated using the 2-1 S(1) and 2-1 S(3) transitions and the ortho to para ratio calculated using the 2-1 S(1) and 2-1 S(2) transitions.

instance, for v=2, the 2-1 S(0) and 2-1 S(2) transitions were used to calculate the rotational excitation temperature, and to calculate the ortho to para ratio, the 2-1 S(0) and 2-1 S(1) transitions were used. As there are 4 transitions measured from this vibrational level it was also possible to calculate a rotational excitation temperature from the 2-1 S(1) and 2-1 S(3) transitions and use the 2-1 S(1) and 2-1 S(2) transitions to calculate an ortho to para ratio. Using equation [3.13] and leaving the spin degeneracy, g_s, as a free parameter, the ortho to para ratio is calculated with the equation,

$$\frac{g_s{}^O}{g_s{}^P} = \frac{(2J_P+1)}{(2J_O+1)}\left[\frac{I_O \lambda_O A_P}{I_P \lambda_P A_O}\right] \exp\left(\frac{\Delta E}{kT_{rot}}\right) \qquad [3.15]$$

where $g_s{}^O$, $g_s{}^P$ = spin degeneracies for ortho and para states; J_O, J_P = rotational quantum number for ortho and para states; I_O, I_P = intensity of ortho and para transitions; A_O, A_P = spontaneous radiative decay probability of ortho and para transitions; ΔE = energy difference between ortho and para energy levels.

Table 3.4 shows the results. Figure 3.6 shows that there are only two trustworthy points for the v=1 level in the data : the 1-0 S(1) and 1-0 S(0) transitions (filled circles).

The others (open circles) originate from the 1-0 Q-branch and are badly affected by blending and atmospheric extinction. Therefore, it has not been possible to calculate a reliable value for the ortho to para ratio in this level. However, from the higher vibrational levels the ortho to para ratio is measured to be lower than the LTE value of 3.

Hasegawa *et al.* (1987) studied the ortho to para ratio in the fluorescent emission from the PDR in NGC 2023 and also found that the ratio was not satisfied by an LTE value of 3. Instead, they suggested that the real value lay in the range 1.4 - 2.0. Further observations by Tanaka *et al.* (1989) suggest that an ortho to para ratio of less than 3 is common in PDRs and that for dense ($n > n_{cr}$) PDRs the ratio differs with vibrational level.

One possible explanation for these and our observations may be given by first considering a H_2 formation model in which the H_2 molecule does not evaporate immediately after formation but stays on the grain long enough to suffer a significant number of spin changing interactions with the grain lattice (Tielens & Allamandola 1987; see also Chapter 4). This produces a proportion of ortho and para states characteristic of the grain temperature. Because of the energy difference between ortho and para states (typically $\Delta E \sim 170$ K for v=1 and J<10) the comparatively cold grains will ensure that the ortho to para ratio is initially small, maybe smaller than 1. Once the molecule is in the gas, interchanges between ortho and para forms are not allowed via photon interactions (absorption or emission), however, spin exchange reactions can occur via collisional interactions with H and H^+.

Now, fluorescently excited H_2 exists mainly in a thin sheet of material at a depth of $A_v \sim 1$-3 (Tielens & Hollenbach 1985a) and the abundance of H^+ is extremely low at this depth, primarily supported by the cosmic ray ionisation of H. Therefore, it can be assumed that spin exchange collisions will be dominated by interactions with neutral H. The rate of this reaction with H_2 in its ground state is $\gamma \sim 10^{-16}$ cm^{+3} s^{-1} (Takayanagi *et al.* 1987). The lifetime of a H_2 molecule in its ground state at any depth A_v, is estimated from the unshielded photoabsorption rate (Shull 1978),

$$\Rightarrow \qquad \text{Absorption rate} \sim 5 \times 10^{-10}\, G_0\, e^{-2.5 A_v} \qquad s^{-1} \qquad [3.16]$$

At a depth of $A_v = 1$, this translates to a mean lifetime for a H_2 molecule in its ground state as,

$$\tau \sim \frac{2.4 \times 10^{10}}{G_0} \quad s \qquad [3.17]$$

Therefore, the H density required to significantly alter the ortho to para ratio within the mean lifetime of a H_2 molecule in its ground state is,

$$\begin{aligned} n &\sim \frac{1}{\gamma\tau} \\ &\sim 4 \times 10^5\, G_0 \qquad \mathrm{cm}^{-3} \end{aligned} \qquad [3.18]$$

Therefore for an object such as M17 where $G_0 \sim 10^4$, the required density must be $\geq 5 \times 10^9\ \mathrm{cm}^{-3}$. Such densities can be found in the dense cold cores of molecular clouds, but as yet there has not been any evidence to suggest that such high densities exist on the warm surfaces of PDRs. The formation process producing low values of the ortho to para ratio and the density not being high enough to induce spin changing interactions, these factors together can contrive to produce the low ortho to para ratios that are measured in PDRs.

The column densities shown in Figure 3.6 have been recalculated using the weighted mean of the ortho to para ratios in Table 3.4. The results are shown in Figure 3.11. One can immediately see that the column densities line up so that both ortho and para populations of each vibrational level are described by the same rotational temperature. This is as expected for a H_2 population whose ortho to para ratio is known, and suggests that, in PDRs at least, the ortho to para ratio is subject to little understood physical interactions which make it different from the LTE value of 3.

A crucial consequence of this difference arises in interpreting line ratios. If the ortho to para ratio does not equal 3 and the values are different for separate vibrational levels, as Tanaka *et al.* (1989) seems to suggest is common in dense PDRs, then the ratio of two lines from different vibrational levels can be either over- or underestimated leading to a misinterpretation of the physical conditions. A case in point is the use of the two component PDR model. As this data has insufficient information to calculate an ortho to para ratio for the first vibrational level, it is not possible to make a thorough reinvestigation of the physical conditions in the northern bar of M17 until further data is obtained.

However, the point is raised that the ortho to para ratio is an important quantity of the H_2 emission spectrum which needs to be measured if the data is not to be misinterpreted. The importance of this quantity also heightens the need for a better understanding of the collision cross sections and of the formation process of the H_2 molecule on grain surfaces, as both processes directly affect the value of the ortho to para ratio. These problems are addressed in greater detail in the next chapter.

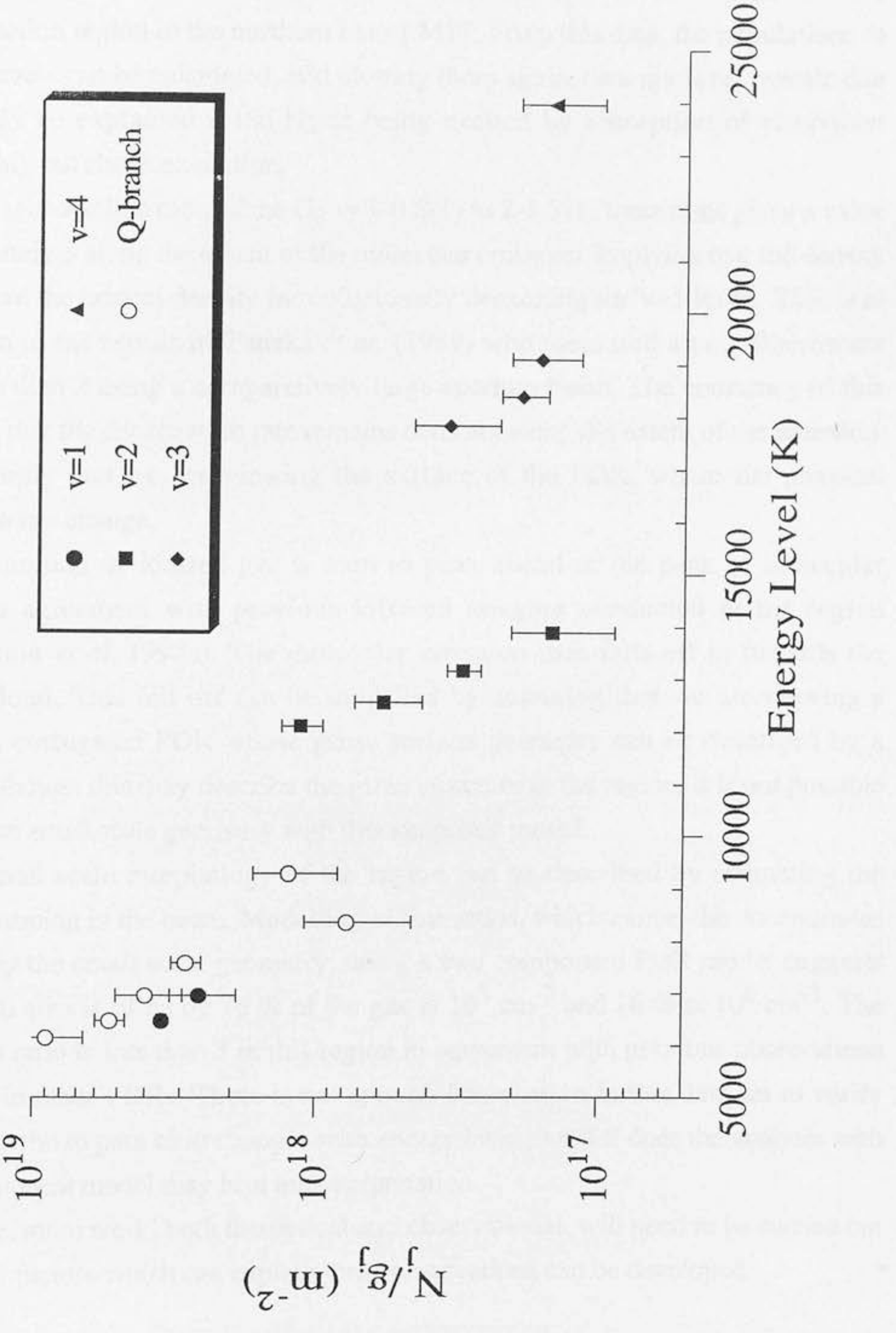

FIGURE 3.11 : The same as for Figure 3.6 but the level degeneracies have been corrected for according to the ortho to para ratio measurements given in Table 3.4.

3.5 CONCLUSIONS

Spectroscopic measurements in the K band have been taken of the photodissociation region in the northern bar of M17. From this data, the populations in the energy levels can be calculated, and plotting them against energy level reveals that they can only be explained if the H_2 is being excited by absorption of ultraviolet photons, ruling out shock excitation.

The diagnostic line ratio of the H_2 v=1-0 S(1) to 2-1 S(1) transitions gives a value of approximately 3 along the extent of the molecular emission, implying that the density must lie above the critical density for collisionally deexciting the v=1 level. This is in contradiction to the results of Tanaka *et al.* (1989) who measured a pure fluorescent value of less than 2 using a comparatively large aperture beam. The constancy of this ratio implies that the deexcitation rate remains constant along the extent of the emission. This may imply that we are viewing the surface of the PDR, where the physical conditions do not change.

The emission of ionised gas is seen to peak ahead of the peak of molecular emission, in agreement with previous infrared imaging conducted in the region (Chrysostomou *et al.* 1992a). The molecular emission then falls off in towards the molecular cloud. This fall off can be modelled by assuming that we are viewing a portion of a corrugated PDR whose gross surface geometry can be described by a parabola. Although this may describe the gross structure in the region, it is not possible to describe the small scale geometry with this simplistic model.

The small scale morphology of the region can be described by estimating the degree of clumping in the beam. Modelling of line ratios, which cancel the uncertainties introduced by the small scale geometry, using a two component PDR model suggests that the beam area is filled by 76 % of the gas at 10^5 cm^{-3} and 16 % at 10^6 cm^{-3}. The ortho to para ratio is less than 3 in this region in agreement with previous observations of this ratio in other PDRs. There is not enough information in this data set to verify whether the ortho to para ratio changes with energy level, but if it does the analysis with the two component model may be a misinterpretation.

Clearly, more work, both theoretical and observational, will need to be carried out before a clear picture which can explain these observations can be developed.

4 The Ortho to Para Abundance Ratio In PDRs

4.1 INTRODUCTION

In the previous chapters the infrared emission from the rotation - vibration transitions of the H_2 molecule has been discussed as commonly occurring on the surfaces of molecular clouds, illuminated by young massive stars producing large sheets of diffuse emission. The infrared spectrum from the molecule has been calculated by several authors (Black & Dalgarno 1976; Black & van Dishoeck 1987; Sternberg & Dalgarno 1989; Burton, Hollenbach & Tielens 1990 hereafter BHT) revealing that the intensities and line ratios are sensitive to the physical conditions in the photodissociation region (PDR), eg. the density and temperature of the gas. This infrared spectrum was first detected and identified as such in spectroscopic observations of the reflection nebula NGC 2023 (Gatley & Kaifu 1987; Gatley *et al.* 1987). Further detections and identifications were then subsequently made in other objects such as planetary nebulae (eg. Hubble 12 - Dinerstein *et al.* 1988; Ramsay *et al.* 1992b) and HII regions (eg. Orion's Bar - Hayashi *et al.* 1985; M17 - Tanaka *et al.* 1989; Chrysostomou *et al.* 1992b).

Hasegawa *et al.* (1987) first studied the abundance ratio between ortho (J=odd) and para (J=even) states of the H_2 molecule (from the first two vibrationally excited levels) in the data from NGC 2023. They found that the ortho to para ratio is significantly lower than 3, the expected value for a hot gas (T > 300 K) in local thermodynamic equilibrium (LTE). They suggested, from their calculations, that the real value of the ortho to para ratio lies in the range of 1.4 - 2.0. More recent measurements of the emission from NGC 2023 (Burton *et al. in preparation*) and further data from other PDR objects such as Hubble 12 and M17 shows a similar disparity between the measured ortho to para ratio and the expected LTE value.

In the following sections these measurements shall be discussed in more detail and compared to the predictions of some simple analytical modelling, and what this may tells us about the physical conditions under which H_2 is formed. The consequence on interpreting diagnostic line ratios is discussed.

4.2 THE ORTHO TO PARA ABUNDANCE RATIO

The ortho to para abundance ratio is a measurement of the overpopulation of ortho states of H_2 over para states. The ratio is first set in the formation of H_2 on grains and probably reflects the physical conditions under which H_2 is formed (eg. grain temperature). Interchanges between ortho and para forms of H_2 are not allowed via photon interactions (ie. absorption or emission), however, spin exchange reactions can occur via collisional interactions with H and H^+ while in the gas phase (Dalgarno *et al.* 1973; Flower & Watt 1984; Takayanagi *et al.* 1987). In this interaction, a proton in the gas collides with the molecule and physically replaces one of the protons in the molecule with itself. If the nuclear spin of the outgoing proton is different from the proton which replaced it then the spin state of the molecule changes.

If the gas is cold, all molecular hydrogen will be in the ground state (v=0, J=0) owing to the energy spacing of the first two rotational levels being 170.5 K above the ground state :

$$H_2\,(J=1) \quad + \quad \text{proton} \quad \Leftrightarrow \quad H_2\,(J=0) \; + \; \text{proton} + 170.5\ \text{K} \qquad [4.1]$$

So, for cold clouds ($T \leq 50$ K) the reverse reaction in [4.1] is very slow and most reactions go in the forward direction, reducing the ortho to para abundance ratio. The ortho to para ratio is therefore a temperature sensitive quantity, as is graphically displayed in Figure 4.1. The spin degeneracy of ortho states is 3 ($g_s = (2I + 1)$ where $I=1$) while the spin degeneracy of para states is 1 ($I = 0$). So in the high temperature limit the ortho to para ratio is expected to be 3.

Early work on ortho to para exchange reactions considered cold, isothermal clouds, where most of the ortho H_2 is modified to para H_2 for large enough timescales ($t \sim 10^{7\text{-}8}$ years, eg. Flower & Watt 1984). These cloud models were fully molecular and so only exchange reactions with H^+, produced from cosmic ray ionisation, were considered. However, in photodissociation regions (PDRs), the bulk of the population of rotation - vibrationally excited H_2 exists mainly in a sheet of material at a depth of A_v

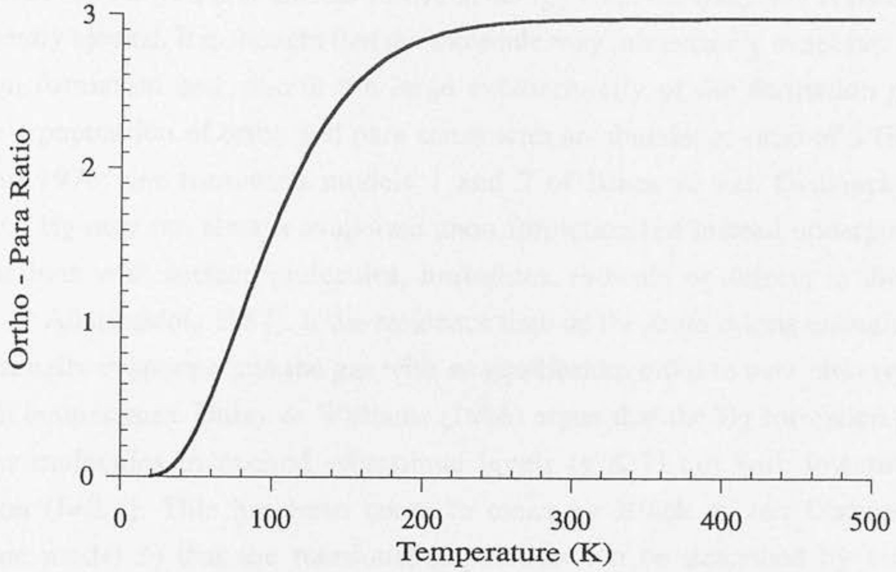

FIGURE 4.1 : The ortho to para ratio as a function of temperature.

~ 1 (see Chapter 2). At this depth, the abundance of H^+ can only be supported by cosmic ray ionisation, since all hydrogen ionising photons have been depleted at the HII/HI transition zone (which is defined to be where $A_v = 0$). The abundance of atomic hydrogen, however, is very high at this depth. Therefore, collisions and hence spin exchange with H will dominate over collisions with H^+ (see later).

If the gas is hot enough the ortho states become overpopulated relative to the para states. The amount of overpopulation is dependent on the timescale for the destruction of the H_2 molecule and how many spin changing collisions the molecule suffers in that time. In general, with no means of destruction, the lifetime of a H_2 molecule in a molecular cloud is very large, approximately the lifetime of the molecular cloud itself. For instance, once a shock has passed through a cloud, the H_2 in the hot and dense postshock gas suffers a large number of collisions and the measured ortho to para ratio is always 3 (eg. Orion - KL; Hasegawa *et al.* 1987), and will stay that way until the cloud subsequently cools to very cold temperatures (T ~ 50 K) after many years (~ 10^7 years).

In photodissociation regions, however, the circumstances are different. The processes occurring in the cold cloud models require long time scales to reach equilibrium (~ 10^{7-8} years - Flower & Watt 1984) whereas in a PDR, the lifetime of an H_2 molecule in its ground state before it is electronically excited by an ultraviolet photon is merely a fraction of a year. In a static PDR, H_2 molecules go through a cycle where they are constantly being formed on grain surfaces and then destroyed by photodissociation, only to be reformed again. It is upon formation that the ortho to para ratio is first set. As yet, it is unclear in which energy state the molecule is formed and subsequently ejected. It is thought that the molecule may immediately evaporate into the gas upon formation and, due to the large exothermicity of the formation process, produce a population of ortho and para states with an abundance ratio of 3 (Black & Dalgarno 1976; see formation models 1 and 2 of Black & van Dishoeck 1987). However, H_2 may not always evaporate upon formation but instead undergo energy loss reactions with surface molecules, impurities, radicals or defects in the lattice (Tielens & Allamandola 1987). If the residence time on the grain is long enough, then it will eventually evaporate into the gas with an equilibrium ortho to para ratio typical of the grain temperature. Duley & Williams (1986) argue that the H_2 formation process produces molecules in excited vibrational levels ($v \leq 7$) but with low rotational excitation ($J=0,1$). This has been taken to mean by Black & van Dishoeck (see formation model 3) that the rotational population can be described by a thermal population at the grain temperature and hence producing an ortho to para population typical of the grain temperature.

Once the molecule is in the gas it is then vulnerable to spin changing collisions with the gas and given enough time, the reaction described in [4.1] will drive the ortho to para ratio towards a value of 3 (as long as the gas is hot enough). In its ground state the lifetime of H_2 is dictated by the rate of absorptions of ultraviolet photons (see equation [3.16]). 10 % of these absorptions will lead to dissociation of the molecule and any information concerning the ortho to para ratio is lost. The remaining 90 % of absorptions will lead to an excited molecule in the electronic ground state, from whence it can fluoresce in the infrared. This infrared emission will carry the relevant information which will allow the ortho to para ratio to be measured. The shortened timescale over which spin exchange reactions can occur in PDRs, defined by the ultraviolet photon absorption rate, coupled with a formation mechanism which produces molecules at grain temperatures, may provide a natural explanation for the low value of the ortho to para abundance ratio which has been measured in NGC 2023.

4.2.1 CALCULATION OF THE ORTHO TO PARA RATIO IN A PDR

With the use of the analytical description of a PDR (presented in Chapter 2) it is possible to calculate the expected value of the ortho to para ratio which might be observed in a PDR. The fraction of molecules in the para state can be calculated using the expression (Burton, Hollenbach & Tielens 1992),

$$f(p,T) = \frac{\sum_{J=\text{even}} g(j)\exp\left(-\frac{T_j}{T}\right)}{3\sum_{J=\text{odd}} g(j)\exp\left(-\frac{T_j}{T}\right) + \sum_{J=\text{even}} g(j)\exp\left(-\frac{T_j}{T}\right)} \qquad [4.2]$$

where f(p,T) = fraction of para molecules in a gas of temperature T; g(j) = 2J + 1; J = rotational quantum number; T_j = energy of level j above the ground state.

The fraction of ortho molecules, f(o,T), can be similarly calculated or can be derived from the simple relation,

$$f(o,T) = 1 - f(p,T) \qquad [4.3]$$

The ratio of equations [4.3] and [4.2] gives the value of the ortho to para ratio.

There are three mechanisms by which the ortho to para ratio may be affected : gas-gas interactions such as the one described by equation [4.1] (H_2 interacting with either H or H^+), gas-grain interactions where the H_2 molecule sticks onto a grain surface and suffers spin changing interactions with any defects or impurities on the grain lattice, and the formation process of H_2 itself. Clearly, if gas-gas interactions dominate over other spin changing processes then the ortho to para ratio will be defined by the temperature of the gas. If, however, the gas-grain interaction is the most dominant process then the ortho to para ratio will be defined by the grain temperature. Lastly, if the formation process is dominant then the value of the ortho to para ratio depends on the choice of formation model. Models with large residence times upon formation will introduce molecules into the gas with an ortho to para ratio defined by the grain temperature (referred to as formation mechanism (a) hereafter). A model with large exothermicity and instantaneous evaporation upon formation will introduce molecules with an ortho to para ratio of 3 (referred to as formation mechanism (b) hereafter).

It is therefore necessary to calculate, at each depth step of the analytical model, which of these spin exchange processes dominates, and thereby determines the ortho to para ratio of the gas, with equations [4.2] and [4.3].

4.2.1.1 Gas-Gas Interactions

Consider the reaction with atomic hydrogen,

$$H_2\,(\text{ortho}) \quad + \quad H \quad \Leftrightarrow \quad H_2\,(\text{para}) \quad + \quad H \qquad [4.4]$$

The reaction rate for this process is,

$$\text{Rate} = n(H_2)\,n(H)\,\langle\sigma v\rangle \qquad [4.5a]$$

where $n(H_2)$ = density of H_2; $n(H)$ = density of H; $<\sigma v>$ = collision cross section.

A value for the collision cross section, estimated at 300 K, is (Blais & Truhlar 1981; Takayanagi *et al.* 1987),

$$\langle\sigma v\rangle \sim 10^{-16} \qquad \text{cm}^{+3}\,\text{s}^{-1}$$

$$\Rightarrow \qquad \text{Rate} \sim 10^{-16}\,n(H_2)\,n(H) \qquad \text{cm}^{-3}\,\text{s}^{-1} \qquad [4.5b]$$

Consider the reaction with ionised hydrogen,

$$H_2\,(\text{ortho}) \quad + \quad H^+ \quad \Leftrightarrow \quad H_2\,(\text{para}) \quad + \quad H^+ \qquad [4.6]$$

The reaction rate for this process is,

$$\text{Rate} = n(H_2)\,n(H^+)\,\langle\sigma v\rangle \qquad [4.7a]$$

where $n(H^+)$ = density of ionised hydrogen.

A value for the collision cross section is given by Flower & Watt (1984) as,

$$\langle\sigma v\rangle \sim 3\times10^{-10} \qquad \text{cm}^{+3}\,\text{s}^{-1}$$

$$\Rightarrow \qquad \text{Rate} \sim 3\times10^{-10}\,n(H_2)\,n(H^+) \qquad \text{cm}^{-3}\,\text{s}^{-1} \qquad [4.7b]$$

We therefore need to know the density of H^+ through the PDR, which the analytical model does not provide. However, it is relatively simple to make a few assumptions at this stage to allow its calculation. Firstly, assume that the density of H^+

is supported by cosmic ray ionisation of H and H_2 and is suppressed by radiative recombination with electrons and charge exchange reactions. There are the following channels and rates by which H^+ may be formed (Flower & Watt 1984):

(i) $H + CR \Rightarrow H^+ + e^- + CR$ Rate $\sim 1.50\zeta$
(ii) $H_2 + CR \Rightarrow H^+ + H + e^- + CR$ $\sim 0.02\zeta$
(iiia) $H_2 + CR \Rightarrow H_2{}^+ + e^- + CR$ $\sim 0.93\zeta$
followed by, [4.8]
(iiib) $H_2{}^+ + H \Rightarrow H^+ + H_2$ $\sim 10^{-10}\ \mathrm{cm}^{+3}\ \mathrm{s}^{-1}$
or followed by,
(iiic) $H_2{}^+ + H_2 \Rightarrow H_3{}^+ + H$ $\sim 2.1 \times 10^{-9}\ \mathrm{cm}^{+3}\ \mathrm{s}^{-1}$

where $\zeta = 3 \times 10^{-17}\ \mathrm{s}^{-1}$ is the cosmic ray ionisation rate.

The formation of H^+ via the ionisation of H_2 and subsequent charge exchange reaction with H can only occur as fast as the $H_2{}^+$ is formed, since reaction *(iiib)* is relatively much faster than *(iiia)*. However, reaction *(iiic)* is faster than *(iiib)* and since it is a destruction mechanism for $H_2{}^+$ it therefore suppresses the formation of H^+. An important formation - destruction chemical equilibrium is initiated with respect to the abundance of $H_2{}^+$,

$$0.93\, n(H_2)\, \zeta \;=\; 10^{-10}\, n(H_2^+)\, n(H) \;+\; 2.1 \times 10^{-9}\, n(H_2^+)\, n(H_2) \qquad [4.9]$$

which gives,

$$n(H_2^+) \;=\; \frac{0.93\, n(H_2)\, \zeta}{\left[10^{-10}\, n(H) \;+\; 2.1 \times 10^{-9}\, n(H_2)\right]} \qquad [4.10]$$

The rate for producing H^+ via reaction *(iiib)* is therefore,

$$\text{Rate} \;\sim\; 10^{-10}\, n(H_2^+)\, n(H) \qquad \mathrm{cm}^{-3}\ \mathrm{s}^{-1}$$

$$\sim\; \frac{9.3 \times 10^{-11}\, n(H_2)\, n(H)\, \zeta}{\left[10^{-10}\, n(H) \;+\; 2.1 \times 10^{-9}\, n(H_2)\right]} \quad \mathrm{cm}^{-3}\ \mathrm{s}^{-1} \qquad [4.11]$$

To determine the density of H^+ we need to establish a timescale for the lifetime of the proton in the gas. The radiative recombination coefficient can be written as (Dalgarno 1973),

$$\alpha(T_e) \sim 5 \times 10^{-13}\left(\frac{1000}{T_e}\right)^{0.7} \qquad \mathrm{cm}^{+3}\ \mathrm{s}^{-1} \qquad [4.12]$$

A typical value for the electron temperature in a PDR is of the order of (Burton, *private communication*),

$$T_e \sim 1{,}000\ \mathrm{K} \qquad [4.13]$$

At these depths ($A_V < 3 - 5$) the electron density is governed by the density of C^+. With an electron density of $n_e \sim 3 \times 10^{-4} n$ (cf. equation [2.10]), the timescale for radiative recombination is,

$$\tau \sim 1.5 \times 10^{-16}\, n \qquad \mathrm{s}^{-1} \qquad [4.14]$$

We can compare this to the charge exchange reaction between H^+ and O, which has a rate of $\sim 2.6 \times 10^{-10}$ $\mathrm{cm}^{+3}\ \mathrm{s}^{-1}$ (Tielens & Hollenbach 1985a). The abundance of O is $\sim 5 \times 10^{-4} n$ (Tielens & Hollenbach 1985a; BHT) giving a timescale for this reaction of,

$$\tau \sim 1.3 \times 10^{-13}\, n \qquad \mathrm{s}^{-1} \qquad [4.15]$$

This dominates over the radiative recombination timescale and will therefore determine the density structure of H^+. From equations [4.8], [4.11] and [4.15] we have,

$$1.3 \times 10^{-13}\, n\, n(H^+) = \zeta\left[1.5\, n(H) + 0.02\, n(H_2) + \frac{9.3\times10^{-11}\, n(H)\, n(H_2)}{10^{-10} n(H) + 2.1\times10^{-9} n(H_2)}\right]$$

$$n(H^+) = \frac{2.3\times10^{-4}}{n}\left[1.5\, n(H) + 0.02\, n(H_2) + \frac{9.3\times10^{-11}\, n(H)\, n(H_2)}{10^{-10} n(H) + 2.1\times10^{-9} n(H_2)}\right] \qquad \mathrm{cm}^{-3}$$

[4.16]

Finally, the spin exchange reaction rate can now be calculated with equation [4.7b]. Note that the results obtained from subsequent calculations will be based on these equations. However, the reaction with O is not the only charge exchange reaction that occurs with H^+ and it is not necessarily the one which dominates. It is chosen for our purposes because the density of O remains constant across our region of interest (see section 2.2.2.3). A more detailed treatment with a full chemical calculation is planned for the near future.

4.2.1.2 Gas-Grain Interactions

We can describe the gas-grain interaction with the following expression,

$$H_2\,(\text{ortho}) \;+\; \text{grain} \;\Leftrightarrow\; H_2\,(\text{para}) \;+\; \text{grain} \qquad [4.17]$$

The rate at which this process can occur is given by the density of the collision partners and their cross section,

$$\text{Rate} \;=\; n(H_2)\, n_{gr} \langle \sigma_{gr} v \rangle\, \alpha_T \qquad [4.18a]$$

where n_{gr} = the density of grains; v = thermal velocity of H_2 (~ 9118 $T^{0.5}$ cm s^{-1}); σ_{gr} = cross section of grain; $n_{gr}\sigma_{gr} = 10^{-21}n$.

The coefficient, α_T, is the thermal accommodation coefficient and describes the probability that a molecule will stick onto the grain surface and thermalise with the grain temperature. If the molecule becomes thermalised then $\alpha_T = 1$. However, following Hollenbach (1989), we adopt a value of $\alpha_T = 0.3$ (see section 1.2.2.3). The reaction rate can therefore be written as,

$$\text{Rate} \sim 2.7 \times 10^{-18}\, n(H_2)\, n\, T^{0.5} \qquad \text{cm}^{-3}\ \text{s}^{-1} \qquad [4.18b]$$

4.2.1.3 H_2 Formation on Grains

The formation of H_2 on the surfaces of grains can be described by the reaction,

$$H \;+\; H \;+\; \text{grain} \;\Rightarrow\; H_2\,(\text{ortho/para}) \;+\; \text{grain} \qquad [4.19]$$

Following Tielens & Hollenbach (1985a), we write the formation rate of H_2 via this process as, (see also section 1.2.1.3),

$$\text{Rate} = 3 \times 10^{-17}\, S(T)\, T^{0.5}\, n\, n(H) \qquad \text{cm}^{-3}\,\text{s}^{-1} \qquad [4.20]$$

where T = temperature of the gas; S(T) = sticking coefficient (see section 1.2.1.3).

The ortho to para ratio is initially set by this process (the value of the ratio dependent on the formation mechanism chosen - see section 4.2.1). However, once the molecule has been formed and introduced into the gas, it becomes vulnerable to spin exchange interactions via the processes discussed above. It is therefore important to consider the timescales available to these interactions in which they can affect the ortho to para populations before the molecule is excited by the absorption of an ultraviolet photon.

The unshielded dissociation rate will be approximately one tenth of the unshielded absorption rate. Therefore, at any depth A_V, the absorption rate can be written as (from equation [3.16]),

$$\text{Absorption Rate} \sim 5 \times 10^{-10}\, G_0\, e^{-2.5A_v} \qquad \text{s}^{-1} \qquad [4.21a]$$

which we can write as,

$$\text{Absorption Rate} \sim 5 \times 10^{-10}\, n(H_2)\, G_0\, e^{-2.5A_v} \qquad \text{cm}^{-3}\,\text{s}^{-1} \qquad [4.21b]$$

for the rate of absorption by the H_2 molecule.

If the rate of absorption exceeds the rate at which spin exchange reactions can occur then the ortho to para ratio is set to the value defined by the formation model. If the reverse is true, then the ortho to para ratio is set to the appropriate temperature for that process (ie. gas temperature for gas-gas interactions, grain temperature for gas-grain interactions). This condition is only taken into consideration if the formation process is dominant.

4.2.1.4 Model Results

Figures 4.2(a-d) show the results of this modelling. The top diagram in each of these figures shows the spin exchange rate for the four processes discussed above. The models chosen show a range in density ($n = 10^{4-6}$ cm^{-3}) and in G_0 ($= 10^{4-5}$). It is clear that for all models, the rate of formation is the dominant process which determines the ortho to para ratio up to a depth of $A_V \sim 1$-3. Deeper than this, gas-grain interactions dominate. The lower diagram in each figure shows the derived ortho to para ratio of H_2

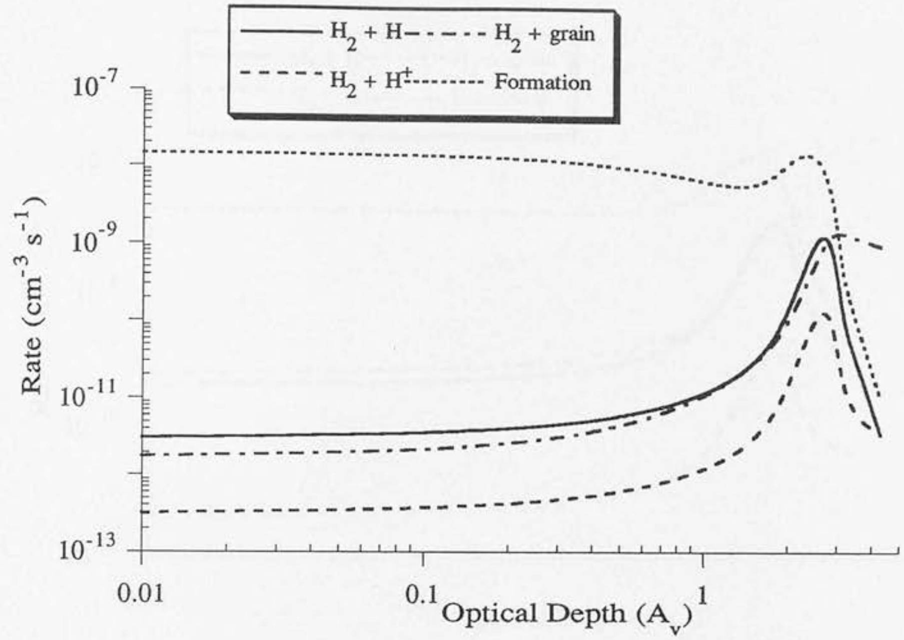

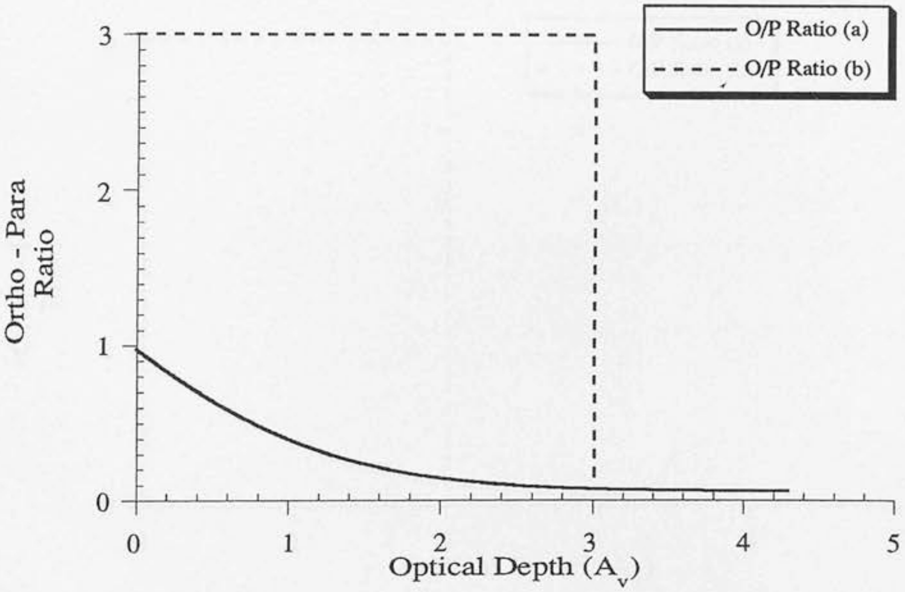

FIGURE 4.2a : The upper diagram shows the spin exchange rates calculated through analytic PDR model with $G_0 = 10^4$ and $n = 10^4$ cm^{-3}. The lower diagram shows the derived ortho to para ratio through this model with formation mechanism (a) - dashed line - and formation mechanism (b) - solid line - (see text).

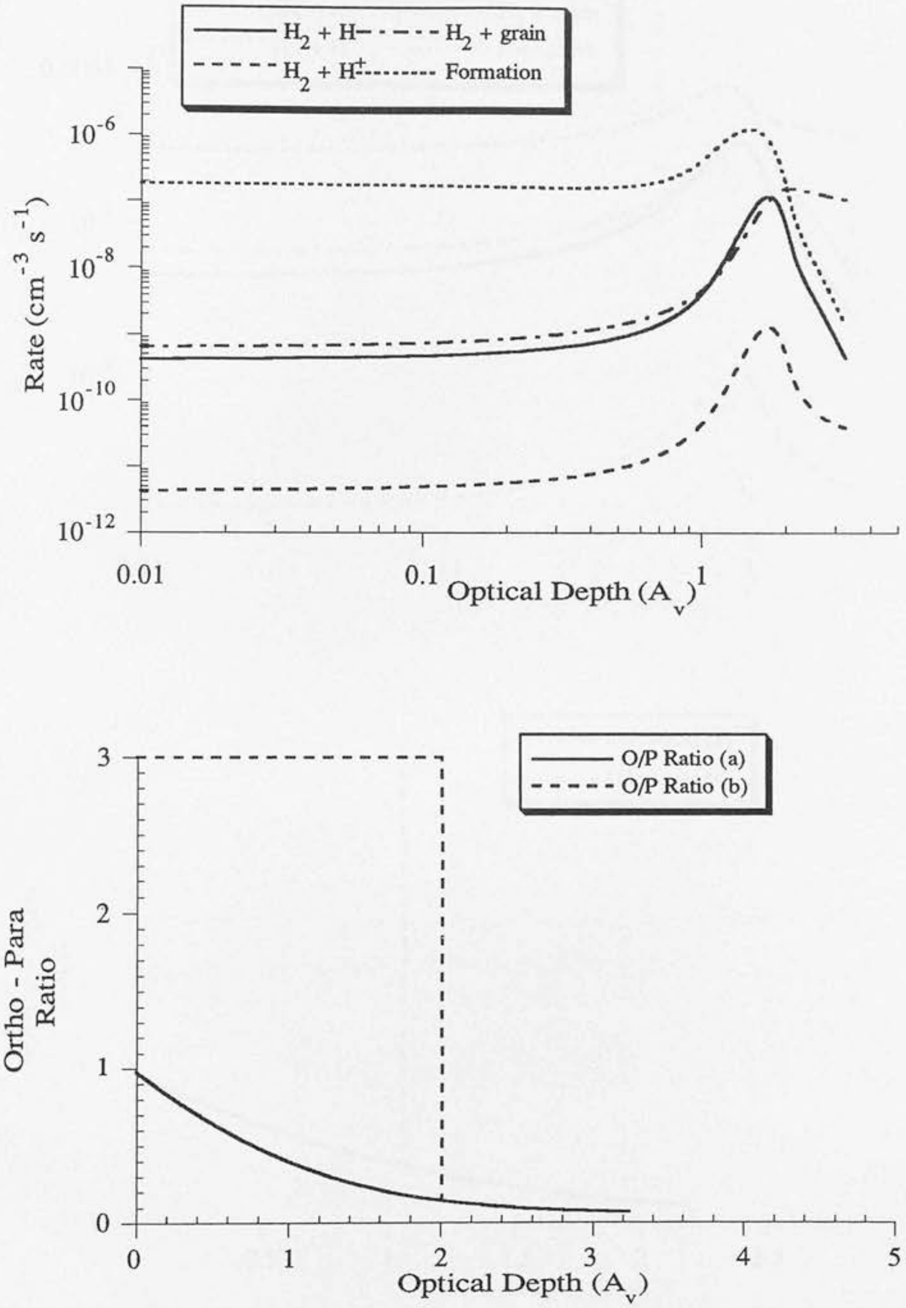

FIGURE 4.2b : The same as for Figure 4.2a but for a PDR model with $G_0 = 10^4$ and $n = 10^5$ cm^{-3}.

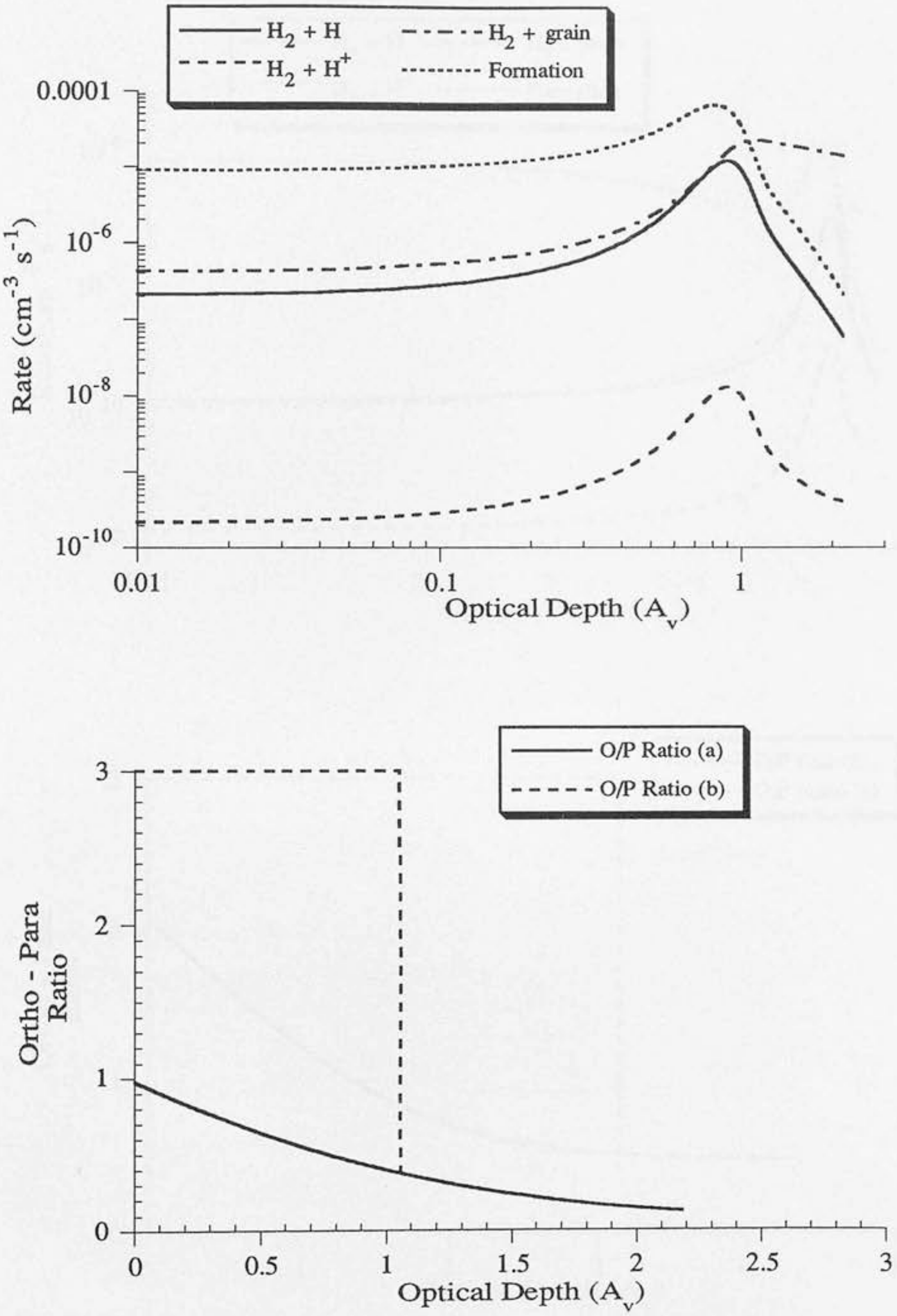

FIGURE 4.2c : The same as for Figure 4.2a but for a PDR model with $G_0 = 10^4$ and $n = 10^6$ cm^{-3}.

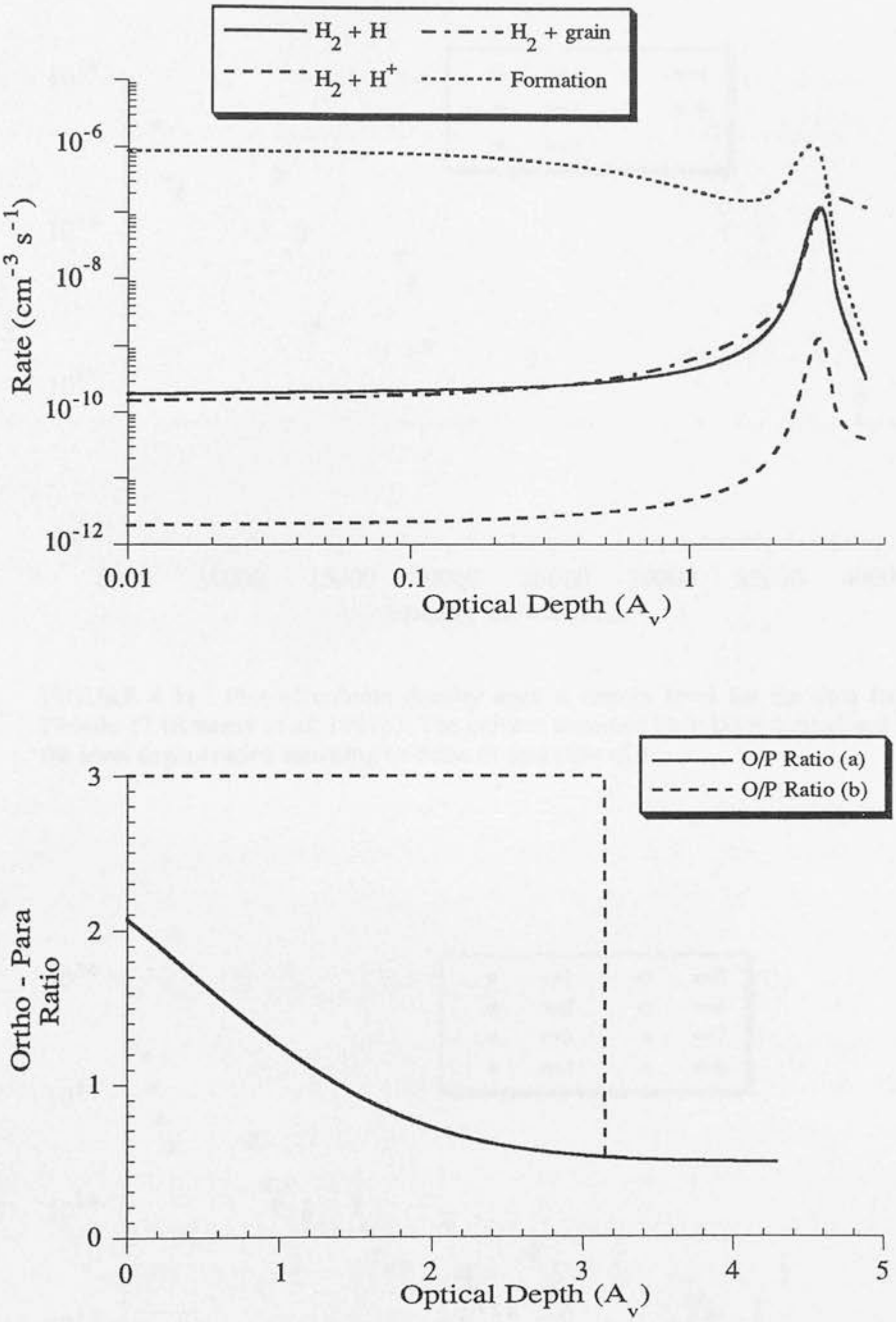

FIGURE 4.2d : The same as for Figure 4.2a but for a PDR model with $G_0 = 10^5$ and $n = 10^5$ cm^{-3}.

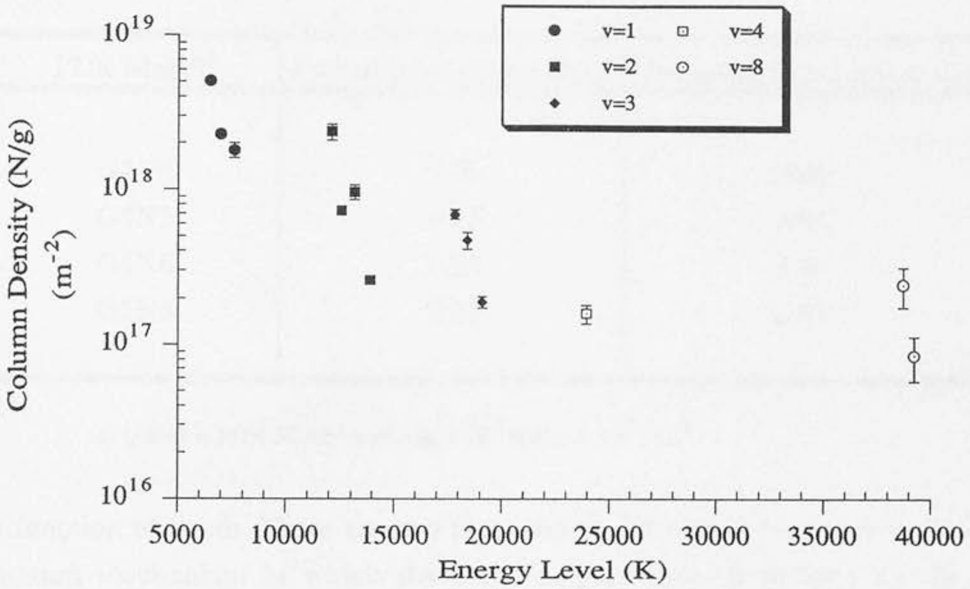

FIGURE 4.3a : Plot of column density against energy level for the data from Hubble 12 (Ramsay *et al*. 1992b). The column densities have been normalised by the level degeneracies assuming an ortho to para ratio of 3.

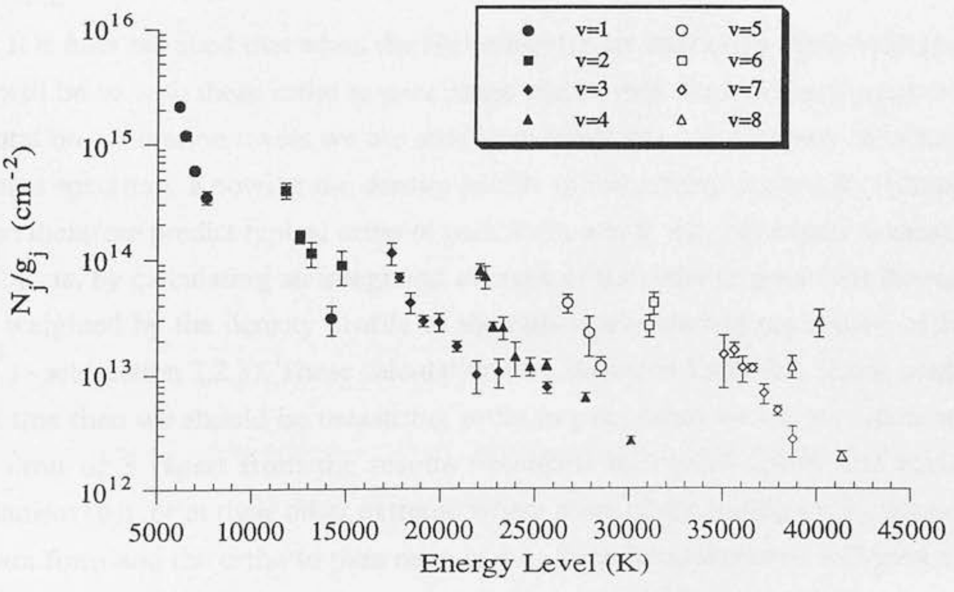

FIGURE 4.3b : Plot of column density against energy level for the data from NGC 2023 (Burton *et al. in preparation*). The column densities have been normalised by the level degeneracies using an average ortho to para ratio calculated from the data.

TABLE 4.1 : AVERAGE ORTHO TO PARA RATIOS INTEGRATED THROUGH A PDR

PDR Model[a]	Formation Mechanism (a)	Formation Mechanism (b)
G4N4	0.20	2.96
G4N5	0.22	2.84
G4N6	0.35	1.44
G5N5	0.58	2.83

a) G4N4 = PDR Model with $G_0 = 10^4$ and $n = 10^4$ cm^{-3}.

as a function of depth. There are two plots shown. The solid line represents a grain formation mechanism in which the ortho to para ratio is defined by the grain temperature (mechanism a). The dashed line (mechanism b) represents a formation mechanism which forms H_2 with an ortho to para ratio of 3. This plot clearly shows the depth over which the formation process has the major influence on the ortho to para ratio. It is evident that the timescale for spin exchange processes in the gas after the ortho to para ratio has been set in the formation process is too long compared to the absorption rate, and so in this modelling, the ortho to para ratio set upon formation is preserved.

It is now assumed that when the H_2 molecules are excited by ultraviolet photons, they will be so with these ortho to para ratios and as they fluorescently cascade down the rotation - vibration levels we are able to measure the ortho to para ratio from the emission spectrum. Knowing the density profile of radiatively excited H_2 (Chapter 2), we can therefore predict typical ortho to para ratios which we may expect to measure in our objects, by calculating an integrated average of the ortho to para ratio through the PDR weighted by the density profile of the radiatively excited population of H_2 (ie. $n(H_2^*)$ - see section 2.2.3). These calculations are shown in Table 4.1. If this modelling holds true then we should be measuring ortho to para ratios which are either at their LTE limit of 3 (apart from the results described by model G4N6 and formation mechanism (b)), or at their other extreme where most of the molecular hydrogen is in the para form and the ortho to para ratio is < 1. Such measurements will give a clear indication which formation mechanism is relevant to the hydrogen molecule.

TABLE 4.2 : MEASURED ORTHO TO PARA RATIOS IN M17 NORTHERN BAR, HUBBLE 12 & NGC 2023

Source	Vibrational Level	Ortho to Para Ratio
M17 NB	2^a	1.60 (0.68)
	2^b	1.83 (0.69)
	3	2.18 (1.37)
weighted average from all levels		1.77 (0.46)
Hubble 12	1	2.11 (0.28)
	2^c	1.36 (0.39)
	2^d	1.42 (0.27)
	3	2.46 (0.70)
weighted average from all levels		1.72 (0.17)
NGC 2023	1	2.13 (0.26)
	2	1.42 (0.26)
	3	2.14 (0.45)
	4	2.13 (0.38)
	5	1.72 (0.83)
	7	2.68 (0.59)
weighted average from all levels		2.16 (0.24)

a) Rotational temperature calculated using the 2-1 S(0) and 2-1 S(2) transitions and the ortho to para ratio using the 2-1 S(0) and 2-1 S(1) transitions.

b) Rotational temperature calculated using the 2-1 S(1) and 2-1 S(3) transitions and the ortho to para ratio using the 2-1 S(2) and 2-1 S(1) transitions.

c) Rotational temperature calculated using the 2-1 S(0) and 2-1 S(2) transitions and the ortho to para ratio using the 2-1 S(1) and 2-1 S(2) transitions.

d) Rotational temperature calculated using the 2-1 S(1) and 2-1 S(3) transitions and the ortho to para ratio using the 2-1 S(2) and 2-1 S(3) transitions.

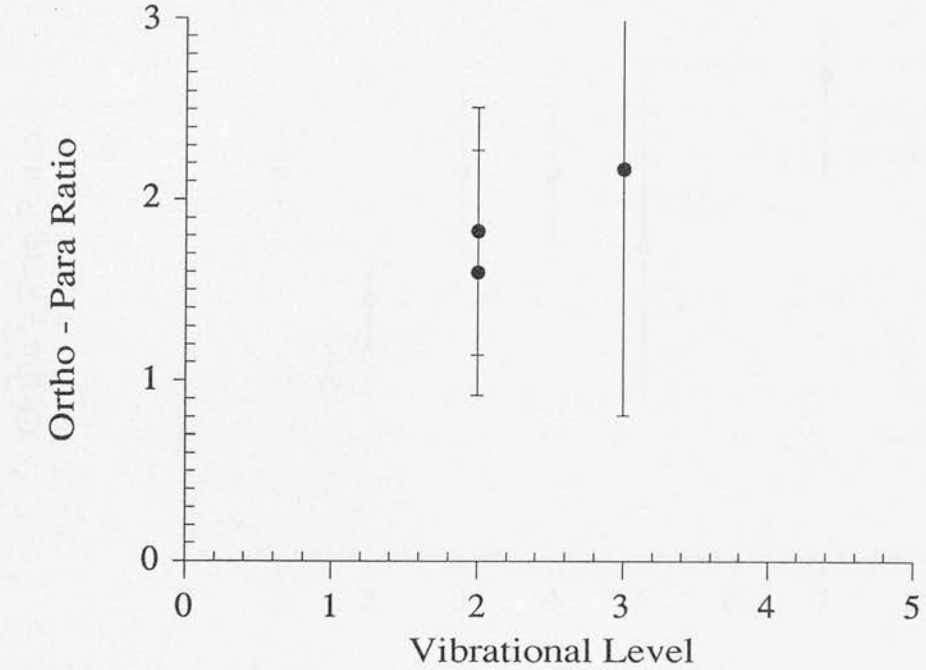

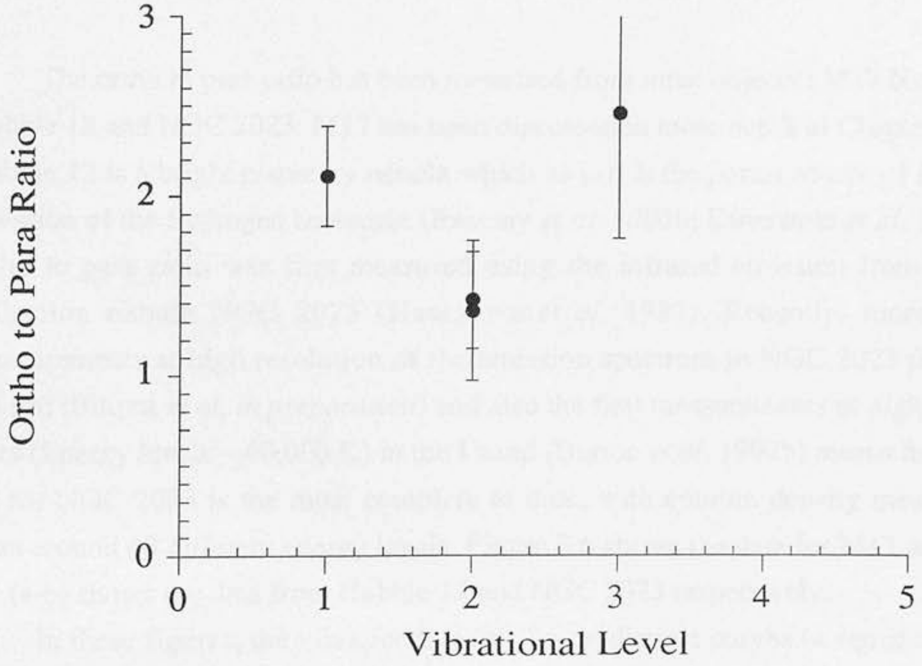

FIGURE 4.4a & 4.4b : Ortho to para ratios from M17 Northern bar and Hubble 12.

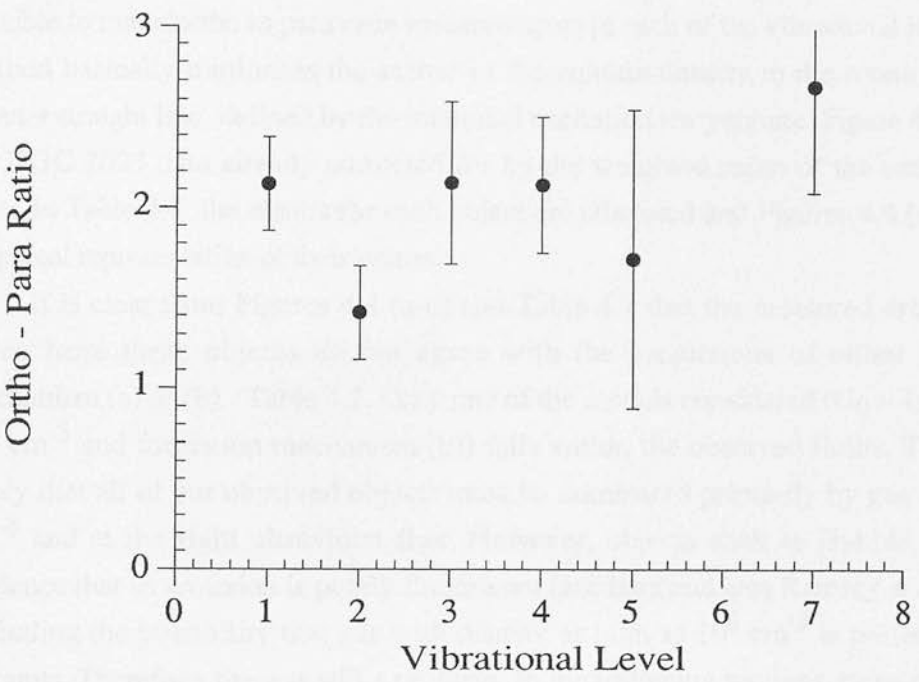

FIGURE 4.4c : Ortho to para ratios from NGC 2023.

4.2.2 OBSERVATIONS OF THE ORTHO TO PARA RATIO

The ortho to para ratio has been measured from three objects : M17 Northern bar, Hubble 12 and NGC 2023. M17 has been discussed in more detail in Chapters 2 and 3. Hubble 12 is a bright planetary nebula which as yet, is the purest source of fluorescent emission of the hydrogen molecule (Ramsay *et al*. 1992b; Dinerstein *et al*. 1988). The ortho to para ratio was first measured using the infrared emission from H_2 in the reflection nebula NGC 2023 (Hasegawa *et al*. 1987). Recently, more accurate measurements at high resolution of the emission spectrum in NGC 2023 from 1.0 to 2.5 μm (Burton *et al. in preparation*) and also the first measurements of high excitation lines (Energy levels ~ 40,000 K) in the I band (Burton *et al*. 1992b) means that the data set for NGC 2023 is the most complete to date, with column density measurements from around 40 different energy levels. Figure 3.6 shows the data for M17 and Figures 4.3 (a-b) shows the data from Hubble 12 and NGC 2023 respectively.

In these figures, the vibrational levels lie on distinct curves (a signature of their fluorescent nature) with (for M17 and Hubble 12) the rotational levels scattered about these curves. The reason for this scatter is because the column densities have been normalised by the level degeneracy assuming an ortho to para ratio of 3. Clearly, this ortho to para ratio is an overestimate. Using the method described in section 3.4.3 it is possible to make ortho to para ratio measurements in each of the vibrational levels. This method basically minimises the scatter of the column density in the rotational levels about a straight line, defined by the rotational excitation temperature. Figure 4.3b shows the NGC 2023 data already corrected for by the weighted mean of the ortho to para ratio. In Table 4.2 the results for each object are tabulated and Figures 4.4 (a-c) give a graphical representation of their values.

It is clear from Figures 4.4 (a-c) and Table 4.2 that the measured ortho to para ratios from these objects do not agree with the predictions of either formation mechanism (a) or (b) - Table 4.1. Only one of the models considered ($G_0 = 10^4$ and $n = 10^6$ cm^{-3} and formation mechanism (b)) falls within the observed limits. This would imply that all of our observed objects must be dominated primarily by gas at $n = 10^6$ cm^{-3} and at the right ultraviolet flux. However, objects such as Hubble 12 shows evidence that its emission is purely fluorescent (see later and also Ramsay *et al.* 1992b) excluding the possibility that gas with density as high as 10^6 cm^{-3} is present in large amounts. Therefore, there is still a problem. In the following sections, three models are considered which may reconcile the observed values in Table 4.2 and the theory.

4.2.3 ALTERNATIVE MODELS

4.2.3.1 Residence Time After Formation

Most models in the literature which have considered the formation of molecular hydrogen have made the assumption that once a molecule is formed it is immediately ejected into the gas with one third of the binding energy (~ 1.5 eV) going towards the kinetic energy of the molecule, one third to the grain lattice and one third to the internal energy of the molecule, producing so-called "hot molecules" (eg. Black & Dalgarno 1976; Black & van Dishoeck 1987; Sternberg & Dalgarno 1989). Tielens & Allamandola (1987) argue however, that the dissipation of the reaction heat through these channels (and others) is important and do not reflect these naive proportions previously considered. For instance, in some cases the molecule may lose so much of its formation energy to the grain lattice that it does not posses enough translational energy to be ejected into the gas. Among the energy loss channels considered by Tielens & Allamandola are : localised phonons of the lattice, vibrational energy transferred to rotational modes of the molecule from where the energy is rapidly transferred to lattice phonons, and the vibrational modes of neighbouring molecules. The timescales for these energy loss channels can range between 10^{-8} - 10^{-12} seconds, whereas the transfer of binding energy to the translational motion of the molecule is approximately 10^{-7} seconds, although this estimate is very uncertain (Tielens & Allamandola 1987). Therefore, the question arises, how long does the molecule remain on the grain surface and how much internal energy does it lose? This is an important question because the amount of internal energy that the molecule is introduced into the gas with will determine the ortho to para ratio.

Due to the uncertainties involved in these timescales, we can hide our ignorance of them by defining the exponential factor,

$$e^{-t/t_{eq}} \qquad [4.22]$$

where t = time that the molecule resides on the grain before ejection; t_{eq} = time in which the molecule, if ejected, would have an ortho to para ratio which is e^{-1} of the equilibrium value determined by the grain temperature.

We can now, therefore, model the value of the ortho to para ratio as a function of the residence time using the equation,

$$\frac{O}{P} = 3e^{-t/t_{eq}} + \frac{f(o)}{f(p)}\left[1 - e^{-t/t_{eq}}\right] \qquad [4.23]$$

Figure 4.5 gives a graphical representation of equation [4.23] for various grain temperatures. The equation satisfies the limits set by formation models (a) and (b) in section 4.2.1.4, ie. for very short residence times ($t \rightarrow 0$) most of the internal energy is retained by the molecule and it is ejected into the gas with an ortho to para ratio of 3. For long residence times ($t \gg t_{eq}$) most of the internal energy of the molecule is lost via the various energy loss channels and the internal population distribution is defined by the grain temperature, hence producing low (< 1) ortho to para ratios. Unfortunately, the actual or average residence time of the newly formed hydrogen molecule on the grain surface can only be speculated on (speculation whose basis relies on theoretical rather than experimental work), however, to match this model to the observed ortho to para ratios, the required residence time will have to be such that $t \sim t_{eq}$.

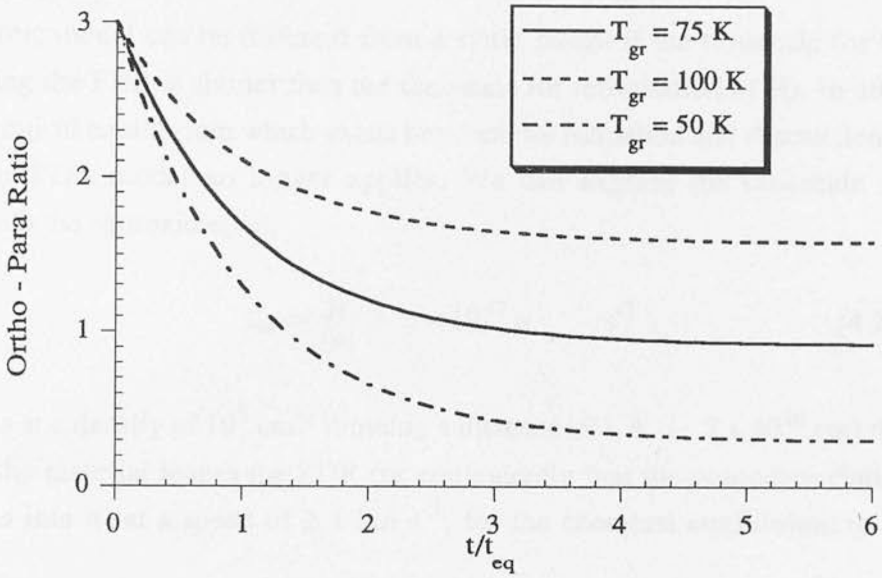

FIGURE 4.5 : The ortho to para ratio of formed molecules as a function of the time it resides on the grain surface before it eventually evaporates into the gas. Values for three grain temperatures are plotted.

4.2.3.2 The Dynamic PDR Model

The PDR model of Tielens & Hollenbach (1985a) is a plane parallel, constant density slab of material, bounded on one side by an HII region and on the other by the molecular cloud. This slab is in pressure equilibrium and therefore the gas remains static. However, more and more observational evidence is confirming that the interface region between the HII region and the molecular cloud is actually a clumpy rather than uniform medium (eg. see data on M17 in Stutzki & Güsten 1990; Chrysostomou *et al.* 1992a). Clumpy structure in regions such as M17 has been observed to scales as small as ~ 0.01 parsecs. Moreover, these observations also indicate that these regions do not conform to a plane parallel geometry, but are corrugated in some complex fashion, or, as in the case of a clump, the surface geometry must be almost spherical.

Consider a clump of gas in a molecular cloud. Initially it is cold and in pressure equilibrium with its surroundings. Now, an O or B star is born in its vicinity. The surface of the clump is bathed in ultraviolet light, quickly heating it up, the material at the surface perhaps being as hot as ~ 1000 K. It is no longer in pressure equilibrium and the surface geometry of the spherical clump allows the gas to stream away at a speed of a few kilometres per second. The PDR in the clump is no longer static and as material is removed from the surface of the clump a photodissociation front advances into it (see Figure 4.6).

A dynamic model can be different from a static model if the timescale for the material leaving the PDR is shorter than the timescale for reformation of H_2. In other words, the chemical equilibrium which exists between the formation and destruction of H_2 in a static PDR model no longer applies. We can express the timescale for reformation with the approximation,

$$\tau_{ref} = \frac{R}{n_H} \sim 3 \times 10^{-17}\, n \qquad s^{-1} \qquad [4.24]$$

For a gas at a density of 10^5 cm^{-3} crossing a distance of 1 A_v (~ 2 x 10^{16} cm) this requires that the material leaves the PDR (or equivalently that the photodissociation front advances into it) at a speed of ≥ 1 km s^{-1}, for the chemical equilibrium to be destroyed.

As the photodissociation front advances into the molecular clump, new material is effectively sweeped into the warm region where H_2 is excited by ultraviolet photons, and from where an ortho to para ratio can be measured. In this region, the gas is typically 200 - 300 K. Ortho to para ratios at these effective temperatures are of the order of 3 (see Figure 4.1). Therefore, the cooler material (T ~ 50 - 150 K) with its lower ortho to para ratio will have to advance into the warm region before it is affected by spin exchange reactions with the gas which will raise its ortho to para ratio. The region needed to be crossed by the gas is typically $\Delta A_v \sim 1$. For a gas at 10^5 cm^{-3} this corresponds to a distance of ~ 2 x 10^{16} cm. From Figure 4.2b we can estimate that the spin exchange rate with the gas at the depth of A_v ~ 1 - 2 is approximately 5 x10^{-8} cm^{-3} s^{-1}. Once again, for a distance of 2 x 10^{16} cm, this requires that the photodissociation front be advancing into the molecular material at speeds greater than ~ 0.1 km s^{-1} so that the low ortho to para ratios are preserved. Notice that this means the PDR is "dynamic and yet static". This means that although there is an advancing photodissociation front in the PDR, it is not moving fast enough to destroy the chemical equilibrium between the formation and destruction of molecular hydrogen, however, it is advancing fast enough such that it excites gas with lower ortho to para ratios.

4.2.3.3 Spin Exchange During The Fluorescent Cascade

The ortho to para ratios predicted by the simple modelling in Table 4.1 and the

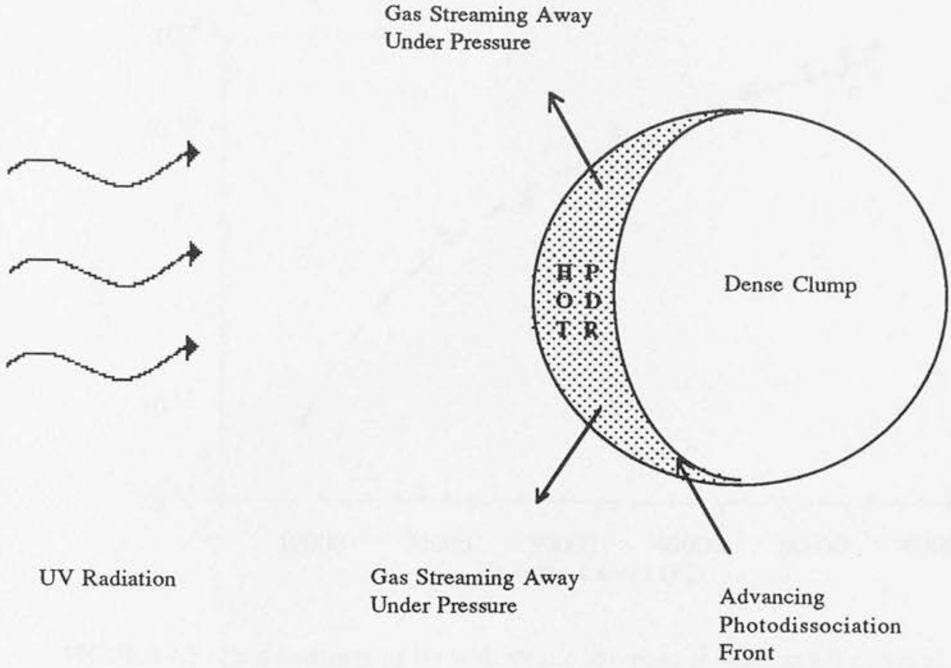

FIGURE 4.6 : Schematic diagram of a Dynamic PDR. The ultraviolet radiation is heating the surface of the clump and the hot gas is able to escape allowing a photodissociation front to advance into the clump.

observed values in Table 4.2, do not agree. The model considered all possible spin exchange mechanisms that could occur between the formation of the molecule and its excitation by ultraviolet radiation. Because of the disparity between the model and observations, we may assume that there must be some processing of the molecule after it has been excited.

Fluorescent emission from excited molecular hydrogen exists in a thin sheet in the PDR at a depth of $A_v \sim 1 - 2$. Typically, the relative abundance between H_2 in its ground state and H_2 in an excited state is $1:10^{-4}$ (BHT). Since most of the molecular hydrogen is in the ground state, we have concentrated on how spin changing collisions affect this population and regarded any spin exchange during the cascade as negligible. However, Blais & Truhlar (1981) have shown, using quasi-classical trajectory calculations, that the spin exchange reaction rate rises rapidly with energy level of the molecule. Blais & Truhlar have studied 3 aspects of the H + H_2 (v>0) interaction : dissociation, non-reactive inelastic collisions (ie. deexcitation), and reactive collisions (ie. spin exchange). The results they have quoted are plotted in Figure 4.7. The dashed line going through these points is a simple power law fit to the data and takes the form,

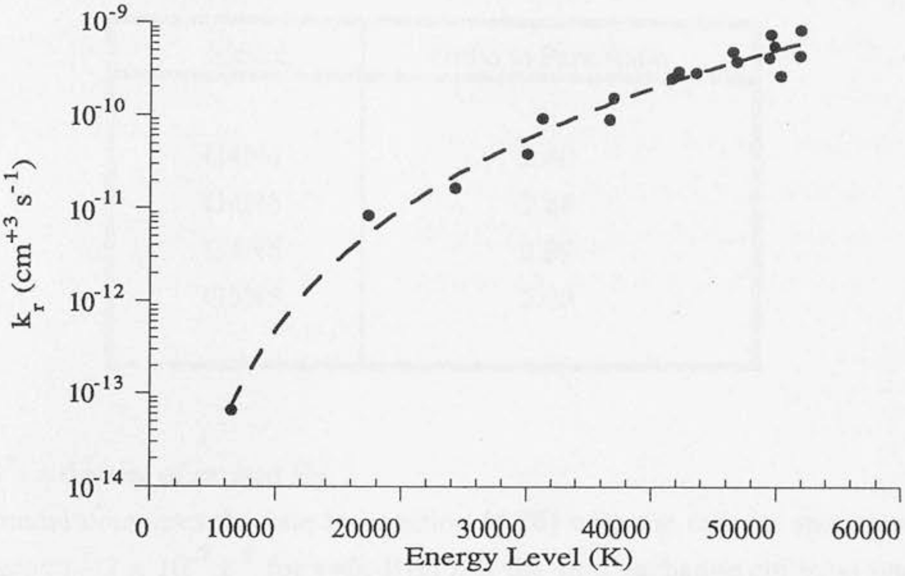

FIGURE 4.7 : Spin exchange of H_2 with atomic hydrogen at 300K as a function of energy level. The points are from calculations by Blais & Truhlar (1981) and the dashed line is a power law fit to the data, given by equation [4.25].

$$k_r = 4.9 \times 10^{-13} \left(\frac{E}{10^4}\right)^{4.36} \quad cm^{+3}\ s^{-1} \qquad [4.25]$$

where k_r = reaction rate; E = energy level.

One can immediately see the significance of this plot. The rate of this reaction at the ground state is approximately 10^{-16} cm^{+3} s^{-1} (Blais & Truhlar 1981; Takayanagi *et al.* 1987). However, once one rises to around 30,000 K above the ground state, typical for a v=6 level, then the reaction rate increases by almost 6 orders of magnitude. The overall spin exchange rate is 100 times greater, per second, for an excited molecule at v=6 than for the molecules in the ground state.

For this reason, the model in section 4.2.1 has been run again but this time also including collisions with excited H_2 as a source of ortho to para conversion. A level at v = 6 and J = 0 (E = 30,948 K) has been chosen to represent the population of excited molecular hydrogen. The rate for reaction of this species with H is (using equation [4.25]),

$$\text{Rate} \sim 6.75 \times 10^{-11}\, n(H_2^*)\, n(H) \quad cm^{-3}\ s^{-1} \qquad [4.26]$$

TABLE 4.3 : RECALCULATION OF ORTHO TO PARA RATIOS WITH PROCESSING OF EXCITED H_2

Model	Ortho to Para Ratio
G4N4	2.80
G4N5	2.88
G4N6	2.89
G5N5	2.90

where $n(H_2^*)$ = density of excited H_2.

The model compares the rate in equation [4.26] with the rate for spontaneous radiative decay (~ 2×10^{-7} s^{-1} for v=6; BHT). If the spin exchange collision rate is greater, then the ortho to para ratio is set to the value defined by the gas temperature. The models were run again with formation mechanism (a) and the results are tabulated in Table 4.3. Comparing with Table 4.1 for the same formation model, we immediately see that the ortho to para ratios have been significantly affected by spin exchange reactions during the fluorescent cascade. These results are encouraging since they tell us that there must be some processing of the ortho and para abundances during the fluorescent cascade. The results from the model imply that this processing is very significant. However, predicted results once again do not agree with the observed values (see Table 4.2). There may be two possible reasons for this: our model is too naive in its simplicity to handle such a complex problem and/or the results of Blais & Truhlar are wrong or grossly overestimated.

The obvious way to proceed is to calculate a complete fluorescent cascade model, rather like Black & van Dishoeck (1987) or Sternberg & Dalgarno (1989), and to fold into the model a spin exchange mechanism which follows the power law given in equation [4.26]. Unfortunately, such a model is beyond the scope of this thesis, but there is good prospect that such a calculation may be attempted in the near future.

At least one question that such modelling will be able to answer is the following: does the *measured* ortho to para ratio change as a function of energy level? Equation [4.25] says that the spin exchange rate changes as the fourth power of the energy level, ie. as one goes from ~ 6000 K to 50,000 K above the ground state, the spin exchange rate changes by approximately 4 orders of magnitude (see also Figure 4.7). If this is believed, then we can go a step further and suggest that because of this and as the total number of spin changing collisions suffered by an excited molecule will increase as it cascades down the rotation - vibration levels, we may expect to see a difference in the value of the ortho to para ratios as it is measured from different levels. If we could measure such a difference then this would surely be an effective way of tracing the history of the excited molecule (eg. the number of collisions suffered), and to perhaps evaluate the ortho to para ratio of the molecules *before* being excited and hence giving an insight into the formation process of the molecule. Figures 4.4 and Table 4.2 give measured ortho to para ratios for different vibrational levels from M17 Northern bar, Hubble 12 and NGC 2023. There is no significant evidence in any of this data of the ortho to para ratio varying with vibrational level.

4.2.4 LINE RATIOS AND THE ORTHO TO PARA RATIO

Line ratios from molecular hydrogen emission have historically been used as powerful probes of the physical conditions prevalent in molecular clouds. A good example is the ratio of the H_2 v=1-0 S(1) and 2-1 S(1) transitions which has traditionally been used to discriminate between shock and ultraviolet excitation of the H_2 molecule (eg. Hayashi *et al.* 1985). In shocks, this ratio is approximately 10 (Shull & Hollenbach 1978) whereas for ultraviolet excitation (ie. PDRs) the ratio is typically to the order of 2 (Black & van Dishoeck 1987). However, recent modelling (BHT; Sternberg & Dalgarno 1989) has shown that in high density PDRs where the density is above the critical density for collisional deexcitation of the lowest vibrational levels, the collisions incurred between H_2 and the gas alters the line ratios such that they appear thermalised (ie. shock like). Clearly, this diagnostic by itself cannot be trusted to determine the nature of the excitation since high density gas can produce ratios which falsely indicate the presence of shocks. It is therefore necessary to obtain data from transitions originating in higher levels, since these levels are harder to thermalise and therefore will preserve their fluorescent nature.

One method of interpreting such data is to ratio them with a pure fluorescent cascade, and look for any deviations from the expected distribution. Figures 4.8(a-c) show plots of the output from the BHT model, ratioed with their coldest, lowest density and therefore most fluorescent model, ie. the model which has a density of n $=10^3$ cm^{-3} and $G_0 = 10^3$. The ratio of the models in Figure 4.8a all produce a distribution of points which is a horizontal line, ie. the emission is from a pure fluorescent cascade (the difference in the absolute values of the ratios is because each model is at a higher density and the column densities are therefore higher). In Figure 4.8b, only the coolest

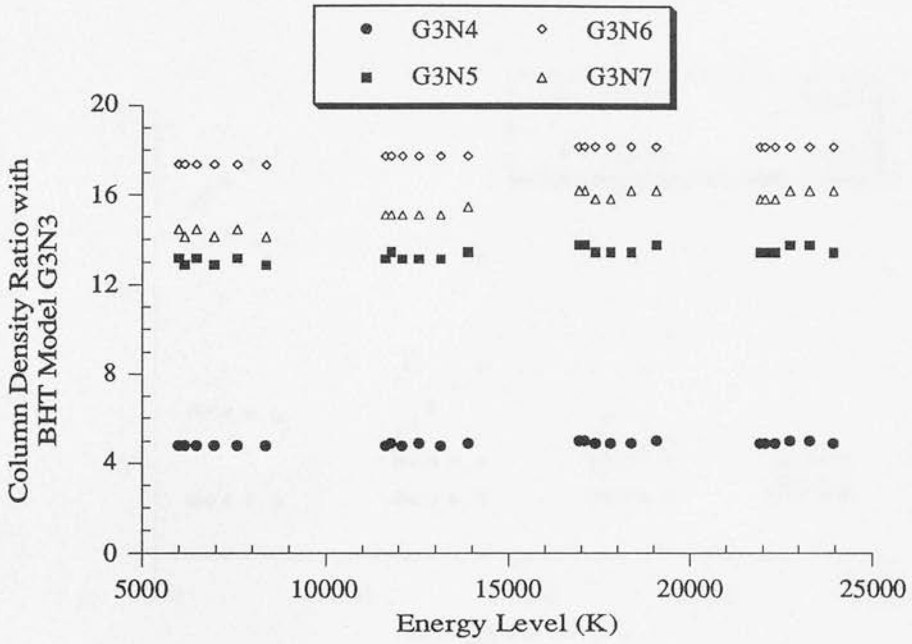

FIGURE 4.8a : Ratio of PDR models of increasing densities, and with incident ultraviolet fluxes of $G_0 = 10^3$, with a cold, fluorescent model. Models from BHT.

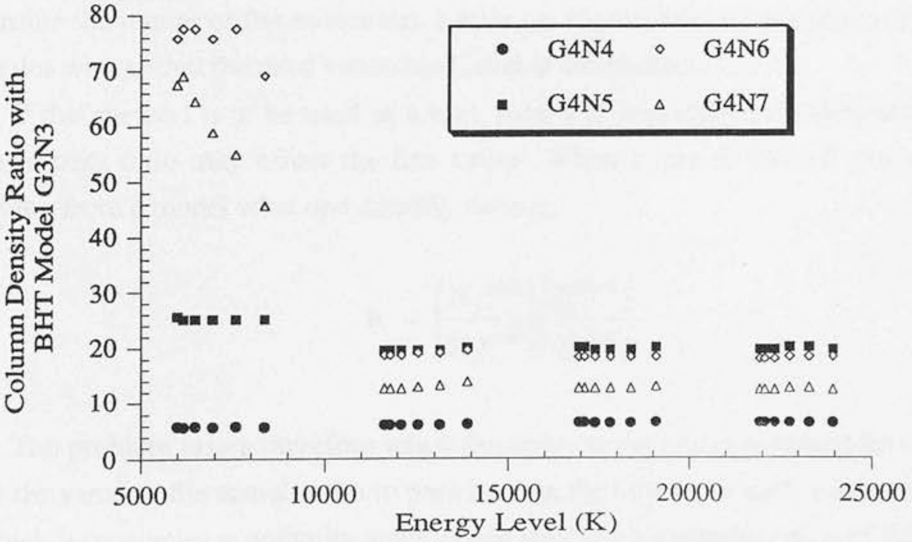

FIGURE 4.8b : The same as for figure 4.8a but for models with an incident ultraviolet flux of $G_0 = 10^4$.

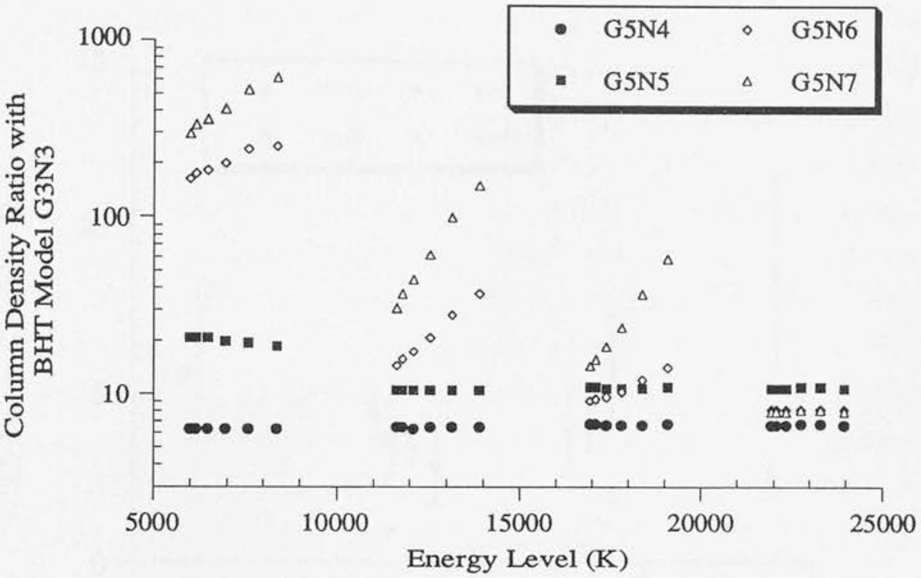

FIGURE 4.8c : The same as for Figure 4.8a but for models with an incident ultraviolet flux of $G_0 = 10^5$.

model (G4N4) remains purely fluorescent while the higher density models are definitely thermalised in the first vibrational level. The higher vibrational levels, however, have preserved their fluorescent ratios. This clearly illustrates the importance of observing transitions from these higher levels, together with the lower levels, to determine the nature of the excitation. Lastly, in Figure 4.8c we see the most extreme examples where even the third vibrational level is thermalised.

If this method is to be used as a tool, then it is important to understand how the ortho to para ratio may affect the line ratios. When a line is ratioed with the same transition from a model what one actually does is,

$$R = \left(\frac{N_j^{\,obs}}{N_j^{\,mod}}\right)\left(\frac{g_j^{\,mod}}{g_j^{obs}}\right) \qquad [4.27]$$

The problem arises therefore when the ortho to para ratio assumed for the model is not the same as the actual ortho to para ratio in the object. In such a case the ratio of the level degeneracies is not unity and this can lead to a misinterpretation of the physical conditions in the source.

In Figures 4.9(a-b) plots of the data from M17 Northern bar and Hubble 12 are shown ratioed with model number 14 from Black & van Dishoeck (1987). The data has

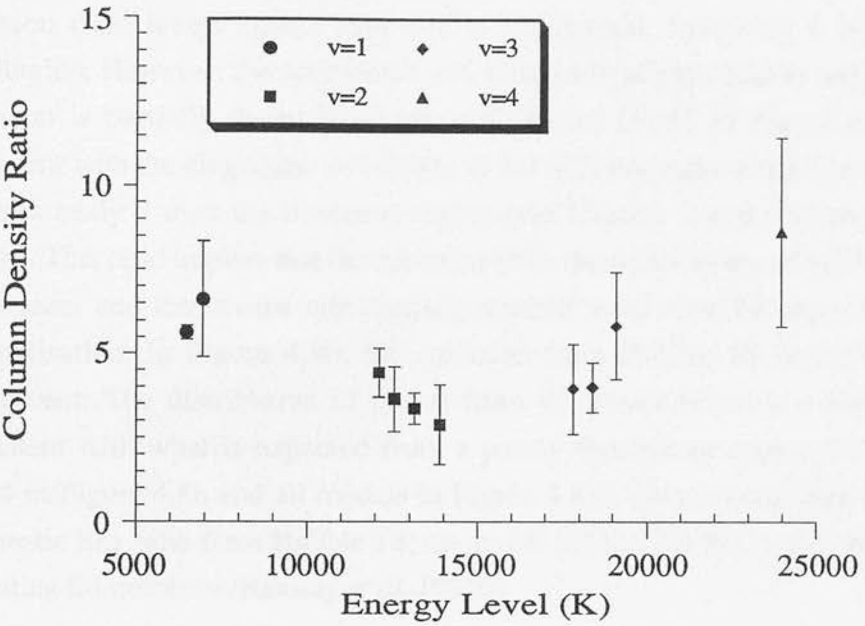

FIGURE 4.9a : Column densities from M17 Northern bar (corrected for by mean ortho to para ratio) divided by Black & van Dishoeck model #14. Higher levels remain fluorescent but the v=1 level may be slightly thermalised.

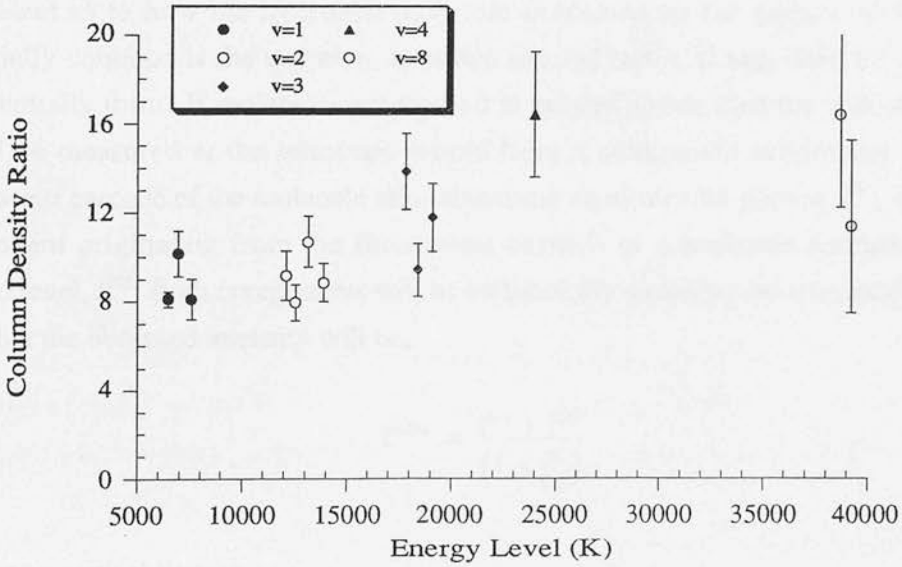

FIGURE 4.9b : Column densities from Hubble 12 (corrected for by mean ortho to para ratio) divided by black & van Dishoeck model # 14. The horizontal distribution of points is a signature that the emission from all levels is fluorescent.

been corrected for by the weighted mean of the ortho to para ratio (Table 4.2) and by the mean ortho to para ratio of the Black & van Dishoeck model (O/P (BvD) = 1.73) which was measured from the first 3 vibrational levels. In Figure 4.9a, the M17 Northern bar emission from levels higher than v=1 is fluorescent, following a horizontal line distribution. However, the ratios from v=1 seem to be slightly higher implying that the emission is partially thermalised (cf. with model G4N5 in Figure 4.8b). This is consistent with the diagnostic v=1-0 S(1) to 2-1 S(1) line ratio which is measured to be approximately 3 over the observed region (see Chapter 3 and Chrysostomou *et al.* 1992b). This ratio implies that the emission from the northern bar of M17 is not purely fluorescent and the lowest vibrationally excited level must be experiencing slight thermalisation. In Figure 4.9b, the emission from Hubble 12 seems to be purely fluorescent. The distribution of points from the lower levels is a horizontal line, consistent with what is expected from a purely fluorescent source (cf. with model G4N4 in Figure 4.8b and all models in Figure 4.8a). This is consistent also with the diagnostic line ratio from Hubble 12, the v=1-0 S(1) to 2-1 S(1) ratio being 2.3 ± 0.1 indicating fluorescence (Ramsay *et al.* 1992b).

4.2.5 H_2 REFORMATION SPECTRUM

As has become apparent from various sections of this thesis, there is no agreement as to how the hydrogen molecule is formed on the surface of the grain. Especially common is the question, in which excited states, if any, does the molecule preferentially form? If molecules are formed in excited states, then the intensity which would be measured at the telescope would have a component originating from the fluorescent cascade of the molecule after absorbing an ultraviolet photon, I^{uv}, and also a component originating from the fluorescent cascade of a molecule formed in some excited level, I^{ref}. Both components will be collisionally quenched by a factor $(1 + n/n_c)$, such that the observed intensity will be,

$$I^{obs} = \frac{I^{uv} + I^{ref}}{\left(1 + \frac{n}{n_c}\right)} \qquad [4.28]$$

where n_c = critical density.

The contribution to the total intensity from reformation will be small since typically, in chemical equilibrium, only one reformation occurs every nine ultraviolet photons that are absorbed. Therefore, the contribution from the fluorescent cascade must be removed to isolate the reformation spectrum. The PDR model of BHT does not consider the contribution to the cascade from reforming molecules, such that

$$I^{BHT} = \frac{I^{uv}}{\left(1 + \frac{n}{n_c}\right)} \qquad [4.29]$$

(where the factor for multiple pumping of the excited levels has been omitted - see equation [1.17]). In principle therefore, information on the reformation spectrum should be obtainable if the pure fluorescent cascade is known. At first sight, there seems to be a problem in that the critical densities are not well defined, due to unknown collision cross sections, and so will introduce uncertainties into the analysis. This is where choice of object becomes important. One needs to choose an object which has a low density. This then minimises the effect of thermalisation of the levels. For instance, an object like M17 whose emission appears to be partially thermalised will introduce difficulties since n/n_c is greater than 1 for the first level. However, the higher levels all seem to originate from a fluorescent cascade untroubled by thermalisation, ie. $n/n_c \sim 0$. Therefore, in principle at least, there should be no trouble isolating the fluorescent fraction due to reformation of H_2. Knowledge of the pure fluorescent cascade from ultraviolet absorption is well defined from a theoretical standpoint, the cascade only depending on calculated Einstein A coefficients. Therefore, this spectrum can be divided into the measured spectrum from the source and any deviations from the pure cascade can be looked for. Quantitatively, dividing equation [4.28] by the pure cascade gives,

$$\frac{I^{obs}}{I^{uv}} = 1 + \left(\frac{I^{ref}}{I^{uv}}\right) \qquad [4.30]$$

The reformation spectrum will therefore become apparent as excesses in such a ratio, the amount of excess defined by the factor in parentheses. Wagenblast (1992) has recently studied the level distribution in the vibrational ground state of highly rotationally excited (J = 5,6,7) H_2 molecules in diffuse clouds. He has concluded that these molecules can only be present in these clouds if they are initially formed in high rotational and vibrational levels. He further suggests that the fingerprints of such a formation mechanism may be observable in PDRs as excesses in highly vibrationally and rotationally excited levels, excesses which cannot be accounted for by ultraviolet or collisional excitation.

Unfortunately, there is not enough information in the data from M17 to make any such excesses obvious (Figure 4.9a). Hubble 12 is in the same situation, suffering from a lack of information, however it does appear to be a very promising candidate since

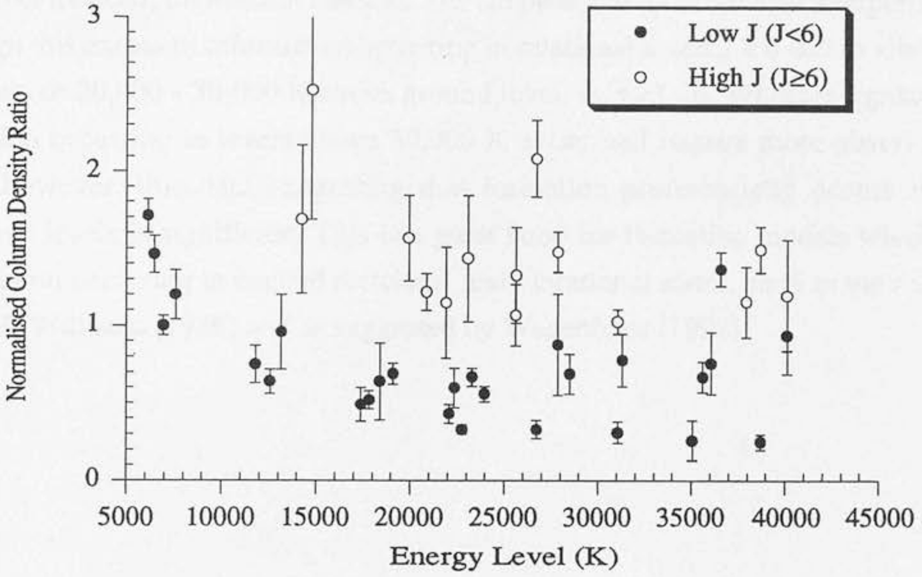

FIGURE 4.10 : Column densities from NGC 2023 (corrected for by mean ortho to para ratio) divided by Black & van Dishoeck model #14. The columns have been normalised such that level from v=1 and J=3 is equal to unity. The emission from the lower levels appears thermalised. Points from levels above J=6 have been plotted as open circles, and their distribution clearly shows an excess in their emission above the normal fluorescent cascade, defined by the filled circles (originating from levels below J=6).

observational evidence shows that this object is a very pure source of fluorescent emission (Ramsay *et al.* 1992b; Dinerstein *et al.* 1988). Further data from higher levels in the J and H windows is awaited from both of these objects. However, the data set for NGC 2023 is more complete, consisting of some 40 measurements taken between 0.8 - 2.5 μm (Burton *et al.* 1992b; Burton *et al. in preparation*) Similar to the data in Figures 4.9 (a-b), the data for NGC 2023 (Figure 4.3b) has been divided by column densities calculated from the Black & van Dishoeck model number 14, and the results are plotted in Figure 4.10. The ratios have been normalised such that the ratio measured at level v=1, J=3 (E = 6952 K) equals unity. The data has been plotted in such a way as to highlight the data points originating from rotational levels higher than or equal to J=6 (open circles). Data points lower than this level are plotted as filled circles. There are three things to notice from this plot. Firstly points from energy levels higher than ~ 10,000 K and from low rotational states (J < 6) define a plateau which is recognisable as a signature for fluorescent emission. Secondly, points from energy levels below ~ 10,000 K (all four points are from vibrational level v=1) lie above this plateau indicating that these levels are thermalised by collisions in a dense ($n > n_c$) warm gas. Thirdly, and the most striking, all the points which originate from above or equal to rotational level J=6 also lie above the plateau signifying an excess of emission above the pure, ultraviolet induced, fluorescent cascade. The simplest and most obvious interpretation is to assign this excess to reformation occurring in rotational levels $J \geq 6$ and in vibrational levels about 20,000 - 30,000 K above ground level, ie. v=3 - 6. Whether signatures of formation occurring in levels above 30,000 K exists will require more observational input, however, this data suggesting that formation preferentially occurs in high rotational levels is significant. This is a great boon for formation models which have reformation occurring in excited rotational and vibrational states, such as the model of Duley & Williams (1986) and as suggested by Wagenblast (1992).

5 Conclusions and Future Prospects

5.1 CONCLUSIONS

The work presented in this thesis has concentrated on the observation and physical interpretation of molecular hydrogen emission from photodissociation regions (PDRs). The motivation for this work stems largely from two aspects. There have been many theoretical advances in the study of PDRs for over 20 years from the 1960's through to the late 1980's (eg. Field *et al.* 1966; Stecher & Williams 1967; Black & Dalgarno 1976; Shull 1978; Tielens & Hollenbach 1985a; Black & van Dishoeck 1987; Sternberg & Dalgarno 1989; Burton, Hollenbach & Tielens 1990). Each theoretical advance has been able to predict certain aspects of the emission from these regions and how they relate to the physical conditions or structure of the PDR. However, these predictions have largely gone by untested by observational evidence. This is especially true in the near infrared region of the spectrum where emission from molecular hydrogen is prevalent. Although the emission from molecular hydrogen constitutes only a very small percentage (~ 0.1 %) of the total line emission, and is thereby weak, it has the advantage that its emission is optically thin (due to the slow rate of radiative decay), therefore making it an excellent probe of the physical conditions in PDRs and, moreover, an excellent tool with which to test the models. With the advent of a new generation of infrared detectors, it is now possible to make these observations, in both imaging and spectral modes, which will test the predictive power of these models.

An analytical model was developed to demonstrate that the structure of a photodissociation region can be described as a function of the density and of the incident ultraviolet radiation field. When the ratio of these parameters, (n/G_0), is high (~ 100 cm^{-3}) then self shielding of the ultraviolet radiation by H_2 molecules dominates the attenuation of the radiation. This has the effect of bringing the HI/H_2 transition zone closer to the edge of the PDR ($A_v < 1$). When the ratio of (n/G_0) is to the order of unity then it is the shielding by dust which dominates the attenuation of the ultraviolet radiation. The ultraviolet photons become attenuated at an optical depth of 1 and the HI/H_2 transition occurs deeper in the cloud, at a depth of $A_v \sim 2 - 3$.

Also affected are the heating and cooling agents in the PDR. The cooling is mostly dominated by the fine structure transition of [OI] 63 μm, however for high densities ($n \sim 10^7$ cm^{-3}) cooling by gas-grain collisions dominates and at low densities ($n \leq 10^3$ cm^{-3}) cooling by the fine structure transition of [CII] 158 μm is dominant. Over most of the parameter space the heating rate by the photoelectric effect dominates. In dense conditions ($n \sim 10^7$ cm^{-3}), when H_2 self shielding is significant in attenuating the ultraviolet flux, heating by the collisional deexcitation of H_2 in excited rotation - vibration states dominates and is able to heat the gas to temperatures of ~ 3000 K. Consequently, the temperature profile of the gas through the PDR is also subject to the parameter ratio (n/G_0). When it is high and self shielding is dominant, the charge on the grains is small, making them efficient heating agents via the photoelectric effect. The temperature profile begins at some level and then drops away as ultraviolet photons become extinguished into the PDR (Figure 2.5a). When (n/G_0) is small and dust shielding is dominant, the charge on grains is high making them an inefficient source of heating (even still, the photoelectric effect is the major source of heating). Deeper into the cloud when the ultraviolet radiation is depleted, recombination decreases the grain charge which increases the heating efficiency and hence there is an increase in the temperature (Figure 2.5b).

Images of the southwestern bar of M17, which were presented in Chapter 2, taken with a 1 % circular variable filter, demonstrated the need of a Fabry-Perot etalon to isolate the H_2 line emission above the continuum. The Fabry-Perot was utilised for the observations in the northern bar. Brackett γ recombination and H_2 v=1-0 S(1) radiation were observed as well as the 3.28 μm emission feature (observed through the 1 % filter). The observations showed that the ionised gas is spatially separate from the molecular gas. There exists a spatial coincidence between the Br γ emission and 21 cm radio continuum emission regions, measured in the region by Felli *et al.* (1984), and there is also a coincidence between the H_2 and 3.28 μm emission regions which is accurate to ~ 1 arcsec. In accordance to previous observations (Burton *et al.* 1988) and theoretical work (eg. Duley & Williams 1990; Duley, Williams & Moorhouse 1991) the 3.28 μm emission feature is used as a tracer of the edge of the PDR, ie. the HII/HI transition zone. The coincidence between the H_2 and 3.28 μm emission regions, also seen in other sources (Burton *et al.* 1988; Moorhouse *et al. in preparation*), can be readily explained if we believe that the sources are clumpy. The spatial coincidence places limits on the density of the clumps. The separation that exists between the 3.28 μm and H_2 emission regions is typically to the order of 1 A_v, requiring that a lower limit on the density be ~ 10^5 cm^{-3} since for densities lower than this a separation of 1 A_v would be resolvable. The ultraviolet radiation field in M17 at the interface of the HII region - molecular cloud is $G_0 \sim 10^4$ times the ambient value, and so it is not clear whether shielding by dust or H_2 molecules is dominating the attenuation of ultraviolet photons.

Spatial coincidence of the 3.28 μm and H_2 emission regions is also observed in the reflection nebula NGC 2023 (Burton *et al.* 1988). In this case, self shielding by H_2 is probably dominating the ultraviolet attenuation requiring densities of the order ~ 10^6 cm^{-3} to be present. Evidence for high density condensations present in the PDR in Orion's Bar is provided by far infrared and millimetre studies (Parmar *et al.* 1991; Graf *et al.* 1990). However, no coincidence is observed between the 3.28 μm and H_2 regions in the small region covered (Figure 2.12a). On the contrary, there is a separation which is compatible with an optical depth of $A_v \sim 3$ if the gas density were 10^5 cm^{-3}, as was suggested by Tielens & Hollenbach (1985b). There also seem to be other inconsistencies in the emission structure. The H_2 peaks behind a minimum of 3.28 μm emission, while the 3.28 μm emission peaks ahead of a minimum in the H_2 emission. An explanation may be as simple as variable foreground extinction across the Bar, but the real reason may not surface until more extensive observations are carried out in the region.

A single component (ie. uniform), high density (n ~ 10^5 cm^{-3}) PDR model is sufficient to reproduce the H_2 line intensity observed in the northern bar of M17, if it is also assumed that the density gradient is inclined at 70° to our line of sight (following Icke *et al.* 1980). However, our images reveal structure on a scale of 2 arcsec suggesting that a two component (ie. clumpy) PDR model is the preferred solution. Although morphologically the ionised and molecular gas are spatially separated it is not clear from this data set whether we are observing the surface of the molecular cloud or whether we are looking at the region in cross section, ie. edge on.

Long slit spectroscopy measurements were taken with CGS4 to follow up on the imaging data. The advantages of using long slit spectrometers with 2D arrays are two-fold (this method of spectroscopy has long been in use in the optical), especially for extended objects. Firstly, one can obtain spectral information on an object as a function of position from a single integration, and secondly, all the exposed rows can be coadded to increase signal-to-noise.

The measurements taken in the northern bar of M17 were in the K band where up to 16 H_2 lines were identified. From this data, populations of the energy levels were calculated revealing that they can only be explained if the H_2 is being excited by the absorption of ultraviolet photons, ruling out shock excitation. Confirmation of this is provided by the disparity in the vibrational and rotational excitation temperatures, the vibrational excitation temperature being nearly 5 times greater than the rotational excitation temperature. The diagnostic line ratio of the H_2 v=1-0 S(1) and 2-1 S(1) transitions is an indicator of how pure the fluorescent radiation is. Values of this ratio which are larger than 2 indicate that thermalisation of the lower levels is occurring. The value of this ratio along the extent of the H_2 emission in the northern bar of M17 is approximately 3 implying slight thermalisation of the lower levels. The constancy of this ratio implies that the collisional deexcitation rate must be constant along this region. This may be taken to mean that the physical conditions do not change along the region observed and we are therefore observing the surface of the PDR. The absolute level of the H_2 emission is seen to sharply rise to a peak, peaking behind the ionised material (in agreement with the imaging data) represented by the Br γ line, and then falls off towards the molecular cloud. This sharp rise and then gradual fall off can be modelled by assuming that we are viewing a portion of a corrugated or clumpy PDR whose large scale surface geometry can be described by a simple parabola. This is consistent with a blister HII region model which the M17 region is supposed to be a typical example of (Icke *et al.* 1980). It is not possible to model the small scale geometry with this simplistic model.

The small scale structure however, can be described by estimating the degree of clumping in the beam. The two component model is used to model the line ratios (since ratios cancel out the uncertainties introduced by the unknown small scale geometry) from the PDR and the results suggest that 76 % of the beam area is filled by gas at 10^5 cm^{-3} and 16 % by gas at 10^6 cm^{-3}. This is in good agreement with the lower limit on the density established by the spatial coincidence of the H_2 and 3.28 μm emission regions.

Arguably the most interesting result from this data set is that the ortho to para ratio is measured to be less than the expected value for a gas in local thermodynamic equilibrium (ie. 3). This is also the case for other PDRs where this quantity has been measured, eg. NGC 2023 (Hasegawa *et al.* 1987; Burton *et al. in preparation*) and Hubble 12 (Ramsay *et al.* 1992b). The ratio in these objects is measured to lie within the range of 1.3 - 2.3.

Modelling of the value of the ortho to para ratio, using the output from the analytical PDR model and relevant approximations to the spin exchange reaction rates, shows that it is not possible to match the observed ratios with the model. The model predicts that the dominant mechanism which determines the value of the ortho to para ratio is the formation of the molecule. This is because the timescale for a H_2 molecule in the gas to be excited by an ultraviolet photon is much shorter than the timescale for spin exchange reactions with the gas to occur. Therefore, one would observe an ortho to para ratio in the fluorescent cascade which is the value set at formation. Two formation mechanisms are considered : one which produces "hot" molecules with an ortho to para ratio of 3, and one which produces molecules with an ortho to para ratio which is defined by the grain temperature. Both of these formation mechanisms do not satisfy the observations.

Inevitably one infers that there must be some other form of processing of the ortho to para ratio, and three possible models are put forward. The first allows the residence time of the newly formed molecule on the grain surface, before it evaporates into the gas, to be a variable in the formation model. If the residence time is long then molecules can dissipate their binding energy through various energy loss channels on the grain (Tielens & Allamandola 1987). The molecules equilibrate to the grain temperature and are formed with an ortho to para ratio characteristic of the grain temperature. If the residence time is very short then the molecules are not able to lose energy to the grain lattice or to surface impurities and they are formed with a "hot" ortho to para ratio (ie. 3). In between these limits there is a continuum of ortho to para ratios with which molecules could be formed, and thereby explain the observed ratios. To match the observed ratios the required residence time will have to be such that t/t_{eq} (see equation [4.23] for definition) is about unity.

The second model introduces the concept of a dynamic PDR model. Here, the hot gas at the surface of the PDR is allowed to escape, thereby setting up a photodissociation front which advances into the molecular cloud. One can imagine a situation therefore, where the speed at which fresh material is sweeped into the front is fast enough such that spin exchange reactions with the gas do not have enough time to alter the ortho to para ratio of the fresh material before it is excited by the ultraviolet radiation. The subsequent fluorescent cascade from these molecules will therefore yield ortho to para ratios which would be characteristic of the cooler gas ahead of the photodissociation front. Note that it is not necessary for the hot gas to be escaping so fast that the chemical equilibrium between the formation and destruction of H_2 is destroyed.

The third model stems from calculations by Blais & Truhlar (1981) which show that the collision cross sections for spin exchange of H_2 with H increase at a rate greater than the fourth power of the energy level. Typically, the spin exchange rate (per second) is 100 times greater for a molecule in v=6 than in the ground state. This implies that molecules are still vulnerable to spin changing interactions after they have been radiatively excited and are in the fluorescent cascade. However, running the model again accounting for the Blais & Truhlar data does not reproduce the observed values. The spin exchange rate is so fast compared to the radiative decay rate that the ortho to para ratio attained (~ 2.9) is characteristic of the gas temperature (~ 200 - 300 K). The failure of this particular model may be attributable to either the simplistic modelling technique or to the results of Blais & Truhlar being false. A more rigorous model is proposed for the near future to check this out.

It is demonstrated that the ortho to para ratio is an important quantity which may prove to be one of the most effective ways of probing the physics of photodissociation regions. It is of obvious significance in helping to understand the formation of the H_2 molecule, and also the dynamic motions of PDRs, as discussed above. It is also important if one wishes to interpret line ratios correctly. Ratioing the observed column densities with those from a cold, low density (ie. pure fluorescent) model reveals that the emission from M17 is subject to slight thermalisation while for Hubble 12 the emission is purely fluorescent. This technique was also employed on the data set for NGC 2023, which has some 40 points between energy levels 5,000 - 40, 000 K, revealing an excess of emission above the expected pure fluorescent cascade (Figure 4.10). This excess occurs in levels which are highly rotationally excited ($J \geq 6$) in vibrational levels about 20,000 - 30,000 K ($v = 3 - 6$) above the ground level. It has been predicted (Wagenblast 1992) that the signature of H_2 formation occurring in excited rotational and vibrational states would be seen from PDRs as excesses in these levels. This is the first direct evidence of the formation of H_2 occurring in these levels and will consequently have repercussions on future H_2 formation models.

5.2 FUTURE PROSPECTS

It is expected that many advances will be made in this field of study in the near future, from both theoretical and observational directions. A project is already underway to study the dynamics (and hence evolution) of photodissociation regions. To date, all PDR models have invoked the constriction on the PDR that the gas remains static. However, it is hard to imagine that the hot gas on the surface of a clump, for instance, will remain in pressure equilibrium with the cooler interclump medium. There will be a general flow away from the clump which will affect the structure, evolution and lifetime of the PDR. It is conceivable, though, that the flow may choke itself in a short time or that the flow is so slow that to all intents and purposes the dynamic PDR is identical to a static one. Obviously, the parameter space will have to be studied carefully for these situations. We will soon be able to search for such flows when the upgrade of the cooled grating spectrometer, CGS4, with a 256x256 pixel array occurs (scheduled for

Spring 1994). In the appropriate configuration (ie. long camera (300 mm) plus echelle grating) it will attain the necessary velocity resolution (~ few km s^{-1}) to make such a search feasible. Target lines will have to be bright PDR lines which are believed to originate from the surface of the PDR, eg. CI 9850 Å.

An interesting prospect is whether the dynamic model will be able to explain the low values of ortho to para ratios that are measured in PDRs. The ortho to para ratio will also come under close scrutiny from another angle, by incorporating the Burton, Hollenbach & Tielens (1990) model with the data from Blais & Truhlar (1981) to see how the ortho to para ratio is affected if one allows spin exchange reactions to occur during the fluorescent cascade.

In tandem with the theoretical work, an observational program has just commenced which, over the next two years, will allow us to collect a large amount of H_2 spectroscopic data at high resolution (R > 1000) from various PDR sources. Complete coverage between 1.0 - 2.5 μm will be obtained from these sources from which we will be able to detect lines from levels as high as ~ 40,000K. With this coverage we would hope to detect over 50 - 100 transitions from each of our objects. Measuring the emission spectrum from a variety of objects will allow us to investigate how it behaves as a function of the excitation conditions, ie. density, ultraviolet field, temperature. A full cascade model, minus any contribution from a reformation cascade, will have to be developed to analyse the data properly. Only now are we in a position from which we can seriously test the PDR models.

These data will also allow us to calculate ortho to para ratios for these objects and to continue to empirically investigate the processes which affect it, ie. formation, dynamics. Data from a series of vibrational levels will allow us to deduce whether there is any variation of the ortho to para ratio with energy level - lending evidence either for or against the Blais & Truhlar data.

Another promising project which will be attempted is a search for emission from vibrationally excited CO in PDRs. The emission has already been detected in shock excited regions (Geballe & Garden 1987, 1990) and if detected in PDRs, will provide a new and powerful tool to explore previously inaccessible parts of the PDR ($A_v \sim 3 - 5$) with the spatial resolution afforded by the CGS4 spectrometer. At these depths the gas is cold enough (T ~ 50 K) that the critical density for deexciting the v=1 level is ~ 10^{15} cm^{-3} (Hollenbach & McKee 1979). So for even the densest PDRs the fluorescent emission spectrum from CO will be a pure one, not plagued by collisional interactions and sensitive only to the ultraviolet flux and CO density, making it a great prospect as a probe of physical conditions. Furthermore, coupled with H_2, 3.28 μm and H^+ recombination observations, it will be an excellent channel with which to further investigations of the structure of PDRs.

The data set for NGC 2023 presented in this thesis includes data which were taken in the I band region of the spectrum, from 7600 - 8600 Å (Burton *et al.* 1992b). These were the first detections of H_2 lines in this spectral region and provided us with enough information to extract the first direct evidence of H_2 formation preferentially occurring in highly excited levels. Further observations in the I band will be carried out in conjunction with our near infrared PDR program. With these two data sets and the work going into the dynamics of photodissociation regions, we will shortly be armed with enough observational evidence and theoretical background to take very positive steps forward in this particular field of study.

6 References

Allison A.C, & Dalgarno A, 1970, *Atomic Data* **1**, 289

Beetz M, Elsässer H, Poulakos C, Weinberger R, 1976, *Atron. & Astr.* **50**, 41

Black J.H, & Dalgarno A, 1976, *Astrophys. J.* **203**, 132

Black J.H, & van Dishoeck E.F, 1987, *Astrophys. J.* **322**, 412

Blais N.C, & Truhlar D.G, 1981, *"Potential Energy Surfaces and Dynamics Calculations"* p.431, ed. Truhlar D.G, (New York : Plenum)

Brand P.W.J.L, Moorhouse A, Burton M.G, Geballe T.R, Bird M, Wade R, 1988, *Astrophys. J.* **334**, L103

Bregman J.D, Allamandola L.J, Tielens A.G.G.M, Geballe T.R, Witteborn F.C, 1989, *Astrophys. J.* **344**, 791

Burke J.R, & Hollenbach D.J, 1983, *Astrophys. J.* **265**, 223

Burton M.G, 1992, *Australian Journal of Physics (submitted)*

Burton M.G, Moorhouse A, Brand P.W.J.L, Roche P.F, Geballe T.R, 1988, *Proc. "Interstellar Dust : Contributed Papers"* NASA CP 3036, p. 87 eds. Tielens A.G.G.M, & Allamandola L.J

Burton M.G, Hollenbach D.J & Tielens A.G.G.M, 1990, *Astrophys. J.* **365**, 620, (BHT)

Burton M.G, Hollenbach D.J, & Tielens A.G.G.M, 1992a, *Astrophys. J.* (submitted)

Burton M.G, Bulmer M, Moorhouse A, Geballe T.R, Brand P.W.J.L, 1992b, *Mon. Not. R. ast. Soc.* **257**, 1P

Cardelli J.A, Clayton G.C, Mathis J.S, 1989, *Astrophys. J.* **345**, 245

Chrysostomou A, Brand P.W.J.L, Burton M.G, Moorhouse A, 1992a, *Mon. Not. R. ast. Soc.* **256**, 528

Chrysostomou A, Brand P.W.J.L, Burton M.G, 1992b, *Proc. "Asronomical Infrared Spectroscopy"* Calgary

Crawford M.K, Genzel R, Townes C.H, Watson D.M, 1985, *Astrophys. J.* **291**, 755

de Jong T, 1977, *Atsron. & Astr.* **55**, 137

de Jong T, 1980, *Highlights Astr.* **5**, 301

Dalgarno A, 1973, *"Atomic Physics & Astrophysics"* vol. 2, p. 286, eds. Chretien M, & Lipworth E, (Gordon & Breach)

Dalgarno A, & Stephens T.L, 1970, *Astrophys. J.* **160**, L107

Dalgarno A, Black J.H, Weisheit J.C, 1973, *Astrophysical Letters* **14**, 77

Dinerstein H.L, Lester D.F, Carr J.S, Harvey P.M, 1988, *Astrophys. J.* **327**, L27

Draine B.T, 1978, *Astrophys. J. Suppl.* **36**, 595

Draine B.T, 1989, *Proc. 22nd Eslab Symposium on "Infrared Spectroscopy in Astronomy"* ESA SP-290, p.93

Duley W.W, 1985, *Mon. Not. R. ast. Soc.* **215**, 259

Duley W.W, & Williams D.A, 1986, *Mon. Not. R. ast. Soc.* **223**, 177

Duley W.W, & Williams D.A, 1988, *Mon. Not. R. ast. Soc.* **231**, 969

Duley W.W, & Williams D.A, 1990, *Mon. Not. R. ast. Soc.* **247**, 647

Duley W.W, Williams D.A, & Moorhouse A, 1991, *Mon. Not. R. astr Soc.* **253**, 505

Felli M, Churchwell E, Massi M, 1984, *Astron. & Astr.* **136**, 53

Field G.B, Somerville W.B, Dressler K, 1966, *Ann. Rev. Astron. Astr.* **4**, 207

Flower D.R, & Watt G.D, 1984, *Mon. Not. R. ast. Soc.* **209**, 25

Gatley I, Becklin E.E, Sellgren K, & Werner M.W, 1979, *Astrophys. J.* **233**, 575

Gatley I, & Kaifu N, 1987, *Proc. "Astrochemistry" IAU Symp 120,* p. 153 eds. Vardya M.S, & Tarafdar S.P

Gatley I, Hasegawa T, Suzuki H, Garden R, Brand P, Lightfoot J, Glencross W, Okuda H, Nagata T, 1987, *Astrophys. J.* **318**, L73

Geballe T.R, & Garden R.P, 1987, *Astrophys. J.* **317**, L107

Geballe T.R, & Garden R.P, 1990, *Astrophys. J.* **365**, 602

Geballe T.R, Tielens A.G.G.M, Allamandola L.J, Moorhouse A, Brand P.W.J.L, 1989, *Astrophys. J.* **341**, 278

Genzel R, Harris A.I, Stutzki J, 1989, *Proc. 22nd Eslab Symposium on "Infrared Spectrocopy in Astronomy"*, ESA SP-290, p. 115

Gould & Harwitt 1963, *Astrophys. J.* **137**, 694

Graf U.U, Genzel R, Harris A.I, Hills R.E, Russell A.P.G, Stutzki J, 1990, *Astrophys. J.* **358**, L49

Habing H.J, 1968, *Bull. Astr. Inst. Netherlands* **19**, 421

Harper D.A, Low F.J, Rieke G.H, Thronson H.A, 1976, *Astrophys. J.* **205**, 136

Harris A.I, Stutzki J, Genzel R, Lugten J, Stacey G, Jaffe D, 1987, *Astrophys. J.* **322**, L49

Hasegawa T, Gatley I, Garden R, Brand P, Ohishi M, Hayashi M Kaifu N, 1987, *Astrophys. J.* **318**, L77

Hayashi M, Hasegawa T, Gatley I, Garden R, Kaifu N, 1985, *Mon. Not. R. ast. Soc.* **215**, 31P

Herzberg G, 1950, *"Molecular Spectra and Molecular Structure"*, D. Van Nostrand Company, Inc.

Hippelein H, & Münch G, 1978, *Astron. & Astr.* **68**, 17

Hollenbach D.J, 1989, *Proc. "Interstellar Dust" IAU Symp. 135*, p. 227, eds. Allamandola L.J, & Tielens A.G.G.M

Hollenbach D.J, & McKee C.F, 1979, *Astrophys. J. Suppl.* **41**, 555

Hollenbach D.J, Takahashi T, & Tielens A.G.G.M, 1991, *Astrophys. J.* **377**, 192

Hummer D.G, & Storey P.J, 1987, *Mon. Not. R. ast. Soc.* **224**, 801

Icke V, Gatley I, & Israel F.P, 1980, *Astrophys. J.* **236**, 808

Lada C.J, DePoy D.L, Merrill K.M, & Gatley I, 1991, *Astrophys. J.* **374**, 533

Leger A, Puget J.L, 1984, *Astron. & Astr.* **137**, L5

Leonas V.B, & Pjampuu A.A, 1981, *Soviet Astr. Letters* **7**, 19

Meadows P, 1986, *MPhil Thesis*, University of Edinburgh

Outred M, 1978, *J. Phys. Chem. Ref. Data* **7**, 81

Pankonin V, Thomasson P, Barshuun J, 1977, *Astron. & Astr.* **54**, 335

Parmar P.S, Lacy J.H, Achtermann J.M, 1991, *Astrophys. J.* **372**, L25

Press W.H, Flannery B.P, Teukolsky S.A, Vetterling W.T, 1986, *"Numerical Recipes"* Cambridge University Press

Puxley P.J, Beard S.M, & Ramsay S.K, 1992, *Proc. "Fourth Data Analysis Workshop"* ESO/STECF, ed. Grosbol P.

Ramsay S.K, Mountain C.M, Geballe T.R, 1992a, *Mon. Not. R. ast. Soc.* (in press)

Ramsay S.K, Chrysostomou A, Geballe T.R, Brand P.W.J.L, Mountain C.M, 1992b, *Mon. Not. R. ast. Soc.* (submitted)

Rieke G.H, & Lebofsky M.J, 1985, *Astrophys. J.* **288**, 618

Russell R, Melnick G, Gull G, Harwitt M, 1980, *Astrophys. J.* **240**, L99

Russell R, Melnick G, Smyers S, Kurtz N, Gosnell T, Harwitt M, Werner M, 1981, *Astrophys. J.* **250**, L35

Sellgren K, Tokunaga A.T, Nakada Y, 1990, *Astrophys. J.* **349**, 120

Shortridge K, 1991, *"FIGARO - General Data Reduction and Analysis"*

Shull J.M, 1978, *Astrophys. J.* **219**, 877

Shull J.M & Hollenbach D.J, 1978, *Astrophys. J.* **220**, 525

Shull J.M, & Beckwith S, 1982, *Ann. Rev. Astron. Astr.* **20**, 163

Stecher T.P, & Williams D. A, 1967, *Astrophys. J.* **149**, L29

Sternberg A, 1988, *Astrophys. J.* **332**, 400

Sternberg A, & Dalgarno A, 1989, *Astrophys. J.* **388**, 197, (SD)

Stutzki J, Stacey G.J, Genzel R, Harris A.I, Jaffe D.T, Lugten J.B, 1988, *Astrophys. J.* **332**, 379

Stutzki J, & Güsten R, 1990, *Astrophys. J.* **356**, 513

Takayanagi K, Sakimoto K, Onda K, 1987, *Astrophys. J.* **318**, L81

Tanaka M, Hasegawa T, Hayashi S.S, Brand P.W.J.L, Gatley I, 1989, *Astrophys. J.* **336**, 207

Tanaka M, Hasegawa T, Gatley I, 1991, *Astrophys. J.* **374**, 516

Tielens A.G.G.M, & Hollenbach D.J, 1985a, *Astrophys. J.* **291**, 722, (TH)

Tielens A.G.G.M, & Hollenbach D.J, 1985b, *Astrophys. J.* **291**, 747

Tielens A.G.G.M, & Allamandola L.J, 1987, *Proc. "Interstellar Processes"* eds. Hollenbach D.J & Thronson H.A

van Dishoeck E.F, & Black J.H, 1988, *Astrophys. J.* **334**, 771

Wagenblast R, 1992, *Mon. Not. R. ast. Soc.* **259**, 155

Webster A.S, 1991, *Nature* **352**, 412

Webster A.S, 1992, *Mon. Not. R. ast. Soc.* **257**, 463

Whittet D.C.B, 1988, *Proc. "Dust in the Universe"* p. 25, eds. Bailey M.E, & Williams D.A

Mon. Not. R. astr. Soc. (1992) **256**, 528–534

The structure of photodissociation regions: M17 northern bar

Antonio Chrysostomou,[1] Peter W. J. L. Brand,[1] Michael G. Burton[2] and Alan Moorhouse[3]★

[1] *Department of Astronomy, University of Edinburgh, Blackford Hill, Edinburgh EH9 3HJ*
[2] *Anglo-Australian Observatory, Epping Laboratory, PO Box 296, Epping, NSW 2121, Australia*
[3] *Department of Mathematics, UMIST, PO Box 88, Manchester M60 1QD*

Accepted 1992 January 3. Received 1991 December 30; in original form 1991 October 17

SUMMARY

We present images of part of the photodissociation region and ionization front in the northern bar of M17, in the infrared lines of H_2, H^+ and the 3.28-μm emission feature, a tracer of the edge of the molecular cloud.

Spatial coincidence between the 3.28-μm and H_2 emission regions is established to within 1 arcsec, which implies a gas density of $n > 10^5$ cm^{-3}. The peak observed surface brightness in the H_2 $v = 1-0$ $S(1)$ line is 1.5×10^{-7} W m^{-2} sr^{-1} and if we assume a 70° inclination to the line of sight, this intensity implies a density of 10^5 cm^{-3}, from modelling of one-dimensional, uniform-density photodissociation regions. However, our images reveal clumpy structure down to a scale of 2 arcsec, which means that a clumpy two-component PDR model, one component of high density and the other component at lower density, would be the preferred solution. The value of the density determines whether the attenuation of FUV photons is dominated by dust shielding or line shielding. The possible geometry of the region is also discussed.

Key words: interstellar medium: clouds – interstellar medium: individual objects: M17 – infrared: interstellar: lines – infrared: interstellar: continuum.

1 INTRODUCTION

A photodissociation region (PDR) is the surface ($A_v \leq 10$) of a molecular cloud irradiated by an ultraviolet flux. The ultraviolet radiation regulates the chemical networks and determines the heating (via the photoelectric effect on grains), while the cooling is dominated by fine-structure transitions (e.g. [O I] 63 μm, [C II] 157 μm). The standard PDR models of Tielens & Hollenbach (1985a) and Black & van Dishoeck (1987) are parametrized by the density and by G_0, the incident UV flux in units of the local interstellar radiation field (1.6×10^{-3} erg s^{-1} cm^{-2} in the 6–13.6 eV band; Habing 1968). In these models the photodissociation of H_2 is balanced by the re-formation on dust grains. At the surface of the molecular cloud, the UV flux – which electronically excites H_2 into the Lyman ($B^1\Sigma_u$) and Werner ($C^1\Pi_u$) bands before decaying to excited rovibrational levels in the ground state – is so great that the H_2 molecules are quickly destroyed. Deeper into the cloud ($A_v \sim 1$–3 mag), the flux is sufficiently attenuated by dust that the molecular abundance increases and H_2 self-shielding becomes the principal process in the attenuation of Lyman- and Werner-band photons.

Burton, Hollenbach & Tielens (1990; hereafter BHT) and Sternberg & Dalgarno (1989; hereafter SD) have modelled PDRs at high densities ($n \geq 10^5$ cm^{-3}). At these densities, collisional redistribution of the low-lying rovibrational levels of H_2 is effective and the spectrum from these levels appears thermalized (Burton, Hollenbach & Tielens 1988a; SD). Increasing the density in the models for the same UV field also affects the structure of a PDR since self-shielding is more effective as the ratio n/G_0 rises. UV attenuation then occurs over a shorter optical depth into the cloud than would result from dust extinction alone. The effect is to move the H I/H_2 transition zone towards the cloud surface where $A_v < 1$ mag, changing the structure of the PDR and increasing the conversion of UV flux to heat via collisional de-excitation of the UV-excited H_2, in addition to photoelectric heating.

M17, the Omega nebula, is an H II region at a distance of 2.2 kpc (Harper *et al.* 1976; Stutzki *et al.* 1988). At this distance 1 arcsec is equivalent to 0.01 pc. M17 has been extensively mapped in the radio continuum (Felli, Churchwell & Massi 1984), in Brγ and H_2 (Meadows 1986; Gatley & Kaifu 1987) and in the infrared continuum (Harper *et al.* 1976; Gatley *et al.* 1979). These maps reveal two obvious regions of emission: a bar which stretches across the north and another which runs south to west. Felli *et al.* (1984) also note that their 21-cm continuum map of the northern bar closely corresponds to the optically visible bar, indicating that the visual extinction in this region is not large. This suggests that

---

★Present address: School of Cosmic Physics, Institute for Advanced Studies, Dublin, Eire.

the associated molecular cloud lies behind the northern bar. The south-western bar, on the other hand, is strongly obscured at visible wavelengths indicating that the south-western molecular cloud forms part of the foreground gas. This view is further supported by *JHK* maps of the M17 region (Lada *et al.* 1991) in which the northern bar is dominated by emission in the *J* band while the south-western bar is dominated by emission in the *K* band – indicating increased extinction towards the south-western bar. Submillimetre and far-IR observations of hot carbon species in the south-western bar (Harris *et al.* 1987; Stutzki *et al.* 1988; Stutzki & Güsten 1990) reveal the presence of warm, dense gas extending deep into the molecular cloud, implying that the south-western bar is a clumped, dense region, the density in the clumps ranging from 10^5 to 10^6 cm^{-3} (Stutzki & Güsten 1990). IR spectroscopy of H_2 has been carried out in the northern bar by Tanaka *et al.* (1989), who determined that the H_2 emission in a 19.6-arcsec beam comes from UV-pumped fluorescence, little affected by thermal reprocessing. From this we infer that the gas is of low density. M17, therefore, appears to contain two differing regions, both being illuminated by the same source ($L \sim 6 \times 10^6$ $L_\odot$ – Harper *et al.* 1976) and forms an excellent laboratory for the study of photodissociation region physics.

2 OBSERVATIONS

Infrared images were obtained of emission from fluorescent molecular hydrogen, ionized hydrogen and the 3.28-μm emission feature, at the interface between the H II region and molecular cloud in the northern ionization bar of the M17 star-forming region. The observations were centred on the peak of H_2 emission (Meadows 1986) at $18^h17^m49\overset{s}{.}3$, $-16°9'59''$ (1950) which is the (0, 0) coordinate in all our images.

All observations were carried out on the nights of 1990 July 11–13 using the 3.8-m United Kingdom Infrared Telescope (UKIRT) on Mauna Kea, Hawaii. The instrument used for the observations was the infrared array camera (IRCAM), which has a 62 × 58 pixel InSb array and a spatial resolution of 0.62 arcsec per pixel. Seeing conditions degraded this resolution to ~1.25 arcsec (FWHM, as measured on standard stars). All observations were taken through narrow-band filters (~1 per cent bandwidth) so as to isolate the particular line of interest. For the 2-μm observations – H_2 $v = 1-0$ $S(1)$ ($\lambda = 2.1218$ μm) and H^+ Brackett γ ($\lambda = 2.1667$ μm) – a tunable Fabry–Perot etalon (FP) was used to increase the equivalent width of the lines. The spectral resolution of the FP was typically 110 km s^{-1} (FWHM), much broader than the expected width of the emission lines from PDRs (a few km s^{-1}).

In the *K* window, maximum on-chip exposures of 300 s (for the fainter H_2 $v = 1-0$ $S(1)$ line) and 60 s (for the brighter Brγ line) were used. In the *L* window, thermal sky emission limited exposures to 1 s, with 150 co-adds made. For each observation, images at a nearby continuum wavelength were also taken. For the 3.28-μm images, the continuum was measured using a filter with a bandpass at 3.1 μm. Through the FP, the continuum was obtained by detuning by 740 km s^{-1}.

Flat-fielding of the images was carried out by median filtering all normalized sky frames for each filter. A second step in the flat-fielding procedure of the on-line frames, which was not applied, would have removed the pixel-to-pixel variations across the chip which arise as a consequence of the phase velocity across the chip (65 km s^{-1} from centre to edge for the 100 km s^{-1} FP) and the line profile. In the off-line frames, this is not a problem since the continuum is flat and the power received at each pixel across the array is assumed constant. These uncorrected variations manifest themselves as edge effects in the H_2 image (see Plate 1).

Standard reduction procedures were carried out to produce the final images. These include: dark current subtraction; removal of bad pixels (originating from faults in the array chip or cosmic ray events) by interpolating between neighbouring pixels, and flat-fielding the frames. The continuum (including the sky level) was then removed from the images taken with the FP by subtracting from each image its corresponding off-line image. The frames were then mosaicked together. For the 3.28-μm images, mosaicking of the frames was not straightforward because the sky emission changes during the night. The sky emission was removed by matching all other frames to one single frame in the mosaic. A constant value was either subtracted or added to the other frames until they all matched the original frame. The median sky value was then obtained from the sky frame closest in time and airmass to this frame. This value was then removed from the whole mosaic, thus removing the sky emission. This, of course, does not remove the continuum emission. Images of the nearby continuum showed that the continuum emission (at $\lambda = 3.1$ μm) is low and no attempt was made to remove it.

Calibration was carried out with images of the standard star HD 161903 ($m_K = 7.02$) observed in each filter. After taking an image, the telescope was slewed 8 arcsec in declination and another image was taken. Dividing the second frame by its median value allows one to use the resultant image as a local flat-field of the first standard star image. The same procedure was carried out on the second standard star image, this time using the first image as its flat-field. An average of the results was used in calibrating data counts to flux.

3 RESULTS

Images of the PDR in the northern bar are shown in Plates 1, 2, 3, 4 and 5. In all these images the source of UV photons, an obscured cluster of maybe 100 OB stars which power the H II region (Beetz *et al.* 1976; Lada *et al.* 1991), is from the south-west (bottom right). Plate 1 shows a mosaic of seven frames in the H_2 $v = 1-0$ $S(1)$ line, a region 80 × 90 $arcsec^2$ in extent. Plate 2 shows the same region in the 3.28-μm feature. The image area is smaller than that of the H_2 image as only four frames were combined together; adverse weather conditions prevented further observations in the *L* band. Plate 3 shows the Brγ emission in the region and finally Plates 4 and 5 show the 3.28-μm image overlaid with contour maps of the H_2 emission and the Brγ emission respectively. It is clear in the former plate that the 3.28-μm and H_2 emission regions show a high degree of spatial coincidence.

The off-line images in all three lines revealed no discernible continuum structure in the region. Three point sources were apparent in all the images and these were used as registration markers, ensuring that the (0, 0) position is the same in all three images.

3.1 The H_2 $v=1-0$ $S(1)$ image

The emission from fluorescing H_2 traces the warm surfaces ($A_v \sim 1$) of molecular clouds which have been irradiated by an ultraviolet flux. The most obvious features in the H_2 image (Plate 1) are the two prominent ridges of emission which run across the image. A possible explanation for this structure lies in the morphology of the cloud surface, such as a wrinkle in which emission is enhanced by limb brightening, or the clumping of dense material within a less dense medium (discussed in Section 4). The peak intensity measured at one pixel is $I_{1-0\,S(1)} \sim 1.5 \times 10^{-7}$ W m^{-2} sr^{-1}.

Edge effects in this mosaic are caused by the angular dependence of the transmission velocity profile of the FP. Difficulties at the telescope meant that it was not possible to align the FP so that the phase centre fell on to the centre of the array, but instead it was at the south-east corner (bottom left) of the array. The phase shift in the north-west corner was therefore larger.

3.2 The 3.28-μm image

The 3.28-μm feature has been assumed to delineate the molecular-cloud/H II-region interface (e.g. Burton *et al.* 1988b; Moorhouse *et al.*, in preparation) and thus to be a tracer of the edge of the molecular cloud. In observations of Orion's Bar (Burton *et al.* 1988b; Sellgren, Tokunaga & Nakada 1990) the 3.28-μm emission peaks ahead of the ionized gas emission and behind the molecular hydrogen emission peak (relative to the source of photons). The fall-off of the 3.28-μm emission also follows the extinction of the radiation which excites it.

The 3.28-μm emission feature derives from the fundamental stretching vibration of a C–H bond on large hydrogenated carbon molecules such as polycyclic aromatic hydrocarbons (PAHs, e.g. Leger & Puget 1984) or rehydrogenated HACs (hydrogenated amorphous carbon, e.g. Duley 1985; Duley & Williams 1988, 1990). The feature has recently been suggested as possibly originating from the excitation of lightly hydrogenated C_{60} molecules (Webster 1991). The conditions which are favourable for rehydrogenation in the HAC model, such as high-temperature gas, high atomic abundance, and a high UV field, are conditions which are found at the edges of the PDR. Within an H II region, the flux of ionizing photons strips hydrogen from large molecules. At the interface with a molecular cloud, the flux of ionizing photons diminishes, but energetic hydrogen atoms can penetrate the HAC lattice and cause bulk rehydrogenation. A high UV field raises the grain temperature and creates localized hotspots on the grain (10–100 hotspots, $T \sim 1000$ K) which is sufficient for the energetic hydrogen atoms to overcome the activation energy for bulk rehydrogenation, leading to 3.28-μm emission. Further into the cloud, the temperature drops, the hydrogen abundance decreases and consequently the 3.28-μm emission falls away. In the PAH model, to produce the 3.28-μm emission the PAHs must be free molecules close to the cloud surface. In the H II region, the ionizing flux and presence of hot electrons will rapidly dehydrogenate and destroy the PAHs. Inside a molecular cloud, away from the surface, the extinction of UV photons reduces the 3.28-μm emission.

The 3.28-μm image (Plate 2) shows the two ridges of emission seen in the H_2 image. There is also an extended knot of emission centred at (15″, −25″), not seen in H_2, and a faint ridge of emission to the west, outside the field of view of the H_2 image. A mean flux density of the 3.28-μm feature (not continuum-subtracted) through the filter is calculated because the band emission is quite broad (Bregman *et al.* 1989; Geballe *et al.* 1989). At the brightest point the flux density is $F_{3.28} \sim 5.2 \times 10^{-5}$ W m^{-2} μm^{-1} sr^{-1}.

3.3 The Br γ image

Brackett γ emission traces the presence of ionized gas. The Br γ emission peaks in an extensive area ~40 arcsec south of (0, 0) where the ionized H II region is located (Plate 3). A ridge of emission runs north-west. We have compared the image to the high-resolution radio continuum measurements made by Felli *et al.* (1984), and find that it coincides with the edge of the ionization front, depicted by the lowest contour of their map. The ridge of emission to the north-west reveals itself as a small (~20 arcsec) clump in their map. The emission measure, at the brightest pixel, is ~1.9 Mpc cm^{-6}. Felli *et al.* (1984) have calculated an average emission measure, across the whole of the northern bar, of 1.90 Mpc cm^{-6}. Using as a size-scale the width of the ionization front (~0.95 pc), we infer an ionized gas density $n_i \sim 10^3$ cm^{-3}, and therefore a density for the neutral cloud of $n \sim 10^5$ cm^{-3}.

There are edge effects contaminating this image, apparent as semicircular distortions at the edges of the individual frames. These result from the frequency of the off-line setting of the FP being inadvertently set to include a telluric emission line, which the phase shift renders visible as a ring in the image.

3.4 Comparison of 3.28-μm image with H_2 and Br γ

The relationship between the 3.28-μm, H^+ and H_2 emission regions is very important in understanding the structure of PDRs. In plane-parallel uniform-density PDR models, the H^+ emission from the H II region peaks before the molecular emission region (Tielens & Hollenbach 1985a). If the geometry of the PDR surface is more complicated, then one would expect to observe a correlated emission structure as the separate emission regions follow the shape of the cloud surface. On the other hand, if the PDR gas is highly clumped, with lower density interclump gas, then ionizing photons may penetrate deeper inside the molecular cloud (the penetration depth obviously depends on the density of the interclump medium and the flux of ionizing photons). In such a situation one might expect to observe a coincidence of all three emission regions.

Plate 4 shows the 3.28-μm image overlaid with a contour map of the H_2 emission. The coincidence of the two emission features is evident, the brightest parts of the emission being coincident to ±1 arcsec. Plate 5 shows the 3.28-μm image overlaid with a contour map of the Br γ emission. The Br γ emission peaks inside the 3.28-μm and H_2 emission regions. The ridge of Br γ emission to the north-west follows the western ridge in the 3.28-μm and H_2 emission. There is no corresponding Br γ emission (or 21-cm continuum emission) associated with the 3.28-μm and H_2 emission at the north-east ridge. For comparison, in the Orion Bar, the hydrogen recombination radiation peaks inside the 3.28-μm and H_2 emission, and the recombination radiation quickly dies away

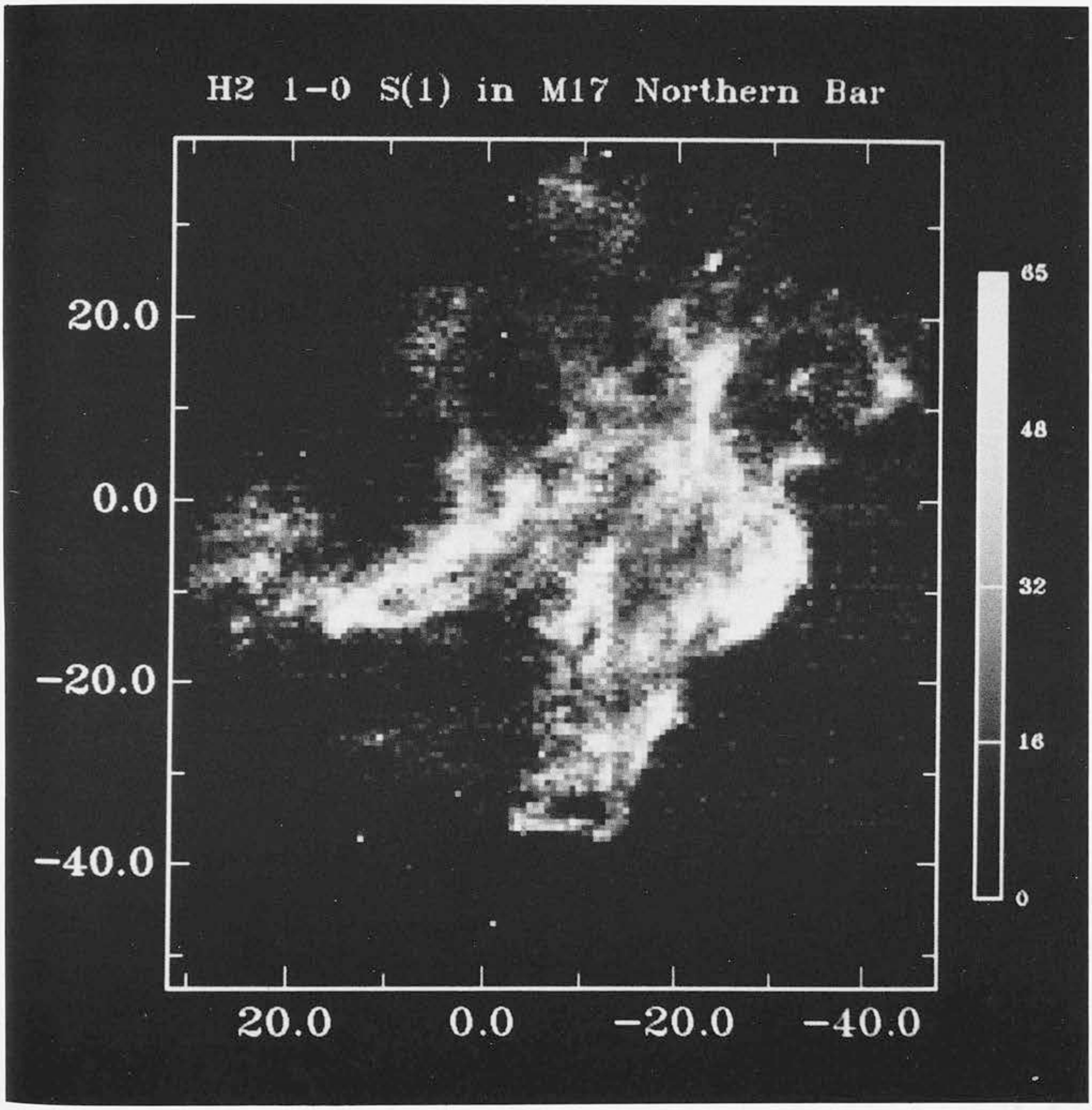

Plate 1. The northern bar imaged in the $v = 1-0$ $S(1)$ transition of molecular hydrogen. The continuum has been subtracted. The numbers in the scale are data counts and the calibration is 2.3×10^{-20} W m^{-2} count^{-1}. The offsets are in arcseconds.

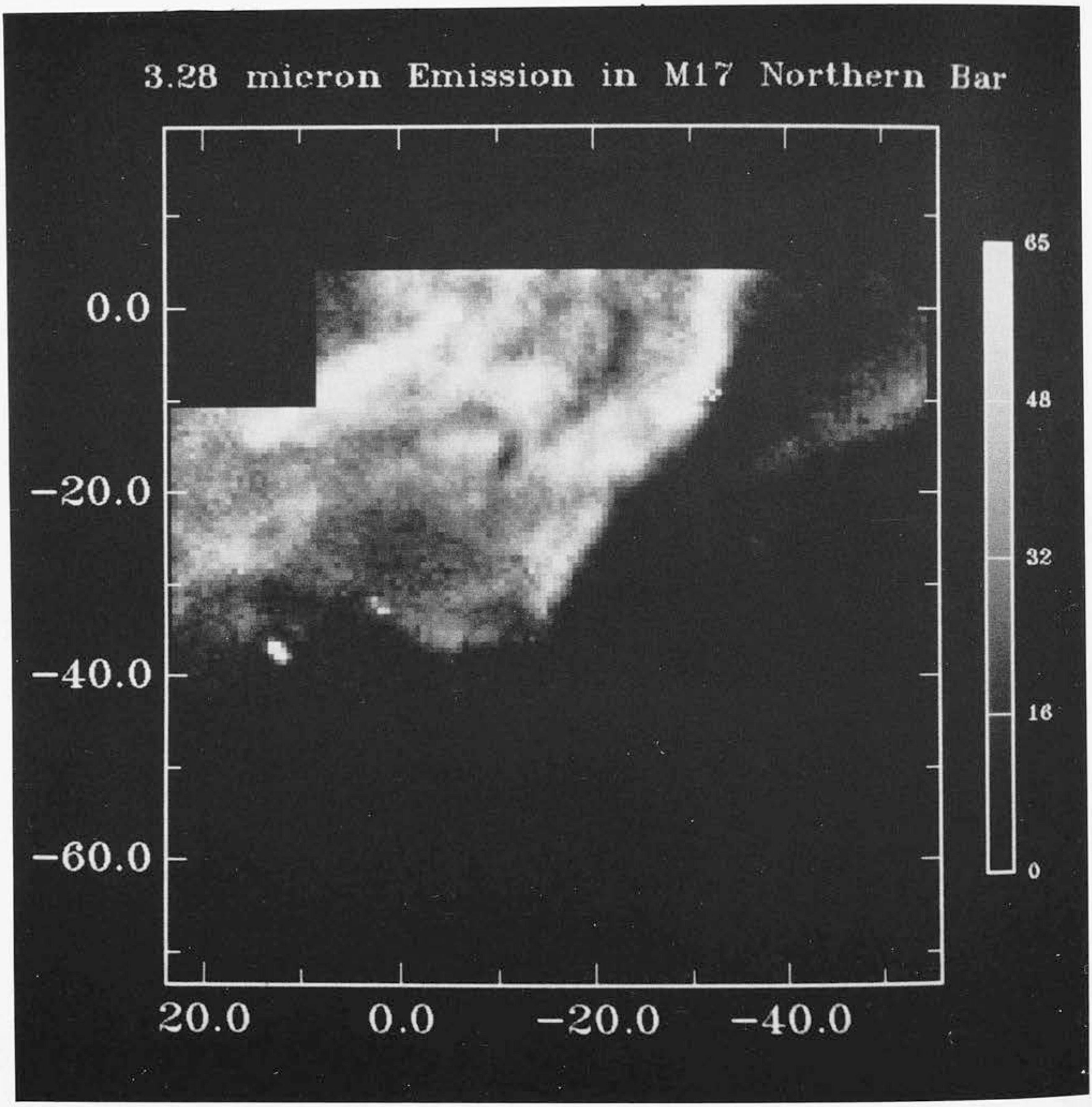

Plate 2. The northern bar imaged in the 3.28-μm emission feature. The continuum has not been subtracted. The corresponding continuum image ($\lambda = 3.1\ \mu$m) is flat, implying that the structure that we see in this image is 3.28-μm emission. The numbers in the scale are data counts and the calibration is 3.1×10^{-31} W m^{-2} Hz^{-1} count^{-1}. The offsets are in arcseconds.

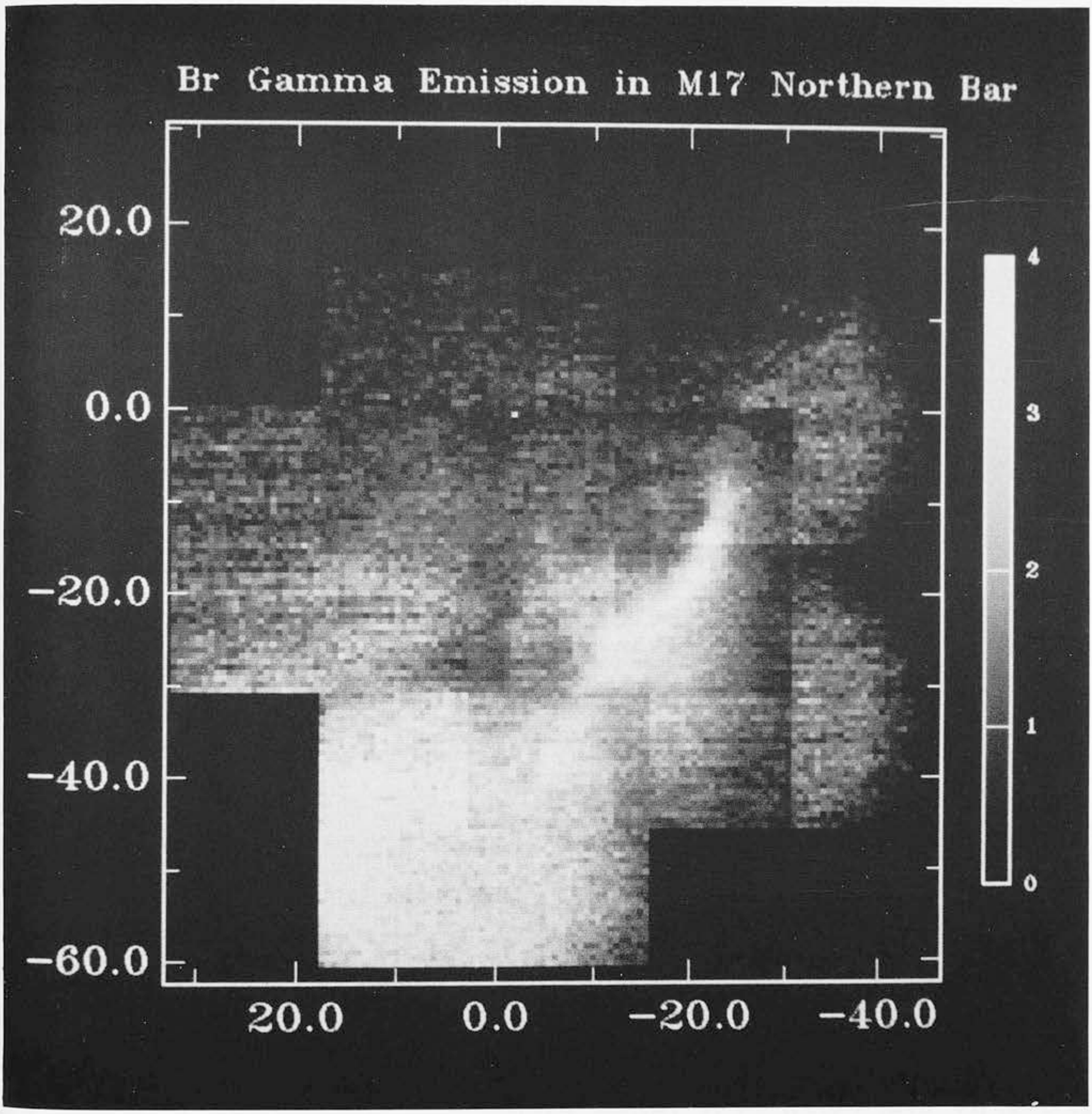

Plate 3. The northern bar images in the Brγ line of H$^+$. The continuum has been subtracted. The numbers in the scale are data counts and the calibration is 2.5×10^{-18} W m^{-2} count^{-1}. The offsets are in arcseconds.

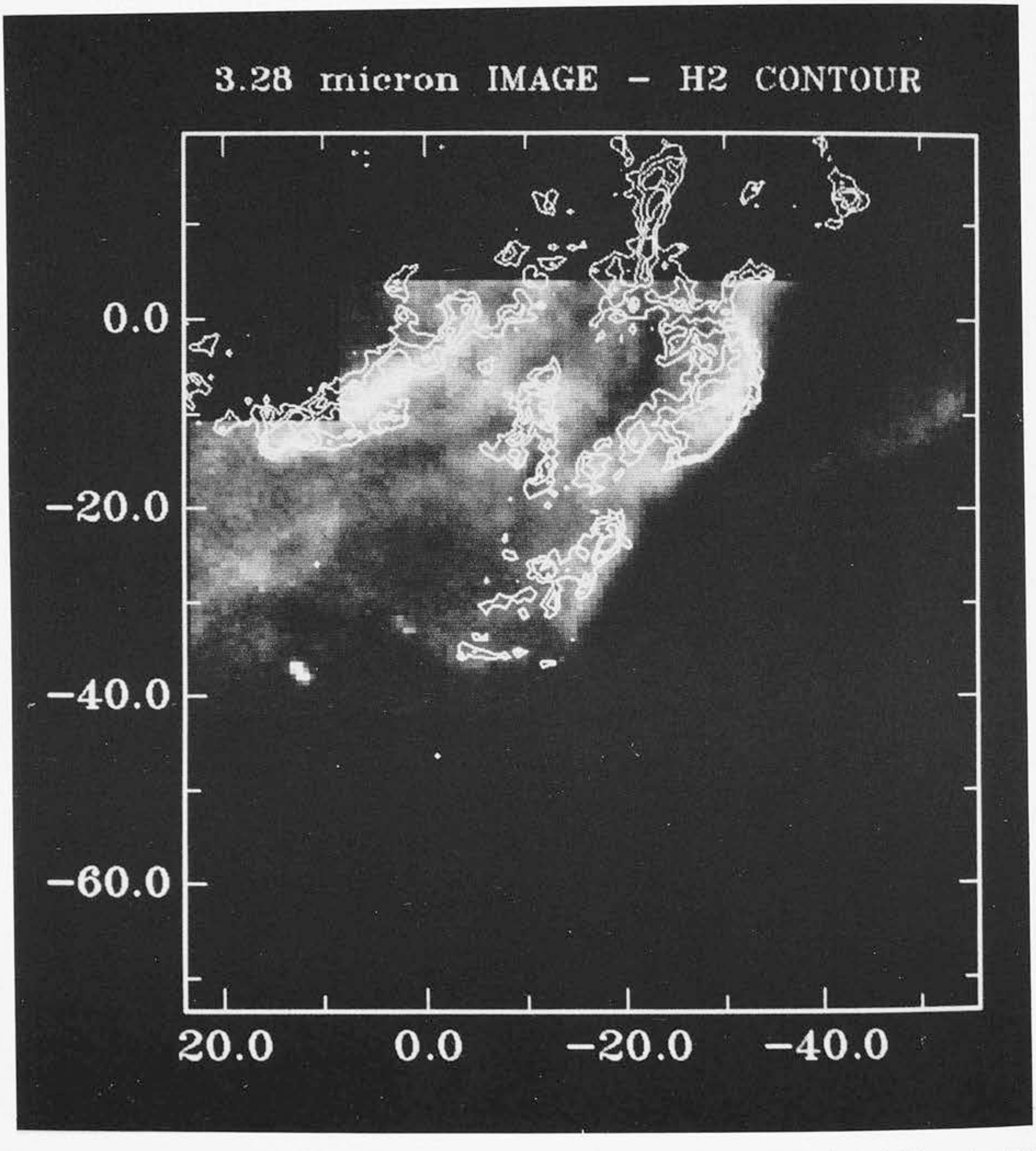

Plate 4. The northern bar showing the molecular hydrogen emission (contour) and the 3.28-μm emission (image). The contour levels are plotted from a base-level defined at 0.3 counts above the background and at intervals of 0.2 counts.

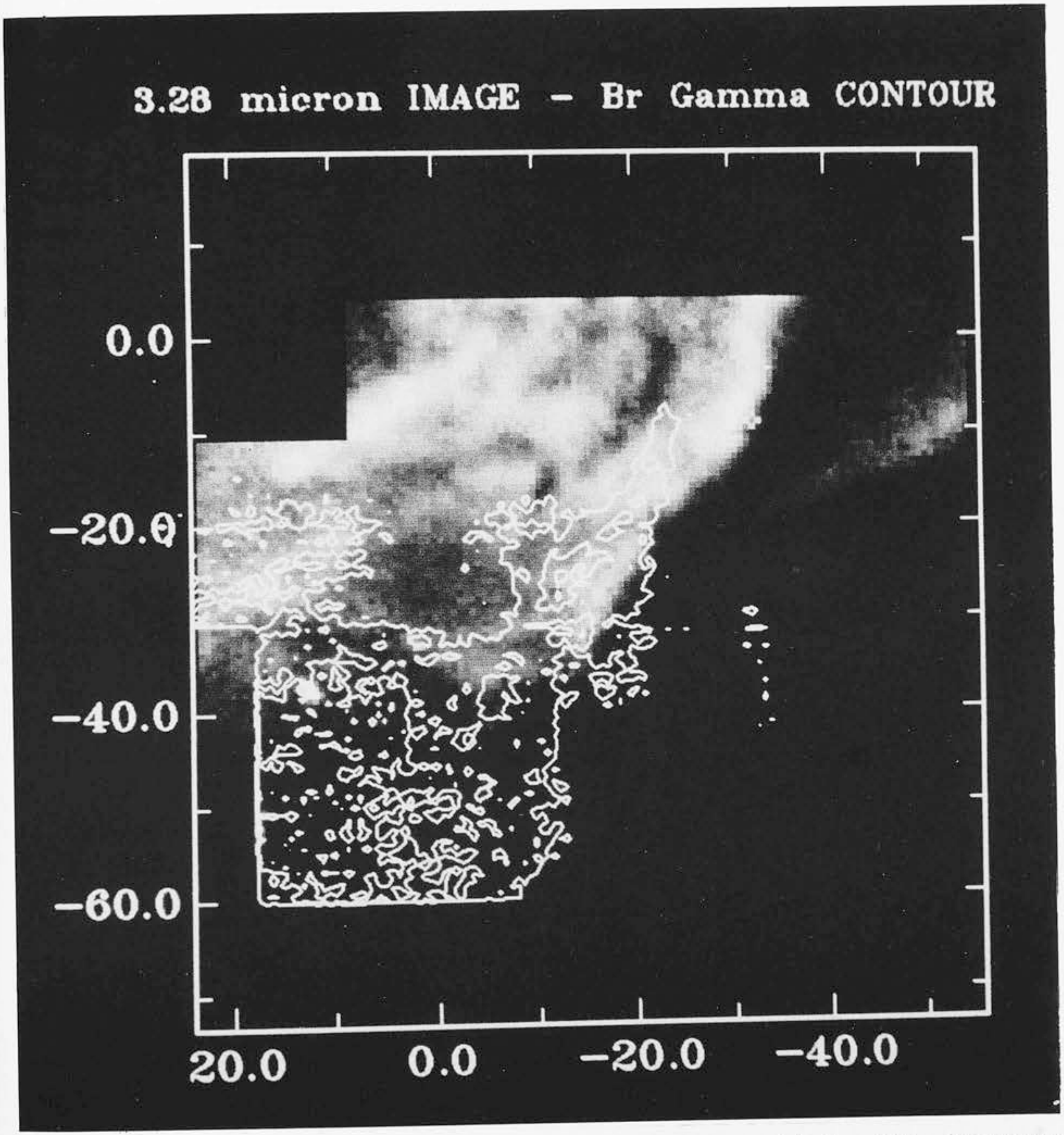

Plate 5. The northern bar showing the Brγ recombination emission (contour) and the 3.28-μm emission (image). The contour levels in the figure are plotted from a base-level defined at 2 counts above the background and at intervals of 1 count.

in the neutral cloud – by 85 per cent at the molecular hydrogen peak (Sellgren *et al.* 1990).

4 DISCUSSION

H_2 line intensities calculated in one-dimensional PDR models are the integrated column densities along a normal through the cloud face as if seen face-on. To make a detailed comparison with models and observations, the geometry of the region must be considered, i.e. the angle between the normal of the cloud face and the line of sight to the observer. Following Icke, Gatley & Israel (1980) and Felli *et al.* (1984), we adopt a value of 70° inclination of the density gradient to our line of sight and find that the intensity at the brightest point in Plate 1, if seen face-on, is $I_{1-0\,S(1)} \sim 5 \times 10^{-8}$ W m^{-2} sr^{-1}. This agrees well with the theoretical modelling (BHT) for 10^5-cm^{-3} gas with a UV flux appropriate for M17 ($G_0 \sim 10^4$), but does assume a surface beam filling factor of unity, i.e. uniform density. However, from our images of the region it is evident that structure down to the ~2-arcsec level is present, implying that the region is clumped. It is possible to model a clumpy medium by a two-component model which fits different beam filling factors of high- and low-density models to the observed intensity (BHT). A possible fit to the line flux occurs if 20 per cent of the flux in the beam comes from gas at $n \sim 10^7$ cm^{-3} and 45 per cent from gas at $n \sim 10^5$ cm^{-3}. To make accurate fits in a two-component model, data from fine-structure and CO rotational lines are necessary in addition to the H_2 data.

In two-component PDR models, the emission is dominated by the high-density component in the beam (BHT). If a two-component PDR model is necessary to describe the PDR in the northern bar of M17, one would expect the H_2 emission spectrum to have thermalized line ratios. This seems in contradiction to the results obtained by Tanaka *et al.* (1989), who measured the diagnostic lines of 1–0 $S(1)$ and 2–1 $S(1)$ of the H_2 spectrum in the northern bar of M17, and found that the ratio was consistent with pure fluorescent emission in a low-density gas (1–0/2–1 ~ 2). However, they were using a large-aperture beam (19.6 arcsec), and from our images it is clear that structures on scales much smaller than this exist in the region. High spatial as well as high spectral resolution spectra will need to be taken to clarify the physical conditions within the northern bar of M17.

The value of the density derived above (assuming unit beam filling factor) is very much dependent on the angle between the normal of the cloud face, i.e. the density gradient, and the observer's line of sight. If the PDR were more edge-on, i.e. $\theta > 70°$, then the density required to match the measured intensity would fall below 10^4 cm^{-3}, inconsistent with the density deduced from the Brγ emission measure. However, smaller angles and hence higher densities, producing higher intensities through the cloud normal, are allowed.

Plate 5 shows the Brγ emission in relation to the 3.28-μm emission. A close comparison of the Brγ image to the 21-cm radio continuum map by Felli *et al.* (1984) shows a good correspondence between the north-western ridge of Brγ emission and a small (~20 arcsec) feature in the radio continuum map, whose emission measure has been increased relative to its immediate surroundings by virtue of its higher density. The radio continuum map also confirms an absence of emission to the north-east, where H_2 and 3.28-μm emission are prominent.

We consider two models to explain these observations. First, the absence of recombination radiation in the north-east is due to a depletion of ionizing photons sustaining the ionization of the H II region, and so we are looking at a cross-section of the region (see Fig. 1a). The PDR in Orion's Bar has a similar morphology, being seen edge-on. In Orion, the 3.28-μm feature is observed (Sellgren *et al.* 1990) to peak ahead of the ionization front, but then quickly dies away to an optical depth of $A_v \sim 2$ mag, as the exciting radiation is attenuated. In the northern bar of M17 (Plate 5), the 3.28-μm emission is seen ahead of the Brγ emission, but is still strong in emission up to 20 arcsec away from the ionization front, corresponding to an optical depth of $A_v \sim 38$ mag, assuming a gas density of at least 10^5 cm^{-3}. This may be reconciled by the presence of clumping, which will allow high-energy FUV photons to penetrate further into the molecular cloud, producing warm surfaces on clumps and thereby exciting the 3.28-μm feature into emission. The idea of clumping of PDRs has already been invoked by Stutzki *et al.* (1988) to explain the detection of [C II] – first ionization potential = 11.3 eV – on a scale of 15 pc, in the south-western bar of M17.

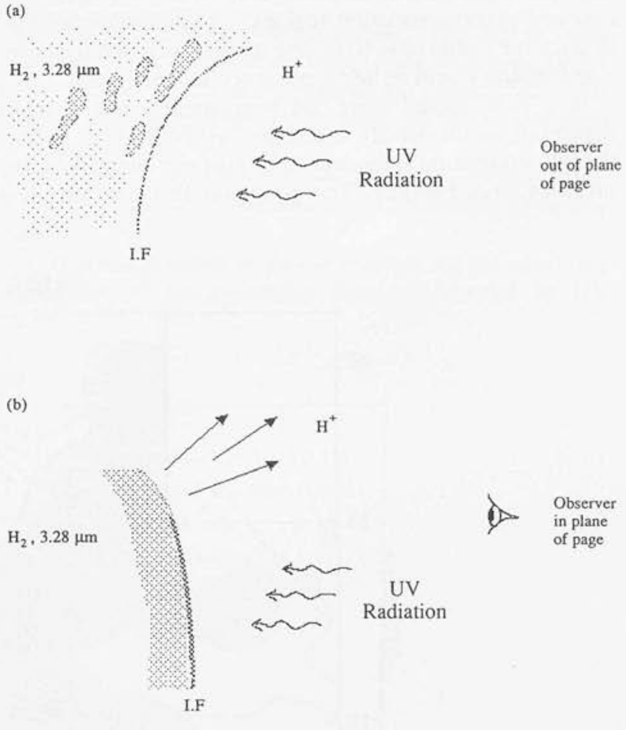

Figure 1. (a) Schematic diagram showing the H II region and the ionization front (IF) as a cross-section, with the observer out of the plane of the page. The molecular cloud is depicted by light shading with high-density clumps in darker shading. The clumpy molecular cloud allows FUV photons ($h\nu < 13.6$ eV) to penetrate deep into the molecular cloud and excite the surfaces of dense clumps. (b) Schematic diagram showing the H II region and ionization front as a cross-section. In this case, the observer is in the plane of the page. The ionized material at the top is streaming away into vacuum, decreasing in density and hence emission measure (until it is below our detection threshold), and therefore only emission from H_2 and 3.28 μm (dark shading) is seen at this position.

Alternatively, if one is looking at the surface of the molecular cloud, then since the 3.28-μm emission traces the edge of the neutral cloud and the Brγ emission the ionization front, one would expect some correlation between the two emission features. However, no correlation is evident; to the north-east of the image the 3.28-μm emission is bright but the Brγ emission is below the detection threshold. In terms of the emission measure this corresponds to a drop in the ionized density by a factor of 3 assuming a small, if not negligible, change in the length-scale. If we are looking at the top edge of the ionization front (see Fig. 1b), then it is possible to imagine the ionized material streaming away, under pressure, over the surface of the molecular cloud into a lower density medium, consequently decreasing in density as it does so. Meanwhile, this surface is still irradiated by soft UV photons, exciting the 3.28-μm and H_2 emission features. Such a model would be consistent with a blister H II region model (e.g. Icke *et al.* 1980).

Similarly, in the south-western bar of M17, comparing the molecular maps of the region from Stutzki *et al.* (1988) and Stutzki & Güsten (1990) to the radio continuum (Felli *et al.* 1984) reveals an anticorrelation between the molecular and ionized regions. As there is [C II] emission associated with the radio continuum and molecular emission (Stutzki *et al.* 1988), another plausible scenario may be that there exists a large predominantly atomic transition zone between the ionized and photodissociation regions. The ionization fraction in this zone would have to be low enough such that the emission measure would be below our detection threshold.

In a PDR model there are two characteristic regimes depending on the density n, and the far-UV field G_0. In one, the UV attenuation is dominated by dust shielding and in the other by line shielding. The condition that line shielding dominates over dust shielding is approximately given by (BHT):

$$\frac{n}{G_0} \geq 40\ \mathrm{cm}^{-3}, \tag{1}$$

and dust extinction dominates when n/G_0 falls below this value. For high values of this ratio, where line shielding of the FUV dominates over dust shielding, the H I/H_2 transition zone is at an optical depth of $A_v \ll 1$ mag, i.e. close to the edge of the cloud where the gas is still hot (~ 1000 K).

As an example of an application of this theory, images of the PDR in Orion's Bar (Fig. 2; Burton *et al.* 1988b) show a structure described by the standard model of Tielens & Hollenbach (1985a, b) in which the H_2 peaks in intensity at $A_v \sim 3$ mag, behind the 3.28-μm feature. The intensity of the 3.28-μm feature in Orion's Bar decreases with distance into the cloud, according to the extinction of the exciting FUV radiation (Sellgren *et al.* 1990; Burton *et al.* 1988b). Although no chemical or complete thermal balance model has been developed for the carrier of the 3.28-μm emission, Sellgren *et al.* infer their conclusions from the fact that the spatial extent of the 3.28-μm emission occurs over one optical depth of the exciting FUV radiation. Tielens & Hollenbach (1985b) have modelled the emission from ionized species (C^+, Si^+, Fe^+), neutral species (C, O) and CO rotational lines in Orion's Bar and find a density to UV flux ratio of

$$\frac{n}{G_0} \approx 1\ \mathrm{cm}^{-3}, \tag{2}$$

satisfying the inequality for dust shielding (*cf.* equation 1), and producing the stratified structure of the H_2 and 3.28-μm emission in the models.

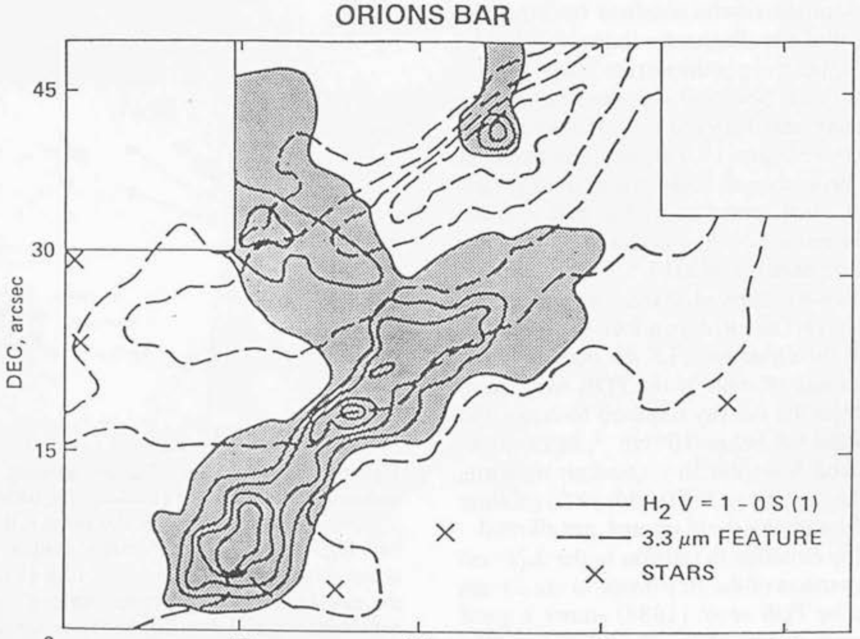

Figure 2. The PDR in Orion's Bar showing the H_2 emission (shaded contour) and the 3.28-μm emission. This figure is taken from Burton *et al.* (1988b). Note that this image has been flipped east to west during the data reduction such that north-east is at the top right-hand corner. The offsets are in arcseconds.

In contrast to Orion, NGC 2023 (Fig. 3; Burton *et al.* 1988b; Moorhouse *et al.*, in preparation) has a quite different morphology. The H_2 and 3.28-μm emission regions are spatially coincident, implying that line shielding may be dominating the extinction and bringing the H I/H_2 transition zone close to the surface. Hasegawa *et al.* (1987) have inferred a low-density region, $n \sim 10^4$ cm^{-3}, with $G_0 \sim 10^4$, implying a value for n/G_0 similar to the Orion Bar and the regime where dust shielding dominates the extinction. The angular scales of the two objects are very similar and hence observation and theory do not agree in this instance. However, recent modelling of a high-resolution H_2 emission spectrum of NGC 2023 using a two-component model requires the presence of high-density gas, $n \sim 10^5$–10^6 cm^{-3}, and G_0 be a little less than 10^4 (Burton, private communication). The value of n/G_0 would thus imply that line shielding may be dominating the extinction and therefore bringing the H_2 closer to the surface and producing the observed coincidence of 3.28-μm and H_2 regions. Recent measurements of reflection and planetary nebulae have shown that the spatial coincidence of the 3.28-μm and H_2 emission regions is quite common (Burton *et al.* 1988b; Moorhouse *et al.*, in preparation).

The value of G_0 at the northern bar of M17 is $\sim 3 \times 10^4$ (Stutzki *et al.* 1988). If dust shielding is dominating the FUV attenuation, the separation of 3.28-μm and H_2 emission regions is of order $A_v \sim 1$, as in Orion's Bar. Our observations show that the emission regions are spatially coincident, ruling out gas densities of $n \ll 10^5$ cm^{-3} since any separation of order $A_v \sim 1$ would then be resolvable (for instance, a gas density of $n = 10^4$ cm^{-3} and separation of $A_v = 1$ is equivalent to 6-arcsec spatial separation at the distance to M17). If the extinction of FUV photons is dominated by line shielding, then equation (1) tells us that the gas density would have to satisfy $n > 10^6$ cm^{-3}. The only result which can be inferred from our observations is that the gas density $n > 10^5$ cm^{-3}, and it is not possible to determine whether dust shielding is attenuating the FUV photons.

The emission spectrum of molecular hydrogen constitutes only a small part of the total emission from a photodissociation region, which is dominated by the cooling transitions of [O I] and [C II]. Therefore, only observations of fine-structure lines as well as the molecular lines from H_2 and CO will be able to determine the physical conditions of the PDR in the northern bar of M17.

5 CONCLUSION

We have imaged a small region of the PDR in the northern bar of M17 in the 1–0 $S(1)$ line of H_2, the Brγ line of H^+ recombination radiation and the 3.28-μm emission feature. We arrive at the following results and conclusions.

(i) The intensity of the H_2 1–0 $S(1)$ line, as seen from a normal to the face of the cloud, if it is inclined at 70° to our line of sight, is $\sim 5 \times 10^{-8}$ W m^{-2} sr^{-1}. The flux density of the 3.28-μm feature is 1.7×10^{-5} W m^{-2} μm^{-1} sr^{-1}.

(ii) The bright parts of the H_2 and 3.28-μm emission regions are spatially coincident to an accuracy of ~ 1 arcsec. This agrees with similar observations of reflection nebulae by Burton *et al.* (1988b) and Moorhouse *et al.* (in preparation).

(ii) The Brγ emission correlates well with 21-cm radio continuum observations of the same region (Felli *et al.* 1984). A Brγ filament to the north-west of our image (Plate 3) is apparent as a clump in the 21-cm map (and at the same position), and bounds the H II region.

(iv) It is not clear whether the extinction of FUV photons in the region is dominated by dust shielding or by line shielding.

(v) It is not possible to decide whether we are observing the surface of the molecular cloud illuminated by UV

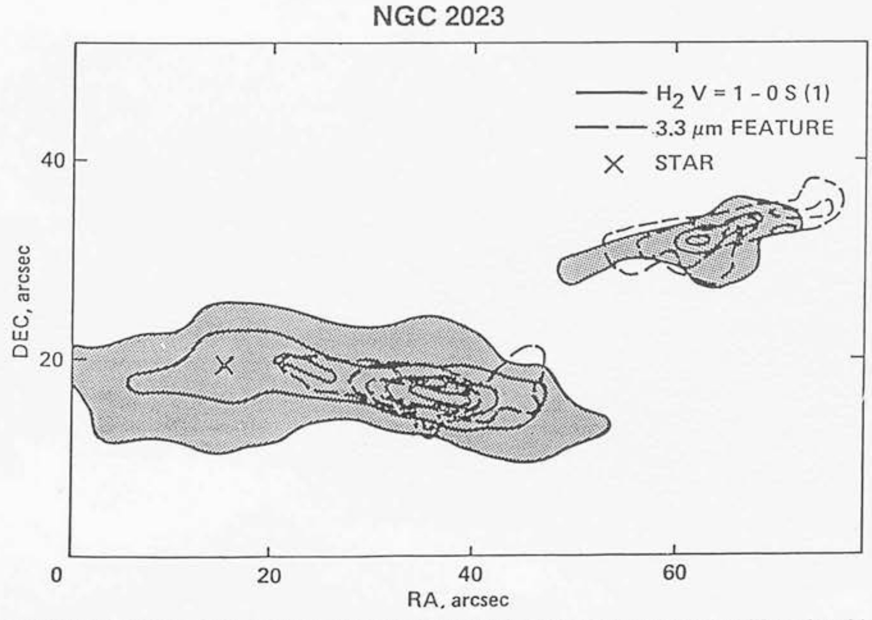

Figure 3. The PDR in NGC 2023 showing the H_2 emission (shaded contour) and the 3.28-μm emission. Note that this image has been flipped east to west during the data reduction such that north-east is at the top right-hand corner. This figure is taken from Burton *et al.* (1988b). The offsets are in arcseconds.

photons, or whether we are looking at a cross-section of the region, i.e. near edge-on (e.g. Orion's Bar).

(vi) A high-density region ($n \geq 10^5$ cm^{-3}) is required to explain the spatial coincidence of the H_2 and 3.28-μm emission regions.

(vii) A single-component high-density ($n \sim 10^5$ cm^{-3}; $G_0 \sim 10^4$) PDR model is sufficient to reproduce the H_2 line intensity observed. However, the fact that our images reveal structure on a scale of ~ 2 arcsec suggests that a two-component PDR model is probably the preferred solution.

ACKNOWLEDGMENTS

We would like to acknowledge the help of staff members of UKIRT, the Royal Observatory Edinburgh Photolabs, and Phil Puxley for useful discussions. AC acknowledges the support of a SERC studentship.

REFERENCES

Beetz, M., Elsässer, H., Poulakos, C. & Weinberger, R., 1976. *Astr. Astrophys.*, **50,** 41.

Black, J. H. & van Dishoeck, E. F., 1987. *Astrophys. J.*, **322,** 412.

Bregman, J. D., Allamandola, L. J., Tielens, A. G. G. M., Geballe, T. R. & Witteborn, F. C., 1989. *Astrophys. J.*, **344,** 791.

Burton, M. G., Hollenbach, D. J. & Tielens, A. G. G. M., 1988a. *IR Spectroscopy in Astronomy, 22nd ESLAB Symposium,* p. 141, ed. Kaldeich, ESA Publications Ltd.

Burton, M. G., Moorhouse, A., Brand, P. W. J. L., Roche, P. F. & Geballe, T. R., 1988b. In: *Interstellar Dust: Contributed Papers, NASA CP 3036,* p. 87, eds Tielens, A. G. G. M. & Allamandola, L. J.

Burton, M. G., Hollenbach, D. J. & Tielens, A. G. G. M., 199C. *Astrophys. J.*, **365,** 620 (BHT).

Duley, W. W., 1985. *Mon. Not. R. astr. Soc.*, **215,** 259.

Duley, W. W. & Williams, D. A., 1988. *Mon. Not. R. astr. Soc.*, **231,** 969.

Duley, W. W. & Williams, D. A., 1990. *Mon. Not. R. astr. Soc.*, **247,** 647.

Felli, M., Churchwell, E. & Massi, M., 1984. *Astr. Astrophys.*, **136,** 53.

Gatley, I. & Kaifu, N., 1987. *Astrochemistry, IAU Symp. No. 120,* p. 153, eds Vardya, M. S. & Tarafdar, S. P., Reidel, Dordrecht.

Gatley, I., Becklin, E. E., Sellgren, K. & Werner, M. W., 1979. *Astrophys. J.*, **233,** 575.

Geballe, T. R., Tielens, A. G. G. M., Allamandola, L. J., Moorhouse, A. & Brand, P. W. J. L., 1989. *Astrophys. J.*, **341,** 278.

Habing, H. J., 1968. *Bull. astr. Insts Neth.*, **19,** 421.

Harper, D. A., Low, F. J., Rieke, G. H. & Thronson, H. A., 1976. *Astrophys. J.*, **205,** 136.

Harris, A. I., Stutzki, J., Genzel, R., Lugten, J. B., Stacey, G. J. & Jaffe, D. T., 1987. *Astrophys. J. Lett.*, **322,** L49.

Hasegawa, T., Gatley, I., Garden, R. P., Brand, P. W. J. L., Ohishi, M., Hayashi, M. & Kaifu, N., 1987. *Astrophys. J. Lett.*, **318,** L77.

Icke, V., Gatley, I. & Israel, F., 1980. *Astrophys. J.*, **236,** 808.

Lada, C. J., DePoy, D. L., Merrill, K. M. & Gatley, I., 1991. *Astrophys. J.*, **374,** 533.

Leger, A. & Puget, J. L., 1984. *Astr. Astrophys.*, **137,** L5.

Meadows, P., 1986. *MPhil thesis,* University of Edinburgh.

Sellgren, K., Tokunaga, A. T. & Nakada, Y., 1990. *Astrophys. J.*, **349,** 120.

Sternberg, A. & Dalgarno, A., 1989. *Astrophys. J.*, **338,** 197 (SD).

Stutzki, J. & Güsten, R., 1990. *Astrophys. J.*, **356,** 513.

Stutzki, J., Stacey, G. J., Genzel, R., Harris, A. I., Jaffe, D. T. & Lugten, J. B., 1988. *Astrophys. J.*, **332,** 379.

Tanaka, M., Hasegawa, T., Hayashi, S. S., Brand, P. W. J. L. & Gatley, I., 1989. *Astrophys. J.*, **336,** 207.

Tielens, A. G. G. M. & Hollenbach, D. J., 1985a. *Astrophys. J.*, **291,** 722.

Tielens, A. G. G. M. & Hollenbach, D. J., 1985b. *Astrophys. J.*, **291,** 747.

Webster, A. S., 1991. *Nature,* **352,** 412.